Dissertation

Oxidation of surfactant stabilized magnetic cobalt nanoparticles

vorgelegt von
Britta Vogel

July 18, 2011

Universität Bielefeld
Fakultät für Physik

For Aleks

Erklärung

Hiermit erkläre ich, dass ich die vorliegende Arbeit selbständig verfasst und keine anderen als die angegebenen Hilfsmittel verwendet habe.

Bielefeld, 18. Juli 2011

Gutachter:
Prof. Dr. Andreas Hütten
Prof. Dr. Dario Anselmetti

Datum des Einreichens der Arbeit: 22. Juli 2011

Contents

0 Introduction

“There is plenty of room at the bottom” was the name of a talk given by Richard Feynman at the annual meeting of the American Physical Society in 1959.

Today the main idea is still more topical than ever. Research in the field of nanoscale structures is booming in modern physics because nanomaterials exhibit outstanding properties. The surface to bulk ratio is extremely large and, therefore, surface effects gain in importance, leading to unique magnetic, electronic and optical effects [1, 2, 3]. The boom has been made possible by the fast development of technology during the last few decades, allowing the visualization of structures in the nanometer range. Improved methods to fabricate nanoparticles have contributed to this development as well. Nanoparticles and physics of nanostructures already play an important role in economy. Products built of or containing nanoparticles are widely spread although the risks and advantages have not been evaluated completely yet [4].

History shows, that nanoparticles accidentally appeared much earlier. By the end of the middle ages colloidal gold was used as heat stable pigment to fabricate red glass [5].
At the present, one of the most impressive discoveries are no doubt ferrofluids [1].
Who would not be fascinated if a previously even, black, oily liquid suddenly exhibits ripples and drops upwards from a petri dish, defying gravity, to a conical tip of an electromagnet located in some distance above the petri dish. It flows on the conical surface, forms a film and then grows spikes with sizes in the several millimeter range, which then suddenly start to shrink. They collapse and flow and drop back as liquid into the petri dish, while a magnetic field is varied over the electromagnet during the whole process. Several videos can be found on the internet platform *youtube* that can be declared as (some kind of) art [7].

Magnetic nanoparticles can be applied directly or as ferrofluid. In the case of the ferrofluid the manipulation of the liquid by the particles is the main task. Further applications of ferrofluids are printing ink for magnetic bar codes or circuit paths [6]. They are also used as sealant for rotatable parts in vacuum devices and space flight vessels, where the particle suspension is kept in place by magnets. They are also used in grease to improve the breaking effect of accelerators or as damping material in loudspeakers and motors [6,8].
A possibility for a direct application of magnetic nanoparticles is their use as magnetoresistive random access memory (MRAM) which would increase the storage density. [9]
Further use of nanoparticles lies in the biological and medical sector. This involves the necessity of a biocompatible coating of the particles. Possible applications are phagokinetic studies, separation and purification of biological molecules and cells, bio detection of pathogens, tissue engineering, probing of DNA structure, detection of proteins and gene delivery. Drug delivery is another application which could improve further cancer therapy

---

[1] Ferrofluids are a colloidal suspension of magnetic (nano)particles, which are stabilized e.g. with surfactants against agglomeration in the liquid and to improve their solubility [6].)

by transporting the drug directly into the tumor. This would enable the use of more potent drugs while the rest of the body would remain less affected [10]. Today particles are already applied successfully in studies as a contrast agent in MRI and for hyperthermia, where the particles are injected directly into a tumor and heated by alternating magnetic fields resulting in an overheating of the surrounding tissue and therefore dying of the heated cells [10, 11, 12]. Another use lies in the field of biotechnology, where the particles could be attached to molecules as magnetic markers to gain control over the molecules on the one hand and to monitor them with magnetoresistive biochips on the other hand [13].

Iron oxide $\mathsf{Fe_xO_y}$ particles embedded in a matrix are mostly used in todays applications. The utilization of other magnetic materials offers a decreased particle size with an equal or increased saturation magnetization. Such materials are among others Fe, FeCo and Co. One problem bears the oxidation propensity of the particles. Metal oxides exhibit lower or none of the desired magnetic properties.
In a ferrofluid the particles have to be stabilized against agglomeration; as well as oxidation. The case of agglomeration can be prevented by covering the particle surface with surfactant molecules. It bears an interesting ansatz to find out, to what extent the surfactants prevent the particles from oxidation as well.

To gain information concerning the protection effects of the surfactants and to improve understanding of the oxidation process on nanoscales, the change of the magnetic properties during the oxidation process as well as the investigation of the microstructural properties of the particles can be used, which are part of this thesis.
First a short introduction to the theory of magnetism, synthesis and formation of nanoparticles is given. The possibilities for stabilization, especially the covering of the nanoparticle surface by amphiphile molecules, called surfactants, and the oxidation process of nanoparticles is described, followed by an overview over the devices used for analysis and a desription of the corresponding sample preparation.
The preparation of cobalt nanoparticles is described and the results of the stabilization with different surfactants are displayed including the influence on size, shape and crystal structure.
Afterwards the reasons for a surfactant exchange are explained.
First the used surfactants and the process of the surfactant exchange are described. Two batches of particles were fabricated with TOPO, one was fabricated with oleylamine. The surfactants deployed during the exchange posses either a amine or a carboxyl headgroup and different chainlengths and number. Investigated were the influence on the size, shape, crystallinity, inter particle distance and surfactant conformation as well as magnetic properties. The oxidation of the samples at room temperature and under ambient conditions, and temperatures of $-18°C$, $48°C$, $80°C$, $121°C$, $180°C$ and $300°C$ was investigated, starting a few hours after an initial exposure to air during sample preparation. A change in the crystallinity of the particles stored at $180°C$ was detected. To gain more insight in the oxidation influence of the surfactants the sample preparation and measurement method were modified and samples were investigated directly after fabrication and surfactant exchange, beginning with the first measurements about one minute after initial exposure to air. The influence of the surfanctant on the crystal structure of the particles is described. Finally a closer look is taken at the oxidation behaviour of large multilayer particle clusters.

1 Theoretical Background

In this chapter the basics about the magnetic effects corresponding to the nanoparticles are described. The formation of nanoparticles is described in theory and the synthesis implementation and an overview of the oxidation of nanoparticles is given, as well.

1.1 Magnetism

Magnetism of solids originates from the magnetic moments of their atoms and especially their electrons. The movement of an electron in the electrical field of an atomic nucleus is connected to two magnetic moments. The weak moment of the nucleus can generally be neglected. The total moment $\vec{m}$ of electrons consists of two contributions, their orbital moment $\vec{m_B}$ and their spin moment $\vec{m_s}$.

$$\vec{m} = \sum_{i,j} \vec{m_s^i} + \vec{m_B^j} \tag{1.1}$$

The magnetic dipole moment, based on the orbital angular moment $\vec{L}$, is given by

$$\vec{m_B} = -\frac{\mu_B}{\hbar}\vec{L} \qquad \text{with} \qquad \mu_B = \frac{e\hbar}{2m_e} \quad . \tag{1.2}$$

The contribution by the spin angular moment $\vec{S}$ is

$$\vec{m_s} = -\frac{2\mu_B}{\hbar}\vec{S} \quad . \tag{1.3}$$

This can be written generalized as

$$\vec{m} = g\frac{\mu_B}{\hbar}\vec{L}_{B/s} \tag{1.4}$$

with $g = 1$ for the orbital angular moment or $g \approx 2$ for the spin angular moment. [14, 15] If a magnetic material is brought into an external magnetic field, the dipole moments align along the field lines. The magnetisation $\vec{M}$ describes the alignment of magnetic moments $\vec{m_i}$ per volume V.

$$\vec{M} := \sum_i \frac{\vec{m_i}}{V} \tag{1.5}$$

An external magnetizing field $\vec{H}$ induces a magnetic field $\vec{B}$ in a material, which consists of the external magnetizing field $\vec{H}$ and the magnetisation $\vec{M}$. Inserted into an external magnetic field the magnetic flux density of the vacuum $\vec{B} = \mu_0\vec{H}$ is increased by the magnetic field in the material.

$$\vec{B} = \mu_0(\vec{M} + \vec{H}) \tag{1.6}$$

To describe the magnetisation of a material a proportionality constant between the magnetisation $\vec{M}$ and the magnetic field intensity $\vec{H}$ is added.

$$\vec{M} = \chi\vec{H} \qquad \rightarrow \qquad \chi = \frac{d\vec{M}}{d\vec{H}} \tag{1.7}$$

χ is called magnetic susceptibility. The linearity in this equation disappears in the case of ferromagnetic materials. See 1.1.1 for further information. Equation 1.6 can be reformed to:

$$\vec{B} = \mu_0(\vec{H} + \vec{M}) = \mu_0(\vec{H} + \chi\vec{H}) = \mu_0(1 + \chi)\vec{H} = \mu_0\mu_r\vec{H} \tag{1.8}$$

Where $\mu_r = 1 + \chi$ denotes the permeability of the material [15]. The permeability is an extent for the transmissibility of a material for magnetic fields.

1.1.1 Forms of magnetism

Magnetism is subdivided into several kinds according to the different behaviour of substances in presence and absence of a magnetic field [15]. Magnetic materials are characterised by their susceptibility.
In general six [1] forms of magnetisation are described: diamagnetism, paramagnetism, ferromagnetism, antiferromagnetism, ferrimagnetism and corresponding to ferromagnetism on nanoscales, superparamagnetism, which is described in detail in section 1.1.2.

Diamagnetism

Diamagnetic materials are expelled from inhomogeneous magnetic fields. Inside the material the field is reduced, compared to the one on the outside. The susceptibility χ is negative.

$$\chi < 0 \tag{1.9}$$

The magnetisation is antiparallel to the external field as depicted in 1.1.1.

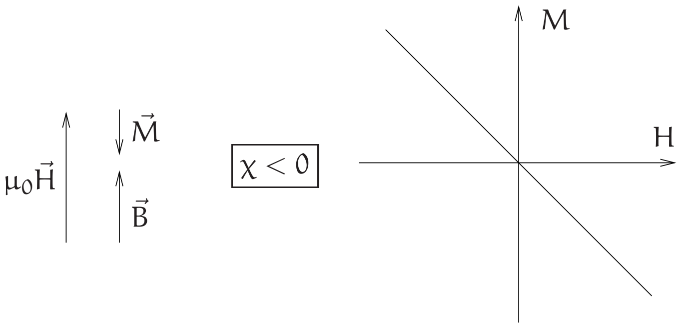

Figure 1.1: Diamagnetism: Magnetisation over applied field - schematic [15].

---

[1] If superparamagnetism is regarded as a separate form of magnetism.

Paramagnetism

Paramagnetism is characterized by an increased field inside the material compared to the one on the outside. A paramagnetic material is drawn into an inhomogeneous magnetic field. The susceptibility χ is positive.

$$\chi > 0 \tag{1.10}$$

This results from the existence of a permanent magnetic moment in the atoms/molecules, which is randomly oriented so that the overall magnetisation in absence of an external field compensates to zero. If an external field is applied, the magnetic moments align parallel to the field, see figure 1.1.1.

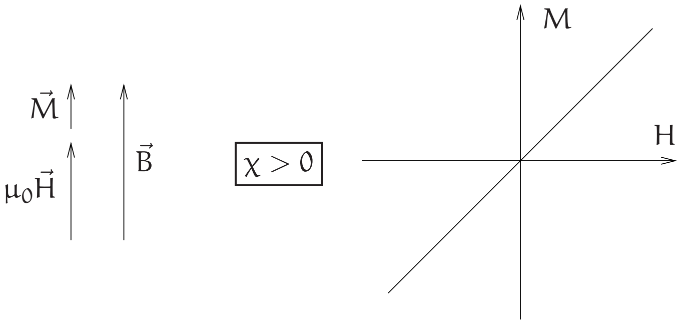

Figure 1.2: Paramagnetism: Magnetisation over applied field - schematic [15].

Ferromagnetism

Ferromagnetism is characterized by a (partly) spontaneously aligned dipole structure. A permanent magnetic moment exists and the strong interaction between the dipoles leads to their alignment, sometimes over macroscopic domains even in absence of an external field. The susceptibility holds:

$$\chi \gg 0 \tag{1.11}$$

If a ferromagnetic material has previously not been exposed to an external magnetic field, the regions of the spontaneously aligned dipoles are generally distributed statistically and the overall magnetisation is zero. An exception form permanent magnets, where the overall magnetisation in absence of an external field does not vanish completely.

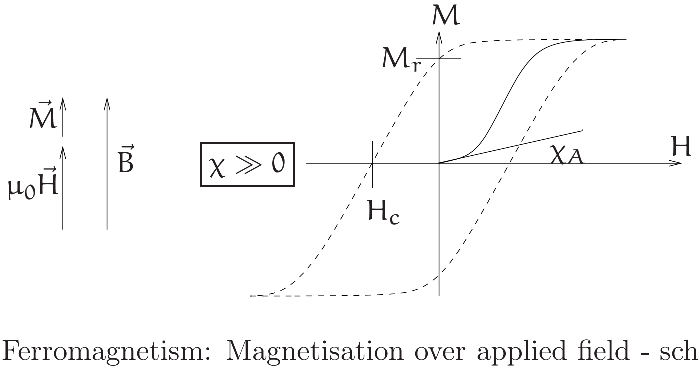

Figure 1.3: Ferromagnetism: Magnetisation over applied field - schematic [15].

Being exposed to an increasing magnetic field, the magnetic moments in a ferromagnetic

material align along the field lines.
If the magnetisation of a sample, previously not exposed to an external field, is plotted over the magnetic field, the initial magnetisation curve is obtained, see 1.1.1 continuous curved line. The magnetisation increases until all dipoles are aligned and the so called saturation magnetisation M_s is reached. After the field decreases to zero some magnetisation remains, the so called remanence magnetisation M_r. To reduce the magnetisation of the material to zero a certain, material dependent field in the opposite direction is necessary, denoted as coercive field H_c. If the field decreases further, the negative saturation magnetisation is reached. Changing the direction of the external field again, leads finally to a full hysteresis curve, see figure 1.1.1 dashed line. The included area describes the work of reversal of magnetisation of the material.

Ferromagnetic materials change to paramagnetic behaviour at exceeding of a critical temperature T_c, the Curie-temperature. At this point a second order phase transition occurs.

Other forms of collective magnetism are antiferromagnetism, where the moments of equal size are aligned antiparallel (figure 1.4) to each other, and ferrimagnetism (figure 1.1.1), where several unequal moments of opposing orientation are aligned. For further information see [14, 16].

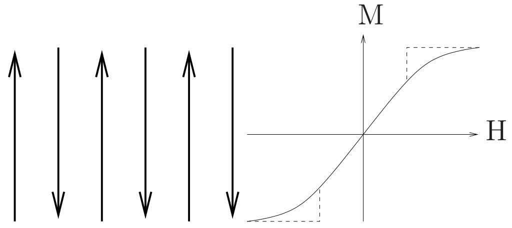

Figure 1.4: Antiferromagnetism: spins and magnetisation curve - schematic [15].

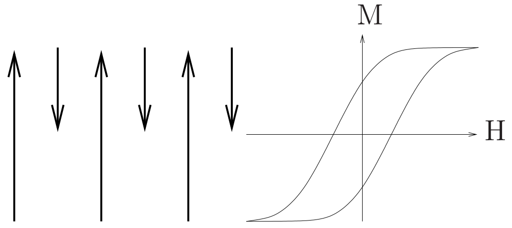

Figure 1.5: Ferrimagnetism: spins and magnetisation curve - schematic [15].

Ferromagnetism is based mostly on the electron spin. In the transition metals it is based on partially filled 3d bands and unpaired electrons in these bands. If the atoms have an adequate distance, the orbitals of unpaired outer electrons overlap in a way that results in a high density of states in the 3d bands. The energy gain caused by the reduction of the electrostatic energy of the electrons that are farther apart is greater than the energy that has to be spent to raise the electrons to states with higher kinetic energy. The exchange energy, which is the difference between the antiparallel and parallel (energy) state becomes positive and favours a parallel alignment of the spins.

The condition described by Stoner and Wohlfahrt [17] for this ferromagnetism is:

$$JN(E_F)\Omega_0 > 1 \tag{1.12}$$

with J: exchange energy per electron, $N(E_F)$: density of states at the fermi level, Ω_0: atom volume.
Iron, Cobalt and Nickel exhibit ferromagnetism at room temperature.

A favoured parallel spin orientation results in ordered domains. The exchange energy aligns the spins parallel to each other, while the magnetic anisotropy keeps them aligned in one direction. Without magnetic anisotropy the spins would randomly change their orientation by thermal fluctuation. The magnetic anisotropy has several contributions; most important is the magnetocrystalline anisotropy, where the energy depends on the direction of the crystallographic lattice. The magnetisation will align along the easy axes. Further contributions are surface anisotropy, shape anisotropy, stress anisotropy, exchange anisotropy and anisotropy induced by magnetic annealing, plastic deformation or irradiation [14]. The magnetocrystalline anisotropy results from the spin-orbit coupling. The energy that has to be applied to change all magnetic moments in the direction of the external field is called crystal anisotropy energy E_c. The magnetocrystalline anisotropy is intrinsic to the material and its crystallographic structure.

As the favoured parallel spin orientation results in ordered domains, an overall ordered state would be less favourable because of the resulting stray magnetic field. The magnetic field energy $E_{mag} := \frac{1}{2\mu_0}\int B^2 dV$ should be minimized. To reduce the magnetic stray field domain walls are formed. The stray field energy is reduced while the domain wall energy is increased, because the spins inside the bloch wall point mostly not in the direction of the easy axes. The magnetic domains form in an orientation that minimizes the stray field and the magnetic flux remains inside the magnet. Thus the formation of several domains is energetically favourable compared to the state of one large single domain [15, 16, 14].

1.1.2 Magnetism on nanoscales

Magnetic properties react differently to the specimen size. If the size decreases M_s remains independent of the size until the amount of the surface atoms and their influence becomes significant compared to the amount of volume atoms, in contrast to the coercivity H_c, which shows a strong size-dependent effect. In elongated particles it can exceed the bulk value [14].

Superparamagnetism

If the specimen size decreases from bulk material to small particles, the number of domains decreases as well. In small volumes below a critical size (diameter D_S) only one domain exists; here the existence of a domain wall is energetically less favourable than the existence of a stray field. At the point of D_S the coercivity reaches its maximum value. With increasing volume the coercivity decreases further until it becomes zero and the particles are superparamagnetic, see figure 1.6.

The energy ΔE that is necessary to change the magnetisation direction in a single domain particle is proportional to the effective anisotropy constant K_{eff} [2] and the particle volume V. The energy ΔE can be provided by the thermal energy $k_B T$ for particles below a certain volume V.

$$\Delta E \sim K_{eff} V < k_B T \tag{1.13}$$

K_{eff}: effective anisotropy constant, V: fixed particle volume, k_B: Boltzmann's constant, T: temperature.

Therefore the directions of the magnetisation alternate between the easy axes.

---

[2] The crystal anisotropy, shape and surface anisotropy as well as magnetoelastic anisotropy contribute to the effective anisotropy constant K_{eff}, which describes the anisotropy energy per volume unit and the dependence of the magnetic properties of a material on the direction.

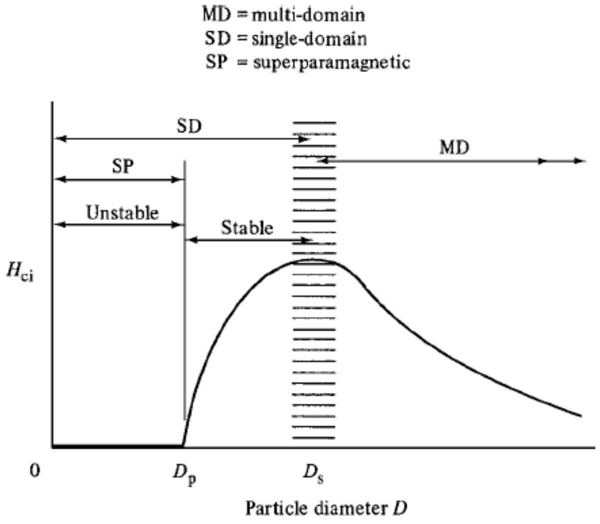

Figure 1.6: Variation of coercivity with particle diameter D [14].

Exhibiting no hysteresis, the magnetisation curve can be described using a Langevin function. For a sample with a particle volume distribution function $P(V)$ the magnetisation process can be described by

$$M(H,T) = M_s \left(\int_0^\infty P(V)\ L\left(\frac{V\mu_0 mH}{k_B T}\right)\ dV \right) \tag{1.14}$$

with L: Langevin function

$$L\left(\frac{\mu_0 m(V)H}{k_B T}\right) = \coth\left(\frac{\mu_0 mH}{k_B T}\right) - \left(\frac{k_B T}{\mu_0 mH}\right) \quad . \tag{1.15}$$

The probability P that a change in the magnetisation direction occurs during the measurement with time t is given by

$$P(t) = 1 - \exp\left(\frac{t}{\tau}\right) \quad . \tag{1.16}$$

The thermal fluctuation time τ is given by the Néel-Arrhenius-equation:

$$\tau = \tau_0 \exp\left(\frac{\Delta E}{k_B T}\right) \tag{1.17}$$

where τ_0 describes the characteristic time constant. Exceeds the thermal fluctuation time τ the time that is needed for detection, a ferromagnetic behaviour can be measured.

For spherical particles $V = \frac{4}{3}\pi r^3$ and an assumed detection time of 100 s the critical radius r_{SP} can be computed by

$$r_{SP} = \frac{D_{SP}}{2} = \left(\frac{25 k_B T}{\frac{4}{3}\pi K_{eff}}\right)^{\frac{1}{3}} \quad . \tag{1.18}$$

The superparamagnetic limit for Co was calculated to a diameter of $D_{sp} = 7.8$ nm - 15.8 nm depending on the crystal structure [18,19,20,21,22,23,24]. If the bulk value anisotopy constant of hcp-cobalt $K = 4.1 \cdot 10^5 \frac{J}{m^3}$ [20] is applied as K_{eff} the critical diameter calculates to $D_{sp} = 7.8$nm. The anisotropy constant for fcc-co $K = 2.7 \cdot 10^5 \frac{J}{m^3}$ leads to a diameter of $D_{sp} = 15.8$ nm. If the mean size of the particles is close to D_{SP} the magnetic behaviour can be described as a superposition of superparamagnetic and ferromagnetic contributions by

$$\begin{aligned} \frac{M(H_{ext})}{M_s} &= f^{FM}(V)\frac{2}{\pi}\arctan\left(\frac{\mu_0 H_{ext} \pm \mu_0 H_c}{\mu_0 H_c}\tan\left(\frac{\pi S}{2}\right)\right) \\ &+ \left(1 - f^{FM}(V)\right)\int_0^\infty f^{SPM}(V)\left(\coth\left(\frac{MVH_{ext}}{k_B T}\right) - \frac{k_B T}{MVH_{ext}}\right)dV \end{aligned} \tag{1.19}$$

$f(V)$: size distribution function, H_{ext}: external magnetic field, FM: ferromagnetic, SPM: superparamagnetic. The squareness S describes the angularness of the magnetisation curve

$$S = \frac{M_r}{M_s} \quad . \tag{1.20}$$

1.2 Formation of nanoparticles

The methods of synthesis of nanoparticles can be divided into two main branches; top-down methods and bottom-up methods. In top-down methods a macro material is reduced in its size until it finally reaches nanometer scales in at least one direction. This is done by mostly physical methods like (ball) milling, attrition, lithography and similar processes. In contrast to this, in bottom-up methods nanoscale materials are built from atoms or molecules by condensation methods like thermal or laser vaporisation, synthesis in reverse micelles, chemical vapour deposition as well as wet chemical methods, like thermal, ultrasonic or photochemical decomposition of precursor molecules such as organo-metallic complexes [25,26,3].

The nanoparticles investigated in this thesis are synthesised by a wet chemical approach, as described in more detail in chapter 2.

1.2.1 Wet chemical approach

Precursors are solved and injected into a boiling solvent with stabilizers. Precursors are molecules that release monomers, atoms or molecules that function as smallest building blocks for particle formation, during the decay. The decay can be caused by temperature or irradiation [3]. Nanoparticles built from monomers have to be stabilized against agglomeration, because bulk materials are energetically favourable. Surface atoms have a greater potential energy compared to bulk atoms, because they are surrounded by similar atoms only in the direction towards the inside of the particle [26,27]. The particles can be stabilized by several methods e.g. spatial separation by polymers due to the size of the molecules, coating with amphiphile molecules for sterical stabilization or separation by charge by electrostatical repulsion [28,25,29]. In our case amphiphile molecules, so called

---

[3] In the case of the investigated nanoparticles dicobalt octacarbonyl $Co_2(CO)_8$ is used as precursor.

surfactants, are used as stabilizers, which are expected to prevent the particles from oxidation to some degree as well. The amphiphilic molecules bind with their hydrophilic heads to the particle surface, while the hydrophobic tailgroup(s) point towards the solvent. This allows the use of unpolar solvents, only. The bonding of the head group on the particle surface influences the growth of the particle in size and shape e.g. by different interaction with different crystallographic planes, while the interaction between the particles is mostly determined by the tail group(s).
The shape of nanoparticles is influenced by the surfactants during formation in a way that the strength of binding to a surface is among other things dependent on the surface energy. For different crystal planes with different surface energies, the growth is limited where the binding is strong. In contrast it is enhanced for surfaces with weak bindings. Especially mixtures of surfactants with selective binding to the different crystal planes were used intentionally to grow various shapes [30,31].

In the following descriptions of particle formation, the influence of the surfactants is neglected for simplification.

Generally the development of the particles can be divided into the main steps nucleation, growth and equilibrium processes. This formation can be described kinetically after the La Mer model and thermodynamically.

1.2.2 Kinetical description of particle formation

The steps of particle formation can be described with the La Mer model [32]:
While the precursor decays, the monomers are released into the solvent. This leads to an increase of the monomer concentration. The system can be assumed as homogeneous until the nucleation threshold is exceeded [33]. Once the monomer concentration exceeds the nucleation threshold, monomers agglomerate to clusters, which act as nuclei for particle formation. During particle formation the concentration of monomers decreases and the particle formation stops after the monomer concentration has dropped below the nucleation threshold, see figure 1.7. Left over monomers attach to the nuclei and the crystals grow until an equilibrium between free and bound monomers has been established. Different precursors vary in their decay velocity, which has remarkable influences in the case, where more than on precursor is used. An example for the case of Co and Fe precursors $\mathsf{Co_2(CO)_8}$ and $\mathsf{Fe(CO)_5}$ with different decay velocities of and the impact on the produced particles can be found in [29,25].

The time period, in which the system is above the nucleation threshold, defines the size distribution of the nanoparticles. The longer the system is above the nucleation threshold, the wider is the resulting size distribution. After the monomer concentration has dropped below the nucleation threshold equilibrium processes occur: smaller particles dissolve in favour of bigger particles, which continue to grow. This process is called Ostwald-ripening [25,34,33]. It leads to an increased size distribution, which can be suppressed by leaving the solution only a short time span in the region above the saturation threshold and injecting the precursor solution fast. The particle size can be affected among other things by solvent, temperature and surfactant(s). An understanding of the processes that lead to agglomeration of monomers, particle growing and stabilization make it possible to fabricate several morphologies of nanoparticles like, spheres, disks, rods, flat triangles, hexagons or cubes and to regulate the obtained sizes [35,36]. A method to fabricate any arbitrary size and shape does not exists yet, but particles with a narrow size distribution can be prepared

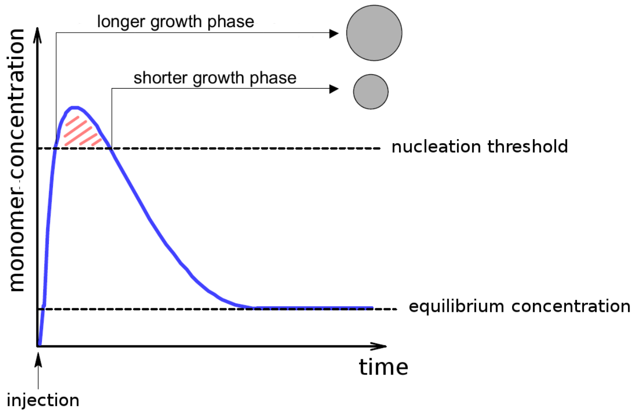

Figure 1.7: Schematic development of the monomer concentration during particle formation [28].

in a relatively predictable and reproducible manner. [29, 37, 3, 38]

1.2.3 Thermodynamical description of particle formation

The growth of the particles is size dependent as noted in the section above. Below a critical radius r^* the particles are thermodynamically unstable and dissolve, while particles above the critical radius grow. This leads to a broadening of the size distribution resulting from the time span the solution is above the nucleation threshold and statistical fluctuations, see figure 1.7. The critical radius r^* can be determined by a thermodynamical reflection of the nucleation process. It can be estimated by calculating the Gibbs free energy ΔG for assumed homogeneous nucleation.
For the formation of a new phase this can be calculated by the sum of a surface contribution ΔG_S and a bulk contribution ΔG_V

$$\Delta G = \Delta G_V + \Delta G_S = \frac{4}{3}\pi r^3 \Delta g_V + 4\pi r^2 \gamma \tag{1.21}$$

with γ: surface energy.
The volume contribution is determined by $\Delta g_V = -\frac{k_B T}{\nu}\ln(1+S)$ with ν atom volume and $S = \frac{c(r)}{c^*}$ supersaturation of the solution, $c(r)$: solubility of a particle with radius r, c^*: equilibrium solubility.
For $\Delta G > 0$ formed particles redissolve again, for $\Delta G = 0$ a metastable state in the solution exists (so called critical state for particle formation) and for $\Delta G < 0$ particles grow after nucleation, see figure 1.8.
The surface contribution ΔG_S is determined by the surface tension ($\gamma \geq 0$). This shows, that the condition for particle formation is given only in the case of an existing supersaturation. Minimization of ΔG leads to the critical radius r^* in a supersaturated solution, the Gibbs-Kelvin equation holds [33, 25]:

$$r^* = \frac{2\nu\gamma}{k_B T \ln(S+1)} = \frac{2\gamma}{\Delta g_V} \quad . \tag{1.22}$$

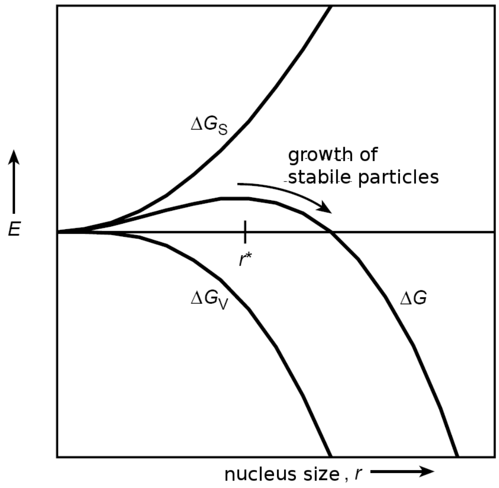

Figure 1.8: Schematic energy diagram of the nucleation process [33].

2 Synthesis of cobalt nanoparticles and oxidation

In this chapter the standard synthesis procedure of nanoparticles used in this thesis is described as well as the purification process, the surfactants in general and the method of surfactant exchange. The stabilization of the particles by surfactants and the oxidation process in nanoparticles is explained subsequently.

2.1 Synthesis of nanoparticles

The synthesis of cobalt nanoparticles is described in several modifications in [29,39,25,37]. The following can be seen as a standard procedure for particles used in this work [1]:
The cobalt nanoparticles are synthesized by thermolysis of a cobalt precursor in an inert gas atmosphere (purified argon) to prevent the particles from the influence of oxygen and hydrogen.

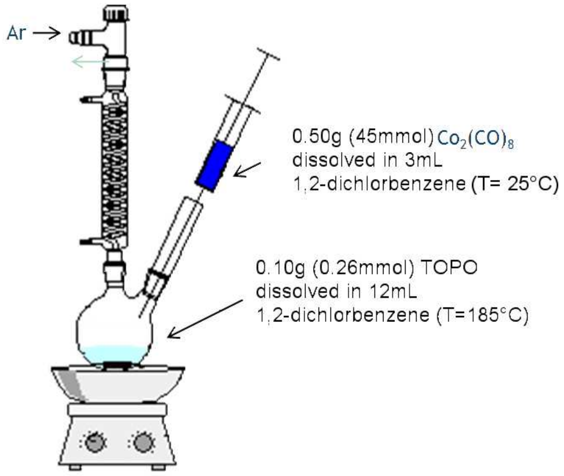

Figure 2.1: Schematic experimental setup [39].

In 3 ml dry 1,2-orthodichlorbenzene 0.50 g dicobalt octacarbonyl is dissolved. Further 0.10 g (0.26 mmol) trioctylphosphin oxide (TOPO) is dissolved in 12 ml dry 1,2-orthodichlorbenzene, heated to 185°C and stirred constantly with a magnetic stirrer. The obtained metal precursor solution is injected into the boiling surfactant solution and kept under reflux for 15-30 minutes. Afterwards the magnetic stirring bar and then the heating is removed. The solution is left to cool down until it reaches room temperature [29,39,40].

---

[1] Deviations will be described shortly in the corresponding sections.

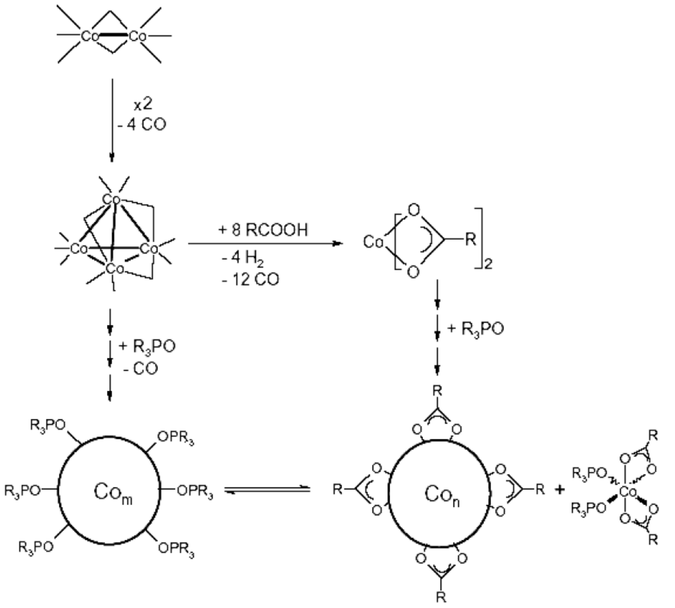

Figure 2.2: Possible mechanism of Co particle formation [39].

In figure 2.2 a possible mechanism for particle formation with $Co_2(CO)_8$ and TOPO (TriOctylPhosphine Oxide) is displayed.
To remove residues from the precursor and side products the particle suspension has to be purified.

As a variation the particles displayed in 2.5 have been stabilized with a combination of two surfactants, and have been stirred with a KPG stirrer instead of a magnetic stirrer and kept under reflux for 1 hour.

2.1.1 Purification

For purification of the obtained suspension acetonitrile is added. Then the solution is centrifuged for 2-10 minutes at 4000 rpm. The supernatant is removed and the precipitate is redisperged in dry 1,2-orthodichlorbenzene. The process beginning with the addition of acetonitrile is repeated two to three times depending on the sedimentation behaviour of the particles. Finally, dry 1,2-orthodichlorbenzene is added and the particles are redisperged. That way spare surfactant molecules and precursor remains are mostly removed. [29,39,40]

In the images in figure 2.6 examples for particles fabricated with a (slightly) modified procedure are given [2].

2.2 Surfactants and surfactant exchange

In this section a short overview over the surfactants that are used in this work and their binding to the particle surface is given.

---

[2] Modifications of the original procedure are mentioned in the captions.

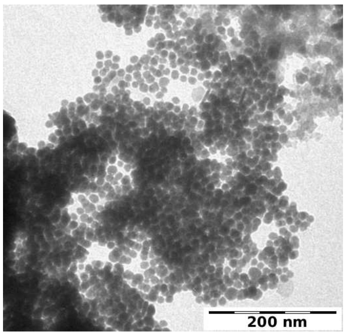

Figure 2.3: Co particles stabilized with TOPO.

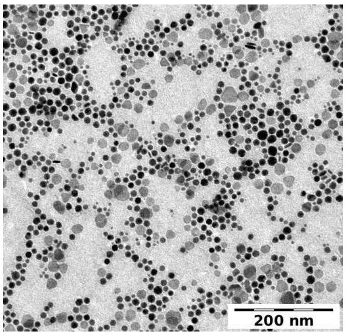

Figure 2.4: Co particles stabilized with oleylamine.

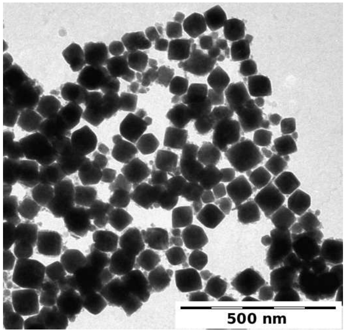

Figure 2.5: Co particles fabricated with a KPG stirrer and stabilized with oleylamine and oleic acid.

Figure 2.6: Particles fabricated in our chemistry lab.

2.2.1 Surfactants

As mentioned in section 1.2 the use of amphiphilic molecules is one of the possibilities for the stabilization of nanoparticles.

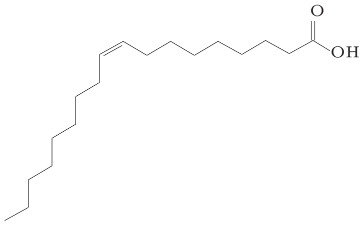

Figure 2.7: Oleic acid with polar alkyl chain and hydrophilic head as example for a surfactant.

The type of bond between surfactant and particle surface depends on the headgroup of the surfactant. Possible sites for occurring bonds between headgroups used in this thesis and particle surface are displayed in figure 2.2.1.
The carboxylic head allows a covalent binding to the surface, whereas the amine head binds by physisorption, considered van-der-Waals forces of hydrogen bonds [18, 37].

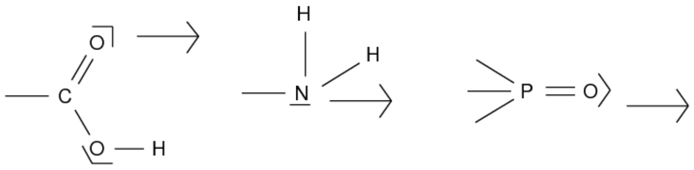

Figure 2.8: Head groups with possible binding sites to the particle surface [18].

The surfactant head groups are displayed in figure 2.2.1 (from left to right: carboxylic, amine, phosphine), sorted by binding strength. The weakest binding surfactant is TOPO with a phosphor based headgroup, the next stronger binding surfactants are the ones that posses an amine head group, which bind by physisorption, and the strongest binding surfactants used in this thesis are those with a carboxyl head group, which bind covalent to the surface [41, 18].

2.2.2 Surfactant exchange

In a nanoparticle solution some of the surfactant molecules are attached to the particle surface, while other molecules diffuse freely through the solvent even after purification. In an equilibrium state molecules leave the surface and are replaced by other free molecules constantly. The mean residence time depends on the strength of the bond to the particle surface. [41]

To change the surfactant that covers the surface of nanoparticles, acetonitrile is added to the particle solution. This causes the surfactant on the surface to curl and the particles agglomerate subsequently. The solution is centrifuged, the sediment is kept and the supernatant is discarded. Afterwards the particles are redispersed in a solution with the new, stronger binding surfactant.

In the case of similar affinity of both surfactants to the surface, the old surfactant uncurls and some of the old surfactant molecules leave the surface and are replaced by new surfactant molecules. In this case fluctuations of bound and free molecules results in a step by step replacement of the old surfactant by the new, because of the oversupply of the new surfactant. This procedure has to be repeated several times, because the concentration of the new surfactant in solution decreases, while the free old surfactant concentration increases until an equilibrium concentration is reached. A further replacement of the old surfactant on the particle surface is only possible, if an oversupply of the new surfactant is rebuild. A nearly complete replacement of the old surfactant can be expected only after few "washes" with new surfactant solution [40, 41].

In the case of greater differences in the surfactant affinity to the particle surface, the old, weaker binding surfactant is replaced by the stronger binding one. In this case one "wash" can be sufficient [41].

The influence of the surfactant on the shape of the nanoparticles during formation was already described in chapter 1.2.

2.2.3 Stabilization

Nanoparticles have to be stabilized against agglomeration because the bulk state is energetically favourable compared to the nanoparticle state due to an increased surface influence [33].

If the inter particle distance becomes small enough, attractive van der Waals forces lead to further attraction at short distances. Therefore the inter particle distance has to be kept above the critical distance. Several methods to achieve a certain inter particle distance exist; two will be described briefly in the following paragraphs.

One possibility is the stabilization by electrostatic repulsion. A look at the total potential curve of the van der Waals and electrostatic potential displayed in figure 2.9 shows that the attractive van der Waals force prevails only at short distances. The particles agglomerate if the energy barrier caused by the electrostatic force is overcome by thermal energy for average distances. An electrostatic stabilization of particles can be achieved by an inhomogeneous charge distribution in the particles that leads to an increased surface charge concentration. This works best when polar solvents are used [42].

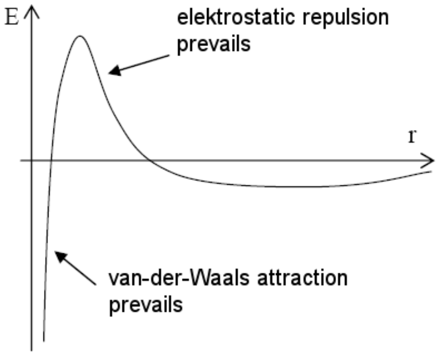

Figure 2.9: Schematic diagram of superposition of van der Waals and electrostatic potential over inner particle distance [42].

Another possibility is the sterical stabilization by binding surfactants to the surface as described earlier. The surfactants stabilize the nanoparticles by two effects, an entropic effect and an osmotic effect:
If the particles approach and the surfactant "shells" overlap, the mobility of the alkyl chains is reduced, which is equal to an increase of entropy and potential energy and is therefore less favourable (see figure 2.10).

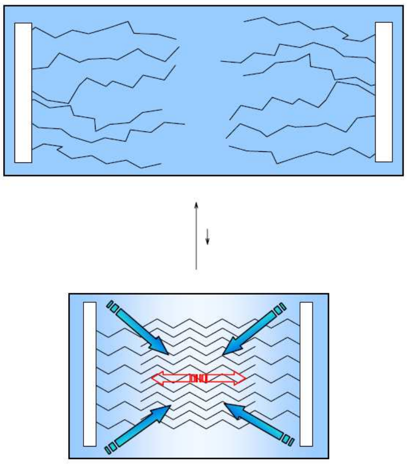

Figure 2.10: Reduction of mobility of alkyl chains on particle surfaces during close approach, the saturation of the blue color depicts the solvent concentration [42].

The second effect is an increase of the osmotic pressure, caused by the extrusion of the solvent between the particles. The solvent concentration between the particles lowers during a close approach, as a backlash, solvent flows between the particles by osmotic pressure and leads to an increase of the inner particle distance.

2.3 Oxidation

Thin oxide films on metal grow rapidly up to a critical thickness at room temperature and under ambient conditions. If the oxide layer has reached the critical thickness, the oxidation rate decreases to either very low or even negligible values. The metal oxide film has a typical thickness of 2-10 nm, depending on the material. At higher temperatures oxide film growth is not limited and a different oxidation process prevails. After the initial state a parabolic oxidation behaviour can be typically observed [43].

At ambient conditions relatively crystalline oxide films form on cobalt [44]. The crystalline structure is close to fcc structure [41]. Generally the surface atoms in nanoparticles have a greater relevance than in bulk material, which results in changed behaviour in many areas. Therefore a closer look has to be taken on the process of oxidation on nanoscales [45,44,46].

2.3.1 Oxidation of nanoparticles

A model describing the kinetics of oxidation on nanoscales was introduced by Cabrera and Mott [43] and improved by Fromhold et al. [46].

The growth of oxide films at room temperature is determined by the diffusion of electrons and ions, which is strongly influenced by their concentration and a self generated electric field. For small geometries, the development of the oxidation process depends on the shape of the oxidized material and, therefore, on the form of the self generated electric field, as well. For nanoparticles with a spherical geometry, the oxidation rate increases compared to those of planar films, because of the non-uniformity of the electric field in the oxide shell [47, 43, 46], for calculations see section 2.3.2.

The growth of the oxide film can be divided into several steps. First these steps are described shortly, than an analytical description of the process is given.

1. Dissociative oxygen adsorption on the particle surface from the gas phase

The dissociative adsorption of O_2 to the surface of transition metals is assumed as a multistep process. At first physical adsorption is considered to occur. Afterwards the O_2 molecules build a chemisorbed monolayer and further dissociation of the O_2 molecules takes place. In many metal-oxide systems it was found, that the oxygen of the chemisorbed layer penetrates into the bulk upon chemisorption [48, 44, 45, 43, 47].

2. Oxidation of surface metal atoms

One supposed reason for the incorporation of oxygen is the instability of chemisorbed oxygen with respect to the incorporated oxygen, for which coordination with the metal atoms is maximal. An alternatively explanation offers that the oxygen is drawn into the surface by charge. At the beginning, ionized surface metal atoms and ionized oxygen combine and form metal oxide. The further oxidation process depends on the stability of the layer of adsorbed oxygen in relation to transport processes in the oxide layer [44,45,43].

A number of examples based on kinetic data suggests that oxygen chemisorption involves oxide nucleation and a change of the surface morphology [44, 48, 45].

3. Ionisation of adsorbed oxygen atoms and metal ions at the metal-oxide interface

Surface potential states form above the oxide valence band and below the fermi level E_F of the metal. As a result electrons tunnel from the metal-oxide interface to the oxide-oxygen interface and accumulate at the surface, while the metal ions remain at the metal-oxide interface.

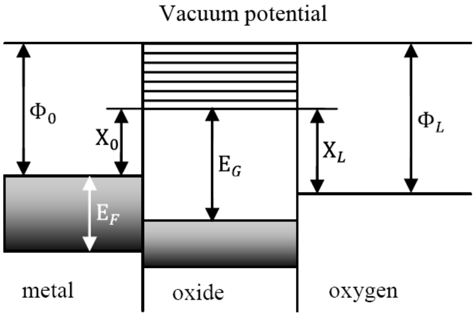

Figure 2.11: Energy level diagram of the metal-oxide-oxygen system. The tunneling process stops as soon as the potentials X_L and X_0 reach equilibrium [45].

Lattice defects are assumed to be generated and annihilated at the interfaces constantly, these are equilibrium processes, which are expected to be fast compared to the electron and ion transport through the oxide layer [43, 45, 49].

4. Build up of the self generated electric field

As mentioned above, electrons tunnel into the layer of adsorbed oxygen at the surface until the electric field between the metal-oxide and the oxide-oxygen interfaces is as strong as the contact potential difference. The accumulated, charged defects at the interfaces are responsible for the electric field. Therefore it is important that the formed oxide layer can be assumed to be quasi free of charge. If the bulk charge of the oxide would not be negligible compared to the charge at both interfaces, the electric field would be significantly influenced [43, 45, 46, 49, 47].

5. Incorporation of metal ions into oxide at the metal-oxide interface

As mentioned in section 2.3.1 lattice defects are generated and annihilated constantly at the interfaces. The strong electric field pulls some of the interstitial metal ions from the metal-oxide interface into the oxide layer [43, 46].

6. Diffusion of metal ions within the oxide layer

These metal ions jump from one defect site to another. Because of the strong field the transport of intermediates (electrons, metal ions, bulk defects as oxygen vacancies, holes, interstitial atoms) can be assumed to be irreversible in its direction [44, 48, 47].

The tunnel current and the ionic diffusion current are assumed to be equal in magnitude and opposite in sign. Further, these currents can be assumed to be steady state. This has been introduced as "‘coupled currents"’ concept by Fromhold [46], and is described in more detail in section 2.3.2.

7. Reaction of metal ions and oxygen ions to form metal oxide

The metal ions reach the oxygen-oxide interface and react with the oxygen ions. The growing rate of the oxide layer depends on the volume of oxide that forms per transported metal ion and the metal ion diffusion rate. The value of the current at the location where the chemical reaction of metal oxidation occurs (one of the oxide interfaces) allows the determination of oxidation rate [45, 44, 43, 46].

8. Final stage of the oxidation process

If the oxide layer thickness reaches a critical value the oxidation rate becomes negligible, the electric field breaks down and the tunneling process of ions stops [48, 43].

In addition a few facts have to be mentioned concerning the applicability of this model. It is not applicable if the formation of oxide is accompanied by the occurrence of cracks in the oxide layer [47]. The particle expands slightly during oxidation. The oxidation process is limited by the jumps of the ions through defect sites. Or if this aspect has a greater influence, the initial oxidation rate may be proportional to the coverage of the surface by atomic oxygen [45, 44].

Therefore, taking a closer look at the surface of the particles is expedient. The relatively strong curvature of the surface leads to a mismatch between the crystal lattice and the surface, resulting in edges and corners of crystallites, which function as potential nucleation sites for the initial rate of topochemical reaction.

This may have an effect for particles covered by amphiphile molecules and may influence the oxidation behaviour of particles with different morphologies.

2.3.2 Mathematical description of the oxidation process

This description is based on a paper by Fromhold [46].
The main focus points are the concept of steady state oxide growth for non planar geometries, the self generated electric field and coupled currents conditions at ambient temperatures and conditions.

As the oxidation rate depends on the ion current to the oxidation interface, the effects of the sample geometry have to be taken into account. Under fixed experimental ambient conditions the currents can be assumed to be steady state. Therefore, the currents have to fulfill the following condition in the steady state limit:

$$-\frac{\partial C}{\partial t} = \nabla \vec{J} = 0 \quad . \tag{2.1}$$

No electric charge or diffusing species concentration C can accumulate or deplete during the time t as the current $\vec{J}$ is assumed to be static.
The increase of the local film thickness L at the reaction interface can be described by

$$\frac{dL}{dt} = R_i J_i \tag{2.2}$$

with R_i: volume of oxide formed per transported ion of type i and J_i: ionic particle current density. Overall the oxide volume V_{oxide} formation rate is given by integrating over the complete reaction interface (RIF)

$$\frac{dV_{oxide}}{dt} = R_i \int\limits_{\text{RIF}} \vec{J_i} d\vec{A} \tag{2.3}$$

where $d\vec{A}$ denotes the reaction interface area vector.

For the spherical geometry a uniform radial flow of current density J_i between concentric metal spheres is considered as depicted in figure 2.12. The metal spheres function as electrodes. If constancy of the concentration C_s of a species of type s is assumed, the total concentration I_s is given by

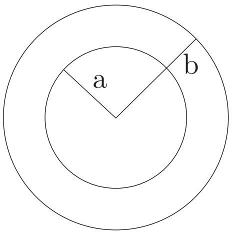

Figure 2.12: Sketch of a spherical particle of radius $r_p = b$ with a metal core of radius $r_c = a$ and an oxide shell of thickness b-a [45].

$$I_s = \int\limits_{\text{sphere r}} J_s(r) dA = J_s(r)[4\pi r^2] \tag{2.4}$$

and it holds $J_s \propto \frac{1}{r^2}$.

The current density vector $\vec{J_s}$ can be expressed by the vector gradient of the electrochemical potential $\tilde{u_s}$ and a proportionality constant B_s

$$\vec{J_s} = B_s \cdot C_s \nabla \tilde{u_s} \quad . \tag{2.5}$$

If the standard form for the electrochemical potential $\tilde{u_s} = u_s^0 + k_B T \ln C_s + q_s V$ is substituted and $-\nabla V = \vec{E}$ the electric field, the equation changes to

$$\vec{J_s} = -k_B T B_s \nabla C_s + q_s B_s \vec{E} C_s \tag{2.6}$$

with q: charge per particle, V: electrostatic potential.
The comparison with the linear diffusion equation

$$\vec{J_s} = -D_s \nabla C_s + \mu_s \vec{E} C_s \tag{2.7}$$

with D_s: diffusion coefficient, μ_s: mobility, leads to a term-by-term agreement and the diffusion coefficient D_s and mobility μ_s:

$$\Rightarrow \quad D_s = k_B T B; \quad \mu_s = q_s B \quad . \tag{2.8}$$

The Einstein relation 2.9 (electrical mobility equation) follows:

$$\frac{\mu_s}{D_s} = \frac{q_s}{k_B T} \quad . \tag{2.9}$$

It can be assumed that no space charge exists in oxide layers < 100 nm [46].

The electrical potential difference V_{gen}, that is generated in the process between the two interfaces, can be described by

$$V_{gen} = V(b) - V(a) = \frac{Q_a}{4\pi\epsilon}\left(\frac{1}{b} - \frac{1}{a}\right) \tag{2.10}$$

with $V(r)$: potential at radius $r = a, b$; Q_a: charge on inner shell, Q_b: charge on outer shell, ϵ: permittivity, and

$$Q_a = -Q_b \quad . \tag{2.11}$$

The coupled currents condition represents a state without net charge transport:

$$q_1 J_1 + q_2 J_2 = 0 \tag{2.12}$$

with $q_{1,2}$: charge of particle of type 1,2 and $J_{1,2}$: charge current of type 1,2.
In case of spherical symmetry:

$$C_s = C_s(r) \quad \Rightarrow \quad \vec{J_s} = \hat{r} J_s; \quad \vec{E} = \hat{r} E \quad . \tag{2.13}$$

This leads to the equation for the radial current

$$J_s = -K_b T B_s \frac{dC_s}{dr} + q_s B_s E_r C_s \quad . \tag{2.14}$$

The particle expansion by the volume increase due to oxidation is taken into account with the expansion parameter σ [3]

$$\sigma = \frac{\text{oxide volume}}{\text{metal volume used in oxide formation}} \tag{2.15}$$

and $V_{oxide} = \sigma V_{metal}$ leads to the equation for the variable particle radius b

$$b = \left(b_0^3 + (\sigma - 1)(a_0^3 - a^3)\right)^{\frac{1}{3}} \tag{2.16}$$

where $b_0 = b(t = 0)$, $a_0 = a(t = 0)$ are time dependent. Therefore the oxide thickness L can be written as

$$L = ((1 - \sigma)(a^3 - a_0^3) + b_0^3)^{\frac{1}{3}} - a = b(t) - a(t) \quad . \tag{2.17}$$

With Ω, a constant quantity depending on the charge per particle in multiple of the electron charge e, the mobility, the volume of oxide formed per transported particle, the concentration profile and the built-in potential
$\Omega = -R_1 \mu_1 V_{gen} \times \left[\frac{C_1(b) - C_1(a)\exp[-Z_1 eV_{gen}/k_B T]}{1 - \exp[-Z_1 eV_{gen}/k_B T]}\right]$; e: electronic charge magnitude, $Z_s = \frac{q_s}{e}$: charge value.

---

[3] The density of cobalt is $\rho_{Co} = 8.9 \frac{g}{cm^3}$ [50], the CoO density is $\rho_{CoO} = 6.44 \frac{g}{cm^3}$ [51]; the relation of the volumes can be computed by dividing the reciprocals: $\frac{1}{\rho_{CoO}} : \frac{1}{\rho_{Co}} = \frac{0.155}{0.112} = 1.38 \sim 1.4$. The expansion factor from Co to CoO is therefore ~1.4.

The oxide growth rate law for spherical particles is:

$$\frac{1}{2}(L^2 - L_0^2) - \frac{1}{3b_0}(L^3 - L_0^3) = \Omega t \quad . \tag{2.18}$$

Compared to the planar growth law

$$L^2 - L_0^2 = 2\Omega t \tag{2.19}$$

it is clearly visible that the law for spherical particles contains an additional cubic term.

Additionally, the particle burn-up time t_{burn} [4] can be expressed by

$$t_{burn} = \frac{\sigma}{2\Omega}\left[a_0^2 - \frac{1}{\sigma - 1}(b_{max}^2 - b_0^2)\right] \tag{2.20}$$

with $\sigma = \frac{(b^2 - b_0^3) + (a_0^3 - a^3)}{a_0^3 - a^3}$: volume expansion parameter, b_{max} the value b approaches for $a \rightarrow 0$
and simplified:

$$t_{burn} = \frac{a_0^2}{6\Omega} \quad . \tag{2.21}$$

Finally the comparison of equation 2.18 and equation 2.19 shows that the burn-up time for a particle of initial radius a_0 is one third of the burn-up time required for a planar film with thickness $2a_0$ oxidized from both sides. The reason is the stronger electrical field at the metal oxide interface in the case of spherical nanoparticles resulting from the strong curvature.

For non spherical geometries the effects have to be adapted accordingly to the procedure above. Particularly discs and cubes would be of interest. For discs a cylindrical symmetry has to be taken into account.

---

[4] The burn-up time is the time, that it takes until the particle is completely oxidized.

3 Devices

To gain information about the fabricated nanoparticles several different physical and chemical methods are used. The most important will be described briefly in the following sections as well as the appendent sample preparation.

Directly after fabrication the particles will be investigated regarding their size, shape and inter particle distance by transmission electron microscopy (TEM), scanning transmission electron microscopy (STEM) and scanning electron microscopy (SEM). The magnetic properties are determined with an alternating gradient magnetometer (AGM). Their chemical composition as well as the level of oxidation are measured by energy dispersive X-ray spectroscopy (EDX). Information concerning the structure of the particles is gained by high resolution transmission electron microscopy (HRTEM) and X-ray diffraction (XRD). The success of a surfactant exchange is proven by infrared spectroscopy (IR-spectroscopy). The corresponding sample preparations and the FIB system are described in this chapter, as well.

3.1 Transmission Electron Microscope - TEM

The TEM used for most of the nanoparticle images in this work is a Philips CM 100 with tungsten cathode, which is operated at an acceleration voltage of 80 kV [1]. Images are taken via a CCD camera (Keenview). The used software is AnalySis Image Processing Pro 3.2. A typical design of a TEM is drafted in figure 3.1 [52].

The electrons are emitted from the gun by thermal emission from a tungsten wire filament. Another possibility (not used in the CM100) is the emission of electrons from e.g. a field emission gun (FEG). The cathode is heated (to about $2000^\circ C$) and the electrons are emitted by thermionic emission. In a TEM with FEG a very high voltage is applied, which leads to a reduction of the emission potential and enables the electrons to overcome the emission barrier by tunneling. Afterwards the electrons are accelerated towards the anode by the acceleration voltage, which determines the wavelength [2] λ_e of the electrons by the relativistic de Broglie equation:

$$\lambda_e = \frac{hc}{\sqrt{2eUE_0 + (eU)^2}} \tag{3.1}$$

with h: Planck's constant, c: velocity of light, e: electron charge, U: acceleration voltage and E_0: rest energy of an electron [52, 53].

After the acceleration the electrons pass through a system of electromagnetic lenses. The condenser lens focuses the electron beam on parallel "trails". In the case of bright field images, the electron beam is focused onto the sample and back to parallel trails by the objective lens afterwards. Towards the fluorescent screen and the camera, diffraction and projection lenses enlarge the image and focus it on the screen or the camera's chip.

---

[1] If another TEM was used, a note is given at the images.

[2] The higher the voltage the smaller the wavelength [53].

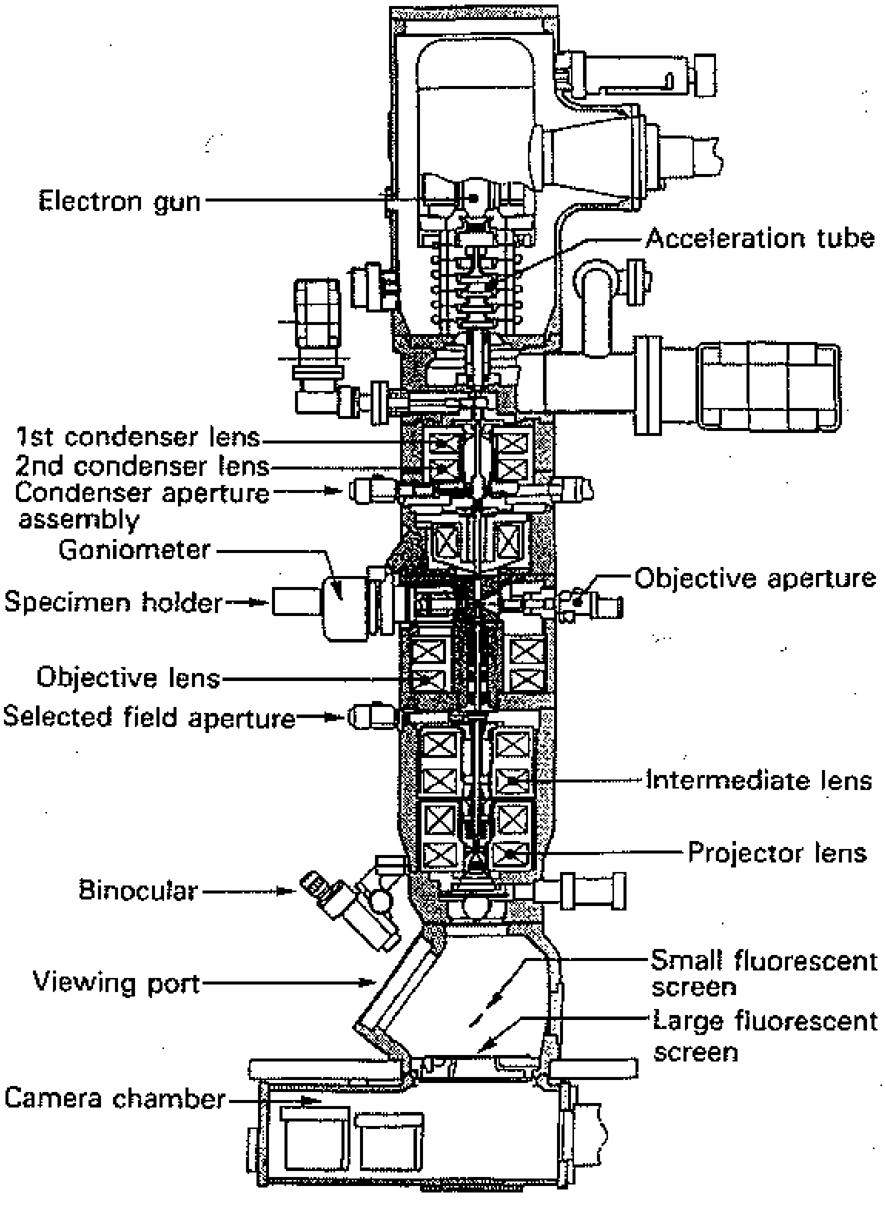

Figure 3.1: Schematic diagram of a TEM [52].

The wavelength and, therefore, the acceleration voltage are important for the resolution of the microscope. But most important are the limitations of the aberrations, which are described in 3.3.1 [54].

High Resolution Transmission Electron Microscopy (HRTEM) - Phase contrast

Higher acceleration voltages are used in HRTEM. The resulting shorter electron wavelengths and higher resolution enables the visualisation of the crystal structure and atomic arrangements of the sample by interference patterns between transmitted and diffracted electrons. Defects can also be identified in this mode. It has to be mentioned that the outcome is affected by the specimen thickness and focus in non-trivial ways and further corrections have to be performed to be able to evaluate the the obtained data [3].

Sample preparation

On a carbon coated TEM grid $2\mu l$ of particle solution is dropcasted and most of the liquid is absorbed with a piece of filter paper instantaneously. A thin film of nanoparticles is obtained this way for excess solution is removed. For an ideal TEM sample only a thin film should remain on the grid. To much electrons are absorbed by the sample, otherwise.

3.2 Scanning Electron Microscope - SEM

A schematic diagram of a SEM is shown in figure 3.2. The electrons are emitted from a gun and accelerated as described in section 3.1 for a TEM. The sample surface is raster-scanned line by line and back-scattered electrons es well as emitted secondary electrons can be detected. The obtained signal is evaluated with a personal computer, which composes a coherent image of the sample surface. Even rough surfaces can be imaged with a three dimensional appearance, because of the high focus depth. Electrons can penetrate the sample a few nanometers. The penetration depth depends on the sample material and acceleration voltage. Secondary electrons are generated by ionization of surface atoms and atoms close to the surface. Backscattered electrons are reflected by the sample by elastic scattering of the (near) surface sample atoms [4]. A problem is the occurring electrostatic charge of the samples from the incident electrons. It leads to an electron beam deflection away from the the detector and results in signal loss [55]. Therefore the samples have to be connected electroconductive to the stage. Nonconducting samples have to be treated carefully, coated with a thin conductive layer or irradiated with positive ions simultaneously.

Sample preparation

Onto a piece of silicon wafer 2 μl of the particle solution are dropped and dried. The result is a thick particle film with many clusters. To get thinner particle films, the particle solution can be distributed in a centrifuge or the piece of wafer can be dipped into the solution [18, 36, 57].

---

[3] More details can be found in [52, 55, 56]

[4] X-rays are emitted as well, which can be detected and evaluated with an X-ray spectrometer. More information concerning EDX is given in section 3.4.

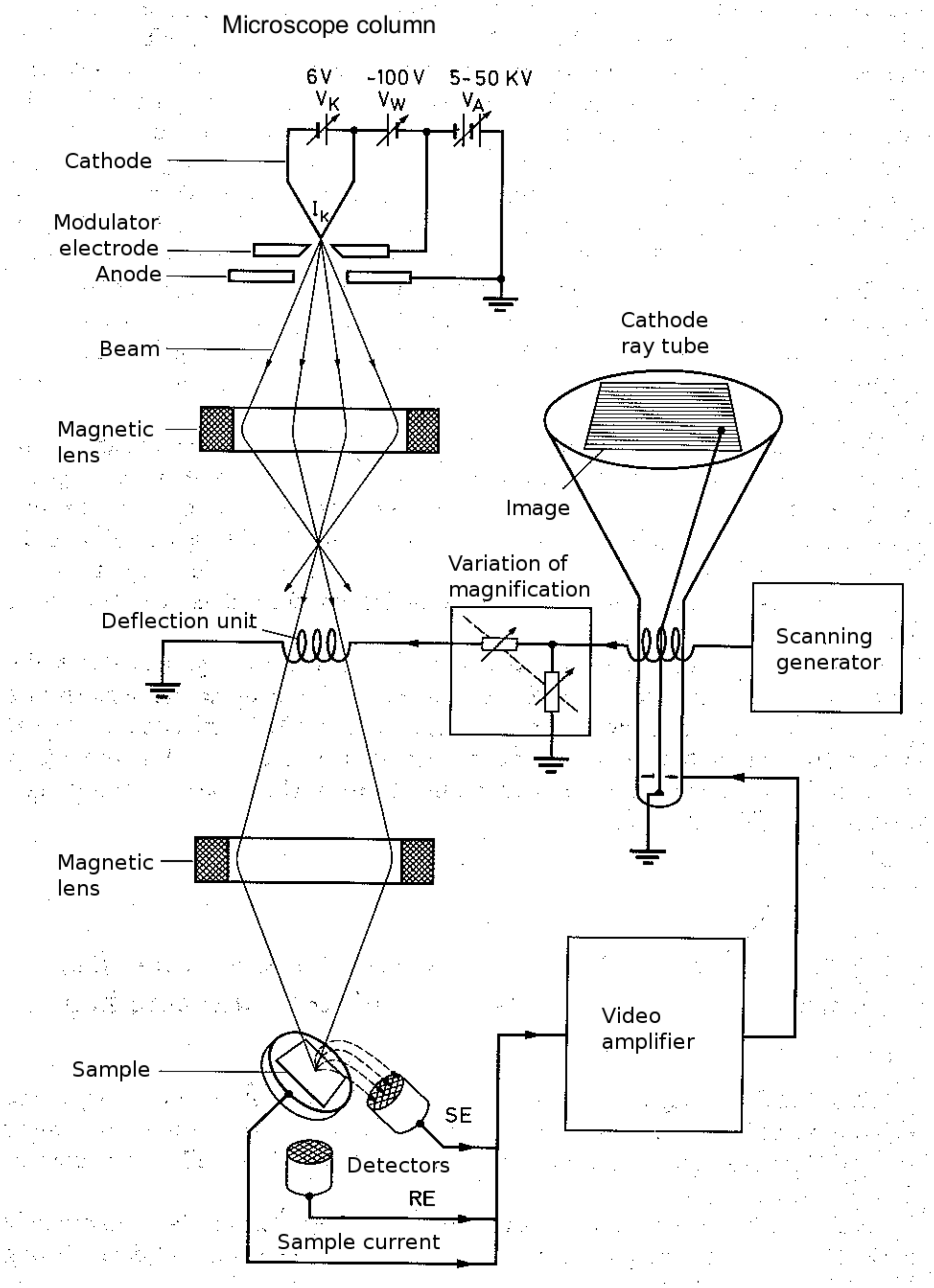

Figure 3.2: Schematic diagram of a SEM [55].

3.3 Scanning Transmission Electron Microscope - STEM

The basic assembly is similar to a SEM, but the detector is located below the sample, so that the electrons that pass trough the specimen are detected. That way a scanned transmission image of the sample is obtained.

Sample preparation

The particle solution is dropped and dried onto a TEM grid as described in the preparation of a TEM sample.

3.3.1 Image modes

As in a TEM different image modes are possible.

Bright field

In this mode only the transmitted primary beam is detected by a detector, a CCD chip in a camera or displayed on a fluorescent screen. Electrons diffracted by the sample are blocked by apertures. Therefore the particles appear dark in contrast to the thin, amorphous carbon foil, which diffracts less electrons. The thicker the sample and the heavier the material, the more electrons are diffracted and the darker the covered area appears (mass-thickness-contrast).

Dark field

Only the electrons that are diffracted in a (lower) angular range are detected in this mode. Regions in which electrons are not diffracted appear dark, while sample areas where electrons are diffracted towards the detector appear bright [5].

High Angle Annular Darkfield (HAADF)

Electrons that are diffracted at larger angles are detected with a zonular detector. This mode is sensitive to heavier elements (Z-contrast).

3.3.2 Lens aberrations

As in optical microscopes the resolution is limited by lens aberrations like spherical or chromatic aberration. In the case of electron microscopes, additional effects like anisotropic distortion occur. [56]

Spherical aberration

Here the focal length close to the optical axis of the lens differs from the one in the outer regions. Electrons closer to and farther away from the optical axis are refracted under different angles. This effect increases with distance from the optical axis, see figure 3.4.

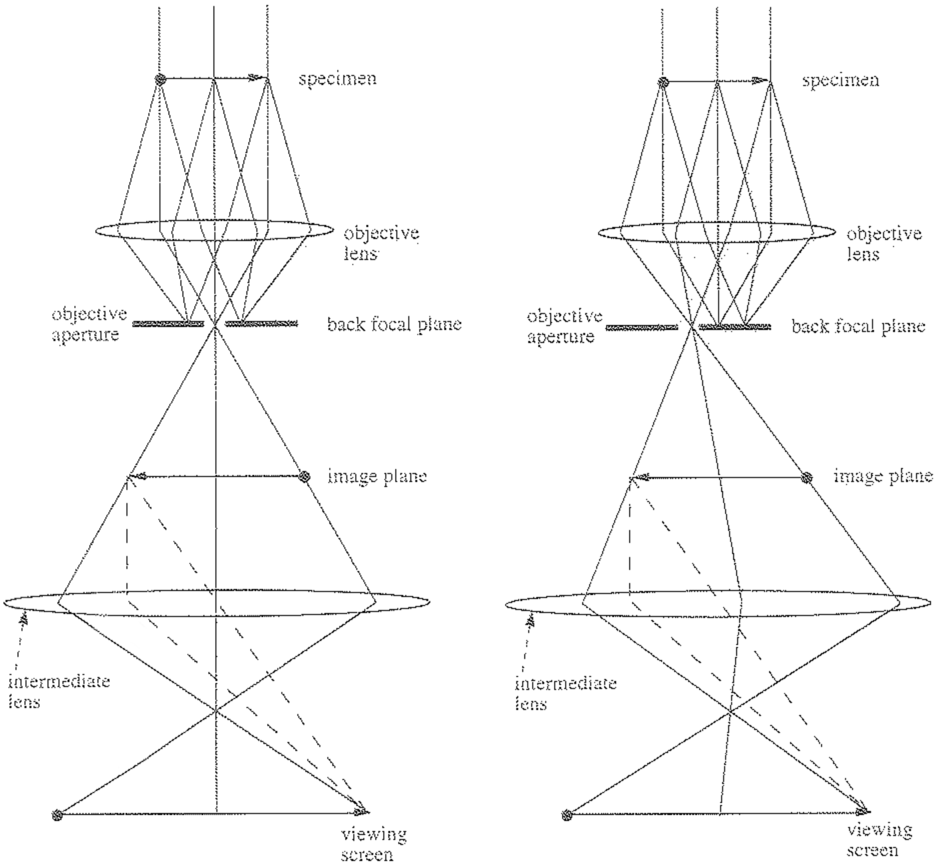

Figure 3.3: Bright field and "dirty" dark field [52].

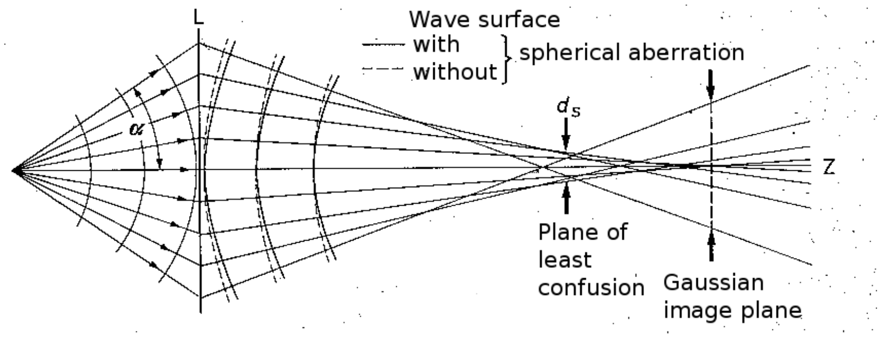

Figure 3.4: Spherical aberration [55].

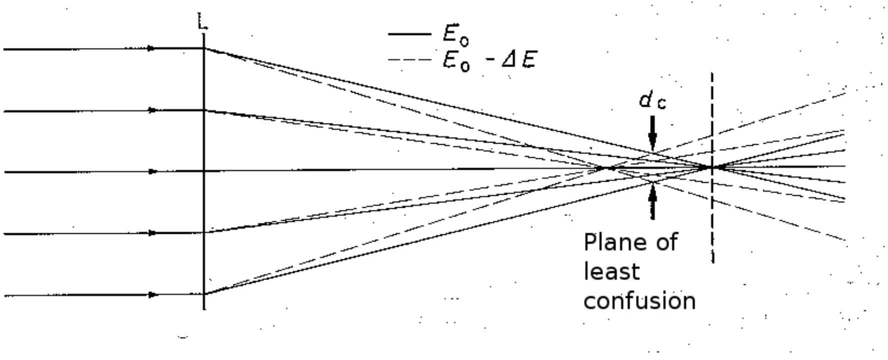

Figure 3.5: Chromatic aberration [55]

Chromatic aberration

Statistical fluctuations during emission and acceleration lead to a broader energy distribution of the electrons.

The focusing depends on the energy and direction of the electrons. Faster electrons with more energy are less focused than slower electrons with less energy. Therefore the electron beam is not focused in one point [56], see figure 3.5.

Distortion

The image scale in the outer zones of the lenses differs from the one close to the optical axis [56], see figure 3.6 for common effects.

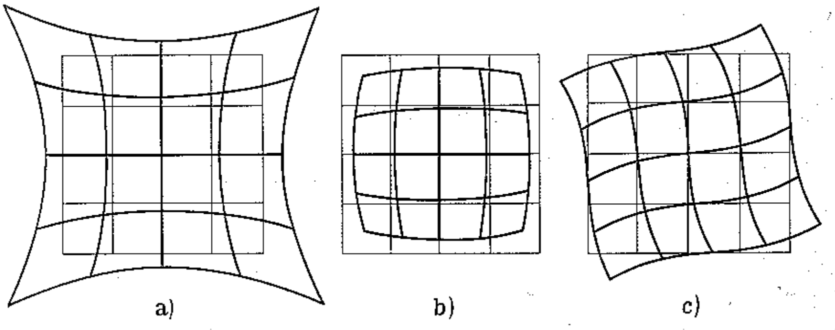

Figure 3.6: Distortion [56], a: pincushion, b: barrel, c: anisotropic.

Axial astigmatism

Axial astigmatism occurs if an electron beam does not hit an axially symmetrical lens in the centre. The image beam can be divided into a sagittal and a meridional part with different focal lines. The result is an image that can be focused only in perpendicular directions (x,y astigmatism) [56], see figure 3.7.

---

[5] In a TEM this mode is a result of a beam tilt or an aperture shift, in a STEM another detector is used.

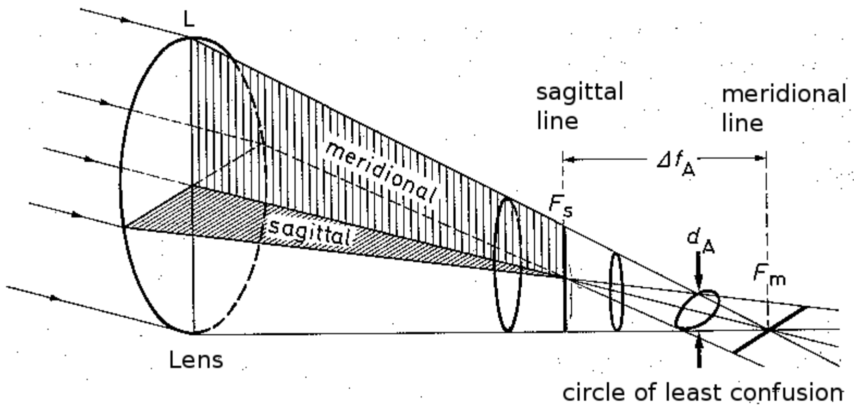

Figure 3.7: Axial astigmatism [55].

Diffraction

The electron waves do not only interfere positively in one point in the gaussian image plane, they exhibit interference patterns, leading to intensity variations in adjacent points. This results in a so called airy disc. The focus exhibits fringes [56], see figure 3.8.

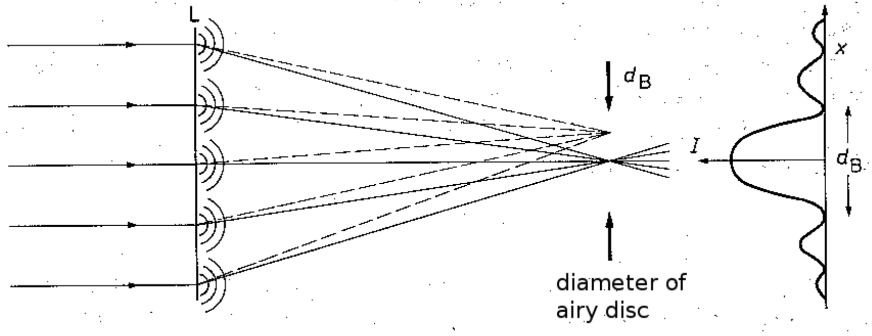

Figure 3.8: Diffraction [55].

3.4 Energy Dispersive X-ray Spectroscopy - EDX

EDX provides information about the specimen composition. Incident electrons can excite atoms in the specimen, so that an electron from an inner shell is ejected. An electron from an outer shell fills the electron hole under emission of the energy difference. The energy is emitted as X-ray. Because the energy difference of the shells is characteristic for every element, the composition of the specimen can be determined by analysation of the X-ray wavelengths. For a quantitative analysis of the element ratio in the sample, further calibration and calculations are necessary.

Sample preparation

Depending on further experiments, 2 µl of the particle solution is either dropped and dried on a piece of silicon wafer or a TEM grid.

3.5 Focused Ion Beam - FIB

A FEI Helios Nanolab 600 system is used for this work. It consists of a dual beam system with an electron beam column, an ion beam column, a gas injection system and a microprobe tool. It can be operated in SEM [6], STEM and EDX and ion mode. As the functions of SEM, STEM, EDX have been described in previous sections, only the ion beam mode and the microprobe system will be described. A schematic diagram of a dual beam FIB system is shown in figure 3.9. An ion beam with a low current density can be used simultaneously to an electron beam to reduce the charging effects that occur during imaging with the electron beam, which is a major problem.

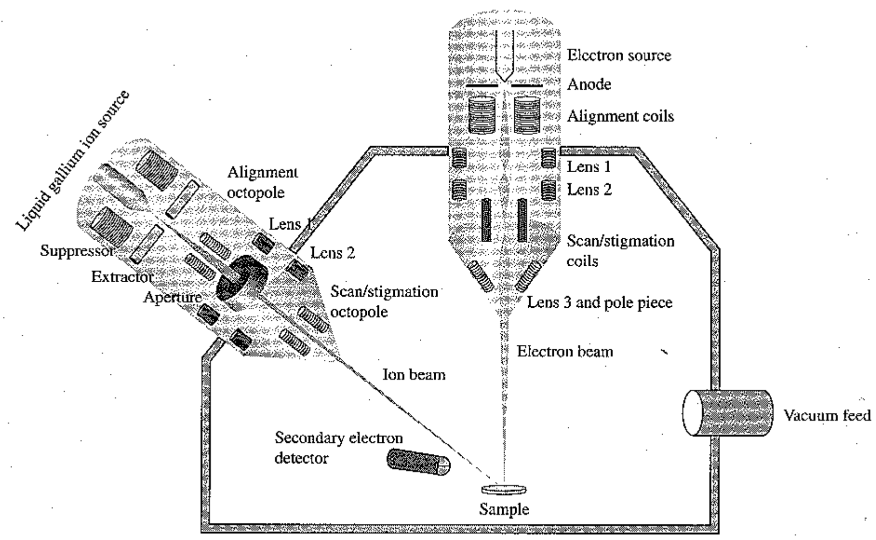

Figure 3.9: Schematic diagram of a two-beam focused ion beam system. [58]

3.5.1 Liquid metal ion source - LMIS

The gallium ions Ga^{+} are provided by a liquid metal ion source (LMIS). Gallium is used in most FIB systems because of its low melting point and, therefore, low interdiffusion with the tungsten tip. Furthermore, it has a low volatility, is long lasting and has a low vapor pressure which allows use of the pure metal without the need a mass separator. A further advantage is the specific weight of gallium. It is heavy enough to allow milling of the heavier elements but is still light enough not to destroy a sample immediately. It can be easily distinguished from other elements in elemental analysis [58].

A liquid metal source consists of a reservoir of a heavy metal, that is heated near to evaporation, and a sharp, heat-resistant tungsten needle with a tip of a few micrometer

---

[6] Acceleration voltage: 5-30 kV.

in diameter. The liquid metal is drawn to the tip of the needle by a potential difference. The liquid metal forms a taylor cone with a tip about 5 nm in diameter from where the gallium can be evaporated and ionized by field evaporation. The Ga^+ ions are accelerated and focused by a series of lenses likewise as in the case of electrons. But in the case of ions, generally only electrostatic lenses are used, whereas in the case of electrons mostly magnetic fields are applied. The higher mass of the Ga^+ ions and the slower velocity have to be taken into account for the construction of the lenses [58].

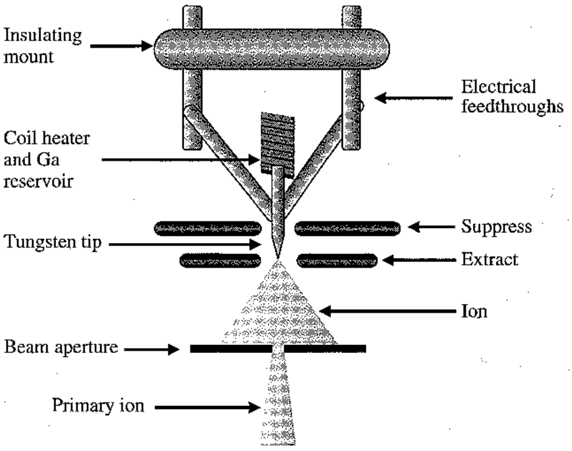

Figure 3.10: Cross-sectional diagram of a liquid metal ion source [58].

3.5.2 Interactions of electrons and ions with the sample

Electrons and ions of the beams interact with the sample during measurements. Following interactions of electrons and ions with the sample occur during the experiments:

Sample alteration by electrons

The sample does not remain unaffected by the irradiation with electrons. The incident electrons that do not leave the sample by backscattered electrons or other effects lead to a local heating of the irradiated parts of the sample. This can lead to an irreversible damage of the sample. If organic substances are included in the sample or the sample is contaminated with organic substances their ionisation and decay can lead to the formation of bubbles and cracks. Induced carbon deposition on the surface makes it difficult to image the surface structure [58].

Sample alteration by ions

Incident ions affect the sample, as well as electrons. The ions are slower, but larger and heavier than electrons and, thus, they own a larger momentum. Ions cannot penetrate the sample surface easily due to their size, which increases the probability of interactions with surface atoms, which leads to a rapid loss of energy. The ion beam and transfer of the ions' energy induces many secondary processes and reactions, such as ionization of surface atoms, breaking of chemical bonds, recoil and sputtering of constituent atoms, defect formation, electron excitation and emission, photon emission, thermal and radiation-induced (inter)diffusion of constituent elements, phase transformation, amorphization, crystallization, track formation, ion implantation and a change of surface morphology [58].

3.5.3 Ion etching and sputtering

Ion etching results from the kinetic collision of incident ions with surface atoms. A part of the kinetic energy is transferred to the atom. Recoiled atoms collide with other atoms and a cascade collision process occurs. Some of the affected atoms are ejected from the sample surface. The sputtering process is dependent on the sample material and very complex. It is used to erode and smoothen the surface but in some cases a random roughening can take place [58].

3.5.4 Gas assisted ion beam etching

To enhance the ion etching a reactive neutral gas is channeled through a fine gas nozzle onto the specimen surface. The gas reacts with the sample and forms volatile products that leave the surface and do not redeposit; these are removed by the vacuum system.

The steps in gas assisted focused ion beam etching processes as described in [58] are:

1. Introduction of a chemically neutral gas to the surface and its adsorption or chemisorption.
2. Reaction of gas and sample either spontaneously or the gas reacts with the sample after decomposition in the presence of the ion beam.
3. The reaction products are desorbed from the surface and removed by the vacuum system.

Based on the gas that is supplied [7], it is possible either to enhance the etching process or to deposit material onto the sample surface.

3.5.5 Gas assisted ion beam deposition

The gas assisted deposition functions quite similar to the gas assisted etching. According to [58] the steps of the deposition process are the following:

1. Introduction of a gaseous precursor close to the surface and its adsorption on the specimen surface.
2. Decomposition of the adsorbed precursor molecules by the ion beam into nonvolatile and volatile components. The ion beam causes sputtering of the sample surface as well.
3. Remaining of the nonvolatile products on the sample surface, forming deposition layers, while the volatile products are desorbed from the surface and removed by the vacuum system.

---

[7] and the ion beam density among other paramaters

A successfull deposition of material depends on several conditions. One condition is the introduction of a proper amount of gas precursor. If the gas flux is too high the deposition rate is reduced. If the gas flux is to low, the gas gets consumed to quickly and the sputtering process dominates. The gas flux can be adjusted by nozzle location, like height from to surface and distance from the scanning ion beam as well as by the temperature of the gas crucible. Furthermore it is important for the location of the gas nozzle, that the ion beam does not get disturbed due to field effects. The gas flux has to be kept constant to achieve a uniform deposition.

Another parameter, which is important for a successful deposition is the ion beam current density. There are mainly three distinct ranges: A low beam current density leads to low decomposition of the precursor and low sputtering. The deposition rate is low as well. An intermediate beam current density results in increasing sputtering and decomposition rates. In this range the deposition rate reaches its maximum and becomes the dominant process. A high beam density does not increase the decomposition rate further, but sputtering processes become dominant.

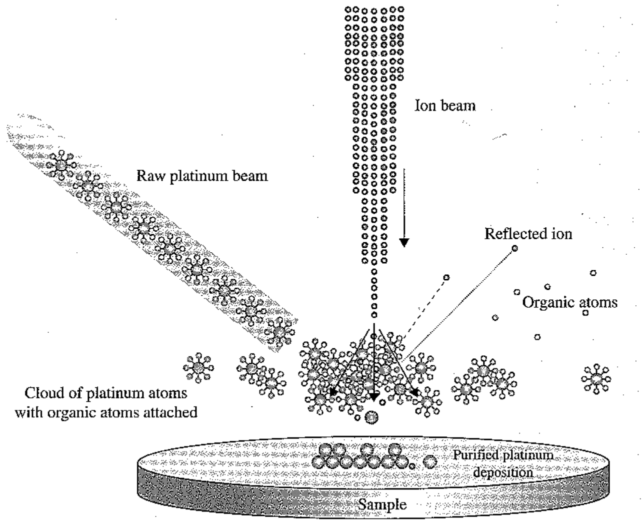

Figure 3.11: Cross-sectional diagram of a liquid metal ion source. [58]

Platin is mainly used for deposition in our system. A slower Pt deposition with electrons is also possible.

3.5.6 Sample manipulation with the micromanipulator

The micromanipulator system consists mainly of long thin stearable rod microtool, which is adjustable in three dimensions. A thin slice cut out of a sample can be removed from the sample for further manipulation and the sample can be contacted with the microprobe as well.

For lamella milling the ion and the electron beam have to be focused well in one point, the sample must be in the focal point of both beams. To cut a cross-section lamella (from a sample) the surrounding area is trench milled to 100 nm. Subsequent the lamella is thinned. The microprobe needle is inserted and "glued" to the slice by platin deposition. Then the lamella is cut free afterwards and lifted out by slight retraction of the rod. The sample is thinned out further to about 40 nm and "glued" to a TEM slot grid by platin deposition.

Sample preparation

The range of possible sample preparation methods is wide. For this thesis 2 μl of particle solution were dropcasted and dried onto a piece of silicon wafer either in air or vacuum in an exsiccator, depending on the fact whether an exposure of the sample to oxygen has to be avoided or not.

3.6 X-ray diffraction - XRD

XRD is used to gain information of the crystal structure of a sample. For a diffraction experiment the wavelength has to be in the range of the interatomic distance. Three types of “waves” are used for diffraction experiments; X-rays (Laue and Bragg), electrons (Davisson and Germer) and neutrons (Shull). X-ray diffraction is used in this thesis only.

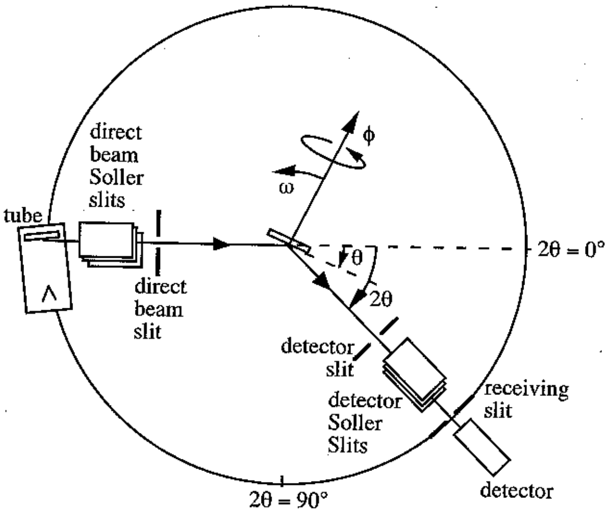

Figure 3.12: Schematic diagram of a XRD-system [52].

The main feature is, that the oscillating field of the incoming x-ray beam accelerates atomic electrons and these generate a secondary beam with the same wavelength as the incoming [52].

Monochromatic x-rays, in our case with a wavelength of $\lambda = 1.5406\,\text{Å}$, are irradiated on the sample, which is placed on a rotatable desk. The rotatable detector and the desk are moved during the measurement, so that the beam irradiates the sample under different angles θ and the outgoing beam is detected under an angle of 2θ. Positive interference occurs if the Bragg condition for the interplanar spacing d of the particles and the angle θ of the incoming beam is fulfilled:

$$2d\sin\theta = n\lambda \tag{3.2}$$

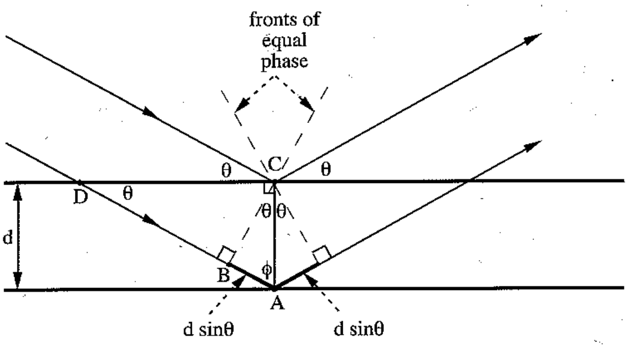

Figure 3.13: Bragg condition [52].

with n = integer. The diffraction pattern of a powder with many crystallites contains various distinct peaks, each corresponding to an interplanar spacing. For a cubic crystal lattice the interplanar spacings are:

$$d_{hkl} = \frac{a_0}{\sqrt{h^2 + k^2 + l^2}} \tag{3.3}$$

with a_0: lattice parameter, d_{hkl}: interplanar spacings, h, k, l: Miller indices. Because of the random orientation of the particles, all possible bragg reflections can be observed with different intensities. The resulting pattern is compared to known patterns to identify the peaks and, hence, the crystal structure. [52]

Sample preparation

Enough particle solution to achieve a few mutilayers of particles covering the surface (depending on the concentration of particles in solution and the area of the sample) is dropped onto a square piece of silicon wafer. The solution is dried in an exsiccator to accelerate the desiccation.

3.7 Alternating Gradient Magnetometer - AGM

The magnetic properties of the samples are measured with a MicroMag ^{TM}2900 Alternating Gradient Magnetometer from Princeton Measurements Corporation. The maximum field is 14 kOe at ambient temperature. It can also be operated at low temperatures starting with the temperature of liquid helium $4K$ as well as high temperatures up to $1073°C$ [59].

3.7.1 Function of an AGM

The sample is attached to the glas plate at the tip of the transducer probe with silicon grease. The probe is attached to the micropositioner, so that the transducer probe assembly can oscillate either in x- or z-direction depending on the micropositioner and the chosen method of measurement. Then the sample is located between two pairs of coils, see figure 3.14, figure 3.15 and figure 3.16. The outer coils apply a static magnetic field up to 14 kOe. The inner gradient coils apply an alternating, sinusoidal gradient field. The resulting alternating periodic force leads to deflection of the sample, which is detected with

a piezoelectric sensing element. Depending on the change of the homogeneous field produced by the field coils, the force on the sample varies. It is proportional to the magnetic moment of the sample and the gradient field [59].
For every sample, the resonance frequency is determined first. Therefor the frequency of the gradient coils is changed. In the case of the resonance frequency the maximum signal is obtained.
The sample can be mounted in plane (parallel) or out of plane (perpendicular) to the external magnetic field. Before samples a measured, the system is calibrated via a nickel foil sample with known magnetic moment, for parallel measurements, and an yttrium iron garnet (YIG) sphere in the case of perpendicular measurements.

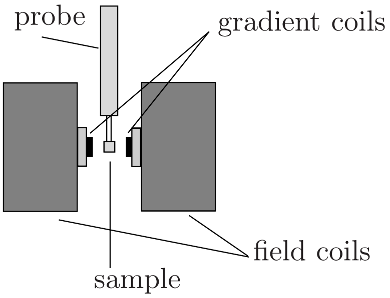

Figure 3.14: AGM x-axis probe parallel.

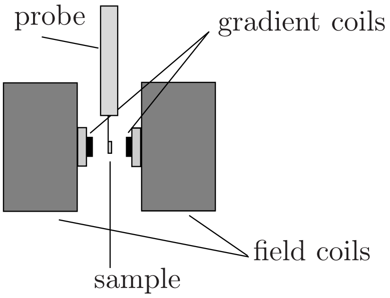

Figure 3.15: AGM x-axis probe perpendicular.

3.7.2 Low temperature setup

The low temperature setup allows to measure the magnetisation at temperatures down to 10 K, with a probe that detects oscillations in Z-direction; the maximum applied field in this setup is 10 kOe. A cryostate is attached to the AGM setup. The cryostate is connected to a liquid He storage device. It has a tube on top which is located between the coils as shown in figure 3.16. During measurement, the sample is mounted inside the tube where it is cooled by a flow of cold He gas.

AGM sample preparation

Silicon wafer is broken into approximately $3\mathrm{mm} \times 3\mathrm{mm}$ to $4\mathrm{mm} \times 4\mathrm{mm}$ large pieces. Then typically 2 µl of particle solution is dropped onto the wafer. The solution is dried

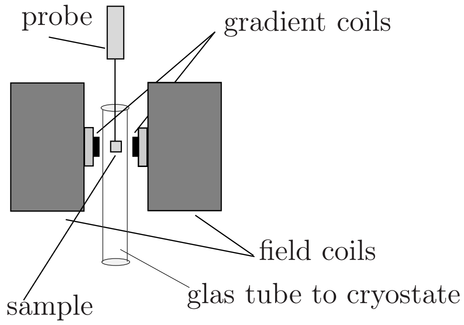

Figure 3.16: AGM z-axis probe (only parallel) with glas tube.

up in an exsiccator. It is important to be cautious not to touch the sample with anything that could lead to magnetic contamination such as stainless steel tweezers. The abrasion is sufficient enough to affect the measurement. Therefore nonmagnetic titanium or plastic tweezers have to be used to handle the samples.

3.8 Infrared spectroscopy

IR spectroscopy is used to identify a substance and its structure. For measurement of an IR spectrum, the substance is filled in a cuvette. A beam of infrared radiation is passed through the sample and the absorption is measured for each wavelength. Infrared light spectrum covers wavelengths from 0.8 μm to 500 μm. This corresponds to wavenumbers from 12500 cm^{-1} to 20 cm^{-1} including near and far infrared. Wavenumbers $< 4000 cm^{-1}$ down to about $30 cm^{-1}$ are commonly used [60].

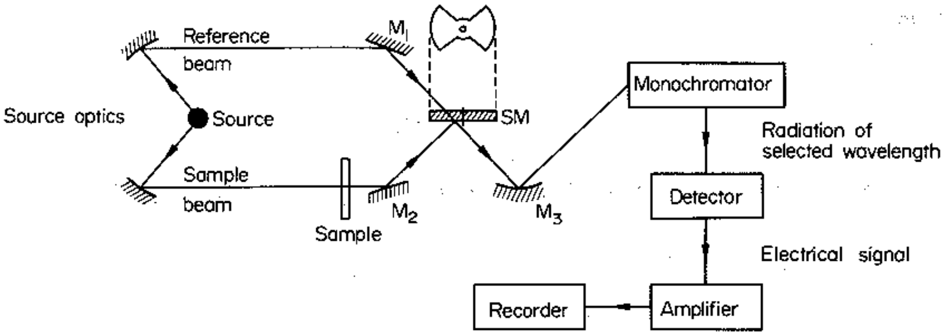

Figure 3.17: Schematic diagram of a double-beam infrared spectrophotometer [60].

A molecule can absorb energy from an electromagnetic field of a light wave if one of its vibrational frequencies matches the frequency of the incident wave. The position, width and intensity of the absorption bands are characteristic for a molecule. The intensity I of the outgoing light wave is reduced compared to the incoming light intensity I_0 depending on the thickness d, the concentration c and the extinction coefficient ε of the sample material. It can be described by the Beer-Lambert law

$$I = I_0 e^{-\varepsilon c d} \quad . \tag{3.4}$$

The transmissivity T is given by

$$\mathsf{T} = \frac{I}{I_0} \quad . \tag{3.5}$$

The whole molecule, in the case of small molecules, or parts of the molecule, in the case of large molecules, are excited into higher quantum states. These can be electronic, vibrational and rotational energy levels. A state can be only excited if the vibration is infrared active, which means if a dipole moment is induced. Stretching vibrations [8], bending and deformation vibrations [9] and libration as well as mixing forms can occur.

For larger molecules the increasing number of atoms causes an increase in the number of vibrations. Symmetry and degeneracy on the other hand reduce the quantity of vibrations. In these large molecules many groups act isolated, so that vibrations are localized only in parts of the molecule. Several functional groups have rather unique vibration transitions. This means compounds with groups in common show absorption bands in the same region. To identify a substance or gain information about its structure the obtained spectrum is compared to reference spectra [61, 62, 60, 63].

---

[8] symmetric and antisymmetric stretching vibration, breathing vibration

[9] symmetric and antisymmetric: wagging vibration, rocking vibration, torsional vibration, twisting vibration

4 Cobalt Nanoparticles - synthesis and characteristics

Cobalt nanoparticles offer a wide range of possibilities for application.

The influence of surfactants on particle properties during fabrication is described in the first part of this chapter. Examples for size distribution, shape and crystallinity are introduced.

In table 4.1 the saturation magnetisation M_s and superparamagnetic limit r_{sp} for different phases of cobalt, iron, iron oxide and two iron-cobalt alloys are given.

Cobalt exhibits an saturation magnetisation lower than iron but greater than iron oxide. According to the lower magnetisation of iron oxide, which is currently widely used in nanoparticles for several applications, e.g. Fe_3O_4 particles in commercial ferrofluids for use in stepper motors [8], cobalt offers an opportunity to fabricate nanoparticles with a higher saturation magnetisation and a smaller volume due to a higher magnetic moment. A high magnetic moment joined with a small volume is desireable for many applications. An example for such an application is the use in cells without size-related rejection combined with good reaction to outer fields [11]. As another example, the high coercivity makes it interesting for application in magnetic recording media [64].

material	M_s $[\frac{emu}{cm^3}]$	r_{sp} [nm] at RT
bcc-Fe	1740	8.0
fcc-Co	1420	7.9
hcp-Co	1400	3.9
$Fe_{50}Co_{50}$	1910	11.8
$Fe_{70}Co_{30}$	1933	8.9
Fe_3Co	1993	8.5
Fe_3O_4	415	14.0
Fe_2O_3	380	17.45

Table 4.1: Saturation magnetisation and superparamagnetic limit [19, 20, 21, 22, 23, 24]

The magnetic properties of nanoparticles dependend on the microstructural order within the particle. Hcp-Co and fcc-Co differ in their radius for the superparamagnetic limit.

The cobalt nanoparticles (Co NP) were stabilized during their fabrication with surfactant molecules as described in section 2.2.3. Their surface is covered with amphiphilic molecules afterwards and it is known that nanoparticles oxidize despite their stabilizing surfactant shell. It bears an interesting question to what extend the oxidation of the nanoparticles is influenced by the coverage of the surface by these molecules. A surfactant, for example with a carboxylic headgroup binding to a metallic nanoparticle surface leads to an initial oxidation of one monolayer of Co atoms at the particle surface [18].

The (microstructural) parameters of the synthesized particles differ depending on several parameters during synthetization such as used surfactants, surfactant and precursor concentration, temperature, solvents, precursors, time interval during injection of the precursor solution into the surfactant solution as well as largeness of the batch. Fluctuations of one or more of the previously mentioned parameters during the steps of particle formation have an important influence as well [29, 25, 38]. An increase of the heating rate, as described in [38], leads to an increase in the nucleation rate and results in smaller particles. The parameters have to be kept constant for reproductible results.

To gain information concerning the influence of the surfactants on the oxidation process, it is necessary to investigate particles with comparable parameters such as same diameter, same shape and same crystal structure [and similar concentrations], where only the stabilizing surfactants are varied [18].

It is not possible to prepare particles with several different surfactants, which are similar in all these properties because of the influence of the surfactants itself during particle formation [29, 3, 38]. To overcome this problem, the method of a surfactant exchange is chosen to examine particles with different surfactants.

The nanoparticles fabricated in our chemistry lab were characterized in size distribution, shape, self-assembly and crystallinity [1] by charting TEM images. The average diameter and variance of a batch of NPs was estimated by measuring diameters of several particles of a TEM brightfield image with the program AnalySIS by Soft Imaging Systems GmbH. A histogram of the obtained particles was compiled and fitted by a gaussian curve [2] with the program Igor Pro 5.05A by WaveMetrics,Inc.. The crystallographic phase is determined by evaluation of HRTEM - data, FFT and XRD curves.

HRTEM analysis makes it possible to gain information of the structure within a single particle or of a few particles while XRD analysis results in an average information of a large amount of particles.

4.1 Cobalt nanoparticles - overview

The stabilizing surfactants were varied in particle fabrication. A short overview over typical outcomes of some of the syntheses of particles stabilized directly with different surfactants is displayed. For the particles displayed in figure 4.1 oleylamine was used for stabilization instead of trioctylphosphinoxid (TOPO). These particles have an average diameter $\langle \mathsf{D} \rangle =$ 11.59 nm ± 1.53 nm. Apart from spherical particles a large amount of flat triangles, truncated triangles, hexagons and nearly circular discs are visible. These flat particles exhibit a nearly uniform contrast. The particles self assemble into larger fields, where larger particles are flanked by smaller ones. The particles depicted in figure 4.2 were stabilized with TOPO and have an average diameter $\langle \mathsf{D} \rangle =$ 15.56 nm ± 1.85 nm. Here only a few flat triangles and truncated triangles can be found. The contrast in the thicker circular particles that are lying upon another indicates that these particles are rather discs than spheres. These particles form mostly bead-on-a-string like structures, that seem to entangle and even cross each other. The particles displayed in image 4.3 were stabilized with a combination of oleylamine and oleic acid and exhibit an average diameter $\langle \mathsf{D} \rangle =$ 5.99 nm ± 1.11 nm. Larger and smaller spherical particles are visible as well as larger discs

---

[1] if assignable

[2] $f_{fitgauss} = y_0 + A \exp\left(-\frac{x-x_0}{w}\right)^2$, $y_0 = 0$

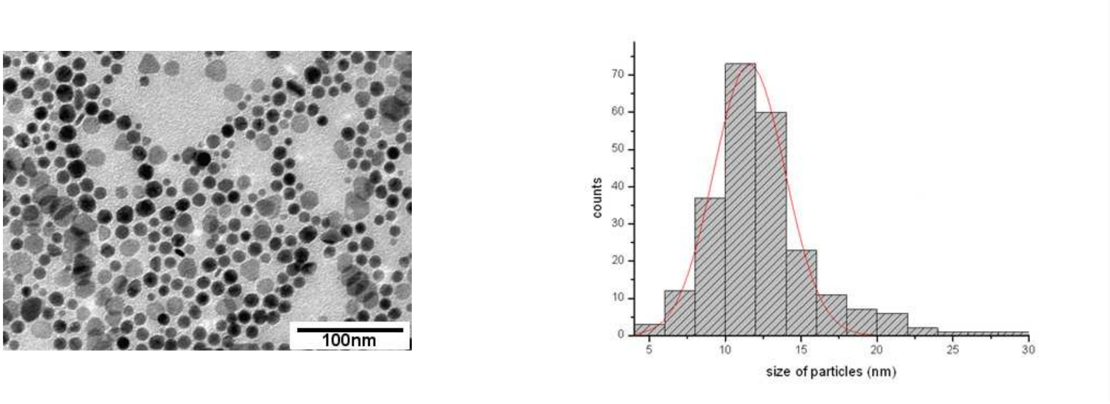

Figure 4.1: Particles stabilized with oleylamine, average diameter ⟨D⟩= 11.59 nm ± 2.35 nm, N=248.

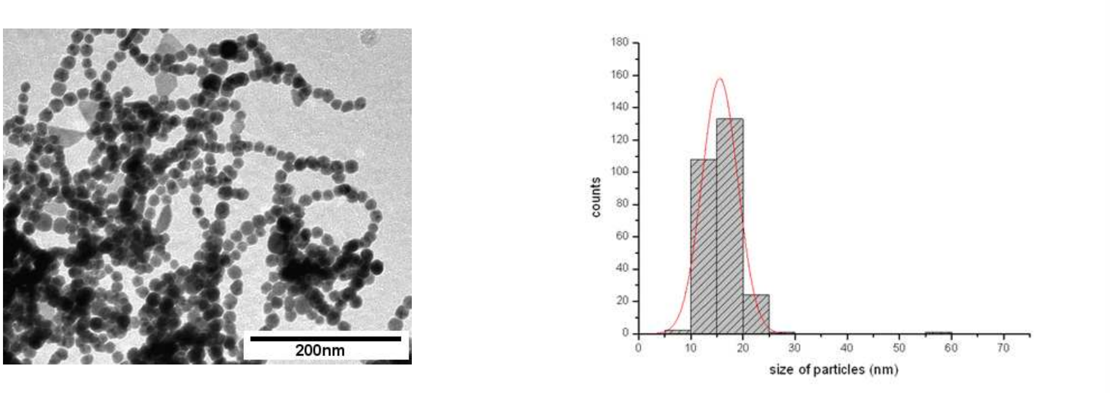

Figure 4.2: Particles stabilized with TOPO, average diameter ⟨D⟩= 15.56 nm ± 3.42 nm, N=274.

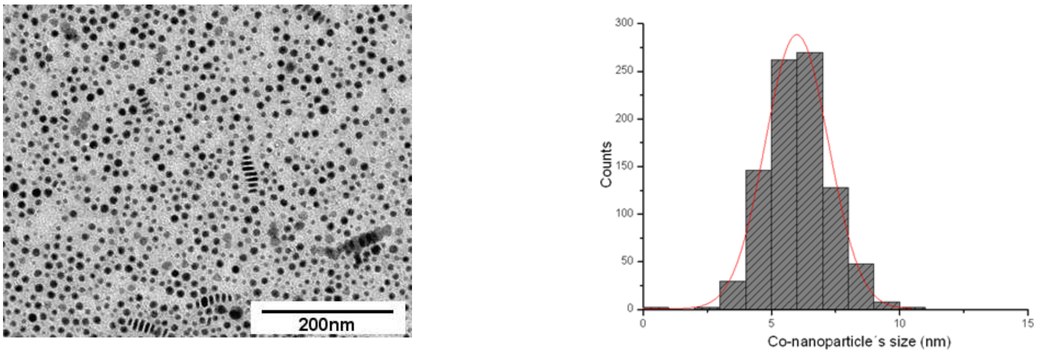

Figure 4.3: Particles stabilized with oleylamine and oleic acid, average diameter ⟨D⟩= 5.99 nm ± 1.23 nm, N=842.

that are aligned mostly upright flat side to flat side next to each other in small rows on the carbon foil of the TEM grid. The discs are mostly circular as can be seen in horizontal stacks. The height of the discs was estimated by measuring a smaller amount of upright discs. Generally these particles have a height between one half radius and one radius. A few triangles, that are slightly smaller than the circular discs, can be found.

It can be clearly seen that the use of different surfactant molecules results in different diameters, standard deviations of the particle diameter distribution, morphologies that occur in the batch and differences in the self assembly and therefore in the particle interaction and magnetic properties.

4.2 Shape

The Co particles that are introduced exemplary at the beginning of this chapter exhibit predominantly spherical and disc like shapes. Furthermore cubes, rods, triangles and hexagons can be found often in batches fabricated in our chemistry lab. In [65] it is described that the edges of the triangles get less pronounced over time and hexagonal discs form. A recrystallisation from discs to spheres was observed as well in [65], as the particles have been stored under ambient conditions at room temperature; the recrystallisation process stretched over several days. Figure 4.4 shows TEM images of cobalt spheres (image on the left), discs (image in the middle, note the upright discs) and cubes (image on the right) as an example for occurring shapes.

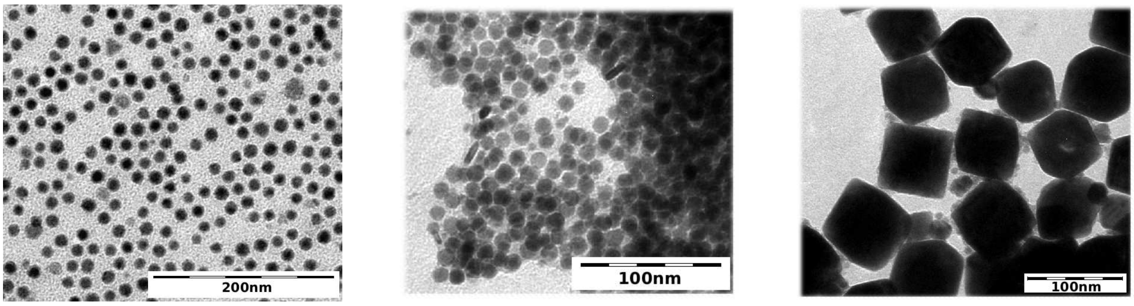

spheres, ⟨D⟩= 12.13 nm ± 2.65 nm, N=275

discs, ⟨D⟩= 11.61 nm ± 2.04 nm, N=142

cubes, ⟨D⟩= 64.1 nm ± 13.99 nm, N=185

Figure 4.4: Co nanoparticles with different morphologies

4.3 Crystallinity of Co particles

During the synthesis mono- as well as polycrystalline particles can form.
To emphasize the difference in crystallinity two distinct examples of the microstructural composition of the particles are given in figure 4.5 and figure 4.6.
The first image 4.5 shows particles with an average diameter ⟨D⟩= 11.52 nm ± 1.25 nm prepared with TOPO. These particles exhibit a uniform contrast in the TEM image, so it can be deduced that they are monocrystalline. The particles in the second TEM image 4.6 with an average diameter ⟨D⟩= 5.44 nm ± 2.72 nm prepared with trioctylamine (TOA) exhibit difference in contrast within each particle. This indicates polycrystallinity of the

particles. Different orientations of crystals lead to different intensities and contrasts in the image, because the electron deflection differs in dependence on the crystal orientation [3].

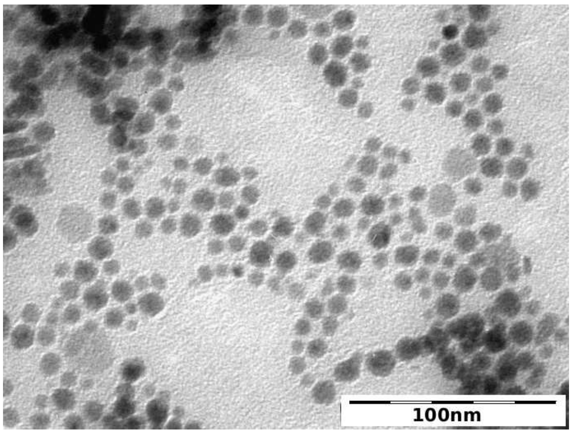

Figure 4.5: Monocrystalline Co NP

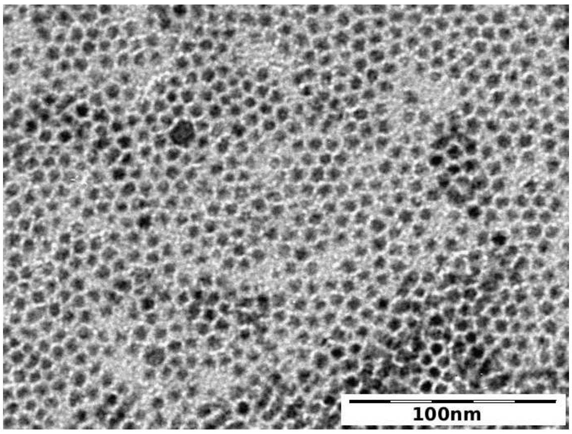

Figure 4.6: Polycrystalline Co NP

4.4 Oxidation of particles prepared with different surfactants

The oxidation of the particles was observed indirectly by monitoring the decrease of the saturation magnetic moment using an AGM. From the measured saturation magnetic moment the saturation magnetisation can be calculated if the concentration of cobalt is determined. The concentration of cobalt in the sample cannot be calculated by using the data of the used precursor, because not the complete cobalt is turned into particles. An excellent calculation of the saturation magnetisation of Co particles, by exerting of the amount of cobalt distributed on the sample, can be found in [18]. The antiferromagnetic CoO shell is assumed not to contribute to the measured saturation magnetic moment. Ideally no stray field is generated by the antiparallel aligned spins. If it is assumed that the decrease of the saturation magnetic moment of the sample is proportional to the amount of cobalt oxide that has formed in the sample the progress of the oxidation process can be deduced. If the sample oxidizes homogeneously and the oxide on the particles forms homogeneously as well, it can be assumed that the amount of oxide formed one every particle is equal (for that all particles being equal). If further the relative decrease of the saturation magnetic moment is proportional to a relative decrease of the Co core in every particle, which is equal to a relative increase of the cobalt oxide shell of every particle, the thickness of the oxide shell and the size of the non-oxidized core can be calculated. An initially existing oxide shell on the particle surface leads to a lower magnetic volume at the first measurement and therefore an error in the oxidation curve as the actual point of origin cannot be measured. This error is neglected for simplification, as oxidation curves are compared and evaluated qualitatively and no absolute values are computed.

The decrease of the saturation magnetic moment of three different particle batches prepared with oleic acid $\langle \mathsf{D} \rangle = 4.01$ nm ± 0.21 nm, oleylamine $\langle \mathsf{D} \rangle = 6.01$ nm ± 1.05 nm and 1-pyrenebutyric acid $\langle \mathsf{D} \rangle = 3.37$ nm ± 1.88 nm is displayed in figure 4.7 [4]. On the

---

[3] For a concrete determination of the crystallinity HRTEM images have to be taken, as presented for a set of samples in section 9.5.

[4] Image taken partly from [18].

right side in figure 4.8 the values are normalized for better comparability. If the curves are compared, while the different radii of the particles are kept in mind, it might be concluded that the surfactants have an extremely strong influence of the oxidation of the particles, due to the different shape of the curves.

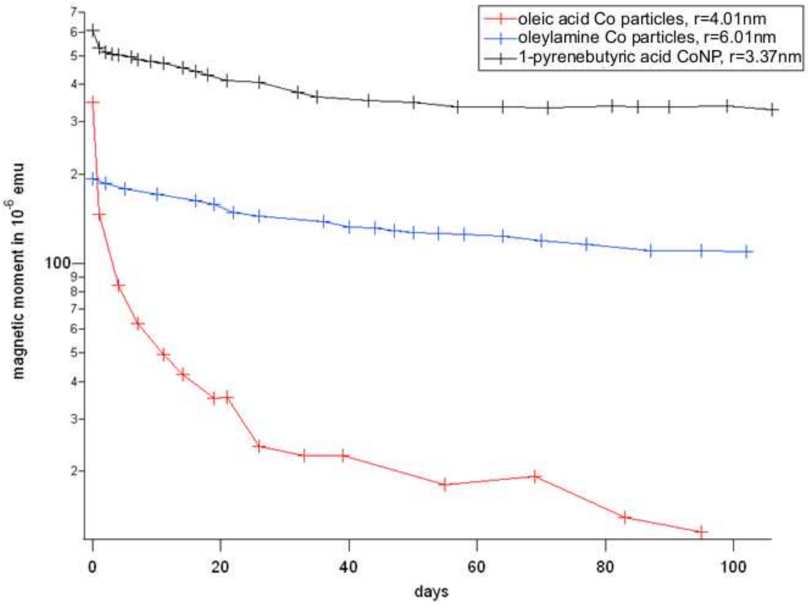

Figure 4.7: Decrease of the saturation magnetic moment over a time of several days.

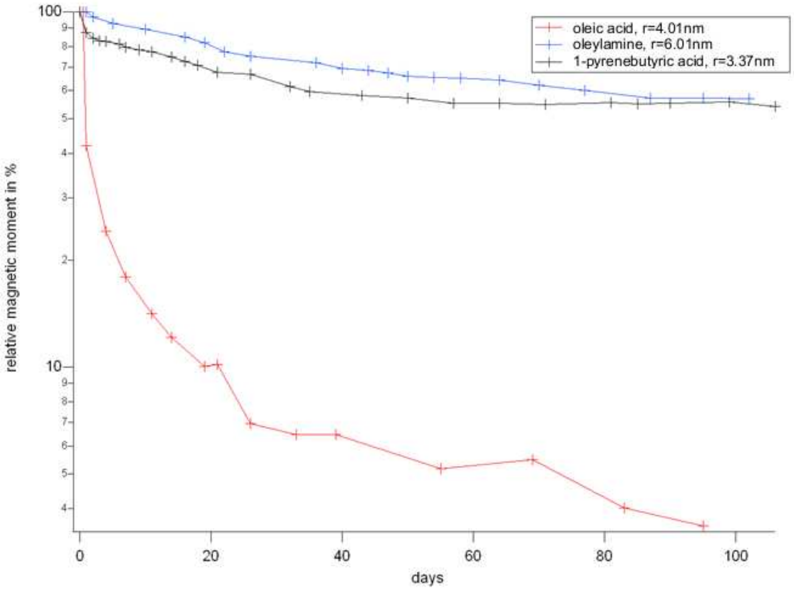

Figure 4.8: Normalized decrease of the saturation magnetic moment over days.

5 Surfactants and surfactant exchange

In this chapter the basic particles and the investigated surfactants are presented as well as the surfactant exchange and its proof by IR-spectroscopy. The influences of the surfactant exchange on the particle properties are evaluated; the properties regarded are diameter with size reduction, self-assembly with minimal inter particle distance and surfactant layer thickness, coercivity, hysteresis curve, shape, crystallinity and saturation magnetic moment.

5.1 Basic particles prepared with trioctylphosphin oxide (TOPO)

The particles were prepared with Trioctylphosphin oxid (TOPO) [1] according to the method described in [35] and described in detail in section 2.

To gain information regarding the size and shape of the cobalt nanoparticles TEM, REM and STEM were used. The suitability for a surfactant exchange was determined by taking TEM images of the initially produced particles. An image of these particles covered with TOPO is shown in figure 5.2.

Their average diameter is $\langle \mathsf{D} \rangle = 12.15$ nm ± 1.68 nm, a quantity of N=372 particles was metered. The discoidal particles self-assemble on the carbon foil of the TEM grid mostly into 3-dimensional structures, sometimes with a monolayer fringe about one particle wide. The average distance between the particles is $\langle d_i \rangle = 1.54$ nm ± 0.49 nm. A hysteresis curve of the particles, measured with an AGM a few hours after preparation is shown in figure 5.3. The sample exhibits a saturation magnetic moment of $m_s = 2.507$ memu, a coercivity of $H_c = 134.7$ Oe and a remanence of $m_r = 632.6$ μemu. With a diameter $\langle \mathsf{D} \rangle = 12.14$ nm the particles are below the superparamagnetic limit for fcc cobalt as displayed in table 4.1, which does not fit well to the measured hysteresis curve. Larger particles with a size above the superparamagnetic limit as well as agglomerates and in particular the dipolar interaction between particles explain of the discrepancy between theory and experiment.

5.2 Surfactant exchange

The surfactant exchange was carried out to systematically investigate the influence of the headgroup, chain length, number of chains and in some cases double bonds and therefore resulting kinks and reduced flexibility in the molecule geometry [2]. For a description the process of the surfactant exchange see section 2.2.2.

The initial cobalt nanoparticles were produced with TOPO. This is the weakest binding surfactant, which allows an uncomplicated surfactant exchange.

---

[1] The surfactant molecule is displayed schematically in 5.1

[2] Double bonds in the alkyl chain lead to kinks and stiffness [25].

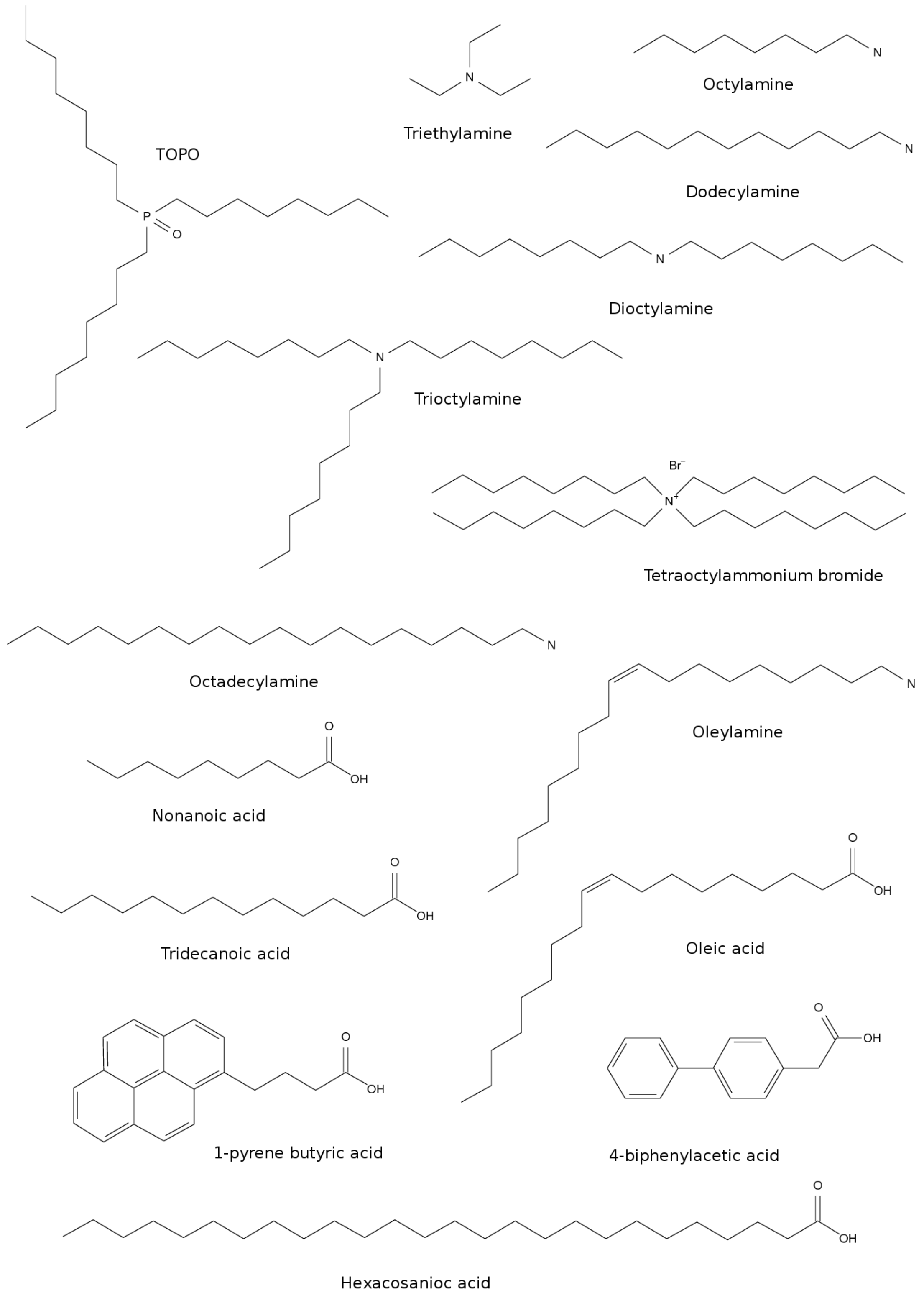

Figure 5.1: All surfactants used in this experiment.

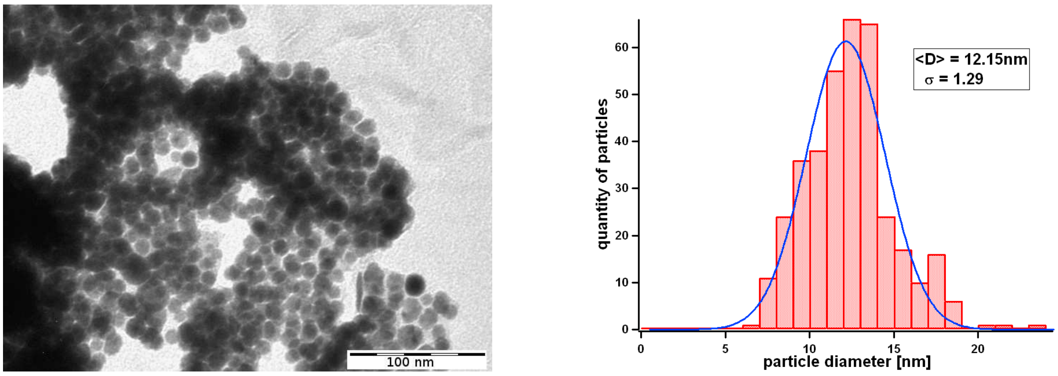

Figure 5.2: Particles prepared with TOPO, ⟨D⟩= 12.15 nm ± 1.68 nm, N=372.

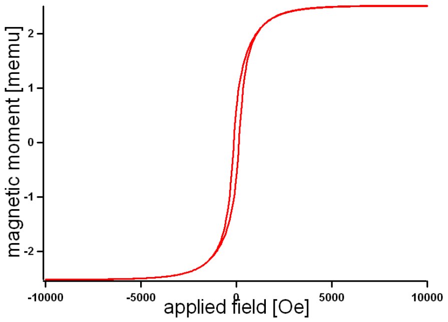

Figure 5.3: Hysteresis curve of fresh Co particles prepared with TOPO.

5.2.1 Used surfactants

The surfactants used in this experiment are depicted as skeletal formulas in figure 5.1. In table 5.1 and table 5.2 an overview over the used ligands and their main properties are given.

TEM bright field images of every sample were taken to determine their size, shape, self assembly and to proof that the particles did not dissolve or formed inseparable agglomerates. The samples were prepared as described in section 3.1. The magnetic properties were investigated by AGM measurements, the sample preparation was carried out as explained in section 3.7.

IR spectroscopy

A successfull realization of the surfactant exchange was determined by IR spectroscopy. In all exchanged samples the typical wavenumber of 1126 cm^{-1} for the $\mathsf{P} = \mathsf{O}$ oscillation on the particle surface [37, 29] could not be detected any more. An example of the difference between the data for the particles with the new surfactant and a typical curve for TOPO is displayed in figure 5.4

---

[3] Reference spectra of dodecylamine and TOPO are taken from [66]

head (group)	**chain length**	**# chains**	**name**
OP	8	3	trioctylphosphine oxide
NH_x	2	3	triethylamine
NH_x	8	1	octylamine
NH_x	8	2	dioctylamine
NH_x	8	3	trioctylamine
NH_x	8	4	tetraoctylammonium bromide
NH_x	12	1	dodecylamine
NH_x	18	1	octadecylamine
NH_x	18	1	oleylamine
COOH	8	1	nonanoic acid
COOH	12	1	tridecanoic acid
COOH	18	1	oleic acid
COOH	25	1	hexacosanoic acid
COOH	2 benzene rings	1	4-biphenylacetic acid
COOH	4 benzene rings	1	1-pyrenebutyric acid

Table 5.1: List of used surfactants - part 1

name	**molecular formula**	**double bond**
trioctylphosphine oxide	$(C_8H_{17})_3PO$	-
triethylamine	$(C_2H_5)_3N$	-
octylamine	$C_8H_{17}NH_2$	-
dioctylamine	$(C_8H_{17})_2NH$	-
trioctylamine	$(C_8H_{17})_3N$	-
tetraoctylammonium bromide	$(C_8H_{17})_4NBr$	-
dodecylamine	$C_{12}H_{25}NH_2$	-
octadecylamine	$C_{18}H_{37}NH_2$	-
oleylamine	$C_{18}H_{35}NH_2$	1
nonanoic acid	$C_8H_{17}COOH$	-
tridecanoic acid	$C_{12}H_{25}COOH$	-
oleic acid	$C_{18}H_{33}COOH$	1
hexacosanoic acid	$C_{25}H_{51}COOH$	-
4-biphenylacetic acid	$C_{13}H_{11}COOH$	-
1-pyrenebutyric acid	$C_{19}H_{15}COOH$	-

Table 5.2: List of used surfactants - part 2

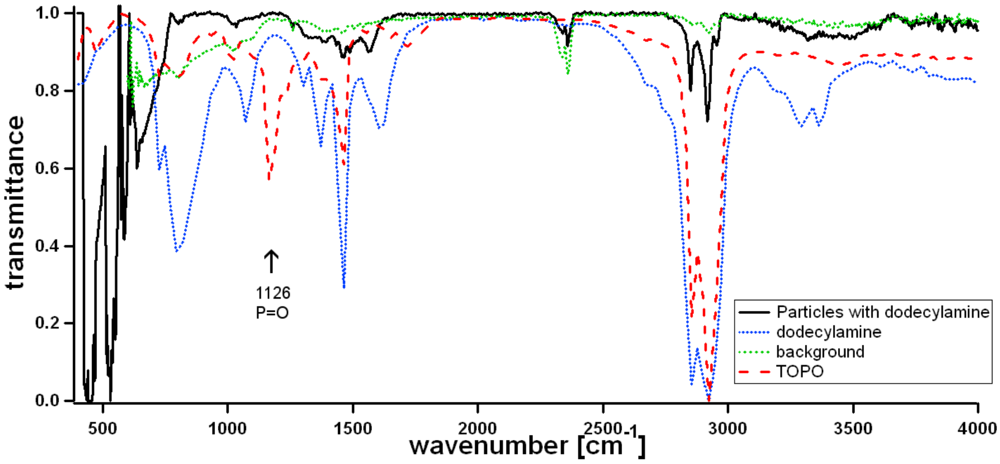

Figure 5.4: IR spectrum of Co NP with dodecylamine, dodecylamine reference spectrum, background and reference spectrum of TOPO.[3]

5.2.2 Amine group as head molecule

Several surfactants with an amino headgroup were chosen with different chain lengths and different number of chains. The amine group binds to the particle surface by physisorption. This bond is stronger than the one in the case of TOPO but weaker than the one of a carboxyl group [41].

Triethylamine

The particles, where case the surfactant was exchanged to triethylamine are displayed in image 5.5 and have an average diameter $\langle D\rangle = 11.78$ nm ± 1.30 nm, N=173. The inter particle distance is relatively small with $\langle d_i\rangle = 1.09$ nm ± 0.36 nm. They form clusters with a thickness of several layers and a single particle wide fringe. Overall the self assembly is close to the one found with TOPO.

Octylamine

These particles, see image 5.6, have an average diameter $\langle D\rangle = 12.11$ nm ± 1.43 nm, N=223. The average minimal inter particle distance $\langle d_i\rangle = 1.53$ nm ± 0.34 nm is larger than with triethylamine. The clusters are several layers thick with a 3-6 particles wide fringe of single layer particles. The clusters are less dense than those found with TOPO and triethylamine. Inbetween the clusters isolated particles are located.

Dioctylamine

The average diameter is $\langle D\rangle = 11.51$ nm ± 1.26 nm, N=185, as can be seen in figure 5.7. Compared to the case of octylamine the inter particle distance remains relatively constant at $\langle d_i\rangle = 1.49$ nm ± 0.38 nm. Again single particles inbetween the clusters can be found. The clusters are thicker than those with octylamine and the monolayer fringe is only about two particles wide.

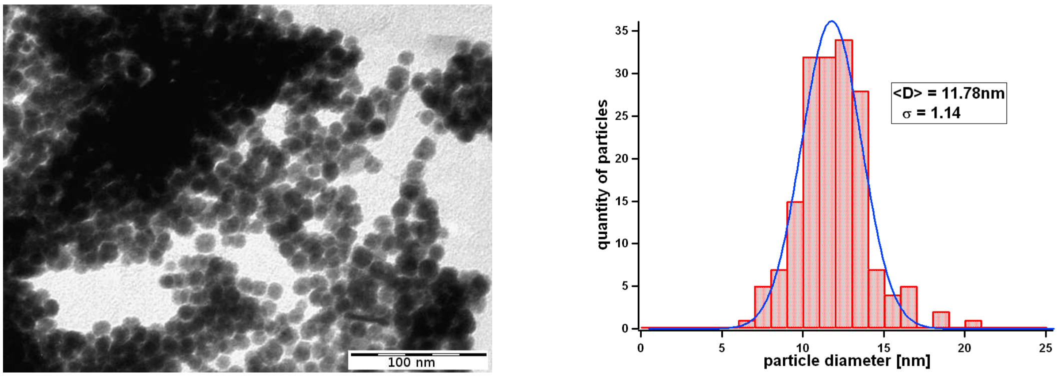

Figure 5.5: Particles covered with triethylamine, ⟨D⟩= 11.78 nm ± 1.30 nm, N=173.

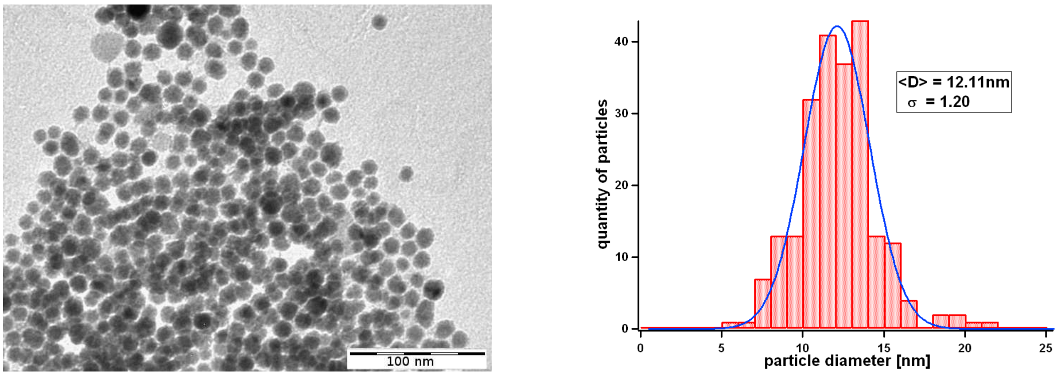

Figure 5.6: Particles covered with octylamine, ⟨D⟩= 12.11 nm ± 1.43 nm, N=223.

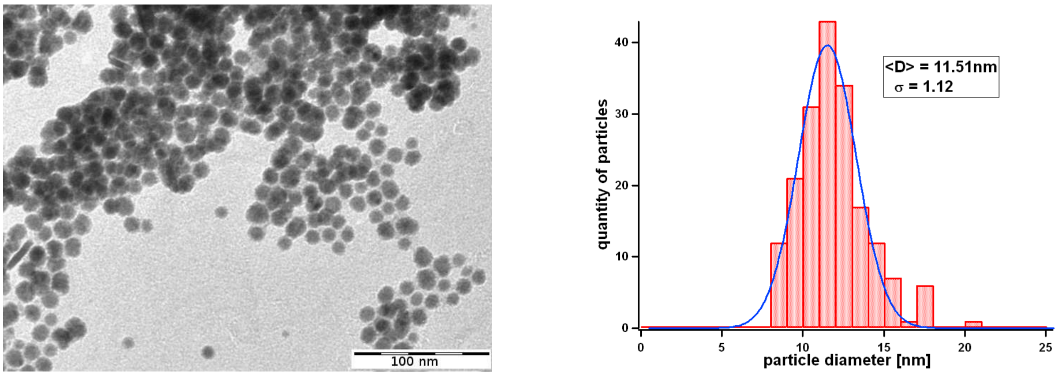

Figure 5.7: Particles covered with dioctylamine, ⟨D⟩= 11.51 nm ± 1.26 nm, N=185.

Trioctylamine

The diameter of the particles stabilized with trioctylamine is reduced to $\langle \mathsf{D} \rangle$= 10.95 nm ± 1.35 nm, N=311. The measured inter particle distance is $\langle \mathtt{d_i} \rangle$= 1.40 nm ± 0.40 nm. It only appears slightly larger than with the last two surfactants in the image, which might result from the lower particle density on the TEM grid. The monolayer fringes around the clusters, depicted in image 5.8, are about 3-8 particles in width. The clusters are less thick than the ones with dioctylamine and slightly thinner than those with octylamine. There can only be found a few isolated particles.

Tetraoctylammoniumbromide

The average particle diameter is $\langle \mathsf{D} \rangle$= 10.98 nm ± 1.23 nm, N=247. Compared to trioctylamine the inter particle distance is about twice the size with $\langle \mathtt{d_i} \rangle$= 2.25 nm ± 0.33 nm, as can be seen in image 5.9. Hardly any isolated particles can be seen. The clusters have a monolayer fringe of about 3-6 particles in width and gain more layers towards the center.

Dodecylamine

These particles are the only ones that have an extended diameter, which was measured to $\langle \mathsf{D} \rangle$= 12.43 nm ± 1.28 nm, N=243, displayed in figure 5.10. The inter particle distance $\langle \mathtt{d_i} \rangle$= 1.64 nm ± 0.43 nm is larger than with octylamine. The monolayer fringes are larger than with octylamine and the clusters consists of multiple layers towards their center.

Octadecylamine

Octadecylamine is displayed schematically in figure 5.1. The average particle diameter is $\langle \mathsf{D} \rangle$= 10.91 nm ± 1.35 nm, N=208. Here the particle distance is larger as well with $\langle \mathtt{d_i} \rangle$= 2.33 nm ± 0.38 nm. The clusters have monolayer fringes and gain multiple layers towards their middle region, see image 5.11.

Oleylamine

The diameter is $\langle \mathsf{D} \rangle$= 11.18 nm ± 1.01 nm, N=318, for these particles, as displayed in figure 5.12. Their distance with $\langle \mathtt{d_i} \rangle$= 2.38 nm ± 0.37 nm is slightly larger than with octadecylamine. This might also be a result of mostly small monolayer areas formed by the particles. The particles might be further apart, as no larger layer forms and the particles are not constricted by several other particles in all directions. Overall the particles self-assemble mostly to monolayers where hexagonal and chaotic regions are mixed. If clusters have more than one layer the additional layers organize hexagonally on top of the bottom layer.

Conclusion for amine headgroup surfactants

The particles decrease overall in size during the surfactant exchange. This effect is also described in [29, 25, 39]. With a longer chain length of the amphiphile molecules the inter particle distance grows. This is investigated in detail in section 5.2.5. For multiple chains a correlation between the number of chains and the particle distance is likely, but could not be found.

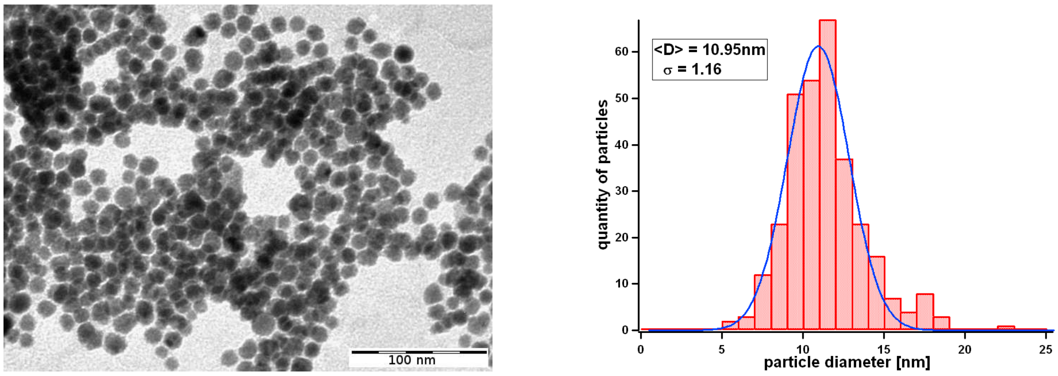

Figure 5.8: Particles covered with trioctylamine, ⟨D⟩= 10.95 nm ± 1.35 nm, N=311.

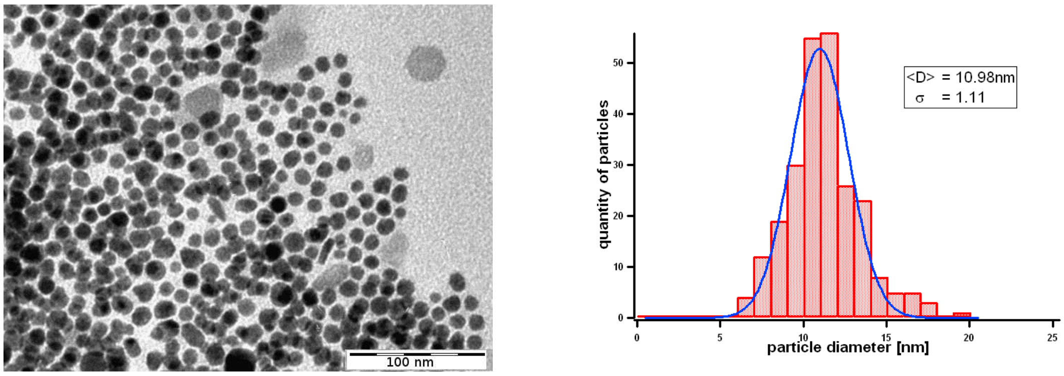

Figure 5.9: Particles covered with tetraoctylammonium bromide, ⟨D⟩= 10.98 nm ± 1.23 nm, N=247.

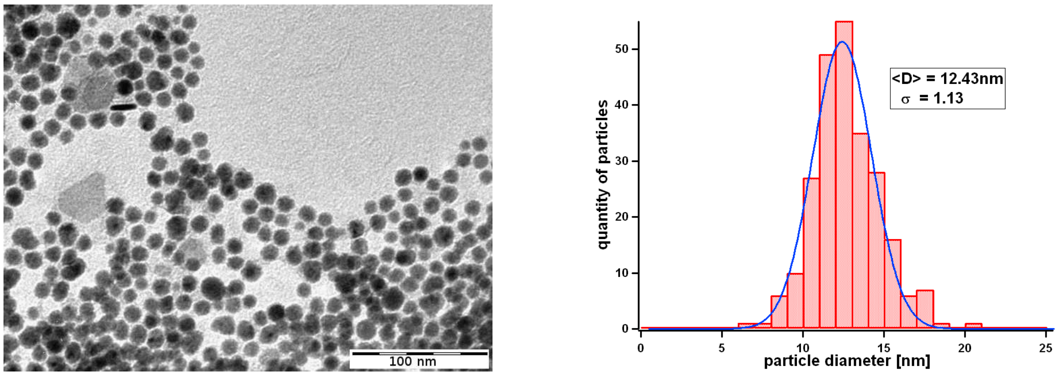

Figure 5.10: Particles covered with dodecylamine, ⟨D⟩= 12.43 nm ± 1.28 nm, N=243.

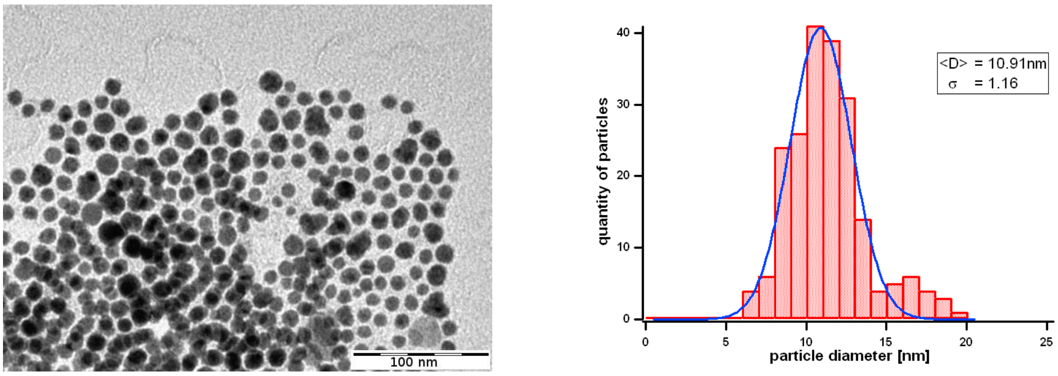

Figure 5.11: Particles covered with octadecylamine, ⟨D⟩= 10.91 nm ± 1,35 nm, N=208.

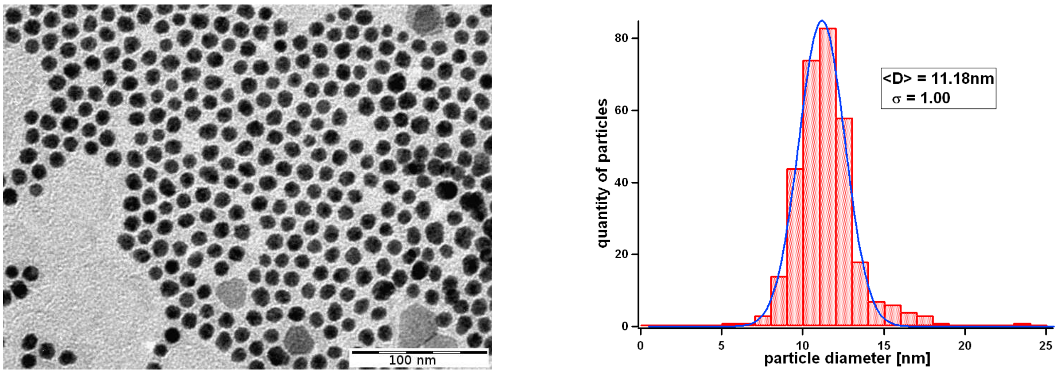

Figure 5.12: Particles covered with oleylamine, ⟨D⟩= 11.18 nm ± 1.01 nm, N=318.

5.2.3 Carboxyl group as head molecule

Surfactants with a carboxyl headgroup were chosen with different chain lengths and two with benzene rings instead of single carbon chains. The carboxyl group binds covalent to the particle surface and therefore stronger than TOPO and the amine group [41, 29, 37, 18, 25].

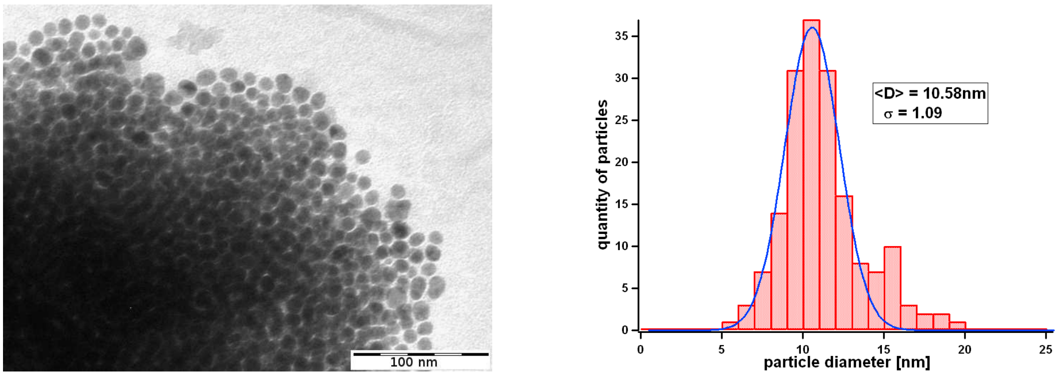

Figure 5.13: Particles covered with nonanoic acid, ⟨D⟩= 10.58 nm ± 1.19 nm, N=173.

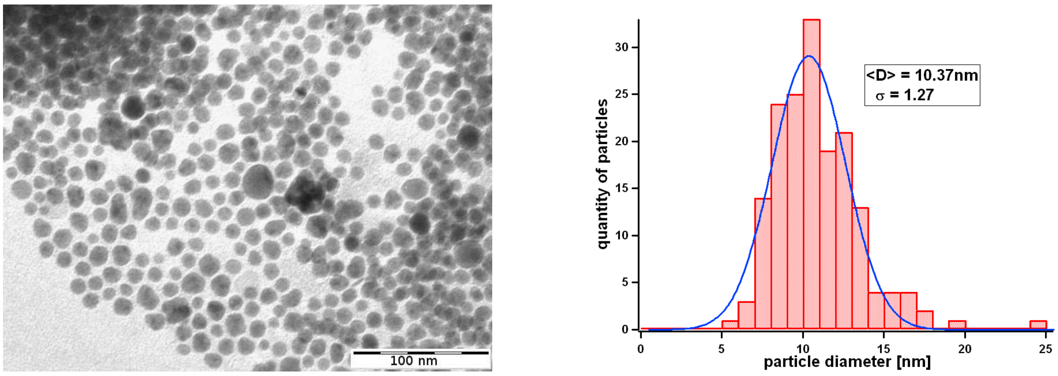

Figure 5.14: Particles covered with tridecanoic acid, ⟨D⟩= 10.37 nm ± 1.60 nm, N=169.

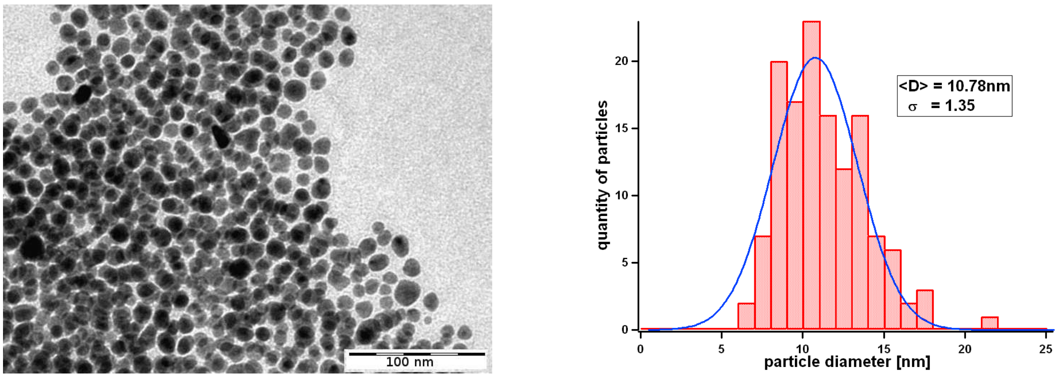

Figure 5.15: Particles covered with oleic acid, ⟨D⟩= 10.78 nm ± 1.84 nm, N=132.

Nonanoic acid

These particles have an average diameter ⟨D⟩= 10.58 nm ± 1.19 nm, N=173. The inter particle distance $\langle d_i \rangle$= 1.34 nm ± 0.43 nm is slightly smaller than in the case of octylamine.

Clusters are formed with a 1-2 particles wide monolayer fringe and are quite thick towards the center, see image 5.13.

Tridecanoic acid

The average diameter is $\langle \mathsf{D} \rangle = 10.37$ nm ± 1.60 nm, N=169. The distance between the particles with $\langle \mathtt{d_i} \rangle = 1.66$ nm ± 0.40 nm is about the same size of the particles with nonanoic acid. The monolayer fringe consists of 1-3 particles and the clusters consists of multiple layers in the middle. The particles are displayed in figure 5.14.

Oleic acid

This surfactant is also depicted in figure 5.1. Here the average diameter is reduced to $\langle \mathsf{D} \rangle = 10.78$ nm ± 1.84 nm, N=132, as depicted in figure 5.15. The inter particle distance $\langle \mathtt{d_i} \rangle = 2.13$ nm ± 0.33 nm is sightly smaller than with oleylamine. These particles form clusters with multiple layers and a one particle wide monolayer fringe and clusters consisting of 1-3 layers with chains and irregular hexagonal structure.

Hexaconsanoic acid

These particles have an average diameter of $\langle \mathsf{D} \rangle = 11.05$ nm ± 1.01 nm, N=272, and an inter particle distance of $\langle \mathtt{d_i} \rangle = 3.12$ nm ± 0.33 nm. They form mostly clouds of single particles with a few small clusters up to three layers, as can be seen in picture 5.16.

Benzene rings instead of carbon chains

The following two surfactants have benzene rings and short alkyl chains attached to the head molecule instead of solely alkyl chains.

4-Biphenylacetic acid

The average particle diameter is $\langle \mathsf{D} \rangle = 11.32$ nm ± 1.06 nm, N=94. These particles form clusters like those stabilized with TOPO. The inter particle distance is $\langle \mathtt{d_i} \rangle = 1.55$ nm ± 0.10 nm. An image of the particles is given in figure 5.17.

1-Pyrenebutyric acid

Here the average diameter was reduced to $\langle \mathsf{D} \rangle = 10.70$ nm ± 1.37 nm, N=268. The inter particle distance is with $\langle \mathtt{d_i} \rangle = 1.75$ nm ± 0.25 nm greater compared to 4-biphenylacetic acid. The clusters formed by these particles are larger than the ones with TOPO or 4-biphenylacetic acid. Some areas with monolayers can be found, which are typically 1-4 particles wide, see image 5.18. This surfactant is depicted schematically in 5.1.

Conclusion for carboxyl headgroup surfactants

The particles decrease to a greater extent in size during the surfactant exchange than in the case of amines, because of the formation of cobalt oleate under removing of Co atoms from the particles [29]. Again a correlation between the length of the amphiphilic molecules and the inter particle distance can be found. A direct effect on the spatial assembly of the

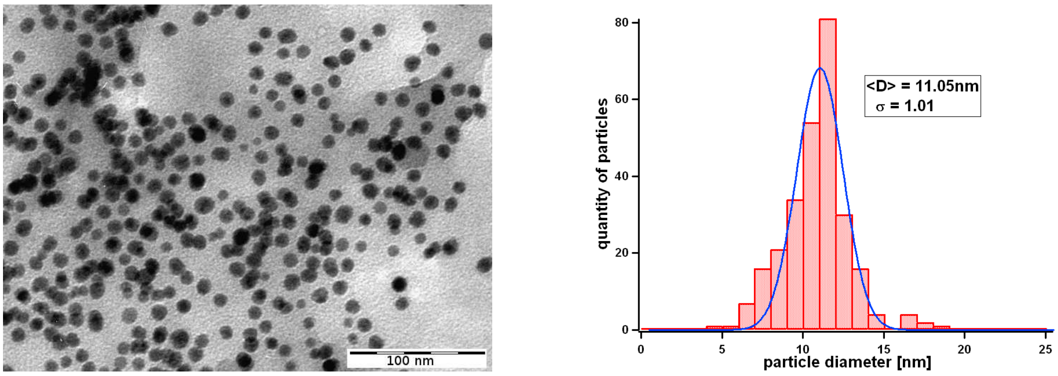

Figure 5.16: Particles covered with hexacosanoic acid, ⟨D⟩= 11.05 nm ± 1.01 nm, N=272.

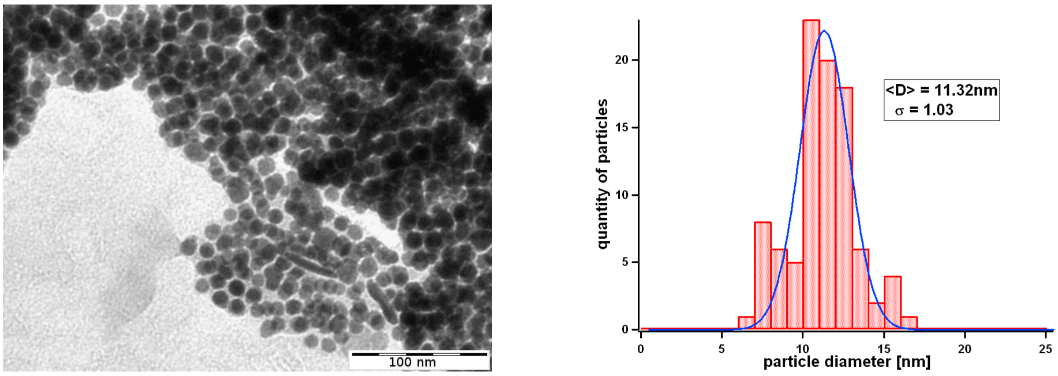

Figure 5.17: Particles covered with 4-biphenylacetic acid, ⟨D⟩= 11.32 nm ± 1.06 nm, N=94.

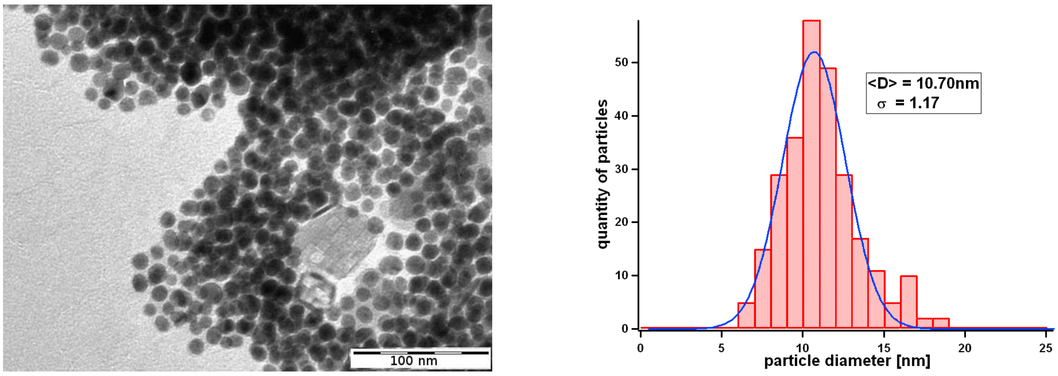

Figure 5.18: Particles covered with 1-pyrenebutyric acid, ⟨D⟩= 10.70 nm ± 1.37 nm, N=268.

particles could not be found. The surfactants with the benzene rings differ only slightly in their effect on the self assembly of the particles.

Conclusion for self-assembly changes by surfactant exchange

Overall a correlation between the length of the alkyl chain and the minimal particle distance in particle monolayers can be found. Longer chains lead to an enhanced inter particle distance. The estimation of the distance is based on relatively few measurements on images with a barely sufficient magnification and resolution. Therefore the relatively large error has to be taken into account.

5.2.4 Size reduction during surfactant exchange

The diameter of the particles is predominantly reduced during the surfactant exchange. It is necessary to take a closer look at the influence of the headgroup on the decrease of the particle size. In table 5.3 the average diameter $\langle D \rangle$ of the particles and the change in nm compared to the initially prepared particles is displayed, as well as the average change per headgroup.

head (group)	**name**	**$\langle D \rangle$ [nm]**	**change [nm]**
OP	trioctylphosphine oxide	12.15 ± 3.31	-
NH_x			
NH_x	triethylamine	11.78 ± 2.61	-0.37
NH_x	octylamine	12.11 ± 2.86	-0.04
NH_x	dioctylamine	11.51 ± 2.53	-0.64
NH_x	trioctylamine	10.95 ± 2.69	-1.2
NH_x	tetraoctylammonium bromide	10.98 ± 2.46	-1.17
NH_x	dodecylamine	12.43 ± 2.56	+0.28
NH_x	octadecylamine	10.91 ± 2.71	-1.24
NH_x	oleylamine	11.81 ± 2.01	-0.34
NH_x	**average change in diameter**		-0.62
COOH			
COOH	nonanoic acid	10.58 ± 2.38	-1.57
COOH	tridecanoic acid	10.37 ± 3.20	-1.78
COOH	oleic acid	10.78 ± 3.68	-1.37
COOH	hexacosanoic acid	11.05 ± 2.03	-1.1
COOH	4-biphenylacetic acid	11.32 ± 2.12	-0.83
COOH	1-pyrenebutyric acid	10.70 ± 2.75	-1.45
COOH	**average change in diameter**		-1.35

Table 5.3: Overview over changes in diameter.

It is noticeable that the particles have reduced in their average size to a larger degree in the case of carboxylic headgroups. A reason for this behaviour could be given by the formation of cobalt oleate during the surfactant exchange if surfactants with a carboxylic acid are used [39,29]. The decrease of the particle size after the addition of oleic acid under the dissolution of parts of the cobalt and formation of cobalt oleate is described in [29]. The reaction path is depicted in figure 5.19

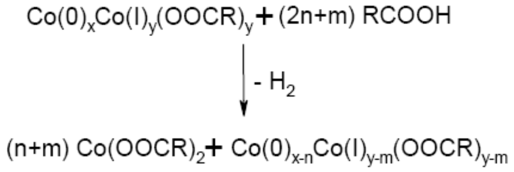

$$Co(0)_xCo(I)_y(OOCR)_y + (2n+m)\ RCOOH \xrightarrow{-H_2} (n+m)\ Co(OOCR)_2 + Co(0)_{x-n}Co(I)_{y-m}(OOCR)_{y-m}$$

Figure 5.19: Reaction scheme of the degradation of cobalt nanoparticles by carboxylic acids.

5.2.5 Inter particle distance

The inter particle distance $\langle d_i \rangle$ can provide information about the state of the surfactant on the surface.

One possibility to estimate the length L_c of the alkyl chains is by taking the length of a $C-C$ bond, assuming that the angle is that of a tetrahedron and calculating the effective bond length, see figure 5.20.

Figure 5.20: Calculation of the effective bond length.

Taking a bond length of l=154 pm and an angle of $\alpha = 109.47°$ the projected length on a line of both bonds d can be calculated by

$$d^2 = 2l^2 - 2l^2 \cdot \cos(\alpha) \quad . \tag{5.1}$$

This leads to $d = 251.48$ pm and therefore to an effective projected bond length of $b = \frac{d}{2} = 125.74$ pm.

Taking TOPO as an example, the length of an alkyl chain can be estimated by taking the 7 $C-C$ bonds and adding the $C-P$ bond and the $P=O$ bond, assuming each to be about the length of an effective $C-C$ bond. In the case of TOPO this leads to a maximum molecule length of L_{mol}= 1131.66 pm.

For an amine headgroup with a $C-N$ bond only one effective length is added, while for a carboxyl head with additional $C-C$ bond and an $C=O$ bond two effective lengths are added. The resulting lengths L_{mol} and the measured half particle distances $\frac{\langle d_i \rangle}{2}$ are displayed in table 5.5. In the case of oleylamine and oleic acid, the $C=C$ bond with a length of l= 134 pm is allowed for by reducing the effective bond length in this place by 20 pm.

In the case of the molecules with the benzene rings, these have been taken into account by taking the bond length of $C \overset{..}{-} C$ with l= 139 pm and assuming the effective lengths as displayed in figures 5.21 and 5.22.

Another more commonly used method to estimate the thickness of the surfactant layer is described in [18]. Here the coverage of the surface by the surfactant and the average

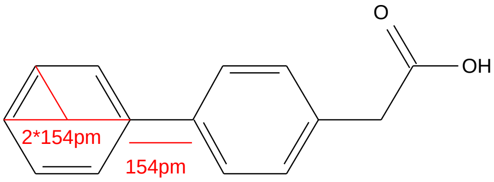

Figure 5.21: Calculation of the effective length of 4-biphenylacetic acid.

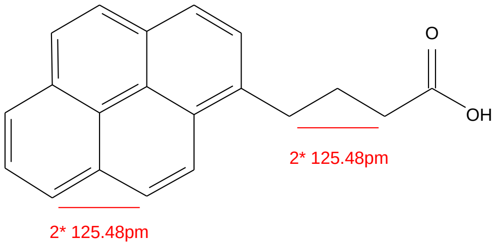

Figure 5.22: Calculation of the effective length of 1-pyrenebutyric acid.

area per headgroup on the surface is taken into account by

$$L = \frac{n\langle l^{\frac{5}{3}}\rangle}{\langle s^{\frac{2}{3}}\rangle} \tag{5.2}$$

where L denotes the thickness on the surfactant layer, n: number of $C-C$ bonds, l= 154 pm (bond length $C-C$) and s: diameter of the surfactant headgroups; for carboxyl headgroups as was estimated from an circular area [4] $A = 22.5\text{Å}^2$ to s = 535 pm, for amine headgroups with $A = 18.2\text{Å}^2$ to s = 481 pm and for the phosphine head both values were tried.

The diameter s of a headgroup can be estimated by measurements of the headgroup area A with a Langmuir-Blodgett trough as described in [18, 29].

For the area A of the headgroups the data found in literature is given in table 5.4. The area for alkyl chains and a carboxyl head (carboxylic acids) are denoted to be between $A = 20-25\text{Å}^2$, for an all trans configuration. The length of the alkyl chain plays a subordinate role for the space needed, which can be clearly seen in the comparison of stearic acid C_{16} and hexatriacontanoic acid C_{24}. In contrast to this additional branches in the alkyl chain lead to a strong increase in required space, as can be seen in the example of isostearic acid.

name	area A [Å^2]
oleic acid [3]	22.4
oleylamine [3]	18.2
1-pyrenebutyric acid [3]	20.2
lignoceric acid [4]	22-25
palmitic acid [4]	22
stearic acid [5]	20
hexatriacontanoic acid [5]	20
isostearic acid [5]	32

Table 5.4: Area of headgroups.

The results of the calculations of the alkyl chain length and the surfactant shell thickness L are displayed in table 5.5.

---

[4] $A = \pi(\frac{s}{2})^2$

[3] taken from [18]

[4] taken from [67]

[5] taken from [68]

head	**name**	L_{mol} **[pm]** effective all trans length	$\frac{\langle d_i \rangle}{2}$ **[nm]** half inter part. dist.	**L [pm]** calc. surfact. shell
OP	trioctylphosphine oxide	1131.66	0.72±0.25	470-505
$\mathbf{NH_x}$				
NH_x	triethylamine	251.48	0.55±0.18	72
NH_x	octylamine	1005.92	0.77±0.17	505
NH_x	dioctylamine	1005.92	0.75±0.19	505
NH_x	trioctylamine	1005.92	0.70±0.20	505
NH_x	tetraoctylammonium bromide	1005.92	1.13±0.13	505
NH_x	dodecylamine	1508.87	0.82±0.21	792
NH_x	octadecylamine	2263.31	1.17±0.19	1225
NH_x	oleylamine	2243.31	1.19±0.19	1225
COOH				
COOH	nonanoic acid	1131.66	0.67±0.23	470
COOH	tridecanoic acid	1634.61	0.83±0.20	739
COOH	oleic acid	2369.05	1.07±0.17	1141
COOH	hexacosanoic acid	3269.22	1.56±0.17	1611
COOH	4-biphenylacetic acid	1087.22	0.78±0.05	-
COOH	1-pyrenebutyric acid	1175.75	0.88±0.13	-

Table 5.5: Overview over changes in inter particle distance.

For better visualization are the different calculated lenghts of the surfactants depited schematically in image 5.23.

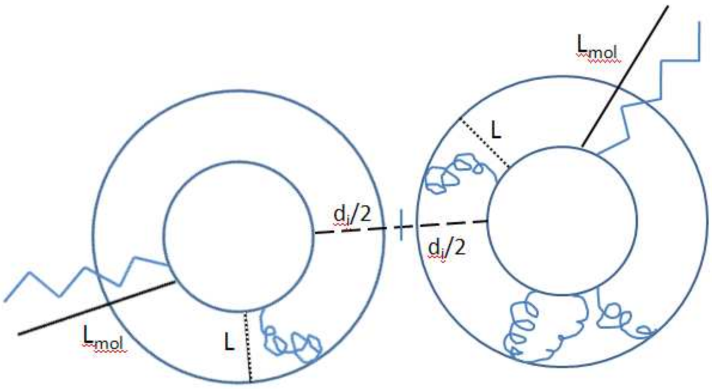

Figure 5.23: Surfactant conformations L_{mol}, $\frac{\langle d_i \rangle}{2}$ and L drawn schematically.

It can be seen, that the measured data for the minimal inter particles fits better to the calculations of the layer thickness L than to the calculation of the length of the all trans configuration of the molecule. For all surfactant molecules, except tetraoctylammonium bromide and dioctylamine, the measured values are well within the range estimated by the measurement inaccuracy. It is remarkable that in all cases the values obtained for chains with eight carbon atoms are quite large. The case of dioctylamine seems to be an error in the measurement of the particle distance, as this value is only slightly out of the range of error. The value for tetraoctylammonium bromide exceeds twice the calculated value. This case could be explained by the difference in the shape of the molecule compared to the other surfactants. Overall, it can be deduced that the ligands are not in all trans configuration [13] and that the interactions between the surfactants on the particles have a great influence on the conformation of the molecules.

Lignoceric acid ($C_{24}H_{48} = O_2$), palmitic acid ($C_{16}H_{32} = O_2$) and a mixed monolayer of both fatty acids have been measured in [67], where the length of a chain of 8 carbon atoms in all trans conformation of a normal alkane was measured to 1.1 nm and calculated to 1.02 nm by estimating each bond to be 0.127 nm by measuring the height difference between two monolayers of the surfactants with an AFM.

To determine the thickness of a surfactant layer, the state of the surfactant layer is important as described in [69]. The investigation of self-assembled monolayers of different alkyl chain length showed, that on titanium oxide short alkyl phosphates (C_{10}-C_{13}) assemble into a less dense and liquid like structure, while longer alkylphosphates (C_{16}-C_{18}) exhibit a more crystalline, all-trans conformation of the chains.

The curved surface in the case of the particles should result in a liquid-like structure of nearly all chain lengths. A similar result was obtained for particles in solution by measurements of the IR spectra and comparison of the stretching oscillations of free and bound to the surface amphiphile molecules in [29]. In [70] it was described, that an alkyl chain consisting of 8 or less carbon atoms was not sufficient for stabilization of particles with a diameter of 9 nm. As a result the particles stabilized with the smaller surfactants should be agglomerated. This would include triethylamine, octylamine and if each alkyl chain is counted separately, as well dioctylamine, trioctylamine and tetraoctylammonium bromide and eventually nonanoic acid if the carbon atom of the headgroup is not taken into account. In contrast to this prediction no agglomeration was found in the corresponding samples; the individual particles can be seen clearly in the corresponding images of particles covered with the surfactants mentioned above.

---

[13] completely stretched

5.2.6 Convolution of the surfactant molecules

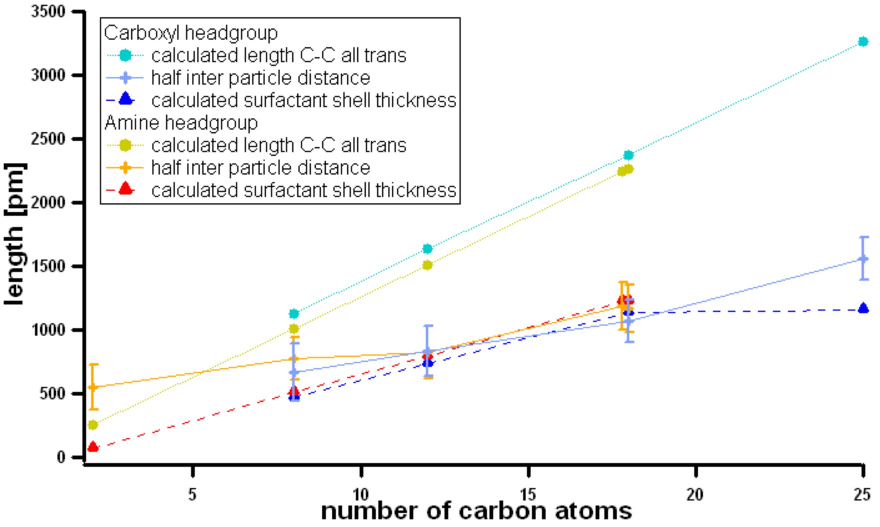

Figure 5.24: Lengths of L_{mol}, $\frac{\langle d_i \rangle}{2}$ and L plotted over the number of carbon atoms of the chaingroup separated by headgroup.

The calculations of the previous subsection 5.2.5 arise the question, to what extend does the conformation of the surfactants deviate from the all trans conformation, which can be seen as the maximal possible length of the molecules without stretching. In image 5.24 the obtained lengths L_{mol}, $\frac{\langle d_i \rangle}{2}$ and L are plotted over the number of carbon atoms in the chaingroups. The curves are drawn separately for each headgroup. The curves for amine and carboxyl headgroup behave similarly.

It can be seen that the curves for the measured half particle distance $\frac{\langle d_i \rangle}{2}$ and the calculated surfactant shell thickness L match to a great extent. The all trans conformation L_{mol} exhibits a steeper ascent with increasing number of carbon atoms in the chain group.

In image 5.25 the lengths for surfactants with an carboxyl headgroup, in image 5.26 the results for surfactants with an amine heagroup and in image 5.27 the obtained lengths for different numbers of chains are displayed.

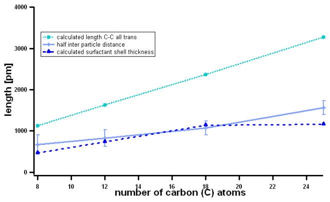

Figure 5.25: Lengths of L_{mol}, $\frac{\langle d_i \rangle}{2}$ and L plotted over the number of carbon atoms of the carboxyl surfactant chaingroups.

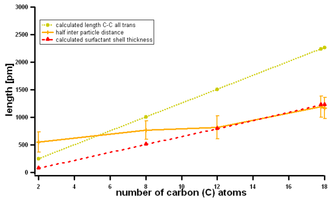

Figure 5.26: Lengths of L_{mol}, $\frac{\langle d_i \rangle}{2}$ and L plotted over the number of carbon atoms of the amine surfactant chaingroups.

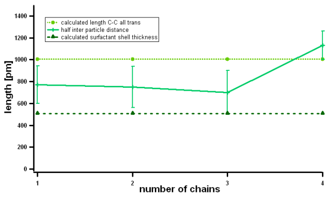

Figure 5.27: Lengths of L_{mol}, $\frac{\langle d_i \rangle}{2}$ and L plotted over the number of chains of the amine surfactants.

To gain information concerning the convolution of the surfactant molecules, the half inter particle distance $\frac{\langle d_i \rangle}{2}$ and the calculated surfactant shell thickness L are normalized to the all trans conformation L_{mol}. The results are displayed in figure 5.28. Apart from the values for very shortest chains length are all measured and calculated values about one half of the corresponding value of L. This means that the surfactants are effectively contracted to half of their maximal possible length.

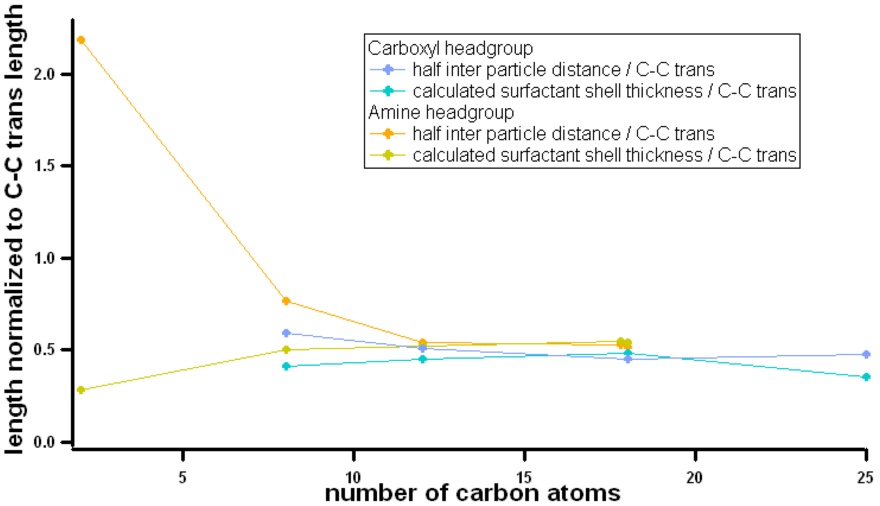

Figure 5.28: Lengths of $\frac{\langle d_i \rangle}{2}$ and L normalized by L_{mol} and plotted over the number of carbon atoms of the chaingroup separated by headgroup.

5.2.7 Change of magnetic properties

As the particle size and possibly the crystallinity change during a surfactant exchange, it can be assumed that the magnetic properties do not remain unaffected. The change of the hysteresis curve and the corresponding parameters before and after the ligand exchange are examined in this part of the chapter. In figure 5.29 the hysteresis curve of the sample with the initially prepared particles is shown. The normalized curves of the samples after the surfactant exchange are added to the normalized hysteresis curve of the TOPO sample for better comparison in figure 5.30.

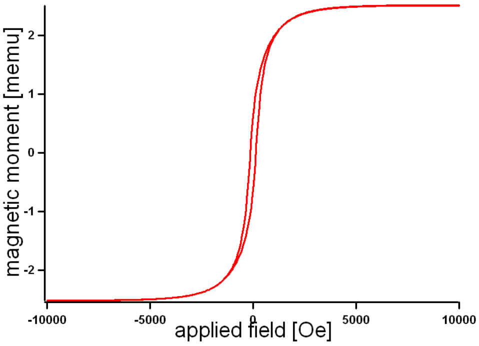

Figure 5.29: Hysteresis curve of the fresh AGM sample of the initial particles with TOPO.

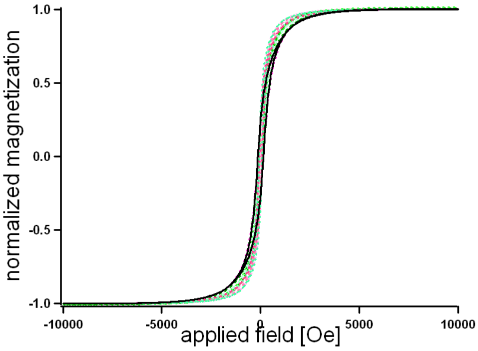

Figure 5.30: Normalized hysteresis curves of the fresh AGM samples of particles covered with different surfactants.

A dependence of the hysteresis curves on the surfactant exchange cannot be observed. All curves become slightly more squarish after surfactant exchange.

The calculated values for the squareness $S = \frac{m_r}{m_s} = \frac{M_r}{M_s}$ are displayed in table 5.6. The average squareness is greater in the case of an amine headgroup. In this experiment the average squareness decreases for stronger bonds between headgroup and particle surface.

head	**name**	**m_s [μemu]**	**m_r [μemu]**	**S**
OP	trioctylphosphine oxide	2520	632.6	0.2510
NH_x	triethylamine	2880	711.5	0.2470
NH_x	octylamine	1420	324.0	0.2282
NH_x	dioctylamine	3662	840.8	0.2296
NH_x	trioctylamine	2091	458.1	0.2191
NH_x	tetraoctylammonium bromide	2513	643.6	0.2561
NH_x	dodecylamine	1193	358.6	0.3006
NH_x	octadecylamine	2489	549.1	0.2206
NH_x	oleylamine	3367	789.7	0.2345
NH_x	average			0.2420
COOH	nonanoic acid	4296	685.5	0.1596
COOH	tridecanoic acid	2474	624.4	0.2524
COOH	oleic acid	2191	468.3	0.2137
COOH	hexacosanoic acid	1963	423.3	0.2156
COOH	4-biphenylacetic acid	2646	548.1	0.2071
COOH	1-pyrenebutyric acid	1609	358.5	0.2228
COOH	average			0.2119

Table 5.6: Squareness S of every sample.

The coercivities H_c are compared in figure 5.31.

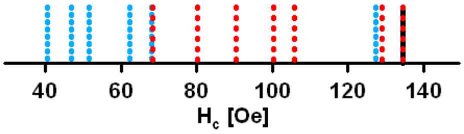

Figure 5.31: Change of the coercive field by surfactant exchange

The blue dotted lines denote particle samples with surfactants with a carboxylic headgroup, while the red ones display the ones with an amine group; the black dotted line stands for the initial sample with TOPO. There is a slight evidence, that the coercivity decreases to a greater amount for the particles with a COOH-head surfactant. Particles with these surfactants are overall smaller. This results in smaller maximum sized particles, which are closer to the superparamagnetic limit $r_{sp} = 7.9$ nm for fcc-Co particles as calculated according to equation 1.18. This size dependent effect might explain the change. Deviations may be also caused by clustered or interacting particles. The chance of the formation of large clusters depends on the surfactant, as some surfactants support or prevent cluster formation better than other.

A change in the shape of the particles induced by the surfactant exchange could not be detected for these samples.

Calculation of the coercivity of the samples

If the magnetic particles are considered to be grains, which are randomly orientated in a thin film plane and magnetically insulated due to a nonmagnetic grain-boundary phase, which is comparable to the surfactant shell on the nanoparticles, their coercivity can be approximated by [71]

$$H_{cr} = 0.556 H_A \left(1 - 0.977 \left[\frac{k_B T}{KV} \ln \left(\frac{f_0 t}{\ln 2} \right) \right]^{\frac{2}{3}} \right) \tag{5.3}$$

with H_{cr}: remanent coercivity, H_A: anisotropy field, k_B: Boltzmann's constant, T: temperature, K: anisotropy constant, V: particle volume[14], f_0: attempt frequency, which is typically in the order of $10^9 Hz$, and $t = 100s$ measurement time [72]. For further information concerning the prefactors of equation 5.3, see [73, 74]. As the anisotropy field of the samples is not known directly, it can be calculated for fcc-Co particles by [75]

$$H_A(fcc) = \frac{4K}{3M_{s(fcc)}} \tag{5.4}$$

and for hcp-Co particles by [76]

$$H_A(hcp) = \frac{2K}{M_{s(hcp)}} \tag{5.5}$$

where M_s denotes the saturation magnetization, for fcc Co $M_{s(fcc)} = 1420 \frac{emu}{cm^3}$ and hcp Co $M_{s(hcp)} = 1400 \frac{emu}{cm^3}$, see table 4.1 for further information.
Using the anisotropy constant of thin film fcc Co $K_{fcc} = 5 \cdot 10^5 \frac{J}{m^3}$ [77] and the anisotropy constant of thin film hcp Co $K_{hcp} = 34 \cdot 10^5 \frac{J}{m^3}$ [77] the corresponding anisotropy fields can be calculated.

$$H_{A(fcc)} = \frac{4 \cdot K_{fcc}}{3 \cdot 1420 \frac{emu}{cm^3}} = \frac{4 \cdot 5 \cdot 10^5 \frac{J}{m^3}}{3 \cdot 1420 \frac{emu}{cm^3}} = 469.48 Oe \tag{5.6}$$

$$H_{A(hcp)} = \frac{2 \cdot K_{hcp}}{1400 \frac{emu}{cm^3}} = \frac{2 \cdot 4.1 \cdot 10^5 \frac{J}{m^3}}{1400 \frac{emu}{cm^3}} = 4857.14 Oe \tag{5.7}$$

The calculated values of the coercivities H_{cr-fcc} and H_{cr-hcp} with a temperature of $T = 294K$ for each sample as well as the averaged measured values are displayed in table 5.7. Additionally the coercivities are calculated with the anisotropy constant for bulk fcc Co $H_{cr-bulkfcc} = 2.5 \cdot 10^5 \frac{J}{m^3}$ [78] and resulting $H_{A(bulkfcc)} = 234.74$ Oe.

In the case of $K_{fcc} = 5 \cdot 10^5 \frac{J}{m^3}$ the calculations determine a non-existing hysteresis. This calculation predicts the particles to be superparamagnetic, with a superparamagnetic limit of $L_{SPM} = 15.77$ nm [15]. The superparamagnetic limit in the case of K_{hcp} is $L_{SPM} = 8.38$ nm. The measured values are closest to the calculated values based on the anisotropy constant for bulk-fcc $K_{bulkfcc} = 2.5 \cdot 10^5 \frac{J}{m^3}$. The magnetic dipole interaction of the particles is not regarded in this calculations, which explains the relatively large differences between calculations and measured values. The measured values are between the calculated values. From the calculations it can be deduced, that these particles are most likely fcc-Co particles with particle interaction effects and a possible small additional amount of hcp- or ε-Co.

---

[14] The calculated particle volumes can be found in table 11.1.

[15] The superparamagnetic limit $L_{SPM} = \left(\frac{6}{\pi} \ln \left(\frac{1}{f_0 \tau} \right) \frac{k_B T}{K} \right)^{\frac{1}{3}}$ describes the maximum particle diameter for superparamagnetic particles.

surfactant	measured H_c	error H_c	H_{cr-fcc}	H_{cr-hcp}	$H_{cr-bulkfcc}$
	[Oe]	± [Oe]	[Oe]	[Oe]	[Oe]
TOPO	130.19	7.69	0	1449.56	57.31
triethylamine	113.46	3.31	0	1369.74	52.49
octylamine	84.20	1.50	0	1441.30	56.81
dioctylamine	83.77	3.61	0	1306.57	48.68
trioctylamine	125.8	1.91	0	1160.34	39.85
tetraoctylam. bromide	97.33	2.66	0	1168.74	40.35
dodecylamine	70.68	1.45	0	1505.28	60.68
octadecylamine	78.96	1.54	0	1149.02	39.16
oleylamine	83.50	0.78	0	1223.06	43.63
nonanoic acid	45.40	1.87	0	1044.47	33.23
tridecanoic acid	52.83	2.35	0	983.23	29.15
oleic acid	56.96	2.35	0	1111.38	36.89
hexacosanoic acid	64.14	0.59	0	1188.09	41.52
4-biphenylacetic acid	126.64	0.68	0	1259.38	45.83
1-pyrenebutyric acid	77.49	2.50	0	1087.52	35.45

Table 5.7: Measured values for H_{cr} and calculated values for H_{cr-fcc} and H_{cr-hcp} and the calculated coercivity with the anisotropy constant for bulk fcc-Co $K_{fcc-bulk}$, $H_{cr-bulkfcc}$.

5.3 Comparison - surfactant exchange on TOPO particles

A second surfactant exchange with TOPO particles with only three surfactants was carried out, additionally, to furnish proof the results of the first TOPO based surfactant exchange.

The particles were prepared according to the particles in section 5.1. The are pictured in figure 5.32. The average diameter is $\langle D \rangle = 11.52$ nm ± 2.50 nm, N=199.

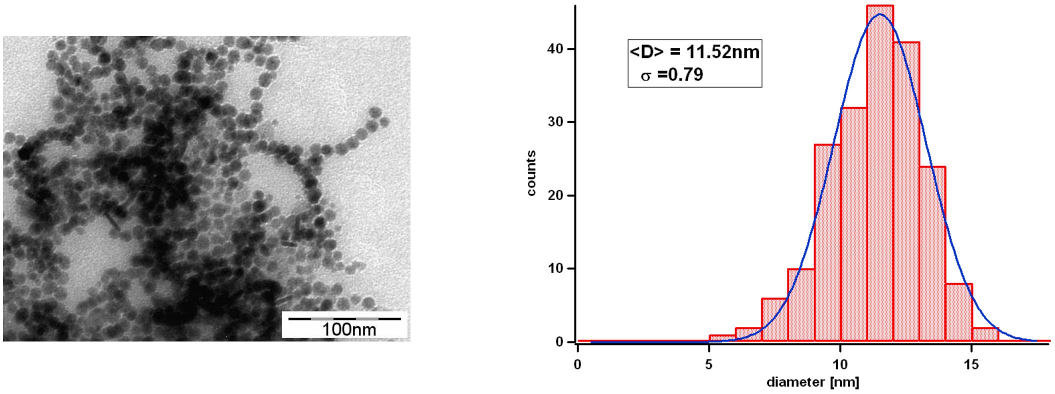

Figure 5.32: Particles prepared with TOPO, $\langle D \rangle = 11.52$ nm ± 2.50 nm, N=199.

As exchange surfactants TOA, oleic acid and oleylamine were used. The comparison of the magnetic properties leads to qualitatively similar results as described in the previous section. The decrease of the coercivity is greater in the case of a carboxyl headgroup.

In figure 5.33 a hysteresis curve of the freshly prepared particles is displayed, which exhibits only a small coercivity. The hysteresis curves for all samples are depicted in figure

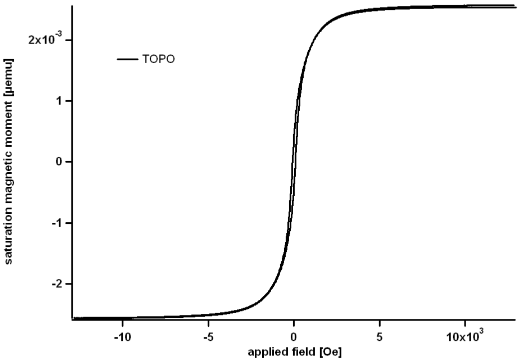

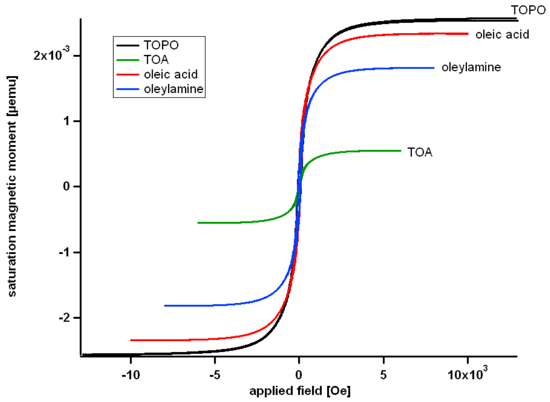

Figure 5.33: Hysteresis curve of fresh Co particles prepared with TOPO

Figure 5.34: Hysteresis curves of all samples

5.34. The particles are smaller than in the first batch and the size distribution is more narrow. This indicates that less particles can be expected to be above the superparamagnetic limit, which fits quite well to the obtained hysteresis curves.

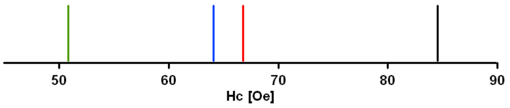

Figure 5.35: Change in coercivity

The squareness S, displayed in table 5.8 is overall smaller than in the case of the first TOPO based exchange. The trend of a smaller squareness for stronger binding head groups could not be verified.

head	**name**	m_s **[µemu]**	m_r **[µemu]**	**S**
OP	trioctylphosphine oxide	2539	411.9	0.1622
NH_x	trioctylamine	549	78.57	0.1431
NH_x	oleylamine	1814	341.2	0.1881
COOH	oleic acid	2341	407.9	0.1742

Table 5.8: Squareness S of every sample.

The change of the coercivity by the surfactant exchange is depicted in figure 5.35. The black line denotes the value for the initial particles prepared with TOPO. The red lines stand for the particles covered with oleylamine, the blue line displays the coercivity for oleic acid and the green one stands for TOA. As the particles coated with TOA seem to have undergone a massive decrease in their magnetic volume (as can be deduced from the comparison of the hysteresis curves in figure 5.34), they are neglected in this regard. Apart from that case, the results fit well to the ones obtained for the first batch.

5.4 Basic particles prepared with oleylamine

To gain more information regarding the influence of the surfactant exchange, particles were initially prepared with oleylamine, then a surfactant exchange with stronger binding surfactants with a carboxyl headgroup was carried out.

$$x\mathrm{Co_2(CO)_8} \xrightarrow[185^\circ \mathrm{C}]{\text{oleylamine+1,2dichlorbenzene}} \mathrm{Co_{2x}[oleylamine]_n} + 8\mathrm{CO} \tag{5.8}$$

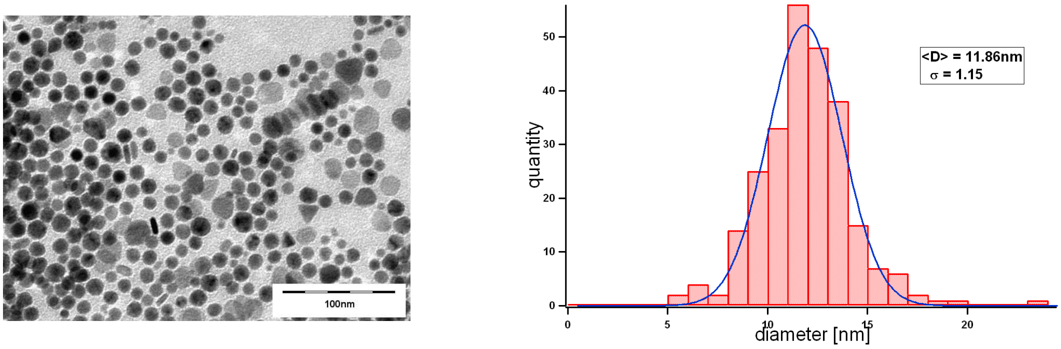

Figure 5.36: Particles prepared with oleylamine, ⟨D⟩= 11.86 nm ± 1.32 nm, N=255.

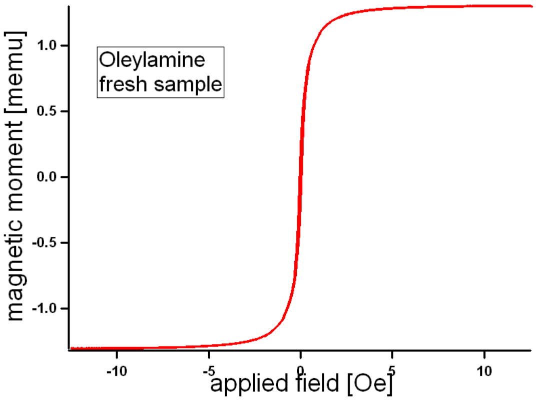

Figure 5.37: Hysteresis curve of fresh Co particles prepared with oleylamine.

The discoidal particles, displayed in image 5.36, have an average diameter ⟨D⟩= 11.86 nm ± 1.32 nm, N=255, the minimal inter particle distance was determinated to be $\langle d_i \rangle$= 2.14 nm ± 0.07 nm. They form mostly monolayered clusters. Inbetween the clusters the particles assemble to short curved chains with single-row and multi-row structures and one or more arms. The predominant orientation of the discs is flat to the surface of the carbon film. Only a negligible fraction stands perpendicular to the surface.

5.4.1 Used surfactants and size reduction

For this surfactant exchange two molecules with an carboxylic head were used - oleic acid and 1-pyrenebutyric acid. The main properties of the surfactant are displayed in table 5.1 and table 5.2. In table 5.9 the decrease of the average diameter ⟨D⟩ and the change compared to the average diameter of the basic particles of the surfactant exchange are displayed. The diameter is reduced in both exchanges.

head (group)	**name**	**⟨D⟩ [nm]**	**change [nm]**
NH_x	oleylamine	11.86 ± 2.63	-
COOH			
COOH	oleic acid	11.36 ± 2.20	-0.5
COOH	1-pyrenebutyric acid	10.15 ± 2.13	-1.71
COOH	**average change in diameter**		-1.11

Table 5.9: Overview over changes in diameter.

Oleic acid

The particles covered with oleic acid are displayed in figure 5.4.1. The average particle diameter is reduced to ⟨D⟩= 11.36 nm ± 1.10 nm, N=259, while the inter particle distance remained with $\langle d_i \rangle$= 2.11 nm ± 0.07 nm similar to the original sample. Their self-assembly is similar to the original particles as well, with the difference, that the clusters are slightly larger, slightly more discs are orientated perpendicular to the surface and that the particle chains consist mostly of multi-rows.

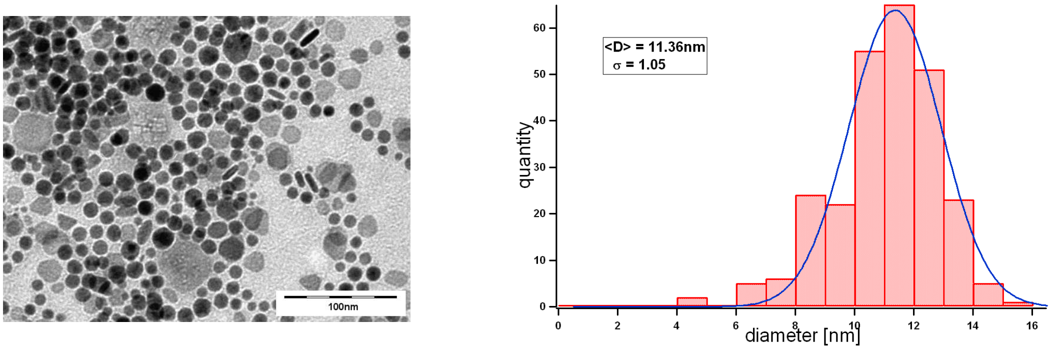

Figure 5.38: Particles with oleic acid, ⟨D⟩= 11.36 nm ± 1.10 nm, N=259.

1-Pyrenebutyric acid

In this case the particles covered with 1-pyrenebutyric acid, depicted in figure 5.4.1, have a decreased diameter of ⟨D⟩= 10.15 nm ± 1.06 nm, N=180. Due to a higher particle concentration in the suspension, monolayers can be found seldomly. Neglecting the effects that result from the higher concentration, the structures which the particles form on the carbon foil seem to be similar to the ones of the previous two samples. The inter particle distance is smaller with about $\langle d_i \rangle$= 1.54 nm ± 0.05 nm.

5.4.2 Conclusion for self-assembly changes by surfactant exchange

The thicknesses of the surfactant shells, displayed in table 5.10, with $\langle d_i \rangle$= 1.07 nm ± 0.07 nm for oleylamine, $\langle d_i \rangle$= 1.06 nm ± 0.07 nm for oleic acid and $\langle d_i \rangle$= 0.77 nm ± 0.05 nm

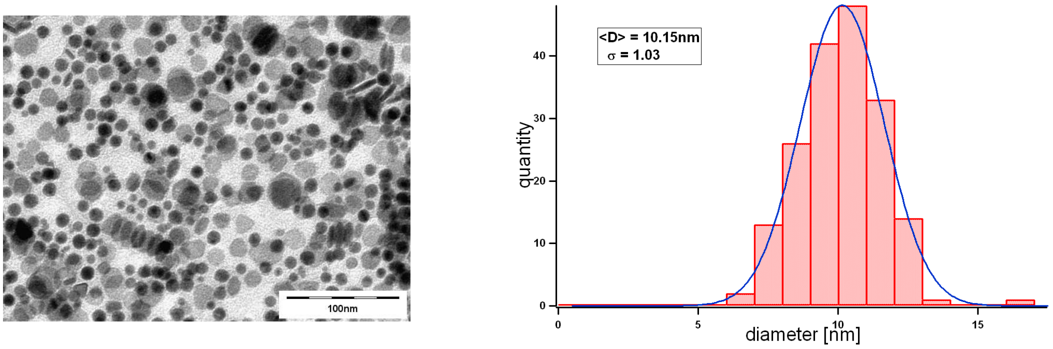

Figure 5.39: Particles with 1-Pyrenebutyric acid, $\langle D \rangle = 10.15$ nm ± 1.06 nm, N=180.

head (group)	**name**	**$\langle d_i \rangle$ [nm]**	**L [pm]**
NH_x	oleylamine	1.07 ± 0.07	1225
COOH			
COOH	oleic acid	1.06 ± 0.07	1141
COOH	1-pyrenebutyric acid	0.77 ± 0.05	-

Table 5.10: Overview over inter particle distances

for 1-Pyrenebutyric acid are comparable to the results obtained in the case of the particles fabricated with TOPO, although the measured values for oleylamine and 1-pyrenebutyric acid are smaller than in the case of the first batch of particle samples prepared with TOPO.

5.4.3 Change of magnetic properties

According to the procedure in 5.2.7 the changes of the magnetic properties of the particles by the surfactant exchange are evaluated.

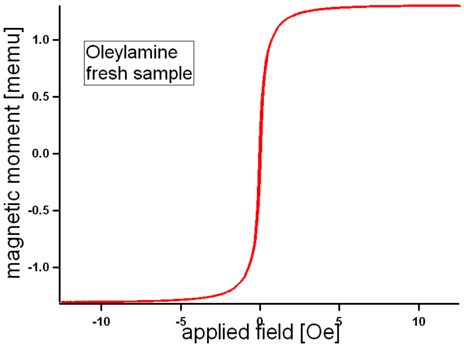

Figure 5.40: Hysteresis curve of the fresh AGM sample of the initial particles with oleylamine.

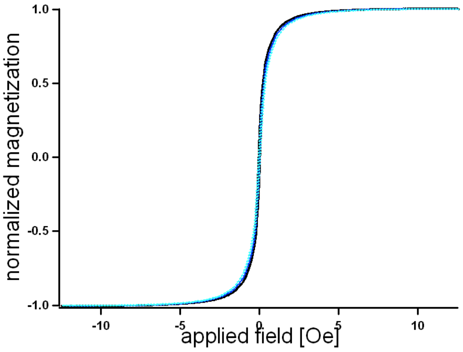

Figure 5.41: Normalized hysteresis curves of the fresh AGM samples of all surfactants.

The normalized hysteresis curves depicted in figure 5.40 and figure 5.41 show a similar change as in the case of the TOPO particles, although the change is smaller. This might be a result of the stronger binding of the oleylamine to the particle surface. The coercivity, values depicted in figure 5.42, decreases as well, which again is in agreement to the first experiment. The black bar denotes the initial particles prepared with oleylamine, the blue bars denote the particles with a carboxyl headgroup (light blue: 1-pyrenebutyric acid, dark blue: oleic acid).

The values for the squareness S can be found in table 5.11. Smaller values are found in the case of a stronger binding headgroup as described for the first TOPO based surfactant exchange.

head	**name**	m_s **[µemu]**	m_r **[µemu]**	**S**
NH_x	oleylamine	1302	224.5	0.1724
COOH	oleic acid	760.3	85.00	0.1118
COOH	1-pyrenebutyric acid	749.6	77.21	0.1030

Table 5.11: Squareness S of every sample.

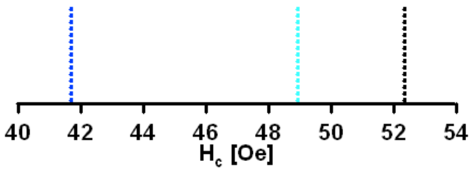

Figure 5.42: Change of the coercive field by surfactant exchange.

5.5 Conclusion

A surfactant exchange was carried out on two particle batches produced with TOPO and one batch produced with oleylamine. The saturation magnetic moment and the coercivity of the samples and therefore the particles in size are reduced, which matches the monitored decrease of the average particle diameter. In the case of surfactants with an carboxyl headgroup, this effect is overall greater than in the case of surfactants with an amine headgroup. An explanation for this behaviour offers the formation of cobalt oleate during the surfactant exchange. The average squareness decreases for stronger bonds between headgroup and particle surface. The inter particle distance increases with increasing surfactant chain length and the measured data meets mostly the calculated theoretical values. For the varying numbers of chains no influence on the inter particle distance was found. A change in shape and crystallinity could not be detected in this experiment.

6 Oxidation of Co Nanoparticles at room temperature

The oxidation behaviour of the particles after the surfactant exchange at room temperature and under ambient conditions is investigated. The change of the hysteresis curves and the decrease of the saturation magnetic moment are monitored. The effective magnetic volume and the corresponding magnetic core radii as well as oxide shell thicknesses are calculated. The contribution of CoO to the magnetic properties is discussed. At first the time dependent changes of the hysteresis curves are examined. The curves of the particles covered with all fifteen surfactants are relatively similar. Therefore, the changes of the hysteresis curves during oxidation of only four samples with different surfactants are displayed exemplary. The hysteresis curves measured at different times are plotted into one graph for comparison. For each sample the saturation magnetic moment m_s decreases, while the coercivity H_c remains close to the initially obtained value. In images 6.1 to 6.4 the progresses of the hysteresis curves of the samples of the particles initially prepared with

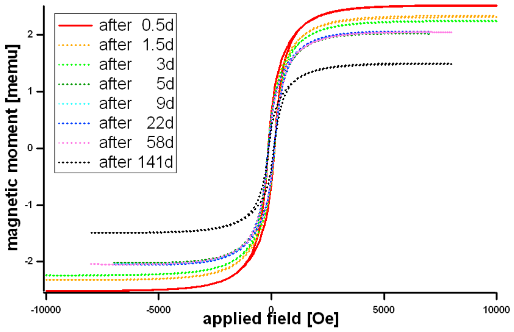

Figure 6.1: TOPO covered particles - change of the hysteresis curve over time.

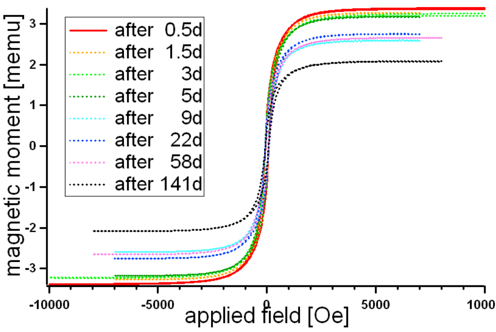

Figure 6.2: Oleylamine covered particles - change of the hysteresis curve over time.

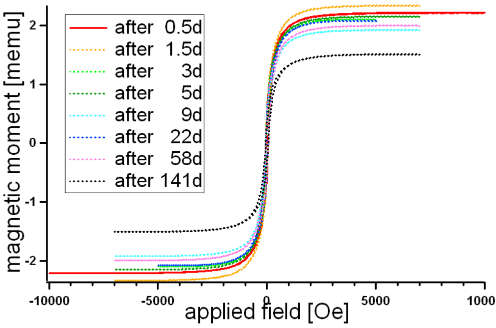

Figure 6.3: Oleic acid covered particles - change of the hysteresis curve over time.

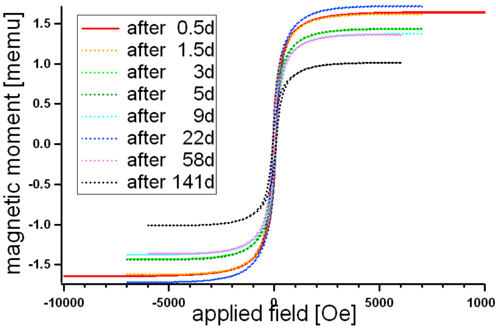

Figure 6.4: 1-pyrenebutyric acid covered particles - change of the hysteresis curve over time.

TOPO and for samples of particles covered with oleylamine, oleic acid and 1-pyrenebutyric acid are depicted. The obtained data is listed in table 6.1. The initially measured values for the saturation magnetic moment and the values after a time of 141 days as well as the percentual decrease are displayed.

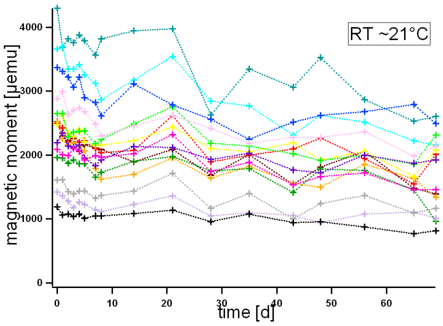

Figure 6.5: Decrease of the saturation magnetic moment, displayed for all samples.

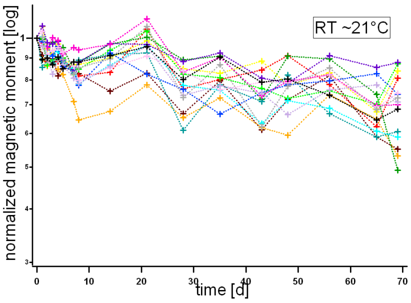

Figure 6.6: Decrease of normalized saturation magnetic moment - all samples displayed.

name	m_s [memu] at $t = 0.5d$	m_s [memu] at $t = 141d$	change in %
trioctylphosphine oxide	2520	1390	-44.8
triethylamine	2880	2144	-25.6
octylamine	1420	1010	-28.9
dioctylamine	3662	2156	-41.1
trioctylamine	2091	1463	-30.0
tetraoctylammonium bromide	2513	1337	-46.8
dodecylamine	1193	814.7	-31.7
octadecylamine	2489	2011	-19.2
oleylamine	3367	2492	-26.0
NH$_x$	**average**		-31.2
nonanoic acid	4296	2605	-39.4
tridecanoic acid	2474	2077	-16.0
oleic acid	2191	1925	-12.1
hexacosanoic acid	1963	965.4	-64.6
4-biphenylacetic acid	2646	2310	-12.7
1-pyrenebutyric acid	1609	1168	-27.4
COOH	**average**		-28.7

Table 6.1: Change of the saturation magnetic moment over time.

In each case the saturation magnetic moment drops below the initial measured value. The change differs from -12.1% up to -64.6% . A strong correlation between the surfactants and the decrease of the saturation magnetic moment through oxidation at room temperature can not be found. There might be a slight indication for a lesser reduction of the magnetic properties in the case of a carboxyl headgroup if the average decrease of the saturation magnetic moment for the headgroups are compared [1].

In figure 6.5 the saturation magnetic moments of all samples is displayed. The same data normalized to the initial value measured at the first measurement is displayed in figure 6.6 allowing a better comparison of the curves. The samples show unusual fluctuations, which are expected to result from external influences, as all samples exhibit them in a similar way and curves measured during a different time span do not show such behaviour. An oxide shell, sufficient for passivation seems to have formed after 60-70 days.

In the figures 6.7 to 6.9 the data are sorted by headgroup. In figure 6.7 the progression for the particles with TOPO, and both surfactants with benzene rings is displayed. Figure 6.8 shows the curves for the surfactants possessing an amine headgroup, while figure 6.9 displays the normalized decrease of the saturation magnetic moment for particles stabilized with surfactants with an carboxyl headgroup. No difference in the development of curves of particle samples with surfactants with different headgroups is identified. The change of H_c over time is depicted in figure 6.10 and in figure 6.11 normalized and sorted by surfactant headgroup (blue: carboxyl headgroup, red: amine headgroup, black: TOPO).

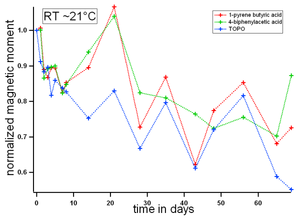

Figure 6.7: Decrease of normalized saturation magnetic moment - TOPO and surfactants with benzene rings.

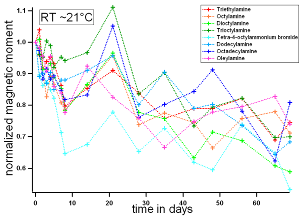

Figure 6.8: Decrease of normalized saturation magnetic moment - surfactants with amine head.

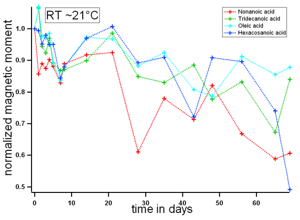

Figure 6.9: Decrease of normalized saturation magnetic moment - surfactants with carboxylic acid head.

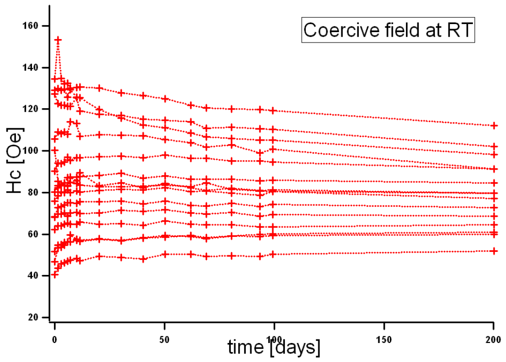

Figure 6.10: Change of coercivity over time.

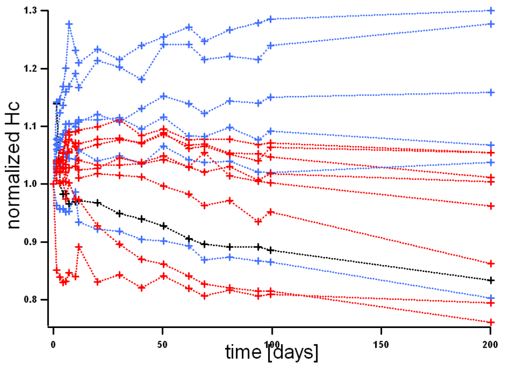

Figure 6.11: Normalized change of coercivity sorted by surfactant headgroup.

As in the case of the saturation magnetic moment no correlation between the change of

---

[1] Even more if the strong reduction in the case of hexacosanoic acid is valued as error or special property of the case of this surfactant.

the coercivity for these samples and the surfactant could be found.

6.1 Calculation of the effective magnetic particle volume and radius

The remaining effective magnetic volume in the particles can be deduced from the decrease of the saturation magnetic moment, if the antiferromagnetic cobalt oxide CoO is assumed to be noncontributing to the magnetization as described in section 4.4. For a sphere the radius of the remaining unoxidized Co core of the particles can be calculated by the analysis of the magnetic volume.

$$\frac{V(t)}{V_0} = \frac{\frac{4}{3}\pi r(t)^3}{\frac{4}{3}\pi r_0^3} = \left(\frac{r(t)}{r_0}\right)^3 = \frac{m(t)}{m_0} \tag{6.1}$$

$$r(t) = r_0 \left(\frac{m(t)}{m_0}\right)^{\frac{1}{3}} \tag{6.2}$$

with r(t): average radius of the Co core at time t, r_0=r(t=0): initially measured average radius, m(t): saturation magnetic moment measured at time t, m_0: initially measured saturation magnetic moment.

In the case of discs with

$$V_d = \pi r^2 h \tag{6.3}$$

r: radius and h: height of the disc, this formula has to be modified.

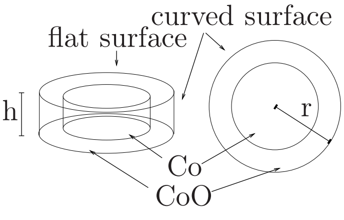

Figure 6.12: Curved and flat surfaces on a disc particle.

The values measured for the height varied between $h = \frac{r}{2}$ and $h = r$. If h is assumed to be fixed, which means that the discs oxidize only through the curved surfaces or that the oxide on the flat surfaces does contribute to the effective magnetic volume by an induced magnetic moment, the correlation between effective magnetic volume and saturation magnetic moment is the following

$$\frac{V_d(t)}{V_{d0}} = \frac{\pi r(t)^2 h}{\pi r_0^2 h} = \frac{\pi r(t)^2 \frac{r_0}{2}}{\pi r_0^2 \frac{r_0}{2}} = \left(\frac{r(t)}{r_0}\right)^2 = \frac{m(t)}{m_0} \tag{6.4}$$

with $h = \frac{r_0}{2}$. It can be seen, that this is independent of the height h. This leads to

$$r(t) = r_0 \left(\frac{m(t)}{m_0}\right)^{\frac{1}{2}}. \tag{6.5}$$

The results for both calculations are displayed in table 6.2.

If a disc oxidises through all surfaces the decrease is faster than in the case of the spheres. If the oxidation through the even surfaces is assumed to be half as fast as through the curved surfaces, the decrease of the effective magnetic volume can be approximated roughly by the calculation for the case of spheres.

As described in section 2.3.2 the oxidation leads to a volume expansion from Co to CoO with a factor of 1.4. This volume expansion in the oxide shell is calculated for both cases as well and noted as oxide shell thickness δ (δ_s: oxide shell thickness for the sphere calculation, δ_d: oxide thickness for the disc calculation) in table 6.2.

The calculations of the magnetic Co core and the thickness of the oxide shell of the particles after 141 days show an average thickness of the shell of about 0.95 nm in the case of spheres or approximation of discs and no contribution of the oxide to the magnetic moment and 1.39 nm for discs and no contribution of the oxide on the curved surfaces, in the case of the amine headgroup and an average Cobalt oxide (CoO) thickness of about 0.77 nm (spheres/discs with no oxide contribution) and 1.12 nm (discs, no contribution on curved surfaces) in the case of carboxyl headgroups. The average oxide shell of particles covered with TOPO is about 1.53 nm (spheres/no oxide contribution) and 1.89 nm (discs, no contribution on curved surfaces) thick.

As can be clearly seen in images 6.13 and 6.14, the oxide shell thicknesses in this long time measurement are independent of the length and number of the surfactant chains as well as the headgroups.

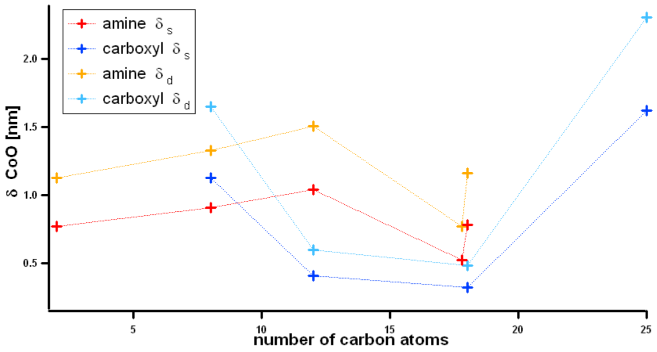

Figure 6.13: Calculated oxide shell thicknesses δ_s and δ_d plotted over the number of carbon atoms in the chains.

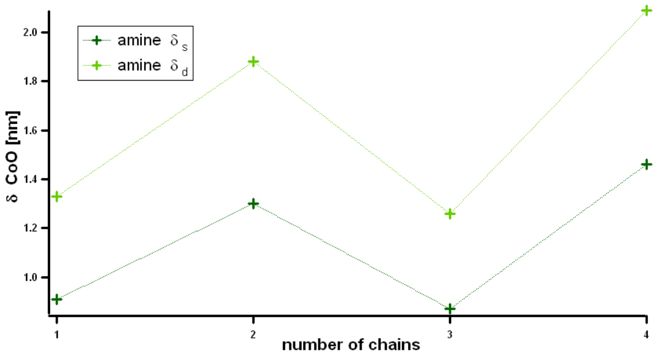

Figure 6.14: Calculated oxide shell thicknesses δ_s and δ_d plotted over the number of chains.

name	m_s [memu] $t = 0.5d$	m_s [memu] $t = 141d$	r_0 (t=0) [nm]	r_{sphere} $(141d)$ [nm]	d_o Co sphere [nm]	δ_s CoO shell [nm]	r_{disc} $(141d)$ [nm]	d_o Co disc [nm]	δ_d CoO shell [nm]
trioctylphosphine oxide	2520	1390	6.08±1.66	4.99±1.36	1.09	1.53	4.52±1.23	1.35	1.89
triethylamine	2880	2144	5.89±1.31	5.34±1.19	0.55	0.77	5.08±1.13	0.81	1.13
octylamine	1420	1010	6.06±1.43	5.41±1.28	0.65	0.91	5.11±1.21	0.95	1.33
dioctylamine	3662	2156	5.76±1.27	4.83±1.06	0.93	1.30	4.42±0.97	1.34	1.88
trioctylamine	2091	1463	5.48±1.35	4.86±1.20	0.62	0.87	4.58±1.13	0.90	1.26
tetraoctylammonium bromide	2513	1337	5.49±1.23	4.45±1.00	1.04	1.46	4.00±0.90	1.49	2.09
dodecylamine	1193	814.7	6.22±1.28	5.48±1.13	0.74	1.04	5.14±1.06	1.08	1.51
octadecylamine	2489	2011	5.46±1.36	5.09±1.27	0.37	0.52	4.91±1.22	0.55	0.77
oleylamine	3367	2492	5.91±1.01	5.35±0.91	0.56	0.78	5.08±0.87	0.83	1.16
NH$_x$	**average**				0.68	0.55		0.99	1.39
nonanoic acid	4296	2605	5.29±1.19	4.48±1.01	0.81	1.13	4.11±0.93	1.18	1.65
tridecanoic acid	2474	2077	5.19±1.60	4.90±1.51	0.29	0.41	4.76±1.47	0.43	0.60
oleic acid	2191	1925	5.39±1.84	5.16±1.76	0.23	0.32	5.05±1.72	0.34	0.48
hexacosanoic acid	1963	965.4	5.53±1.02	4.37±0.81	1.16	1.62	3.88±0.68	1.65	2.31
4-biphenylacetic acid	2646	2310	5.66±1.06	5.41±1.01	0.25	0.35	5.29±0.99	0.37	0.52
1-pyrenebutyric acid	1609	1168	5.35±1.38	4.81±1.24	0.54	0.76	4.56±1.00	0.79	1.11
COOH	**average**				0.55	0.77		0.80	1.12

Table 6.2: Change of the effective magnetic volume and the radius of the corresponding cobalt core; average Co oxide (CoO) thickness.

6.2 Second surfactant exchange on TOPO

The hysteresis curves of the second surfactant exchange batch with TOPO were measured at several different times, as well. In figure 6.15 the decrease of the saturation magnetic moment over time is displayed for the sample of the particles initially prepared with TOPO. The according curves of the particle samples after the surfactant exchange are displayed in figure 6.16.

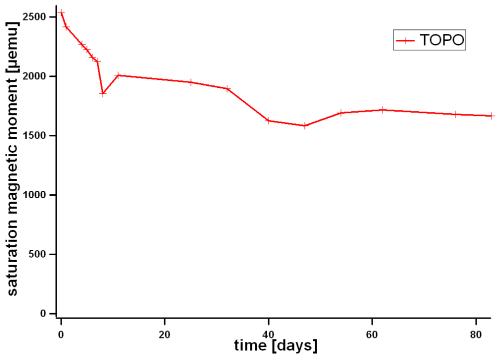

Figure 6.15: Decrease of the saturation magnetic moment of the particles prepared with TOPO.

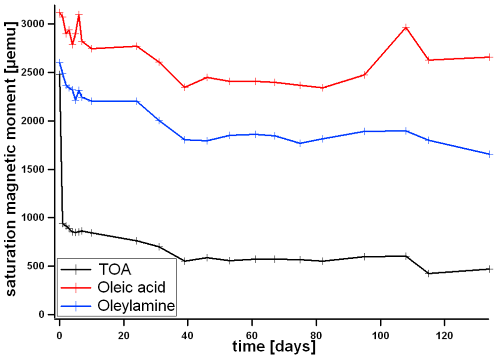

Figure 6.16: Decrease of the saturation magnetic moment of the particles covered with TOA, oleic acid and oleylamine.

In figure 6.17 the oxidation curves of all samples are displayed normalized to the initial value for better comparison. The curves of particles stabilized with TOPO, oleylamine and oleic acid take a relatively similar course, while the curve for TOA drops at the second measurement to much smaller values and takes a slope parallel to the other curves thenceforth.

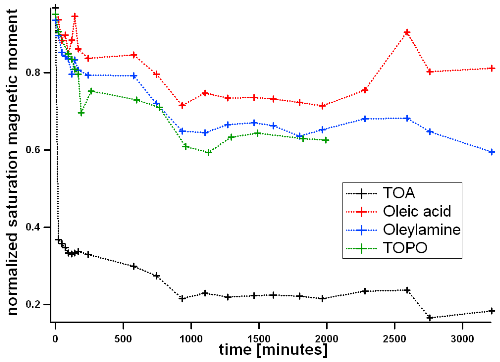

Figure 6.17: Decrease of the normalized magnetic moment for all samples with TOPO, TOA, oleylamine and oleic acid.

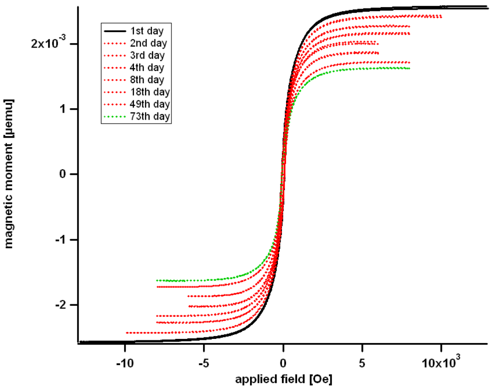

Figure 6.18: Hysteresis curve of fresh Co particles prepared with TOPO.

The hysteresis curves measured at different times for the sample with TOPO are depicted in figure 6.18. The saturation magnetic moment decrease as the sample ages while the coercivity remains relatively stable. The same behaviour occurs for the other samples of this batch. This is in good agreement with the results from the first surfactant exchange on particles fabricated with TOPO.

6.3 Surfactant exchange based on oleylamine

The change of the saturation magnetic moment over time for the particles fabricated with oleylamine is shown in figure 6.19. The aging curves for the particles after the surfactant exchange and a curve for another sample of the initial particles fabricated with oleylamine measured at the same dates are depicted in 6.20.

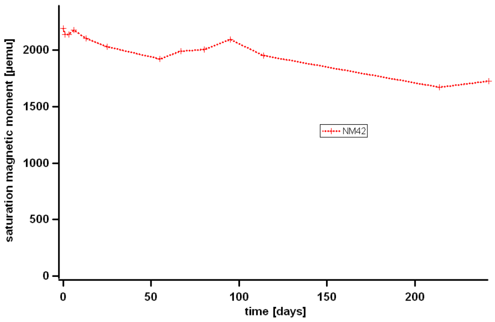

Figure 6.19: Change of saturation magnetization of particles prepared with oleylamine.

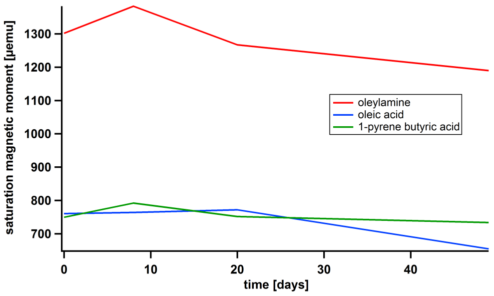

Figure 6.20: Change of saturation magnetization of particles after surfactant exchange.

The thickness of the oxide shell is calculated as described in section 6 and the values are displayed in table 6.21. For the particles stabilized with oleylamine a second and longer series of measurements exists, see figure 6.19. The calculation for the thickness of the unoxidized Co core and the oxide for these measurements can be found in table 6.22.

name	m_s [memu] $t = 0.5d$	m_s [memu] $t = 49d$	r_0 (t=0) [nm]	r_{sphere} $(49d)$ [nm]	Co sphere [nm]	δ_s CoO shell [nm]	r_{disc} $(49d)$ [nm]	Co disc [nm]	δ_d CoO shell [nm]
oleylamine	1302	1190	5.93±1.32	5.75±1.28	0.18	0.25	5.67±1.26	0.26	0.36
oleic acid	760.3	654.7	5.68±1.10	5.40±1.05	0.28	0.39	5.27±1.02	0.41	0.57
1-pyrenebutyric acid	749.6	733.6	5.08±1.07	5.04±1.06	0.04	0.06	5.03±1.06	0.05	0.07
COOH	**average**				0.16	0.22		0.23	0.32

Figure 6.21: Change of the effective magnetic volume and corresponding Co core radius; oxide shell thickness.

name	m_s [memu] $t = 0.5d$	m_s [memu] $t = 242d$	r_0 (t=0) [nm]	r_{sphere} $(242d)$ [nm]	Co sphere [nm]	δ_s CoO shell [nm]	r_{disc} $(242d)$ [nm]	Co disc [nm]	δ_d CoO shell [nm]
oleylamine	2194	1725	5.93±1.32	5.51±1.22	0.42	0.59	5.26±1.17	0.67	0.94

Figure 6.22: Change of the effective magnetic volume and corresponding Co core radius; oxide shell thickness.

6.4 Conclusion

The saturation magnetic moment decreases over time while the coercivity remains relatively stable, as depicted in figure 6.10.

Three surfactant exchanges were carried out, two TOPO based and one oleylamine based. In contrast to the expectations resulting from the oxidation curves of particles fabricated with different surfactants, which are displayed in section 4.4, in all cases no surfactant dependence of the oxidation behaviour (decrease of the saturation magnetic moment) could be detected for the investigated time spans starting with about half an hour to half a day after fabrication [2].

A passivating oxide shell, which leads to a slow down or stopping of the oxidation process had formed after 60 days to 100 days. The calculated thickness of the oxide shell is between δ_s= 0.32 nm and 1.62 nm and δ_d= 0.48 nm and 2.31 nm for the first surfactant exchange, see table 6.2. A dependence on the surfactants could be not found.

The calculations in the case of discs show a thicker oxide layer on the curved surfaces.

A determination of the oxide layer thickness by measurements on HRTEM images is presented in chapter 9.5.

---

[2] In chapter 9 the oxidation behaviour directly after and during the first thirty minutes after fabrication is investigated.

7 Temperature dependence of the oxidation process

In this chapter the influence of different surfactants on the temperature dependence of the oxidation process is investigated.

To gain more insight into the oxidation process of the particles and the influence of the surfactant, samples of the particles were prepared as described in section 3.7 and were stored in air at 7 different temperatures ranging from $-18°\mathrm{C}$ to $300°\mathrm{C}$ afterwards. The samples stored at the highest temperature were not investigated asthoroughly as the other samples because the particles were already oxidized to an extent that made further investigations pointless by the time of the first measurement.
The other samples were measured over different time spans, depending on the rate of the oxidation process. The measurements were stopped, when either the signal decreased below a critical value for successfull detection or the oxidation rate slowed down to a quasi steady state. The temperatures and corresponding time spans are displayed in table 7.1. The high temperature samples were stored on a programmable heating plate with cover.

temp.	$-18°\mathrm{C}$	RT ~ 21°C	48°C	80°C	121°C	180°C	300°C
time	$>$ 2 months	$>$ 100 d	~28 d	~20 d	~17h	2h	$<$ 5 min

Table 7.1: Temperatures and corresponding time spans

The temperature was verified by a thermocouple. All AGM measurements were carried out at room temperature [~ 21°C]. [1] [2]

7.1 Particles stored at a temperature of $-18°\mathrm{C}$

These samples were stored in a refrigerator at $-18°\mathrm{C}$. They were removed from the freezer for the measurement only, defrosted, and measured after they reached room temperature. Afterwards they were freezed again. Per measurement they were warmed up to room temperature for about one and a half hours.
The development of the hysteresis curves are displayed in figure 7.1 and the decrease of the saturation magnetic moment is depicted in figure 7.2. The effective magnetic radii r_{disc} and r_{sphere} and the average oxide shell thicknesses δ_s and δ_d of the particles aged at $-18°\mathrm{C}$ were calculated as described in chapter 6. The results are shown in table 7.2.

---

[1] The properties of the fresh samples are discussed in chapter 5.

[2] For the description of the oxidation behaviour of the samples stored at room temperature under environmental conditions, see chapter 6.

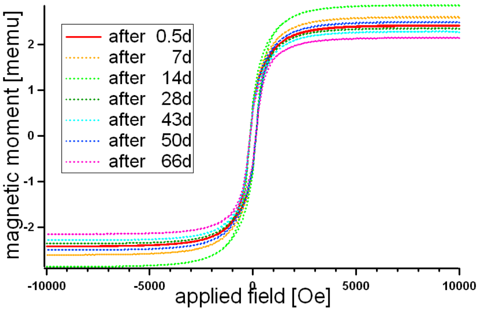

Figure 7.1: decrease of hysteresis curve of particles stored at $-18°$C- exemplary for one sample.

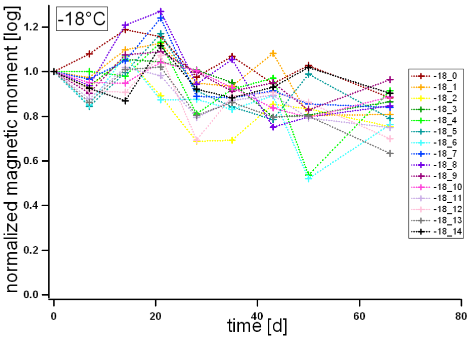

Figure 7.2: Normalized saturation magnetic moment of all samples - particles stored $-18°$C.

name	m_s [memu] $t = 0.5d$	m_s [memu] $t = 60d$	in %	change r_0 (t=0) [nm]	r_{sphere} ($60d$) [nm]	d_o Co sphere [nm]	δ_s CoO shell [nm]	r_{disc} ($60d$) [nm]	d_o Co disc [nm]	δ_d CoO shell [nm]
trioctylphosphine oxide	2407	2127	-11.6	6.08±1.66	5.83±1.59	0.25	0.35	5.72±1.56	0.36	0.50
triethylamine	3033	2277	-24.9	5.89±1.31	5.35±1.19	0.54	0.76	5.10±1.14	0.79	1.11
octylamine	1543	1081	-29.9	6.06±1.43	5.38±1.27	0.68	0.95	5.07±1.20	0.99	1.39
dioctylamine	3796	3192	-15.9	5.76±1.27	5.44±1.20	0.32	0.45	5.28±1.16	0.48	0.67
trioctylamine	2386	2118	-11.2	5.48±1.35	5.27±1.30	0.21	0.29	5.16±1.27	0.32	0.45
tetraoctylammonium bromide	3225	2435	-24.5	5.49±1.23	5.00±1.12	0.49	0.69	4.77±1.12	0.72	1.01
dodecylamine	1315	1189	-9.6	6.22±1.28	6.01±1.24	0.21	0.29	5.91±1.22	0.31	0.43
octadecylamine	2012	1628	-19.1	5.46±1.36	5.09±1.27	0.37	0.52	4.91±1.22	0.55	0.77
oleylamine	5935	5022	-15.4	5.91±1.01	5.59±0.96	0.32	0.45	5.44±0.93	0.47	0.66
NH_x	**average**		-18.8	**average**		0.39	0.55		0.67	0.94
nonanoic acid	4710	3592	-23.7	5.29±1.19	4.83±1.09	0.46	0.64	4.62±1.04	0.67	0.94
tridecanoic acid	3074	2658	-13.5	5.19±1.60	4.94±1.52	0.25	0.35	4.83±1.49	0.36	0.50
oleic acid	2269	2189	-3.5	5.39±1.84	5.33±1.82	0.06	0.08	5.29±1.81	0.10	0.14
hexacosanoic acid	2048	1872	-8.6	5.53±1.02	5.49±0.99	0.04	0.06	5.41±1.01	0.08	0.11
4-biphenylacetic acid	3296	2607	-20.9	5.66±1.06	5.23±0.98	0.43	0.60	5.03±0.94	0.63	0.88
1-pyrenebutyric acid	1754	1113	-35.5	5.35±1.38	4.60±1.19	0.75	1.05	4.26±1.10	1.09	1.53
COOH	**average**		-17.6	**average**		0.33	0.46		0.49	0.69

Table 7.2: Change of the the saturation magnetic moment, the effective magnetic radii with time, average CoO shell thicknesses of particles stored at $-18°C$.

The samples were exposed to room temperature for about 13.5 hours during a time span of 66 days (for 9 measurements). The saturation magnetic moment decreased between 3.5% and 35.5%, see table 7.2. The calculated oxide shell thicknesses are δ_s= 0.06 nm to 1.05 nm for the case of no contribution of the oxide to the magnetic properties and δ_d= 0.11 nm to 1.53 nm for the case that only the oxide at curved surfaces does not contribute to the magnetic properties. The comparizon of the decrease of the saturation magnetic moment, shown in table 7.2, to the decrease of the samples stored at ~ 21°C after 1 day (or in the case where the saturation magnetic moment inexplicably increased, after 2 days), shows that the loss of magnetic moment in the case of the cooled samples is twice to three times greater. This leads to the conclusion, that the oxidation does continue at the lower temperatures and that the oxidation cannot result only from the time the samples were warmed to room temperature. No clear dependence of the oxidation on the surfactant can be deduced.

As can be clearly seen in images 7.3 and 7.4, the oxide shell thicknesses in this long time measurement are independent of the length and number of the surfactant chains as well as the headgroups.

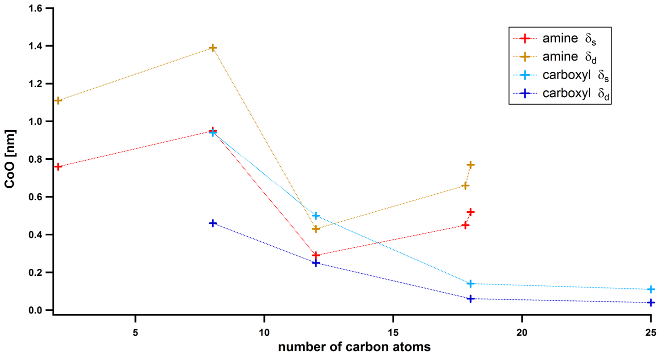

Figure 7.3: Calculated oxide shell thicknesses δ_s and δ_d of samples stored at −18°C plotted over the number of carbon atoms in the chains.

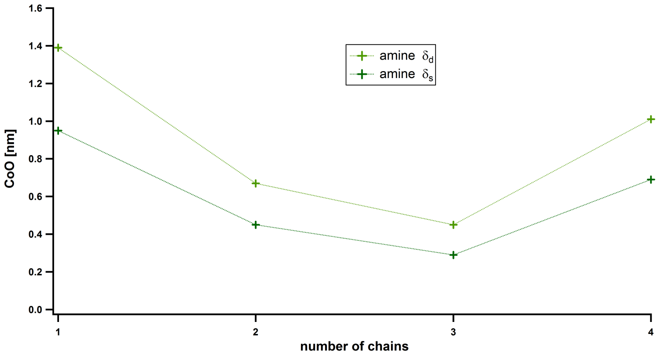

Figure 7.4: Calculated oxide shell thicknesses δ_s and δ_d of samples stored at −18°C plotted over the number of chains.

7.2 Particles stored at a temperature of 48°C

For the measurements each sample was removed from the heating plate and was treated at room temperature for about 5 minutes. This time is not counted for the overall exposure time to higher temperatures, because the oxidation during exposure to higher temperatures is assumed to have a greater influence on the oxidation. The decrease of the saturation magnetic moment between 25.1% and 46.8% is depicted in figure 7.6 and displayed in table 7.3. The change of the hysteresis curve of one sample is depicted in figure 7.5 and the calculated thickness of the oxide shell δ can be found in table 7.3. The calculated oxide shell thickness varies for different surfactants between δ_s = 0.76 nm to 1.61 nm and δ_d = 1.12 nm and 2.30 nm. In the case of a storage temperature of 48°C no dependence of the decrease of the saturation magnetic moment by oxidation on the surfactant could be found. Neither a connection to the headgroup nor to length of the alkyl chain could be deduced. The fluctuations in the oxidation behaviour appear to be statistically distributed and measurement setup dependent in this case. Measurements were stopped as a quasi steady state of the saturation magnetic moment was reached.

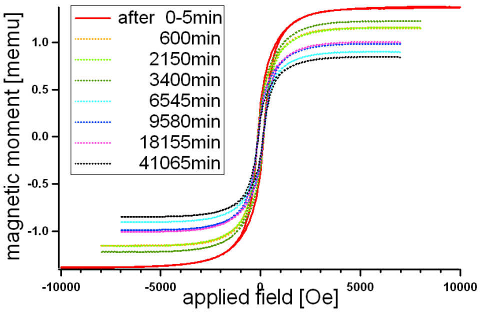

Figure 7.5: Decrease of hysteresis curve of particles stored at 48°C - exemplary for one sample.

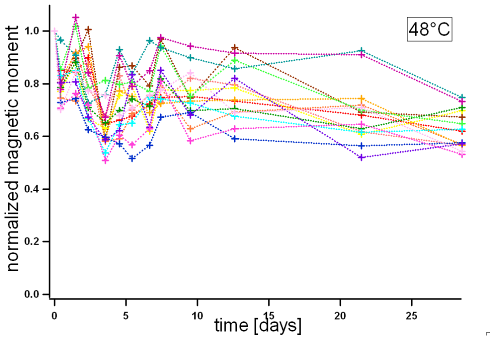

Figure 7.6: Normalized saturation magnetic moment of all samples - particles stored 48°C

As can be clearly seen in images 7.7 and 7.8, the oxide shell thicknesses in this long time measurement are independent of the length and number of the surfactant chains as well as the headgroups.

7.3 Particles stored at a temperature of 80°C

The samples stored at 80°C were treated as described in the previous section 7.2.
The time of the first measurement, here denoted with t=0min, was about 5 hours after fabrication of the particles.
A typical decrease of the hysteresis curve is depicted in figure 7.9. The saturation magnetic moments were evaluated after 27910 minutes [3] to compare the effects of the surfactants on the oxidation process. The normalized oxidation curves for all samples are depicted in figure 7.10. The saturation magnetic moment had decreased between 85.6% and 97.8% at that time. The oxide shell thickness was calculated to δ_s= 4.03 nm to 5.66 nm and δ_d=

---

[3] Instead of the ones after 38020 minutes, because in the latter case, some samples did not show enough signal for a valuable measurement any more.

name	m_s [memu] $t = 0.5d$	m_s in $t = 28.5d$	change [memu] %	r_0 (t=0) [nm]	r_{sphere} $(28.5d)$ [nm]	d_o Co sphere [nm]	δ_s CoO shell [nm]	r_{disc} $r(28.5d)$ [nm]	d_o Co disc [nm]	δ_d CoO shell [nm]
trioctylphosphine oxide	1361	843.8	-38.0	6.08±1.66	5.18±1.42	0.90	1.26	4.79±1.31	1.29	1.81
triethylamine	1526	874.2	-42.7	5.89±1.31	4.89±1.09	1.00	1.40	4.46±0.99	1.43	2.00
octylamine	615.6	450.5	-26.8	6.06±1.43	5.46±1.29	0.60	0.84	5.18±1.22	0.88	1.23
dioctylamine	1609	1042	-35.2	5.76±1.27	4.98±1.10	0.78	1.09	4.64±1.02	1.12	1.57
trioctylamine	1321	761.0	-42.4	5.48±1.35	4.56±1.12	0.92	1.29	4.16±1.02	1.32	1.85
tetraoctylammonium bromide	970.5	653.0	-32.7	5.49±1.23	4.81±1.08	0.68	0.95	4.50±1.01	0.99	1.39
dodecylamine	520.1	282.4	-45.7	6.22±1.28	5.07±1.04	1.15	1.61	4.58±0.94	1.64	2.30
octadecylamine	1106	627.0	-43.3	5.46±1.36	4.52±1.13	0.94	1.32	4.11±1.02	1.35	1.89
oleylamine	1373	1028	-25.1	5.91±1.01	5.37±0.92	0.54	0.76	5.11±0.87	0.80	1.12
NH_x	**average**		-36.7	**average**		0.83	1.16		1.19	1.67
nonanoic acid	1244	883.8	-29.0	5.29±1.19	4.72±1.06	0.57	0.80	4.46±1.00	0.83	1.16
tridecanoic acid	1205	687.9	-42.9	5.19±1.60	4.31±1.33	0.88	1.23	3.92±1.21	1.27	1.78
oleic acid	1287	806.5	-37.3	5.39±1.84	4.61±1.57	0.78	1.09	4.27±1.46	1.26	1.76
hexacosanoic acid	1293	731.3	-43.4	5.53±1.02	4.57±0.84	0.96	1.34	4.16±0.77	1.37	1.92
4-biphenylacetic acid	1582	1104	-30.2	5.66±1.06	5.02±0.94	0.64	0.90	4.73±0.89	0.93	1.30
1-pyrenebutyric acid	949.7	505.0	-46.8	5.35±1.38	4.33±1.12	1.02	1.43	3.90±1.01	1.45	2.03
COOH	**average**		-38.3	**average**		0.81	1.13		1.19	1.67

Table 7.3: Change of the effective magnetic radius with time, average CoO shell thickness, particles stored at 48°C.

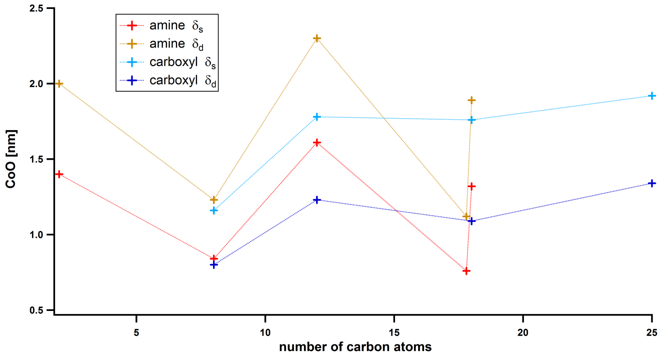

Figure 7.7: Calculated oxide shell thicknesses δ_s and δ_d of samples stored at 48°C plotted over the number of carbon atoms in the chains.

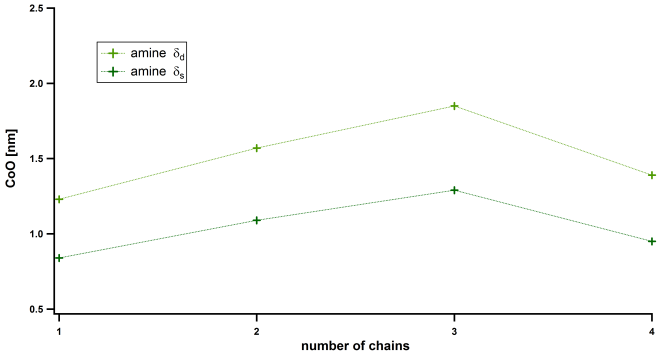

Figure 7.8: Calculated oxide shell thicknesses δ_s and δ_d of samples stored at 48°C plotted over the number of chains.

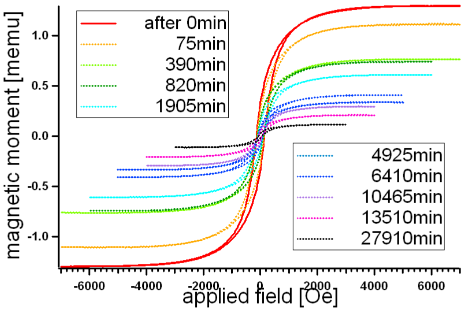

Figure 7.9: Decrease of hysteresis curve of particles stored at 80°C - exemplary for one sample.

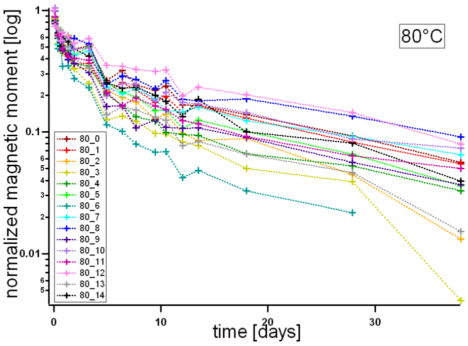

Figure 7.10: Normalized saturation magnetic moment of all samples - particles stored 80°C - logscale.

5.24 nm to 6.31 nm. A surfactant dependence of the decrease of the saturation magnetic moment could be found in the case of a storage temperature of 80°C. Particles covered with a surfactant with a carboxylic head seem to undergo a faster oxidation process. The decrease of the saturation magnetic moment after 27910 minutes (~ 20 days) is overall greater in the case of a carboxyl headgroup. After ~26 days the particles have lost nearly all magnetic moment. This is an indication, that the particles have transformed to cobalt oxide almost completely [18].

As can be clearly seen in images 7.11 and 7.12, the oxide shell thicknesses in this long time measurement are independent of the length and number of the surfactant chains as well as the headgroups.

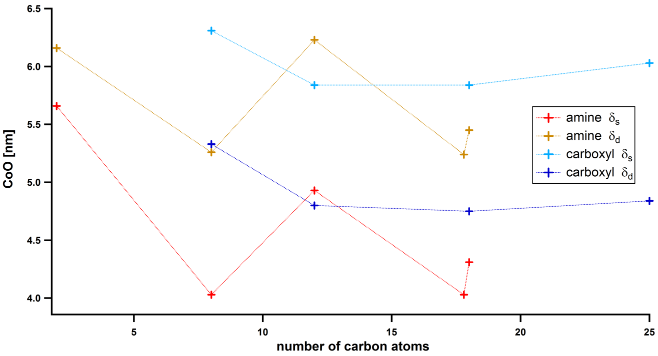

Figure 7.11: Calculated oxide shell thicknesses δ_s and δ_d of samples stored at 80°C plotted over the number of carbon atoms in the chains.

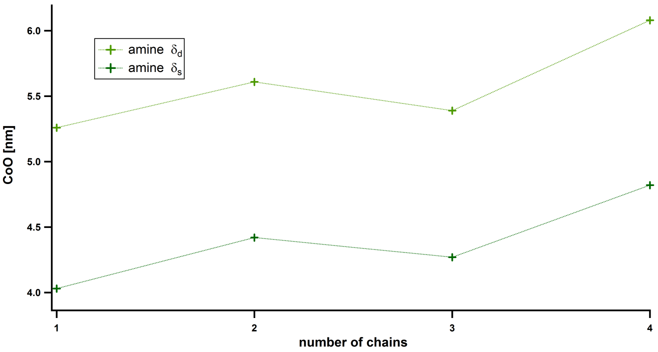

Figure 7.12: Calculated oxide shell thicknesses δ_s and δ_d of samples stored at 80°C plotted over the number of chains.

7.4 Particles stored at a temperature of 121°C

In figure 7.13 the change of the hysteresis curves of a sample is displayed and in figure 7.14 the decrease of the normalized saturation magnetic moment of all samples is shown. For the comparison a point in time was chosen where all samples still had significant signal. Therefore the obtained data after 2340 minutes (39 hours) was evaluated. At this time a decrease between 96.6% and 99.8% of the saturation magnetic moment had occurred. The particles have transformed to CoO nearly completely. The oxide shell thickness is

name	m_s [memu] $t = 0min$	m_s [memu] $27910min$	change in %	r_0 (t=0) [nm]	r_{sphere} (27910min) [nm]	d_o Co sphere [nm]	δ_s CoO shell [nm]	r_{disc} (27910min) [nm]	d_o Co disc [nm]	δ_d CoO shell [nm]
trioctylphosphine oxide	1294	120.4	-90.7	6.08±1.66	2.76±0.75	3.32	4.65	1.85±0.51	4.23	5.92
triethylamine	1370	87.44	-93.6	5.89±1.31	2.35±0.52	3.54	5.66	1.49±0.33	4.40	6.16
octylamine	653.4	94.29	-85.6	6.06±1.43	3.18±0.75	2.88	4.03	2.30±0.54	3.76	5.26
dioctylamine	1623	149.6	-90.8	5.76±1.27	2.60±0.57	3.16	4.42	1.75±0.41	4.01	5.61
trioctylamine	1140	99.98	-91.2	5.48±1.35	2.43±0.60	3.05	4.27	1.63±0.36	3.85	5.39
tetraoctylam. brom.	1041	45.64	-95.6	5.49±1.23	1.94±0.43	3.44	4.82	1.15±0.27	4.34	6.08
dodecylamine	489.1	39.83	-91.9	6.22±1.28	2.70±0.55	3.52	4.93	1.77±0.37	4.45	6.23
octadecylamine	986.7	81.63	-91.7	5.46±1.36	2.38±0.59	3.08	4.31	1.57±0.39	3.89	5.45
oleylamine	1683	227.8	-86.5	5.91±1.01	3.03±0.52	2.88	4.03	2.17±0.37	3.74	5.24
NH_x	**average**		-90.9	**average**		3.19	4.47		4.06	5.68
nonanoic acid	1106	24.14	-97.8	5.29±1.19	1.48±0.33	3.81	5.33	0.78±0.18	4.51	6.31
tridecanoic acid	1064	41.50	-96.1	5.19±1.60	1.76±0.54	3.43	4.80	1.02±0.32	4.17	5.84
oleic acid	1158	59.51	-94.9	5.39±1.84	2.00±0.68	3.39	4.75	1.22±0.42	4.17	5.84
hexacosanoic acid	1116	58.47	-94.8	5.53±1.02	2.07±0.38	3.46	4.84	1.22±0.23	4.31	6.03
4-biphenylacetic acid	1393	91.02	-93.5	5.66±1.06	2.28±0.43	3.38	4.73	1.45±0.27	4.21	5.89
1-pyrenebutyric acid	851.8	39.67	-95.3	5.35±1.38	1.92±0.50	3.43	4.80	1.15±0.30	4.20	5.88
COOH	**average**		-95.4	**average**		3.48	4.87		4.26	5.96

Table 7.4: Change of the effective magnetic radius with time, average CoO shell thickness, particles stored at 80°C.

name	m_s [memu] $t = 0min$	m_s [memu] $t = 2340min$	change in %	r_0 (t=0) [nm]	r_{sphere} (2340min) [nm]	d_o Co sphere [nm]	δ_s CoO shell [nm]	r_{disc} (2340min) [nm]	d_o Co disc [nm]	δ_d CoO shell [nm]
trioctylphosphine oxide	2780	72.95	-97.4	6.08±1.66	1.81±0.49	4.27	5.98	0.98±0.27	5.10	7.14
triethylamine	2596	44.48	-98.3	5.89±1.31	1.52±0.34	4.37	6.12	0.77±0.17	5.12	7.17
octylamine	1392	45.55	-96.7	6.06±1.43	1.94±0.46	4.12	5.77	1.10±0.26	4.96	6.94
dioctylamine	3817	94.20	-97.5	5.76±1.27	1.68±0.37	4.08	5.71	0.90±0.20	4.86	6.80
trioctylamine	2596	68.06	-97.4	5.48±1.35	1.63±0.40	3.85	5.39	0.89±0.22	4.59	6.43
tetraoctylam. bromide	2612	19.02	-99.3	5.49±1.23	1.06±0.24	4.43	6.20	0.47±0.10	5.02	7.03
dodecylamine	1312	20.71	-98.4	6.22±1.28	1.56±0.32	4.66	6.52	0.78±0.16	5.44	7.62
octadecylamine	2462	38.17	-98.4	5.46±1.36	1.04±0.34	4.42	6.19	0.68±0.17	4.78	6.69
oleylamine	5602	192.6	-96.6	5.91±1.01	1.92±0.33	3.99	5.59	1.10±0.19	4.81	6.73
NH_x	**average**		-97.8	**average**		4.24	5.94		4.95	6.93
nonanoic acid	3424	8.519	-99.8	5.29±1.19	0.72±0.16	4.57	6.40	0.26±0.16	5.03	7.04
tridecanoic acid	3187	8.192	-99.7	5.19±1.60	0.74±0.22	4.45	6.23	0.26±0.08	4.93	6.90
oleic acid	2642	47.79	-98.2	5.39±1.84	1.41±0.48	3.98	5.57	0.72±0.25	4.67	6.54
hexacosanoic acid	2276	25.13	-98.9	5.53±1.02	1.23±0.23	4.30	6.02	0.58±0.11	4.95	6.93
4-biphenylacetic acid	3269	51.45	-98.4	5.66±1.06	1.42±0.27	4.24	5.94	0.71±0.13	4.95	6.93
1-pyrenebutyric acid	1891	15.97	-99.2	5.35±1.38	1.09±0.28	4.26	5.96	0.49±0.13	4.86	6.80
COOH	**average**		-99.0	**average**		4.30	6.02		4.94	6.92

Table 7.5: Change of the effective magnetic radius with time, average CoO shell thickness, particles stored at 121°C.

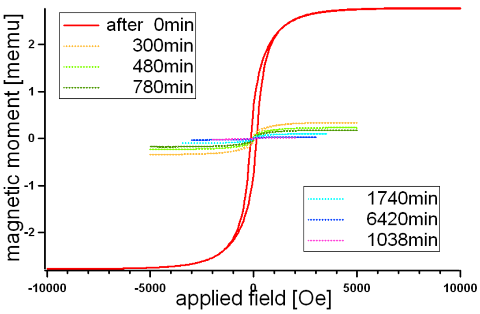

Figure 7.13: Decrease of hysteresis curve of particles stored at 121°C - exemplary for one sample.

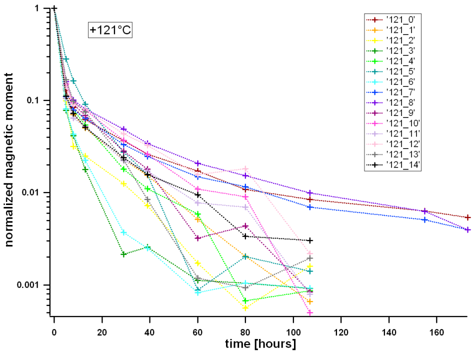

Figure 7.14: Normalized saturation magnetic moment of all samples - particles stored 121°C.

δ_s= 5.39 nm to 6.52 nm and δ_d= 6.43 nm to 7.62 nm. Again the decrease of the samples with a carboxyl headgroup exhibit a slightly stronger decrease with an average of 99.0% compared to the average of 97.8% in the case of an amine headgroup. This is assumed to be based on the smaller average size in the case of particles covered with surfactants with an carboxyl headgroup.

As can be clearly seen in images 7.15 and 7.16, the oxide shell thicknesses in this long time measurement are independent of the length and number of the surfactant chains as well as the headgroups.

7.5 Particles stored at a temperature of 180°C

The decrease of the hysteresis curve of one sample is shown in figure 7.17, the decrease of the normalized saturation magnetic moment is depicted in figure 7.18. These samples exhibit a rapid decrease of the saturation magnetic moment. After two hours the particles are oxidized completely. For these samples the relative decrease and the calculated oxide shell thicknesses after an exposure to 180°C of 15 minutes were compared. The relative decrease of the saturation magnetic moment is between 56.6% and 98.9%. The formed oxide shell thickness is between δ_s= 1.90 nm to 5.98 nm and δ_d= 2.67 nm to 6.87 nm. Here again no clear surfactant dependence on the decrease of the saturation magnetic moment could be found. These samples were investigated in further detail concerning their crystal structure and size after heating with HRTEM in chapter 8 as they undergo a change of their crystallinity during heating.

As can be clearly seen in images 7.19 and 7.20, the oxide shell thicknesses in this long time measurement are independent of the length and number of the surfactant chains as well as the headgroups.

7.6 Particles stored at a temperature of 300°C

The samples stored at 300°C were not investigated any further after the second measurement. The particles were already oxidized nearly completely after five minutes. In figure 7.21 the decrease of the saturation magnetic moment is shown. Only two samples

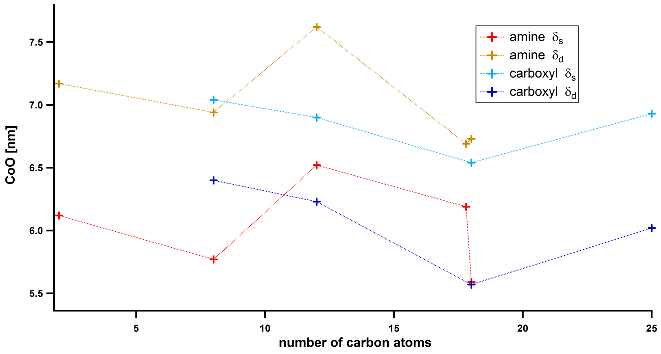

Figure 7.15: Calculated oxide shell thicknesses δ_s and δ_d of samples stored at 121° C plotted over the number of carbon atoms in the chains.

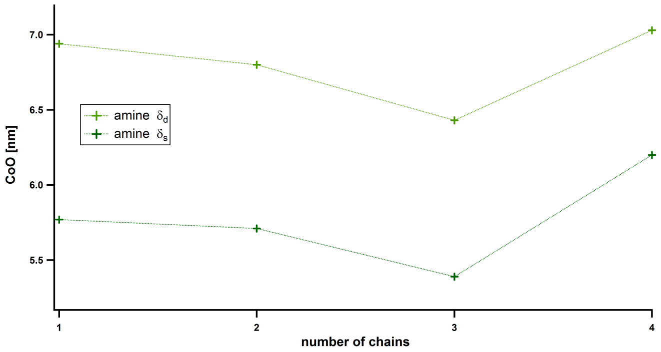

Figure 7.16: Calculated oxide shell thicknesses δ_s and δ_d of samples stored at 121° C plotted over the number of chains.

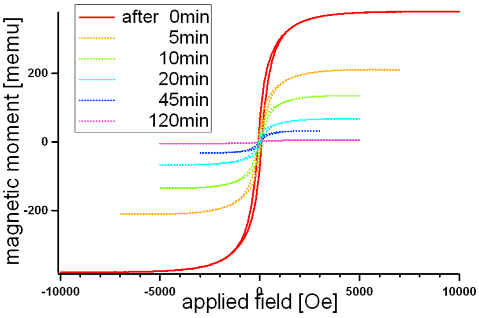

Figure 7.17: Decrease of hysteresis curve of particles stored at 180° C- exemplary for one sample.

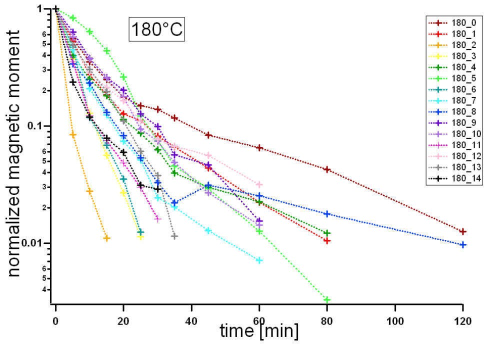

Figure 7.18: Normalized saturation magnetic moment of all samples - particles stored 180° C.

name	m_s [memu] $t = 0\mathrm{min}$	m_s [memu] $t = 15\mathrm{min}$	change in %	r_0 (t=0) [nm]	r_{sphere} (15min) [nm]	d_o Co sphere [nm]	δ_s CoO shell [nm]	r_{disc} (15min) [nm]	d_o Co disc [nm]	δ_d CoO shell [nm]
trioctylphosphine oxide	379.3	94.46	-75.1	6.08±1.66	3.83±1.04	2.25	3.15	3.03±0.83	3.05	4.27
triethylamine	686.3	51.20	-92.5	5.89±1.31	2.48±0.55	3.41	4.77	1.61±0.36	4.28	5.99
octylamine	422.9	89.51	-78.8	6.06±1.43	3.61±0.85	2.45	3.43	2.79±0.66	3.27	4.58
dioctylamine	1080	133.7	-87.6	5.76±1.27	2.87±0.63	2.89	4.05	2.03±0.45	3.73	5.22
trioctylamine	549.7	141.7	-74.2	5.48±1.35	3.48±0.86	2.00	2.80	2.78±0.69	2.70	3.78
tetraoctylam. bromide	597.8	6.600	-98.9	5.49±1.23	1.22±0.27	4.27	5.98	0.58±0.13	4.91	6.87
dodecylamine	432.1	34.12	-92.1	6.22±1.28	2.67±0.55	3.55	4.97	1.75±0.36	4.47	6.26
octadecylamine	877.7	163.0	-81.4	5.46±1.36	3.12±0.78	2.34	3.28	2.35±0.59	3.11	4.35
oleylamine	811.4	106.4	-86.9	5.91±1.01	3.00±0.51	2.91	4.07	2.14±0.37	3.77	5.28
NH_x	**average**		-86.6	**average**		2.98	4.17		3.78	5.29
nonanoic acid	377.1	25.85	-93.1	5.29±1.19	2.16±0.49	3.13	4.38	1.39±0.31	3.90	5.46
tridecanoic acid	757.3	42.48	-96.3	5.19±1.60	1.99±0.61	3.20	4.48	1.23±0.38	3.96	5.54
oleic acid	653.1	169.0	-74.1	5.39±1.84	3.43±1.17	1.96	2.74	2.74±0.94	2.65	3.71
hexacosanoic acid	812.1	147.1	-81.9	5.53±1.02	3.13±0.58	2.40	3.36	2.35±0.43	3.18	4.45
4-biphenylacetic acid	893.5	392.4	-56.1	5.66±1.06	4.30±0.81	1.36	1.90	3.75±0.70	1.91	2.67
1-pyrenebutyric acid	525.1	102.9	-80.4	5.35±1.38	3.11±0.80	2.24	3.14	2.37±0.61	2.98	4.71
NH_x	**average**		-80.5	**average**		2.38	3.33		3.01	4.21

Table 7.6: Change of the effective magnetic radius, average CoO shell thickness, particles stored at 180°C.

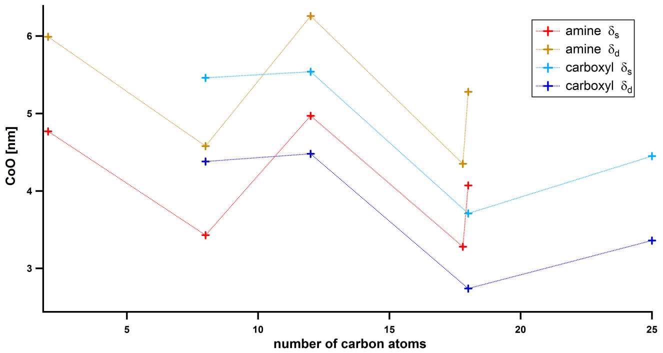

Figure 7.19: Calculated oxide shell thicknesses δ_s and δ_d of samples stored at 180°C plotted over the number of carbon atoms in the chains.

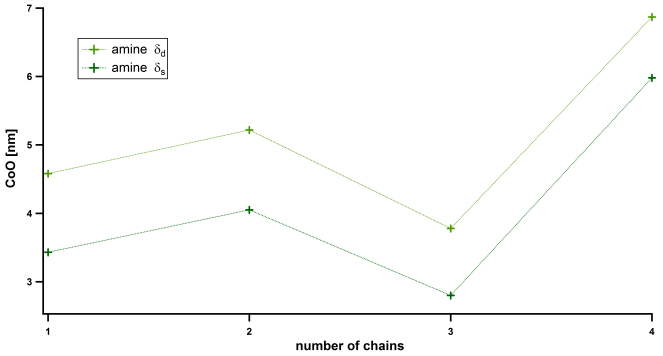

Figure 7.20: Calculated oxide shell thicknesses δ_s and δ_d of samples stored at 180°C plotted over the number of chains.

(with octadecylamine and with oleylamine) exhibited a measureable and apparently stable saturation magnetic moment. This effect could not be verified in further measurements.

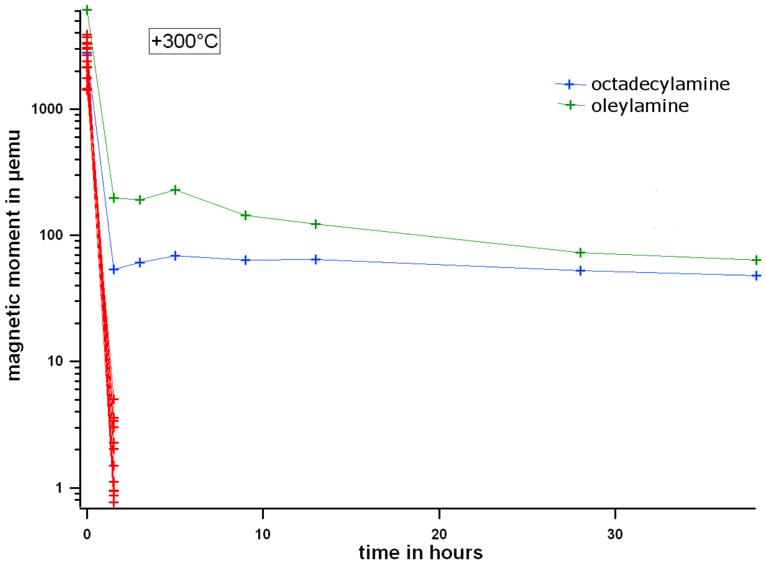

Figure 7.21: Samples stored at 300°C

7.7 Conclusion

Samples of particles after a surfactant exchange were stored at temperatures of −18°C, room temperature (∼ 21°C), 48°C, 80°C, 121°C, 180°C and 300°C.
For temperatures of −18°C, room temperature (∼ 21°C) and 48°C a passivating oxide layer was formed. For the higher temperatures the particles oxidized completely. No clear dependence of the oxidation on the covering surfactant could be found in the investigated time spans starting with particles about 2 hours to half a day old after fabrication.
For these long time spans only the diffusion of oxygen in the nanoparticles could be observed. The curves of the decrease of the saturation magnetic moment for all temperatures for four surfactants are displayed in figures 7.12, 7.13, 7.14 and 7.15 exemplary.

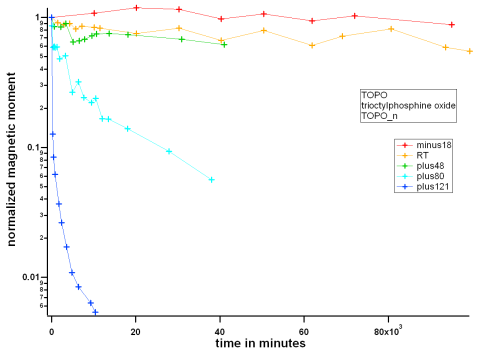

Figure 7.22: TOPO - all temperatures, saturation magnetic moment normalized.

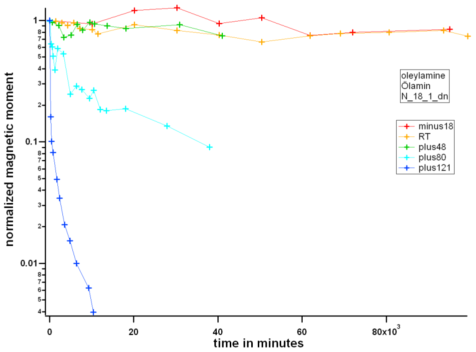

Figure 7.23: Oleylamine - all temperatures, saturation magnetic moment normalized.

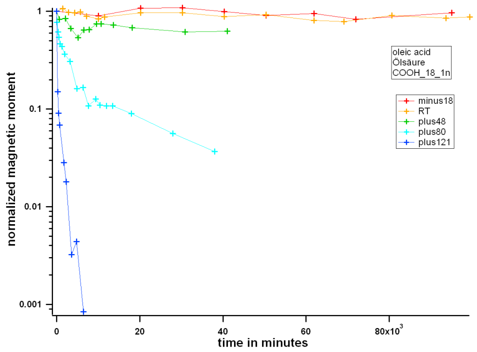

Figure 7.24: Oleic acid - all temperatures, saturation magnetic moment normalized.

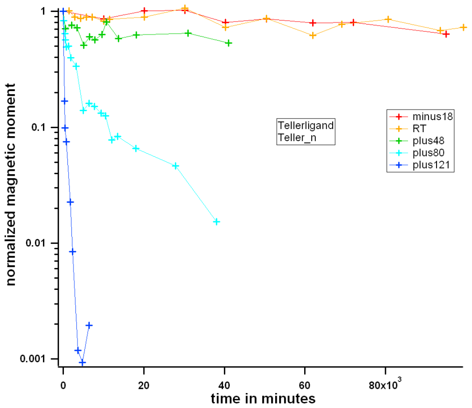

Figure 7.25: 1-pyrenebutyric acid - all temperatures, saturation magnetic moment normalized.

8 Change in crystallinity and shape of cobalt nanoparticles in dependence of temperature

After finishing the oxidation experiment, TEM images of the particles stored at room temperature and stored at 180°C were taken. It was found that the particles that were stored at 180°C for two hours had undergone a change in their crystal structure and their shape from a round shape to a more irregular round shape. The result is displayed in figure 8.1. An image of the original particles prior to oxidation is displayed next to the image for comparison in figure 8.2. The particles oxidized at room temperature are displayed in figure 8.3. The particles stored at room temperature show no change in their crystal structure. The size distribution of the particles after oxidation shows that the average diameter has increased in both cases. For octadecylamine the diameter has grown from $\langle \mathsf{D} \rangle = 10.91$ nm ± 2.38 nm at the beginning to $\langle \mathsf{D} \rangle = 13.69$ nm ± 2.73 nm during the storage at 180°C. The difference of these diameters denotes the increase of the average diameter by volume expansion and therefore an oxide shell thickness of 2.78 nm. In the case of the particles oxidized at room temperature, the diameter has increased to $\langle \mathsf{D} \rangle = 11.62$ nm ± 1.19 nm, which is equivalent to a diameter increase by volume expansion of 0.71 nm.

The particles from the experiment of the surfactant exchange based on the particles fabricated with oleylamine were stored at 180°C with a similar result. Images of the particles before and after the experiment are displayed in figures 8.7 and 8.8. The particle diameter has increased from $\langle \mathsf{D} \rangle = 11.86$ nm ± 2.63 nm to $\langle \mathsf{D} \rangle = 16.81$ nm ± 3.38 nm, which denotes anincrease of the diameter by volume expansion of 4.95 nm; the size distribution has broadened, see figures 8.9 and 8.10.

The heated particles of the first surfactant exchange have been investigated by HRTEM [1]. The HRTEM images of the particles stored at room temperature displayed in figure 8.11 and the ones stored at 180°C shown in image 8.12 show clearly that the particles are not hollow, but consist of several crystallites, which are differently orientated and show therefore a different contrast in the electron beam.

If the measured values for the average diameter $\langle \mathsf{D} \rangle$ and the measured volume expansion are compared to a calculated values based on the initially measured average diameter, depicted in table 8.1, it is visible that the calculated volume expansion fits to the measured data. For the particles fabricated with TOPO where the surfactant was exchanged to dodecylamine an average diameter $\langle \mathsf{D} \rangle = 10.91$ nm ± 2.38 nm was measured. After complete oxidation at a storage of 2 hours at 180°C the average diameter had increased to $\langle \mathsf{D} \rangle = 13.69$ nm ± 2.73 nm. The corresponding calculated average diameter for completely

---

[1] Images taken by Inga Ennen at TU Wien

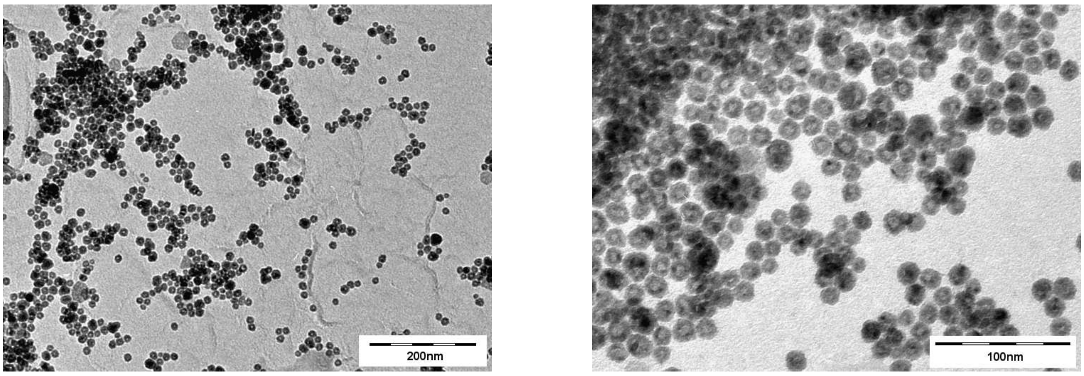

Figure 8.1: Particles stored at 180°C for 2h.

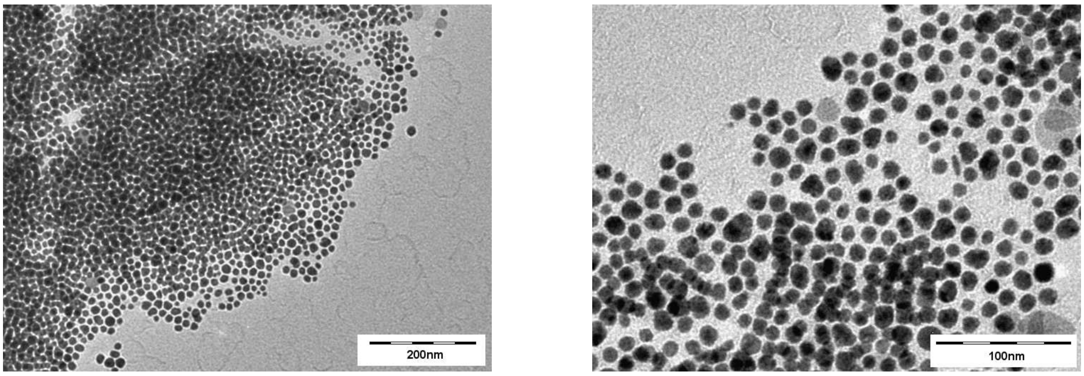

Figure 8.2: Particles directly after surfactant exchange.

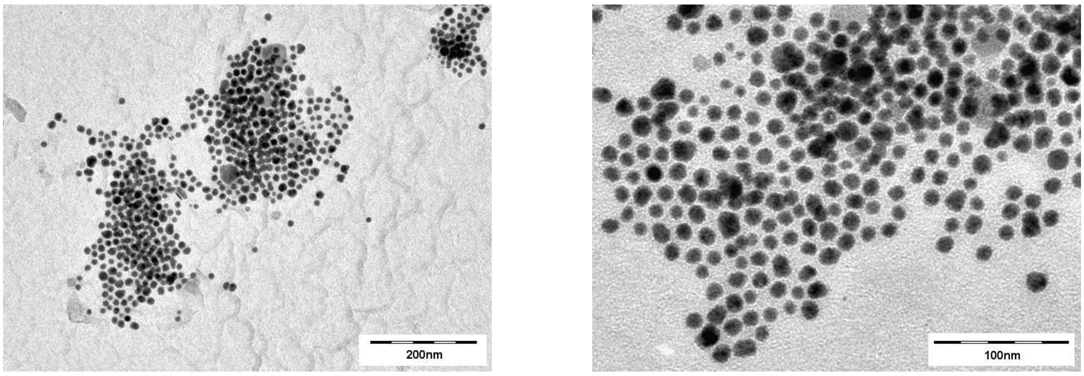

Figure 8.3: Particles stored at room temperature.

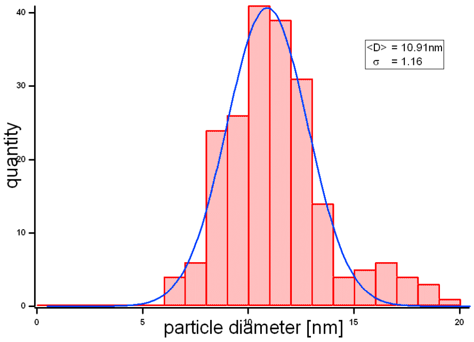

Figure 8.4: Size distribution of fresh particles, ⟨D⟩= 10.91 nm ± 1.35 nm, N=208.

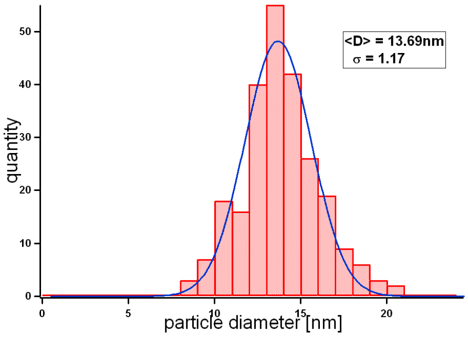

Figure 8.5: Size distribution of particles stored at 180°C, ⟨D⟩= 13.69 nm ± 2.73 nm, N=246.

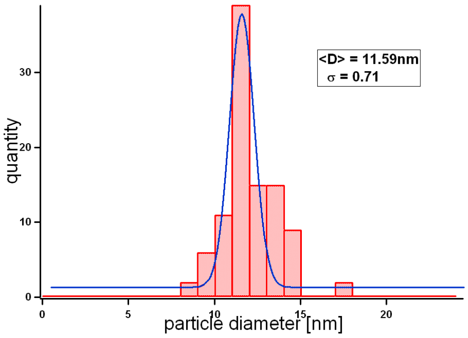

Figure 8.6: Size distribution of particles stored at RT, ⟨D⟩= 11.59 nm ± 1.02 nm, N=99.

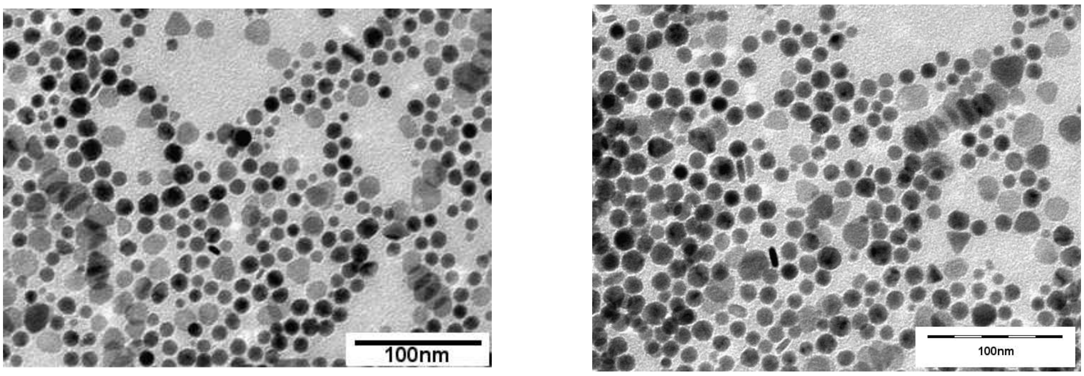

Figure 8.7: Particles before oxidation.

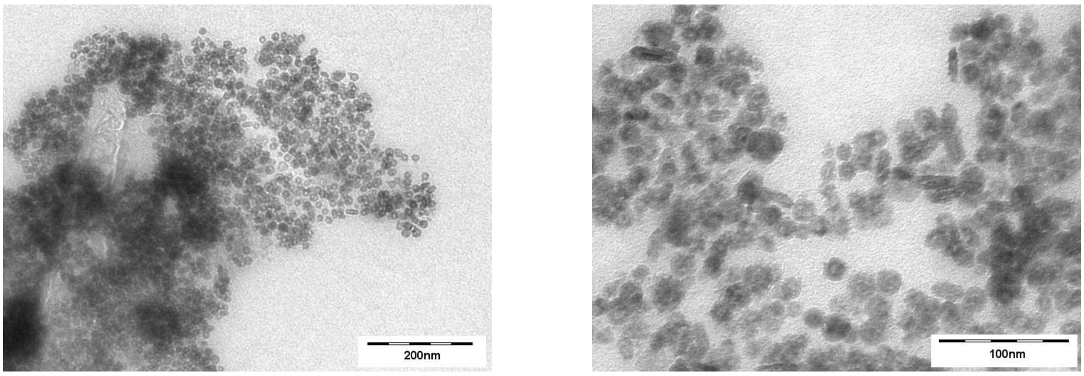

Figure 8.8: Particles stored at 180°C for 2h.

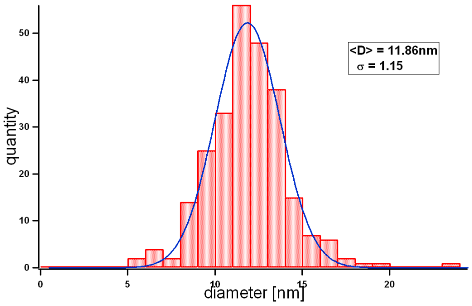

Figure 8.9: Size distribution of fresh particles, $\langle D \rangle = 11.86$ nm ± 2.64 nm, N=255.

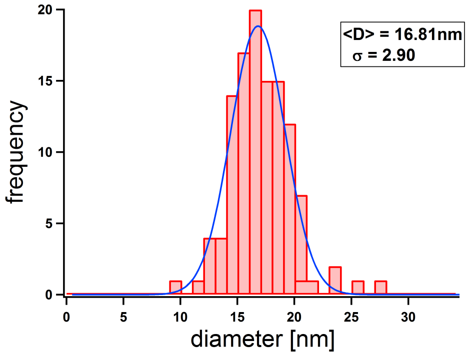

Figure 8.10: Size distribution of particles stored at 180°C, $\langle D \rangle = 16.81$ nm ± 3.38 nm, N=122.

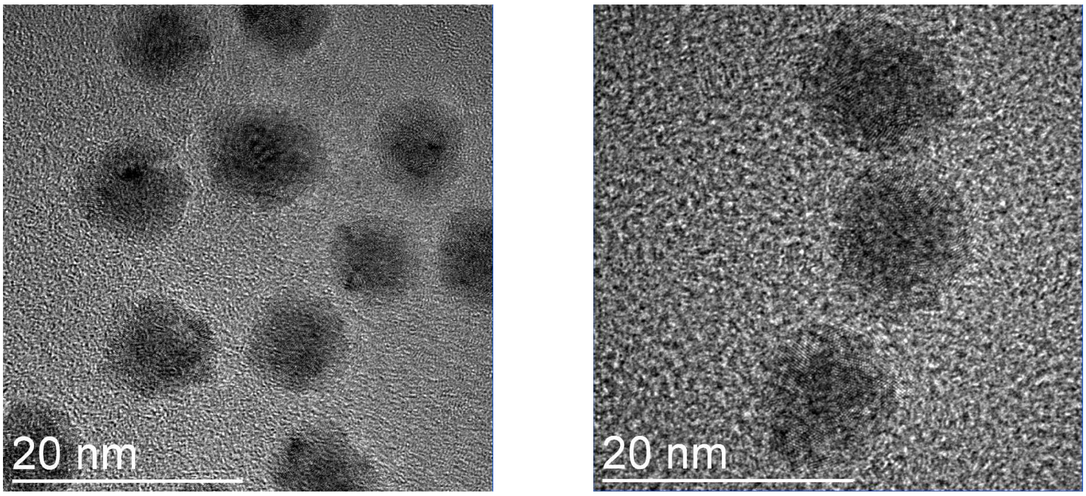

Figure 8.11: Particles stored at room temperature.

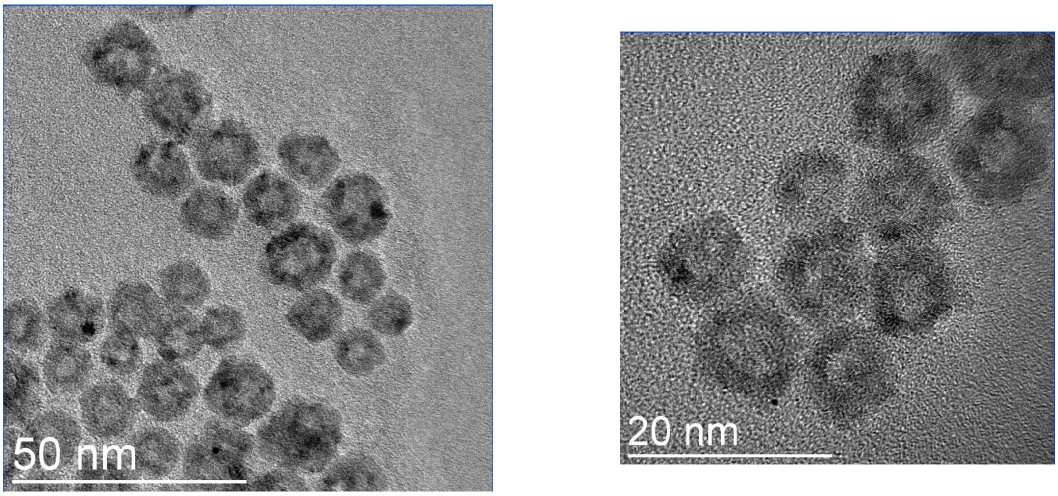

Figure 8.12: Particles stored at 180°C for 2h.

oxidized particles is ⟨D⟩= 15.27 nm ± 3.33 nm, which is greater than the measured values, but still within the error range. The particles fabricated with oleylamine have an average diameter ⟨D⟩= 11.86 nm ± 2.63 nm directly after fabrication. After being stored at 180°C for two hours these particles are oxidized completely as well and the average diameter has increased to ⟨D⟩= 16.81 nm ± 3.38 nm. The calculated diameter for completely oxidized particles is ⟨D⟩= 16.60 nm ± 3.68 nm. In this case the measured and calculated values fit very well.

	octadecylamine	oleylamine
fresh particles ⟨D⟩ [nm]	10.91 ± 2.38	11.86 ± 2.63
oxid. room temperature ⟨D⟩ [nm]	11.59 ± 1.19	-
oxid. 180°C ⟨D⟩ [nm]	13.69 ± 2.73	16.81 ± 3.38
diameter increase RT measured [nm]	0.71	-
diameter increase 180°C measured [nm]	2.78	4.95
complete oxidation calculated ⟨D⟩ [nm]	15.27 ± 3.33	16.60 ± 3.68
diameter increase calculated [nm]	4.36	4.74

Table 8.1: Change of the effective magnetic volume and corresponding Co core radius; diameter increase.

9 Oxidation measurements during the first 30 minutes after fabrication

In the previous measurements, where the particles were initially measured after an exposure time to air between one hour and half a day after fabrication, no correlation between the covering surfactant and the oxidation behaviour was found. From [45] and the previous investigations it was deduced, that an influence of the surfactant can be discovered only during the first 30 minutes of oxidation at room temperature. Therefore the sample preparation and especially the transportation had to be modified. The particles were again prepared in an argon atmosphere to prevent oxidation as described in chapter 2. After the particle suspension was dropped onto the piece of wafer under argon (instead of in air) to shield the particles from oxygen, the gas was removed and the solvent evaporated fast in vacuum. For the transport to the laboratory, the flask with the sample was flooded with argon again and sealed, to keep out oxygen. Te sample was removed from the flask in the laboratory, placed on the probe and inserted into the helium gas stream.
The time the sample was exposed to air during installation was measured and was in all cases less than one minute.

9.1 AGM oxidation setup

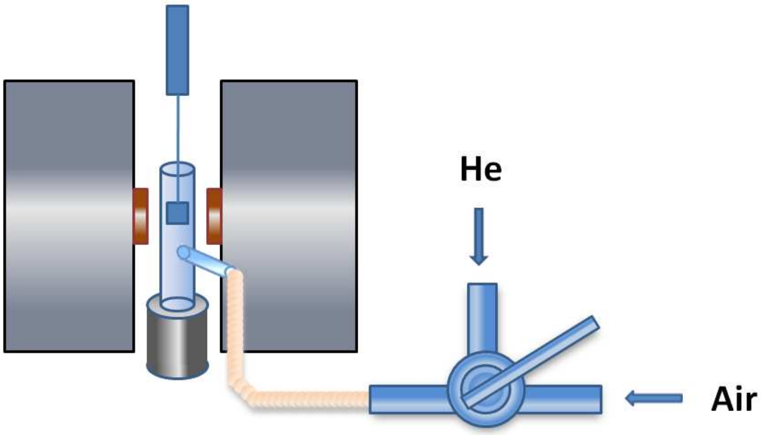

Figure 9.1: Oxidation setup of the AGM.[1]

To achieve detailed information about the oxidation of the particles during the first thirty minutes, the AGM setup was modified in a way that was based upon the low temperature setup displayed in figure 3.16 to allow a controlled exposure to air of the sample. The glas tube with an aluminum holder which is connected to the cryostate in the low temperature

---

[1] vgl. Seyr (1980), S. 134

setup, was rebuilt with an additional smaller glas tube attached to its side, forming a T-like structure. See figure 9.1 for a drawing of the setup. A silicon tube was attached to the smaller side tube, which was connected to a three-way valve. The second one of the tubes of the three-way valve was connected to a bottle of compressed He, and the last one was connected to a bottle of artificial air (80% N_2 and 20% O_2). The pressure was adjusted in a way, that a light flow of gas was detectable through the open top of the glas tube. The sample was therefore exposed to either helium or artificial air during the experiment. Measurements were always carried out under helium flow, to keep a stable oxidation state during the measurements. Inbetween measurements the samples were exposed to artificial air for time intervals between 30 seconds at the beginning, which then were gradually extended up to 5 minutes for the last interval. The oxidation is assumed to be fast compared to the exposing time to artificial air and the time span of a measurement, so that a stable state can be assumed during measurements.

9.2 Used surfactants

The cobalt particles were prepared with TOPO as described in chapter 2. The surfactants that were used for the exchange are oleylamine, oleic acid, 1-pyrenebutyric acid and trioctylamine (TOA).

TOPO

The particles prepared with TOPO are discs with an average diameter $\langle D \rangle = 13.72$ nm ± 2.70 nm. The height of the discs is about $h = \frac{\langle D \rangle}{4}$ to $h = \frac{\langle D \rangle}{2}$ and is not investigated in further detail [2]. A bright field TEM image and the size distribution are shown in figure 9.2.

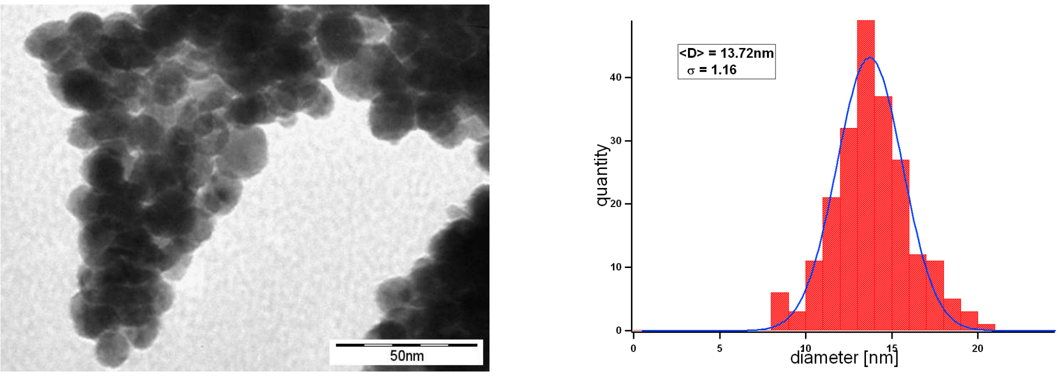

Figure 9.2: Particles with TOPO, $\langle D \rangle = 13.72$ nm ± 2.70 nm, N=218.

Oleylamine

After the surfactant exchange with oleylamine the average particle diameter was found to be reduced to $\langle D \rangle = 13.13$ nm ± 2.51 nm. These particles are depicted in image 9.3.

---

[2] Because on the one hand not much upright discs can be found and on the other hand the height is neglected for the oxidation examination.

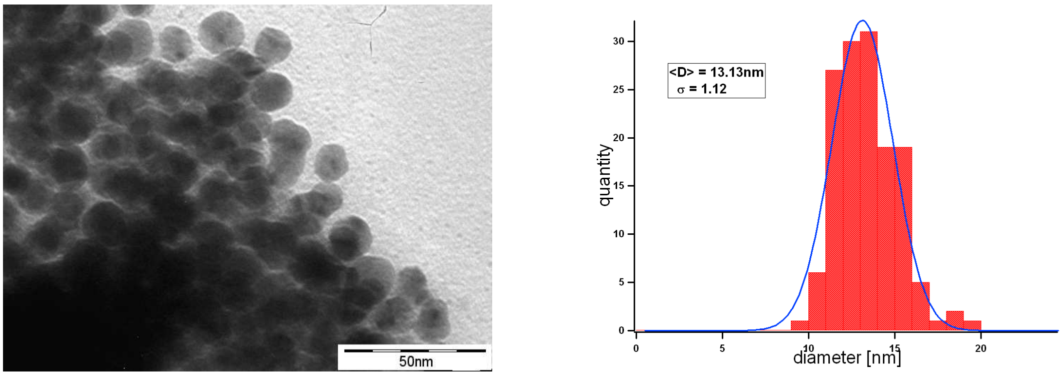

Figure 9.3: Particles with oleylamine, ⟨D⟩= 13.13 nm ± 2.51 nm, N=142.

Oleic acid

The particles covered with oleic acid are displayed in image 9.4. They exhibit a reduced diameter ⟨D⟩= 11.99 nm ± 1.91 nm. This sample is the only one of this batch, where an inter particle distance could be measured. Compared to the other samples from this experiment, these particles show an increased inter particle distance.

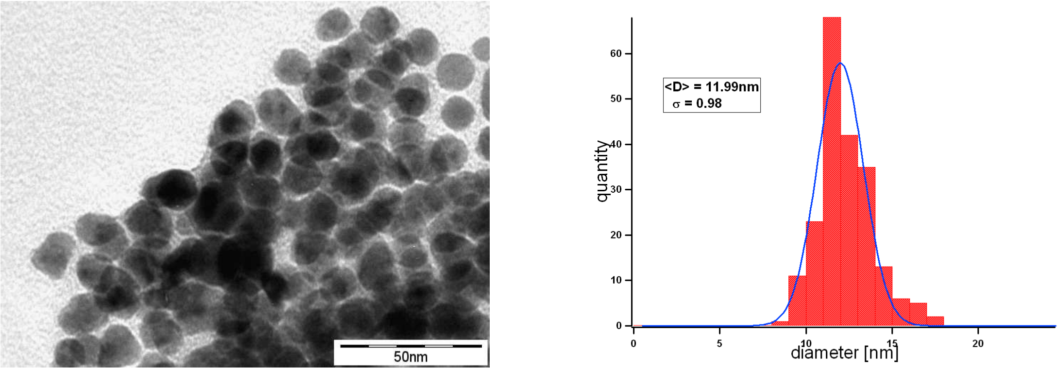

Figure 9.4: Particles with oleic acid, ⟨D⟩= 11.99 nm ± 1.91 nm, N=206.

1-pyrenebutyric acid

In the case of 1-pyrenebutyric acid the average diameter is reduced to ⟨D⟩= 12.05 nm ± 1.83 nm. These particles are displayed in figure 9.5.

TOA

The TOA leads to a reduction of the average particle diameter to ⟨D⟩= 13.30 nm ± 2.83nm. For an image of these particles see figure 9.6.

9.3 Effects of the surfactant exchange

If the changes in the average diameter, displayed in table 9.1, are compared to the changes displayed in table 5.3 it can be seen that the reduction in the case of the new exchange is

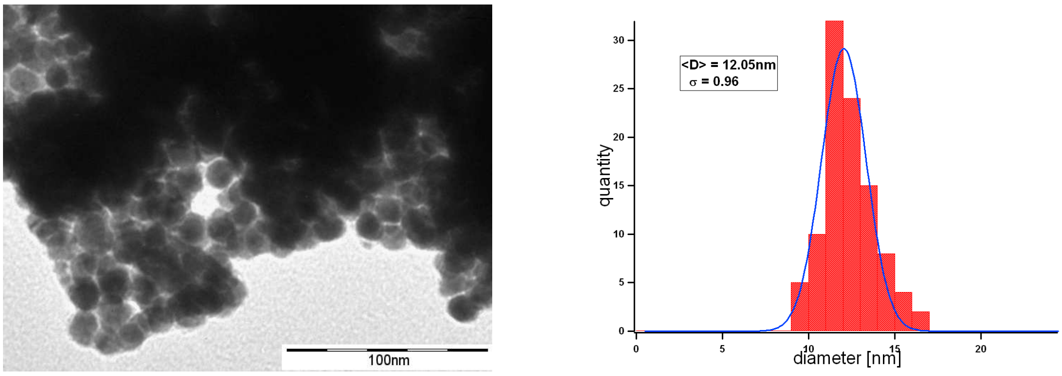

Figure 9.5: Particles with 1-pyrenebutyric acid, ⟨D⟩= 12.05 nm ± 1.83 nm, N=100.

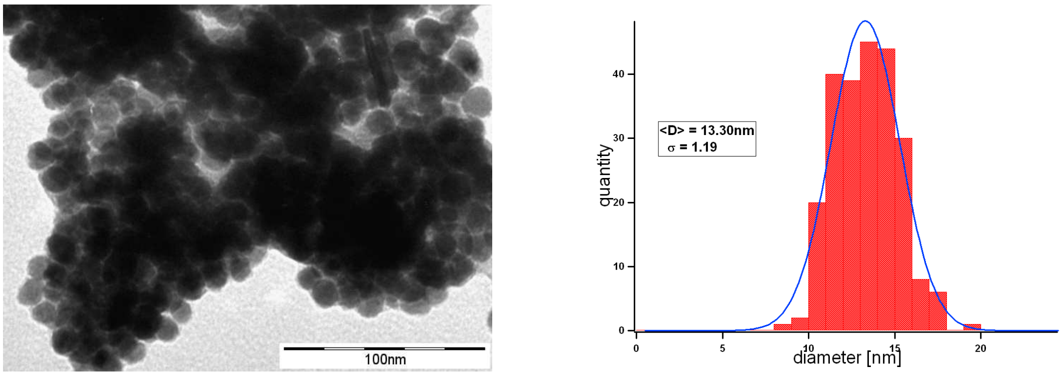

Figure 9.6: Particles with TOA, ⟨D⟩= 13.30 nm ± 2.83 nm, N=236.

head (group)	**name**	**⟨D⟩ [nm]**	**change [nm]**
OP	trioctylphosphine oxide	13.72±2.70	-
NH_x	oleylamine	13.13±2.51	-0.59
NH_x	trioctylamine	13.30±2.83	-0.42
NH_x	**average**		-0.51
COOH	oleic acid	11.99±1.91	-1.73
COOH	1-pyrenebutyric acid	12.05±1.83	-1.67
COOH	**average**		-1.70

Table 9.1: Overview over the changes in the average diameter ⟨D⟩.

slightly larger. The degree of decrease is similar.
In this experiment an explicitly larger decrease in size was measured for the particles where the exchanged surfactant has a carboxyl group compared to those with an amine group. The decrease is more than three times the decrease than in the case of an amine group.

9.3.1 Magnetic properties

In image 9.7 the normalized hysteresis curves of the fresh samples are displayed. Apart from the samples with 1-pyrenebutyric acid, the shape of the hysteresis curves did not change compared to the hysteresis curve of the particles initially prepared with TOPO. In the case of the particles covered with 1-pyrenebutyric acid the slope is less steep, the other parameters did not change.

The coercivities of the samples are displayed in figure 9.8. The black line denotes the value for the particles stabilized with TOPO, the blue lines denote the values for the particles stabilized with a surfactant with a carboxyl headgroup and the red lines denote the samples with an amine headgroup. In the case of TOA the coercivity is larger than in the initial sample. This might be a result of the thicker clusters that occur for this surfactant and assumed resulting stronger influence of the particle interaction, therefore.

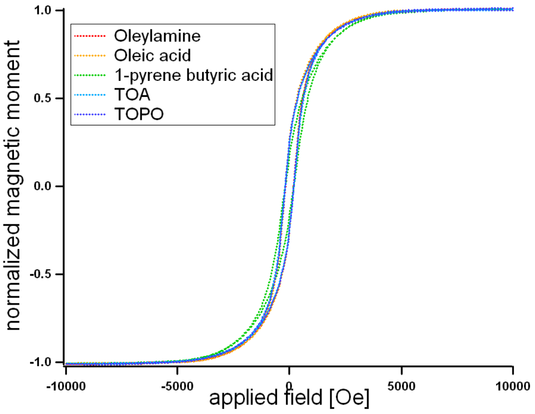

Figure 9.7: Hysteresis curves of the initial particles and the particles after the exchange covered with different surfactants.

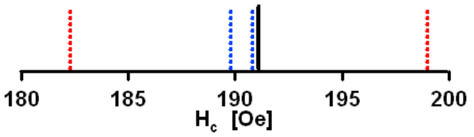

Figure 9.8: Coercivity of the samples, red: amine headgroup, blue: carboxyl headgroup, black: TOPO.

9.4 Oxidation during the first thirty minutes after fabrication

The change of the hysteresis curves by oxidation at room temperature of the sample with TOPO is imaged in figure 9.9. The initial curve is drawn in black, the red curves denote later measurements. The saturation magnetic moment decreases with time. The progress of all five samples of this batch looks similar, therefore only one image is shown here as an example.

In figure 9.10 the change of the saturation magnetic moment over time is depicted for all samples. For better comparison the saturation magnetic moment values are normalized to the associated initial value. These curves are displayed in figure 9.11.
All curves show an increase prior to a decrease of the saturation magnetic moment. The

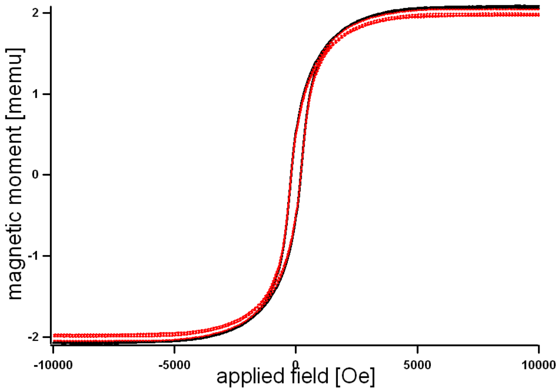

Figure 9.9: Hysteresis curves recorded at different times during the oxidation process for the particles stabilized with TOPO.

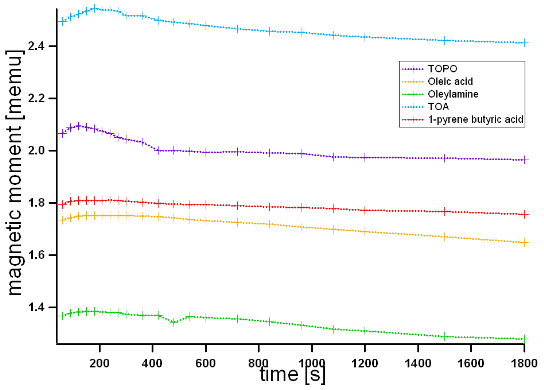

Figure 9.10: Change of the saturation magnetization during oxidation.

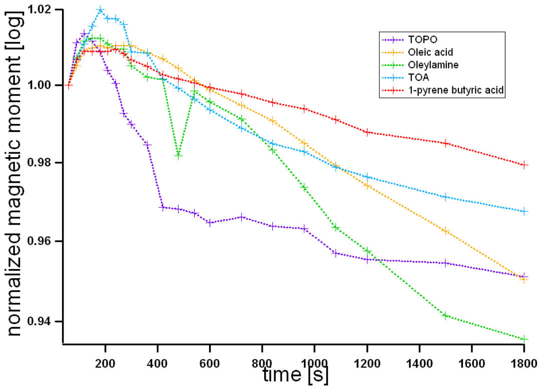

Figure 9.11: Change of the saturation magnetization during oxidation - normalized data.

increase is about 2% in the case of TOA, for the other samples the increase is between 0.9% and 1.4%.

This can be explained by an induced magnetic moment in a monolayer of dissociatively chemisorbed oxygen atoms on the particle surface. For low coverage couples the oxygen layer to the ferromagnetic substrate. An exchange splitting of the 2p level of the oxygen and an increase of the magnetic moment of the surface atoms were described for a oxygen-on-iron-system. In [79, 80, 81] an induced magnetic moment between 0.2 μ_B and 0.7 μ_B for each oxygen atom is described for the case of iron. "Magneticlly dead" layers at the surface begin to form with the incorporation of the oxygen atoms into the bulk and the oxidation process, respectively [82]. A similar exchange splitting of the oxygen 2p level was found in [83, 82] for the system oxygen on cobalt which implies an induced magnetic moment in the adsorbed oxygen layer as well. [3] A detail of the first 700s of figure 9.11 is displayed in figure 9.12, because the course of the curves differs significantly from the ones of the previous measurements. To emphasize point of decrease below the initially measured values a black line at the normalized magnetic moment of 1 is added. The corresponding values are displayed in table 9.2.

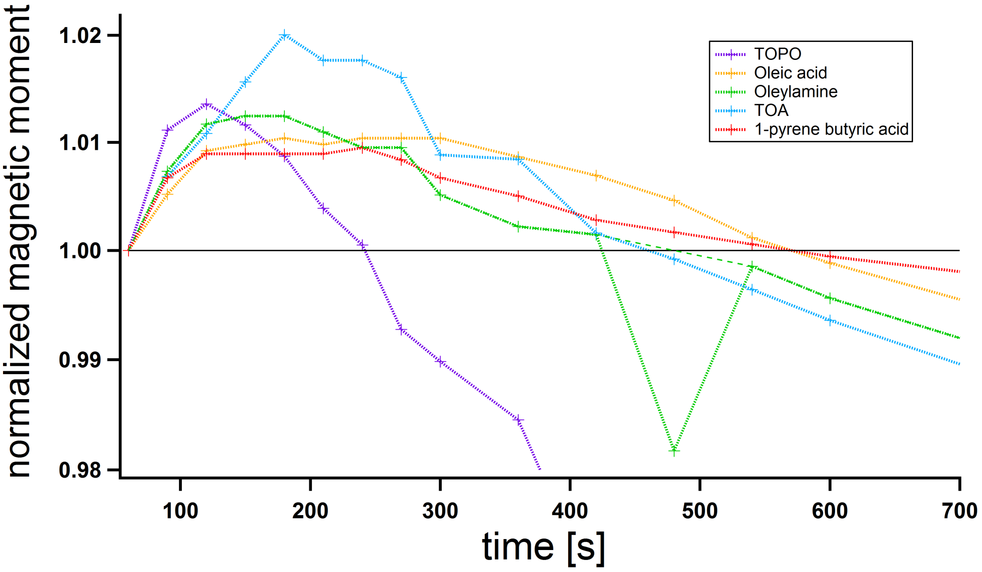

Figure 9.12: Detail of the first 700s of figure 9.11.

After a steep increase to 101.4% of the initial value, the particles covered with TOPO exhibit a steep decrease of the saturation magnetic moment. The decrease rate of the saturation magnetic moment is reduced after t=420s. The further course of the curve shows a slight decrease.

The curves for the particles with surfactants with equal headgroups show a lot of similarities. The samples of the particles stabilized with oleylamine and TOA undergo a less steep increase than in the case of TOPO. After t=180s (TOA) and 150s-180s (oleylamine) the

---

[3] In the case of cobalt coexistence of chemisorbed oxygen and CoO occurs, because oxygen diffuses into the bulk and forms antiferromagnetic CoO. Therefore oxygen exists at the surface as well and exhibits hybridization between adsorbate and substrate. With ongoing oxidation descreases the the exchange splitting by further formation of CoO at the surface [83].

maximum values of 102.0% (TOA) and 101.2% (oleylamine) are reached, directly followed by a decrease. From t=420s to t=720s the curves run parallel and between t=420s-480s the curves fall below the initial value. Around t=840s the curves separate and a steeper decrease in the case of oleylamine occurs, while the curve becomes shallower in the case of TOA, where it finally runs parallel to the later part of the TOPO curve.

The samples of the particles stabilized with oleic acid and 1-pyrenebutyric acid undergo the same increase as the particles stabilized with an amine headgroup at first. The increase stops earlier and leads to a plateau. The maximum values of 101.0% (oleic acid) and 100.9% (1-pyrenebutyric acid) are slightly below the values for the amine headgroup samples. The plateaus stretch from t=120s to t=360s with a small maximum from t=240s-300s in the case of oleic acid and from t=120s to t=270s with a slightly higher maximum at t=240s for 1-pyrenebutyric acid. Afterwards they undergo a slight decrease, which becomes steeper in the case of oleic acid, and runs parallel to the curve of oleylamine finally. In the case of 1-pyrenebutyric acid, the curve becomes shallower and this curve runs finally parallel to the curves of TOA and TOPO. Both curves of samples with a carboxyl headgroup fall below the initial values between t=540s-600s.

name	$(m_s)_{max}$ after t [s]	$(m_s)_{initial}$ [memu] at $t = 60$ s	$(m_s)_{max}$ in [memu]	$(m_s)_{max}$ in %	t_{return} to $(m_s)_{initial}$ [s]
TOPO	120	2066	2094	101.4	240-270
TOA	180	2495	2545	102.0	420-480
oleylamine	150-180	1368	1385	101.2	420-480
oleic acid	240-300	1735	1753	101.0	540-600
1-pyr. acid	240	1794	1811	100.9	540-600

Table 9.2: Increase and decrease of the saturation magnetic moment m_s.

9.4.1 Conclusion

The initial similarity of the curves in the case of equal headgroups marks a dependence on the headgroups of the surfactants for the first period of the oxidation. The further development of the curves exhibits a dependence on the tailgroups of the surfactant, as the curves of oleylamine and oleic acid run parallel after some time. The curves of TOA and TOPO underline this result.

The correlation to 1-pyrenebutyric acid cannot be explained by this. But if it is regarded that oleylamine and oleic acid are rather string- or line-like molecules and the other surfactants are rather area-covering molecules, an explanation for the parallel development of the curves is given.

The oxidation is influenced by the surfactant only during the first minutes of oxidation. The headgroup appears to be of greater importance during the first seconds, followed by a chaingroup influenced part. In the longer term only the size, shape and crystallinity of the particles exhibit an influence on the oxidation, as the oxidation depends on the diffusion of oxygen in the nanoparticles, then.

9.5 Crystallinity of particles

To gain information concerning the crystal structure, the particles investigated in section 9, were investigated with XRD, additionally. The curves are displayed in figure 9.13. They are shifted vertically on top of each other for better comparison. The curves are quite homogeneous. They differ only slightly in the height and shape of the peaks. 1-pyrenebutyric acid exhibits some extra peaks at low angles, which correspond the the π-π-interaction of the benzene rings. Therefore it can be deduced that all particles have the same crystal structure, and that the overall crystal phase was not influenced by the surfactant exchange.

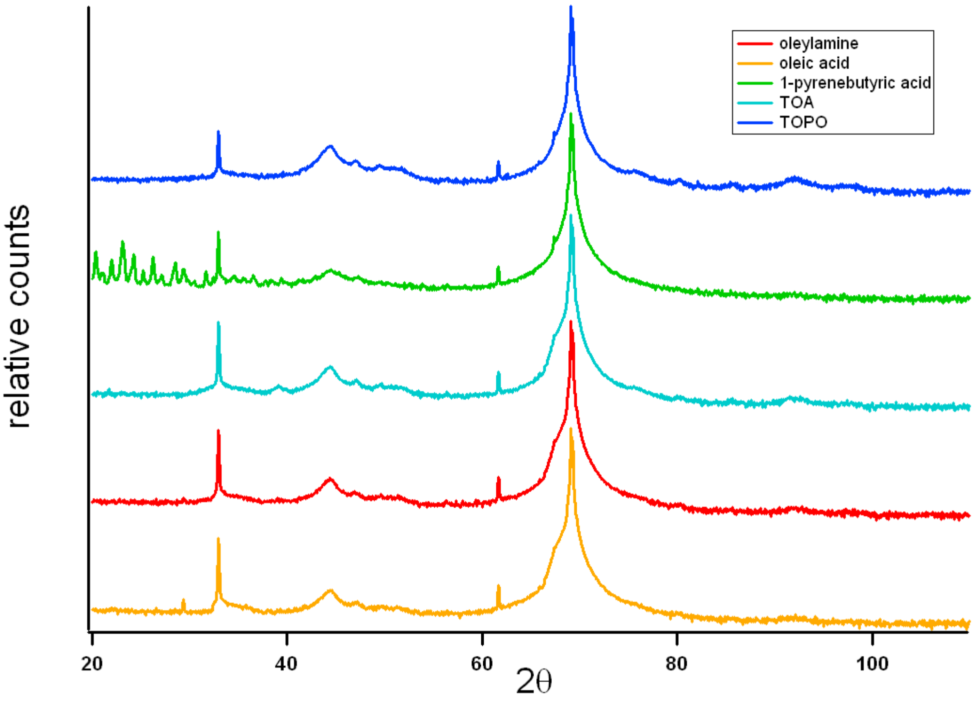

Figure 9.13: XRD curves of all samples, shifted vertically for better comparison.

To determine the crystal structure, simulations with the program WinPlotr from the Fullprof Suite Toolbar [84] have been run. The data for the simulation was taken from the FindIt - Inorganic Crystal Structure Database [85], additional data such as atom positions in the lattice were calculated with the program Crystal Maker [86].

All available Co and CoO lattice structures with most of the lattice constants were simulated. Lattice constants differing only the slightest fractions were neglected. The comparison to simulated data, depicted in image 9.14, shows that all particles consist mostly of fcc cobalt with a lattice constant of a=0.35442 nm. These particles were measured shortly after preparation, therefore the existence of CoO can only be assumed.

To proof this results, particles prepared with TOPO and particles after a surfactant exchange with oleylamine and oleic acid have been investigated with HRTEM and SAD measurements on single or a few particles.

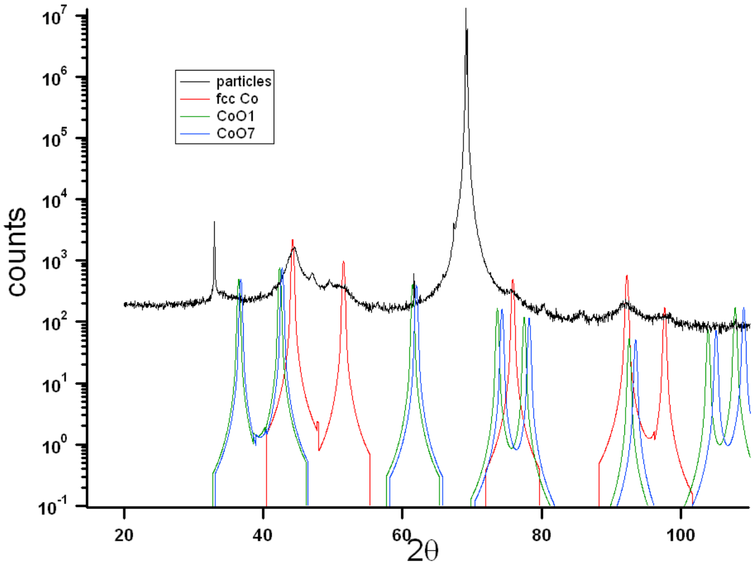

Figure 9.14: Simulated peaks and measured XRD curve of particles covered with TOPO.

TOPO

The HRTEM images show that some of the particles stabilized with TOPO exhibit an oxide shell with a thickness of $\delta = 5.2$ nm, as shown in figure 9.15 [4]. A lot of particles are agglomerated, which can often be found in the case of TOPO [54].

It can be seen in figure 9.16 [5] that the particles consist of smaller agglomerated particles, which are about $\langle D \rangle = 4$ nm in diameter, marked with yellow circles in the red box. From the FFT image displayed in figure 9.17 [6] where the reflexes are on three distinct circles it can be concluded that these particles are polycrystalline. The yellow arrow indicates reflexes of d_{hkl}=0.173 nm, which result from fcc 200 plane. The red one marks reflexes of d_{hkl}=0.2045 nm, which result from the fcc 111 plane and the green one points to d_{hkl}=0.244 nm, which are connected to fcc CoO 111 plane.
The selected area (electron) diffraction (SAD) taken from the circled area in the left image in figure 9.18 [7], is displayed in the large image on the right side. The small image shows the integrated image of the diffraction image taken with a 200 nm SA aperture. The SAD spectrum is displayed in figure 9.19. Mostly fcc Co, CoO peaks and possibly ε-Co peaks can be found.

---

[4] taken with FEI Tecnai F20 at TU Vienna by I. Ennen

[5] taken with ZEISS Libra 200 MC by I. Ennen

[6] taken with ZEISS Libra 200 MC by I. Ennen

[7] taken with FEI Tecnai F20 at TU Vienna by I. Ennen

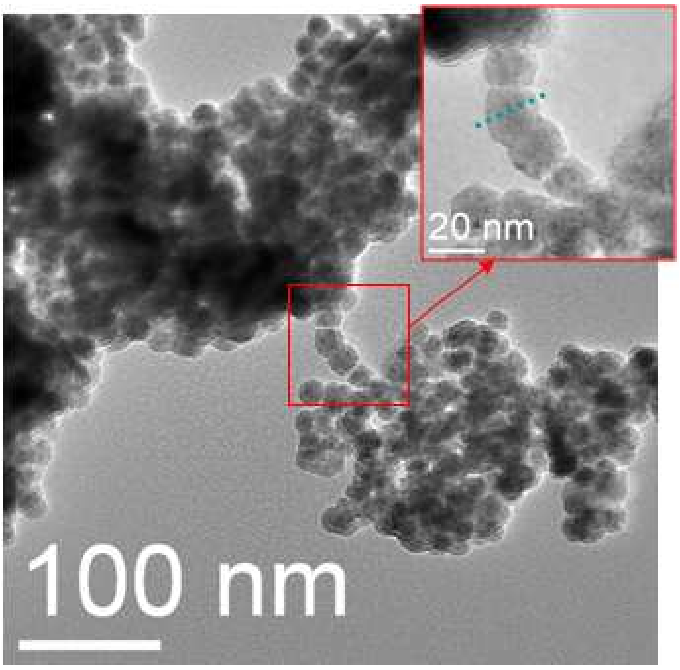

Figure 9.15: HRTEM image of particles covered with TOPO.

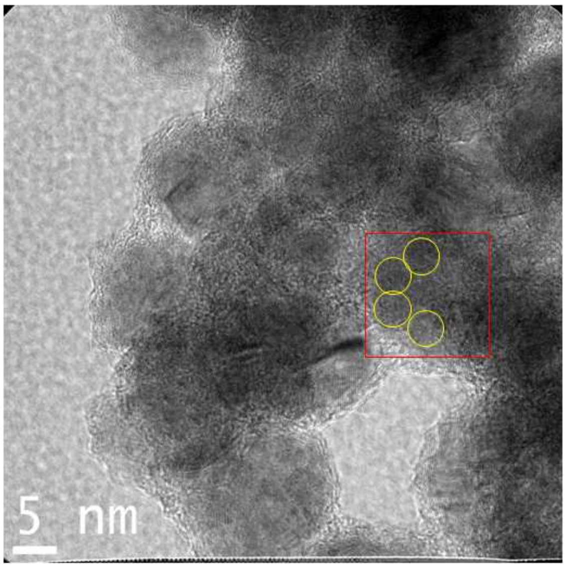

Figure 9.16: HRTEM micrograph of particles prepared with TOPO.

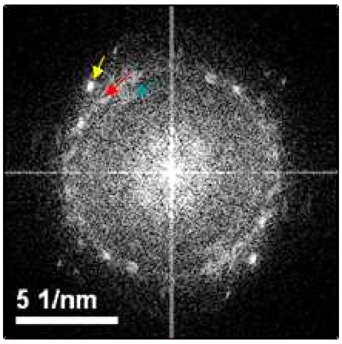

Figure 9.17: FFT image of the particles prepared with TOPO.

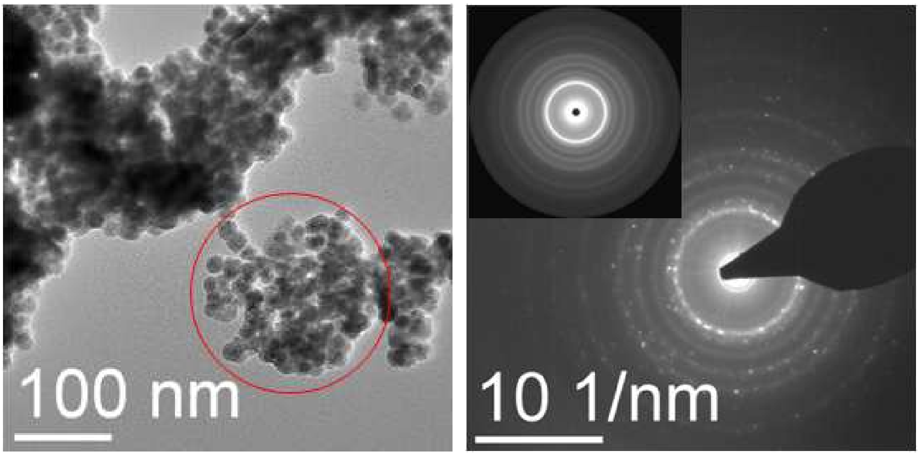

Figure 9.18: Picture of the particles on the left, the 200 nm SA aperture was positioned on the particles marked by the circle. The SAD image and radial integration (small image) is shown on the right.

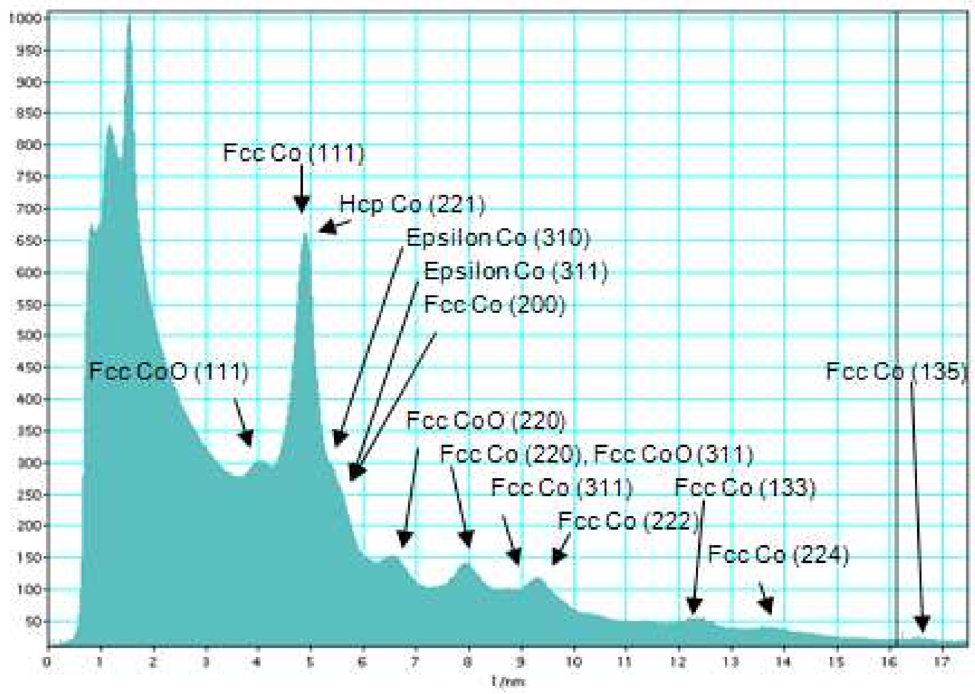

Figure 9.19: SAD spectrum of Co particles covered with TOPO.

Oleylamine

The particles covered with oleylamine are not agglomerated. The oxide shell thickness of particles covered with oleylamine after a surfactant exchange seems to be dependent on the direct environment of the particles. Oxidized particles with oleylamine are displayed in figure 9.20 [8]. In areas that are not shielded by adjacent particles, the oxide shell appears to be thicker than in the area directly next to other particles in a lot of cases. The most obvious oxide shells on particles are marked with arrows.

The HRTEM images of the particles covered with oleylamine after the surfactant exchange exhibit mixed crystallinity. As displayed in image 9.21 [9] monocrystalline particles (one marked by the yellow circle) and particles consisting of several crystallites (marked by the red box) can be found. The polycrystalline oxide shell of the monocrystalline particles is between $\delta = 2.0$ nm and $\delta = 2.3$ nm thick, for the polycrystalline particles an oxide shell thickness cannot be measured, because of the lack of contrast between shell and polycrystalline particle. The disc marked with the blue box is in fcc (111) orientation. A FFT image of the boxed area is displayed in figure 9.22 [10]. The angle inbetween the reflexes is $\theta = 60°$ and the distance is determinated to be $d_{hkl} = 0.2045$ nm or $d_{hkl} = 0.207$ nm; the value for fcc (111) found in literature is $d_{hkl} = 0.2046$ nm [87, 88].

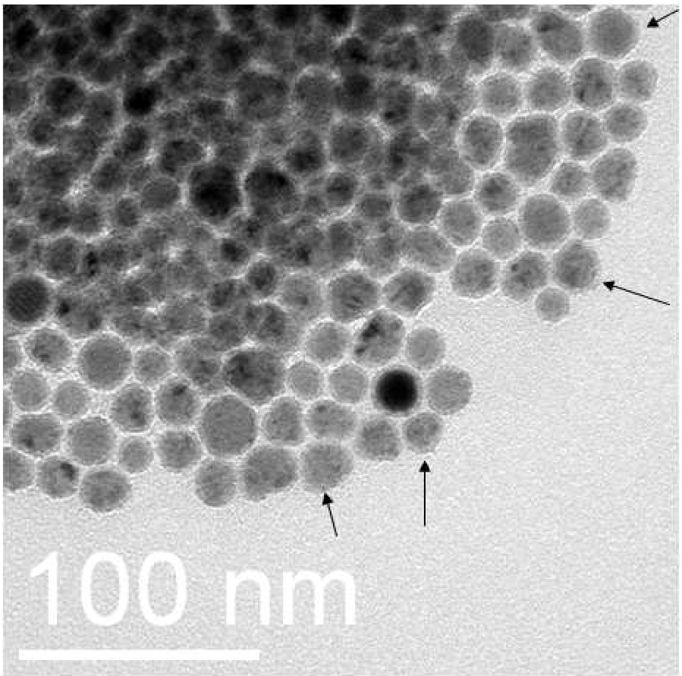

Figure 9.20: HRTEM image of particles covered with oleylamine, the oxide shells are clearly visible.

Reflexes of CoO fcc (111) can be found es well. Flat truncated triangular and hexagonal discs can additionally be found in this sample. A SAD spectrum of a few particles is displayed in figure 9.23. Predominantly fcc peaks can be found. The particles consist mainly of fcc cobalt.

---

[8] taken with ZEISS Libra 200 MC by I. Ennen

[9] taken with ZEISS Libra 200 MC by I. Ennen

[10] taken with ZEISS Libra 200 MC by I. Ennen

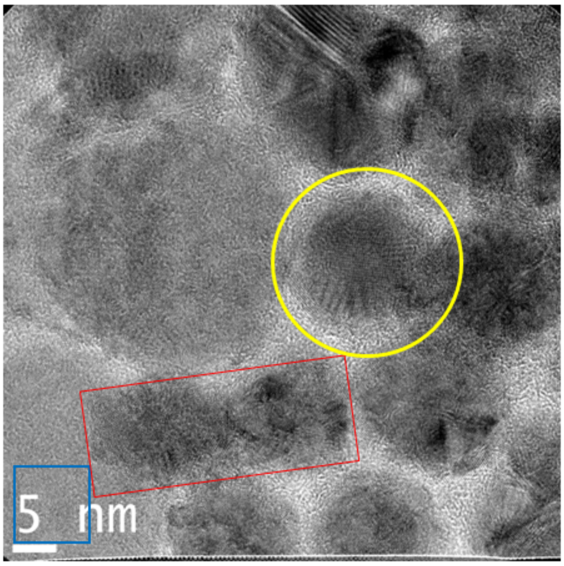

Figure 9.21: HRTEM image of particles covered with oleylamine.

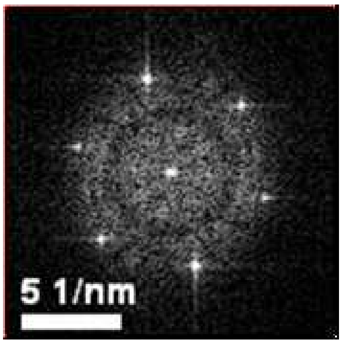

Figure 9.22: FFT image of a Co disc covered with oleylamine.

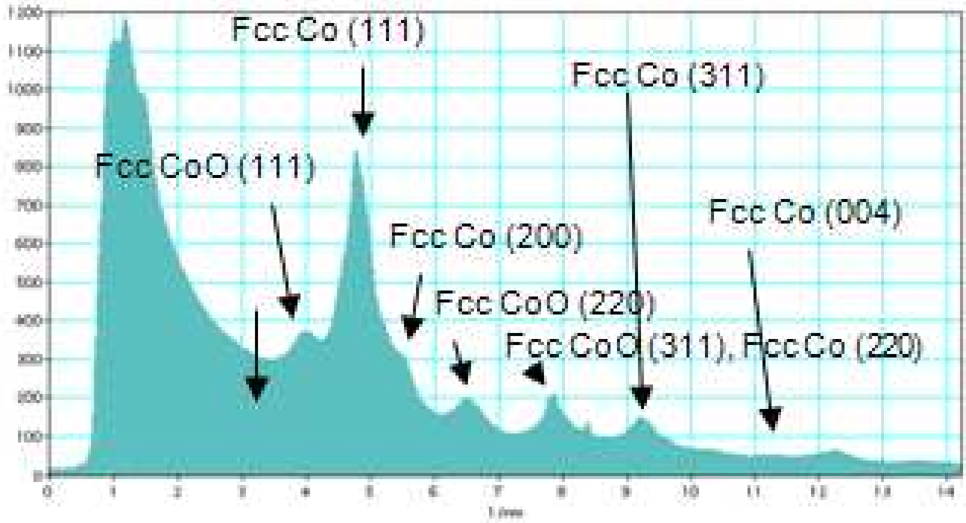

Figure 9.23: SAD spectrum of Co particles covered with oleylamine.

fcc Co (a=0.3544 nm)			fcc CoO (a=0.4261 nm)			ε-Co (a=0.6097 nm)		
hkl	d_{hkl}	rel. Intensity	hkl	d_{hkl}	rel. Intensity	hkl	d_{hkl}	rel. Intensity
111	0.2046	100	111	0.2455	100	221	0.2023	100
200	0.1772	40	200	0.2126	40	310	0.1928	58
220	0.1253	38	220	0.1503	38	311	0.1838	25
311	0.1069	50	311	0.1282	50	510	0.1196	21
222	0.1023	15	222	0.1227	15	520	0.1132	19

Table 9.3: Interplane spacings d_{hkl} for fcc Co (a=0.3544 nm), fcc CoO (a=0.4261 nm), and ε-Co (a=0.6097 nm) lattice structures and their relative intensities [87].

Oleic acid

Apart from the shapes mentioned for the particles stabilized with TOPO and oleylamine, additional shapes can be found for the particles stabilized with oleic acid as cubes and irregularly formed triangles and discs. The particles where the surfactant was exchanged to oleic acid exhibit an oxide shell with a thickness between $\delta = 1.3$ nm and $\delta = 2.2$ nm, as displayed in the left image of figure 9.24. The right image shows mono- and polycrystalline particles with an amorphous oxide shell.

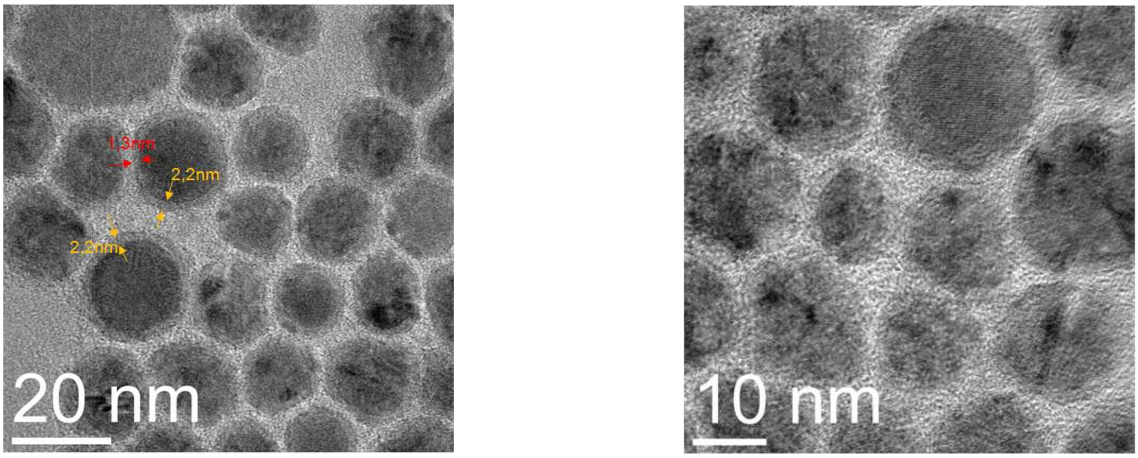

Figure 9.24: HRTEM images of particles covered with oleic acid.

A diffraction image of the particles marked with the circle in the left image of figure 9.25, was taken. The SAD and the integrated image are displayed on the right. The intensity distribution of the SAD integration image is displayed in figure 9.26. The peaks have been identified according to table 9.3. Most of the particles appear to be fcc Co with fcc CoO,

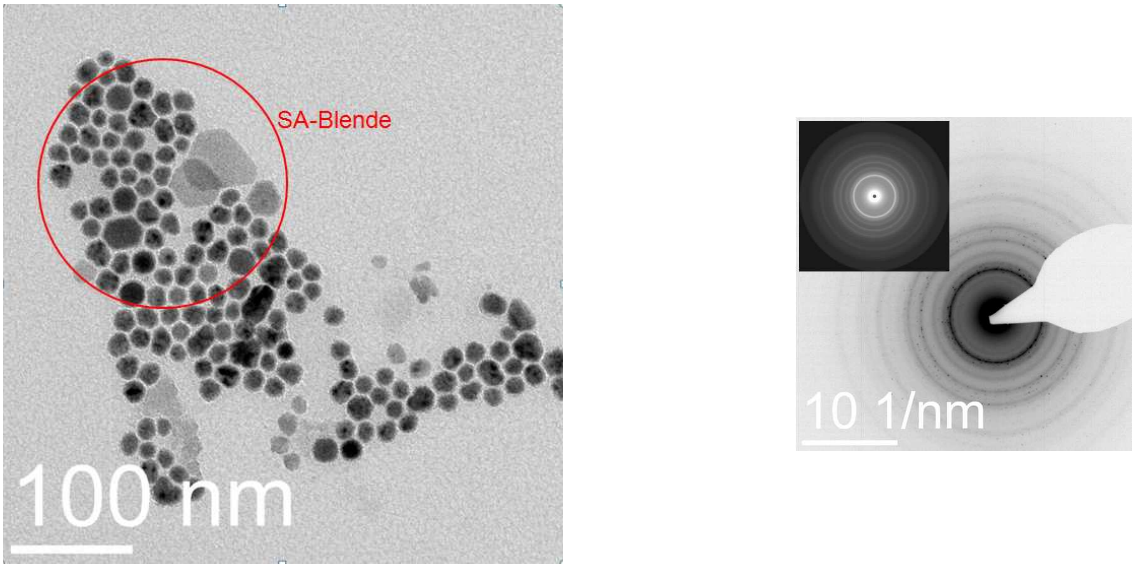

Figure 9.25: Picture of the particles, the 200nm SA aperture was positioned on the particles marked by the circle and SAD image and radial integration (small image)

as some ε-Co peaks occur additionally as displayed in figure 9.26.

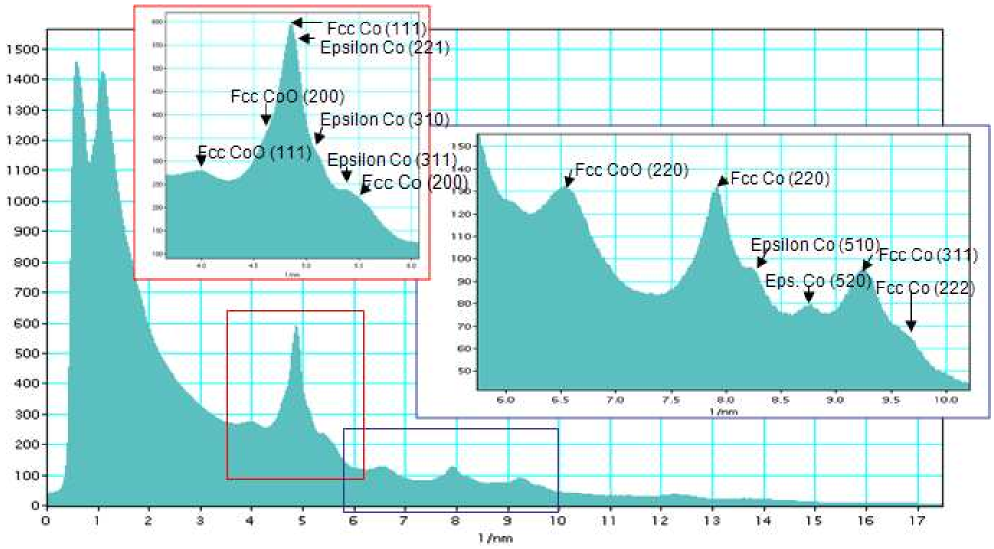

Figure 9.26: SAD spectrum of Co particles covered with oleic acid.

Elemental maps of a string of particles show a Co core and an oxide shell. As expected from previous measurements that a passivating oxide layer forms on the cobalt core. These maps are depicted in image 9.27.

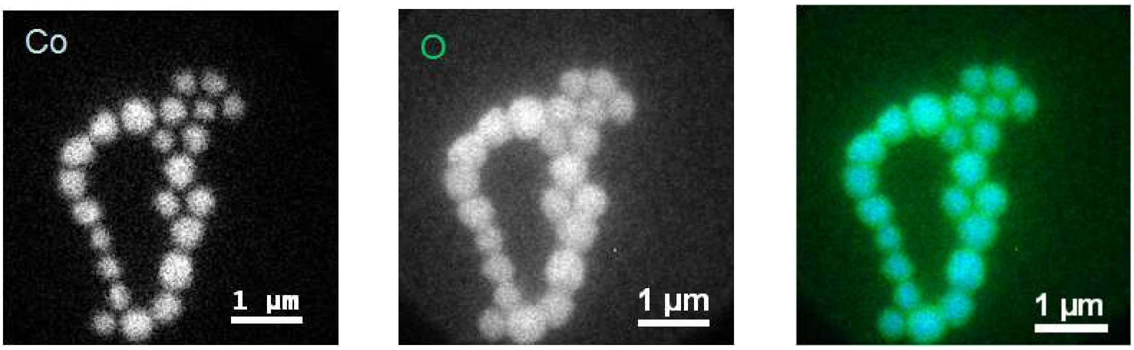

Figure 9.27: Co, O and combined elemental maps.

9.6 Oxide shells - conclusion

The CoO signal is more significant in these aged samples, than in the fresher samples used for XRD.

If the values for the oxide shells measured on HRTEM images are compared to the calculated data, displayed in table 9.28 and table 9.29, it is clearly visible, that the measured values are to a great extend larger than the values calculated based on the magnetic measurements. This underlines to the conclusion, that the oxide shell does contribute to the magnetic properties because of a coexistence of CoO and incorporated oxygen as described in section 9.4 in contrast to the assumptions, that the oxide shell does not exhibit magnetic properties.

name	m_s [memu] $t = 60s$	m_s [memu] $t = 1800$	r_0 (t=0) [nm]	r_{sphere} $(1800s)$ [nm]	d_o Co shell [nm]	δ_s CoO sphere [nm]	r_{disc} $(1800s)$ [nm]	d_o Co disc [nm]	δ_d CoO shell [nm]
TOPO	2066	1965	6.86±1.35	6.75±1.34	0.11	0.15	6.69±1.32	0.17	0.24
TOA	2495	2414	6.65±1.42	6.58±1.40	0.07	0.10	6.54±1.40	0.11	0.15
oleylamine	1386	1280	6.57±1.26	6.40±1.23	0.17	0.24	6.31±1.21	0.26	0.36
oleic acid	1735	1649	6.00±0.96	5.90±0.94	0.10	0.14	5.75±0.94	0.25	0.35
1-pyrenebutyric acid	1794	1757	6.03±0.92	5.99±0.91	0.04	0.06	5.97±0.91	0.06	0.08

Figure 9.28: Change of the effective magnetic volume and the radii of the corresponding cobalt core and average Co oxide (CoO) thickness.

name	δ measured [nm]	d_o Co sphere calculated [nm]	δ_s CoO shell [nm]	d_o Co disc calculated [nm]	δ_d CoO shell [nm]
TOPO	5.2	1.09	1.53	1.35	1.89
oleylamine	2.0-2.3	0.56 (0.42)	0.78 (0.59)	0.83 (0.67)	1.16 (0.94)
oleic acid	1.3-2.2	0.23 (0.28)	0.32 (0.39)	0.34 (0.41)	0.48 (0.57)

Figure 9.29: Measured and calculated thickness δ of the oxide shell, the values for the surfactant exchange based on oleylamine are displayed in brackets.

10 Oxidation behaviour in dependence on shape

During particle formation, different shaped particles develop as described in section 4.2. This is a result of the different bonding capacities of the surfactants to the different crystallographic sites. In our experiments mainly spheres, discs and cubes were observed. Flat triangles and flat hexagons were found less often. They are expected to be an intermediate state in the formation of discs and eventually spheres and were therefore not investigated in detail.

10.1 Measurements

Samples with different particle geometries have been investigated and the oxidation process has been monitored indirectly by measurement of the saturation magnetization with an AGM as in chapter 9. The investigated nanoparticles are spheres with a diameter $\langle \mathsf{D} \rangle =$ 8.02 nm ± 0.21 nm, stabilized with oleylamine, discs with a diameter $\langle \mathsf{D} \rangle =$ 12.75 nm ± 2.40 nm, stabilized with a mixture of oleylamine and oleic acid, discs with a diameter $\langle \mathsf{D} \rangle =$ 11.61 nm ± 2.04 nm, stabilized with TOPO, and cubes with an average edge length $\langle \mathsf{D} \rangle =$ 115 nm ± 28 nm, stabilized with oleylamine and oleic acid. The height of the discs, varying between $\frac{\langle \mathsf{D} \rangle}{4}$ and $\frac{\langle \mathsf{D} \rangle}{2}$ is neglected as in the previous chapters. In figure 10.1 the curves of the decrease of the normalized saturation magnetic moment are displayed. The spheres exhibit a rapid loss of magnetization, while the discs show a mild decrease. The cubes, which are not directly comparable to the measured spheres and discs because of their much larger size, show barely any decrease of magnetization. The extremely small decrease of the saturation magnetic moment in case of the large cubes is a result of the different ratio of surface to volume atoms. For these large particles the fraction of surface atoms is much smaller than in the cases of the investigated discs and spheres.

10.2 Finite elements simulation

A finite elements simulation based on a level set approach was carried out (by A. Auge) [45]. The oxidation was modelled in a core shell approach to describe the influence of the surfactant. The shell represents oxidation of surface atoms [1], which have to undergo a complete, homogeneous oxidation before the oxidation of the core, the bulk oxidation, starts. The bulk oxidation of nanoparticles is described in further detail in 2.3. The nanoparticles were modeled as spheres, discs (cylinders with hemispherical edges) and cubes and a simulation of moving interfaces was executed. It was used to track the motion of the metal oxide interface. For further information see [89]. Due to the late onset of the measurements only the bulk oxidation was regarded. The ionic current $\mathsf{J_i}$ of species i [2]

---

[1] That is described by the Johnson-Mehl-Avrami-Kolmogorov (JMAK) equation or isothermal growth.

[2] ions or electrons

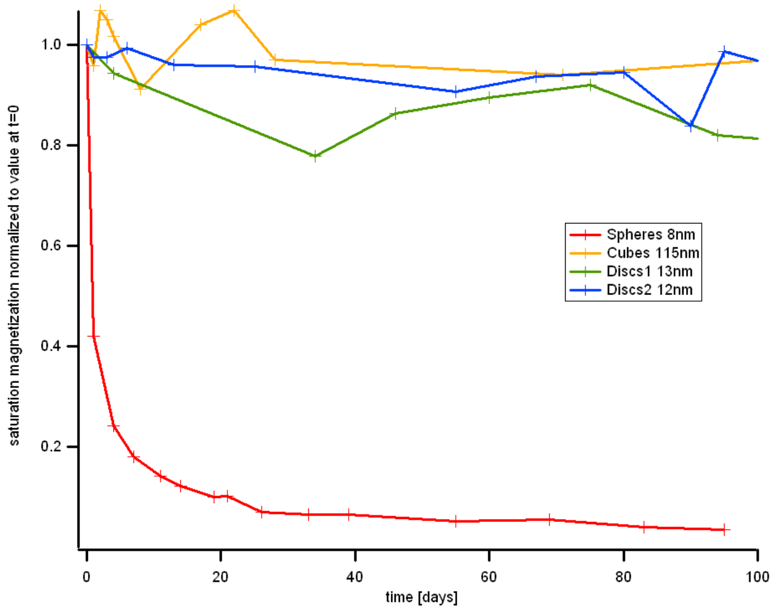

Figure 10.1: Measured oxidation curves for differently shaped particles.

was simulated according to

$$J_i = 4a\nu C_i \exp\left(\frac{-W}{kBT}\right) \exp\left(\frac{Z_i V_m a X}{k_B T L}\right) \tag{10.1}$$

with $X = \frac{R}{R-L}$ in the case of spheres with radius R, see chapter 2.3. The charges of each sign are distributed on spheres with radius R and R-L, where L denotes the thickness of the oxide layer. The effective charge is denoted by $Z_i e$, the thermal activation energy for ionic motion by W, the lattice constant is given by a, and ν denotes the ionic vibration frequency [45].
For simulations over time spans up to 4×10^6s (~ 46d 7h) the following parameters have been applied:

- Discs: diameter D= 12 nm, height H= 5 nm
- Spheres: diameter D= 10 nm
- Cubes: edge length D= 20 nm
- Discs: diameter D= 12 nm, height H= 5 nm, oxidized only from one side
- Cubes: edge length 115 nm

The results are depicted in figure 10.2. It can bee seen that the simulation predicts fastest oxidation and decrease of saturation magnetic moment for discs, second fastest oxidation for spheres and slowest oxidation for cubes. For discs that are oxidized only from one side a slower oxidation was calculated and the simulation of large cubes exhibits an extremely slow oxidation.

A comparison of the measured data and the simulated curves shows a large discrepancy. Both sets of curves are displayed in figure 10.3.

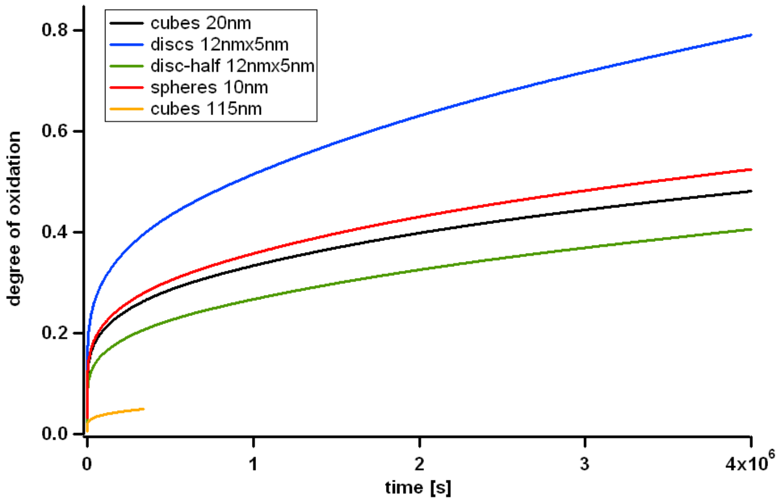

Figure 10.2: Simulated oxidation curves for differently shaped particles [45].

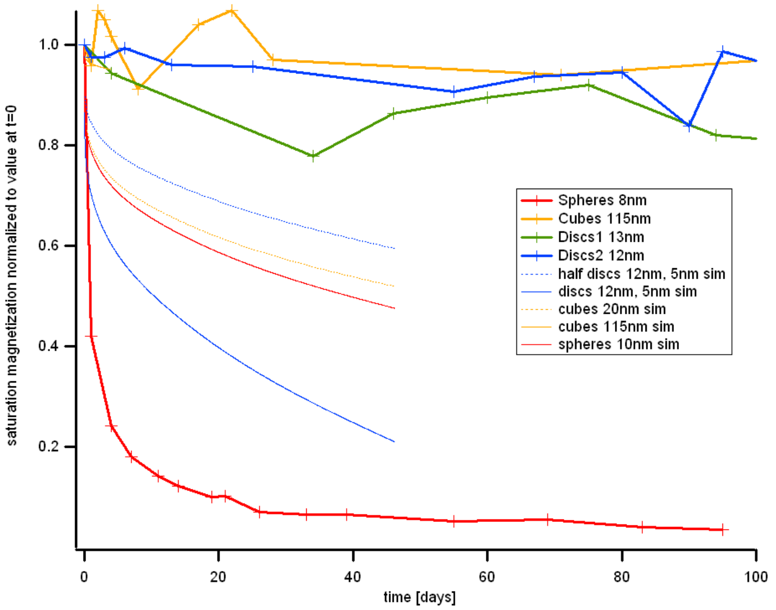

Figure 10.3: Simulated oxidation curves for differently shaped particles [45].

10.3 Volume consideration - oxidation only through curved surfaces or oxide on curved surfaces does not contribute to the magnetic properties?

As the simulated and the measured data show large differences, a simple approach was tried, which takes the surface curvature into consideration. The simple model used here assumes, that the oxidation takes solely place through curved surfaces or that the oxide on the curved surfaces does not contribute to the magnetic properties, but the oxide on the flat surfaces does contribute to some extent. The influence of the degree of curvature onto the (induced) magnetic moment in the oxide layer and the concrete particle size are not taken into account in this approach [3]. The assumption of a comparable particle sizes is made instead. Therefore the following (effectiive magnetiv) volume investigation was carried out:

Considering oxidation only through curved surfaces or no contribution of the curved oxide to the magnetic properties:

- Spheres
$$V_{R_S}(t) = \frac{4}{3}\pi(r_0 - r(t))^3 \tag{10.2}$$
- Discs
$$V_{R_D}(t) = \pi h(r_0 - r(t))^2 \tag{10.3}$$
- Spheres
$$V_{R_C}(t) = r_0^3 \tag{10.4}$$

with: r_0: radius of the magnetic effective metal core at $t = 0$ and $r(t)$: radius of magnetic effective metal core at time t. The oxidation through edges and nucleation sites resulting from a mismatch of the crystal lattice and the particle shape is neglected in this consideration. This would lead to stable particles in the case of cubes, although cubes show a decrease through oxidation. Non ideal cubes could be assumed or edges might have to be taken into consideration, as well. Instead of the assumption of non ideal cubes, a line-factor for oxidation through edges is added. This leads to the following equations:

- Spheres
$$V_{R_S}(t) = \frac{4}{3}\pi(r_0 - r(t))^3 \tag{10.5}$$
- Discs
$$V_{R_D}(t) = \pi h(r_0 - r(t))^2 + C_D(t) \tag{10.6}$$
  with $C_D = 2\pi(r_0 - r(t))$,
- Spheres
$$V_{R_C}(t) = r_0^3 + C_C(t) \tag{10.7}$$
  with: $C_C = 2 * 12 * (r_0 - r(t))$.

The obtained functions have been fitted to the data and the results are displayed in figure 10.4.

---

[3] The different curvatures of spheres and discs are not regarded further and the particle sizes of all batches are assumed to be comparable.

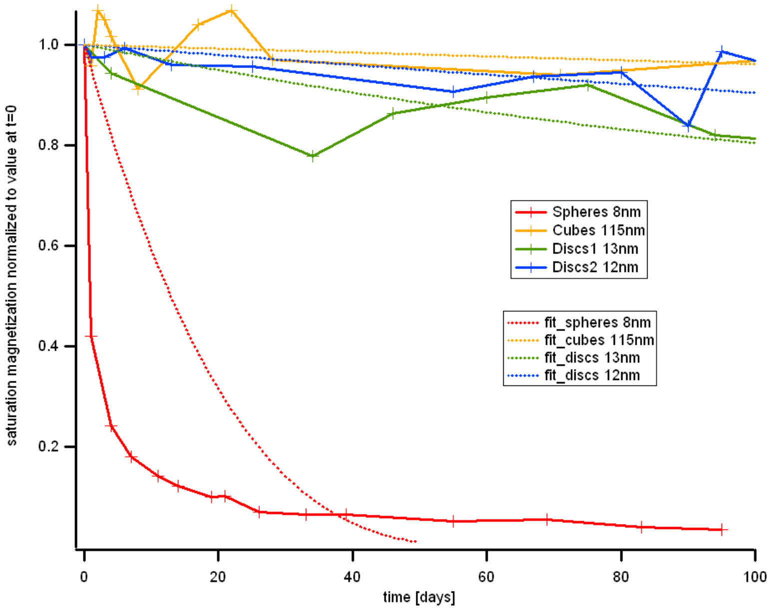

Figure 10.4: Normalized saturation magnetization, decreased by oxidation over time and corresponding volume fits.

In figure 10.5 the simulated and fitted curves are displayed with the measured oxidation curves. The assumption of oxidation only through curved surfaces (and edges) or a loss of magnetization only on curved surfaces fits the measured curves better than the assumption of an overall equal oxidation or overall equal contribution of the oxide to the magnetic properties with reduced extent. It offers an explanation for the faster oxidation of spheres than discs. But it describes not the concrete oxidation process, as the oxidation curve of spheres is fitted best with a double exponential function $f(x) = a + b\exp(-c * x) + d\exp(-e * x)$ as displayed exemplary in figure 10.6.

10.4 Conclusion

Nucleation sites and edges have to be taken into account, as well as processes of oxygen uptake, dissociation and transportation through the oxide and the influence of lattice deformation by curvature on the magnetic properties. An improved version of the simulation, considering curvature and nucleation sites, should lead to a better description.

Several possibilities for a preferred oxidation through curved surfaces can be found. The mismatch of the crystal lattice and the particle shape leads to more edges and therefore more nucleation sites on the curved surfaces. (If the oxidation starts preferredly on these edges.) For an equal coverage with surfactant heads, the surfactant tails are further apart on a positive curved surface than on a plane. A distorted lattice might influence both oxygen uptake and surfactant binding to the surface.

The optional case of a smaller but not negligible contribution of the cobalt oxide to the magnetic properties depending on the shape and lattice distortion, might be explained by a coupling of the antiparallel orientated spins, which might be dependent on the lattice geometry, so that it evens out in some geometries but not in other.

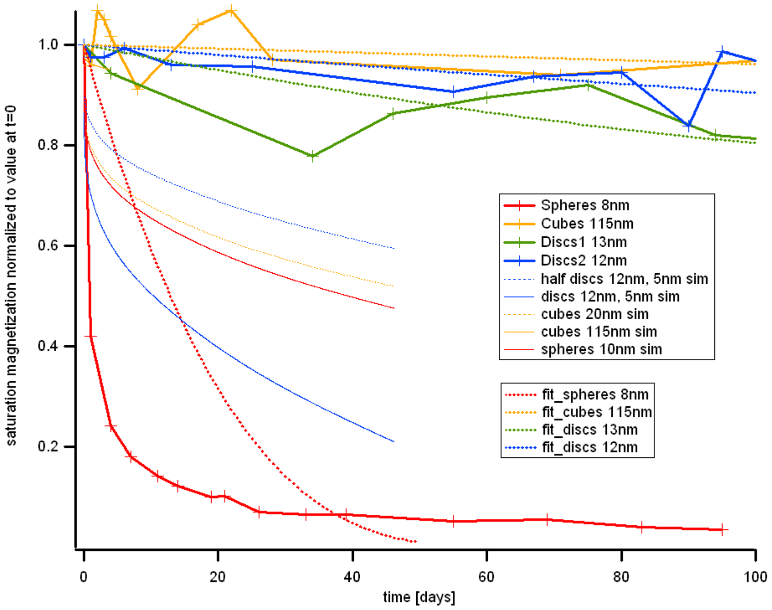

Figure 10.5: Normalized saturation magnetization, decreased by oxidation over time, corresponding volume fits and simulated curves.

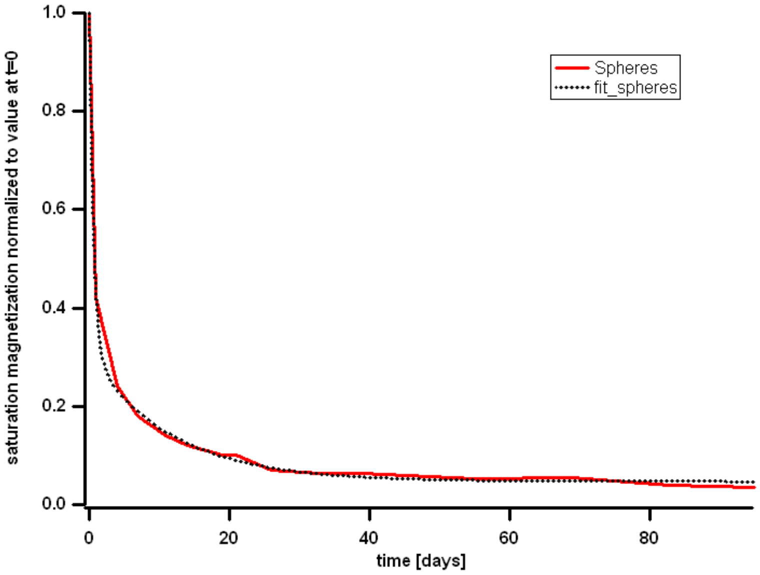

Figure 10.6: Normalized saturation magnetization decrease by oxidation over time for the case of spheres and an exemplary double exponential fit.

10.5 Discussion: oxidation only through curved surfaces versus partly contribution of the oxide to the magnetic properties and no contribution from the oxide on the curved surfaces

The curves describing the decrease of the saturation magnetic moment as well as the calculation of the oxide thickness and the observed oxide shell on the nanodiscs, which are depicted in figures 10.7, put the assumption of an oxidation through only curved surfaces into question.

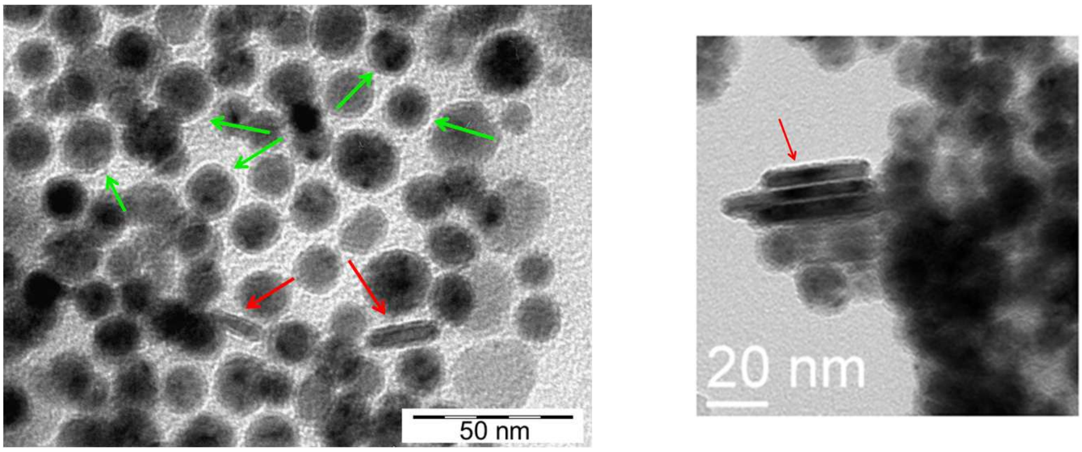

Figure 10.7: Discs with oxide shell,particles covered with oleylamine (left image) and TOPO (right image).

The images reveal an overall oxide formation on the discs. The oxide layer on the curved surfaces on horizontal orientated discs is marked by dark blue arrows. The oxide layer on the flat sides is clearly visible, marked by the red arrows.

In contrast to this observation, the curves of the disc approach [4] fit better to the measured curves than the spherical approach [5], as shown in section 10.3.

This confirms to the conclusion, that the oxide contributes partly to the magnetic properties, even for thicker oxide layers. The contribution of the oxide on the curved geometries appears to be less strong, which has to be determined by further measurements.

---

[4] With no oxidation through flat surfaces or a contribution of the oxide to the effective magnetic volume on the flat surfaces and no or a far lesser magnetic contribution of the oxide on the curved surfaces.

[5] It has to be regarded, that the concrete decrease in the case of discs' sample saturation magnetic moment with an overall equal oxidation and corresponding loss of magnetic properties would be even greater.

11 Oxidation of nanoparticle clusters

In this chapter the oxidation behaviour of particle clusters is investigated. When dropped onto a piece of oxidized silicon wafer for AGM measurements, monolayers seldomly form. They can be achieved by dipping the wafer into the solution [36, 57, 18]. One disadvantage is, that it results in fewer material on the wafer and during oxidation there may be a point achieved where not enough magnetic material is left for a sufficient signal. When $2\mu l$ of the particle solution was dropcasted onto the wafer, multilayers and clusters formed during drying. Two examples of different structures that formed are given in the images 11.1 and 11.2.

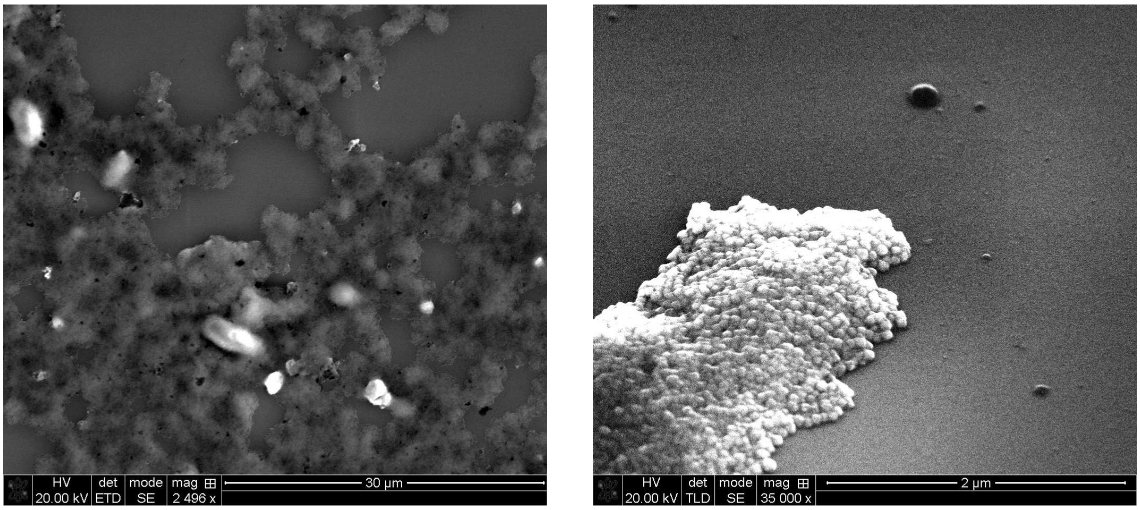

Figure 11.1: relatively flat clusters

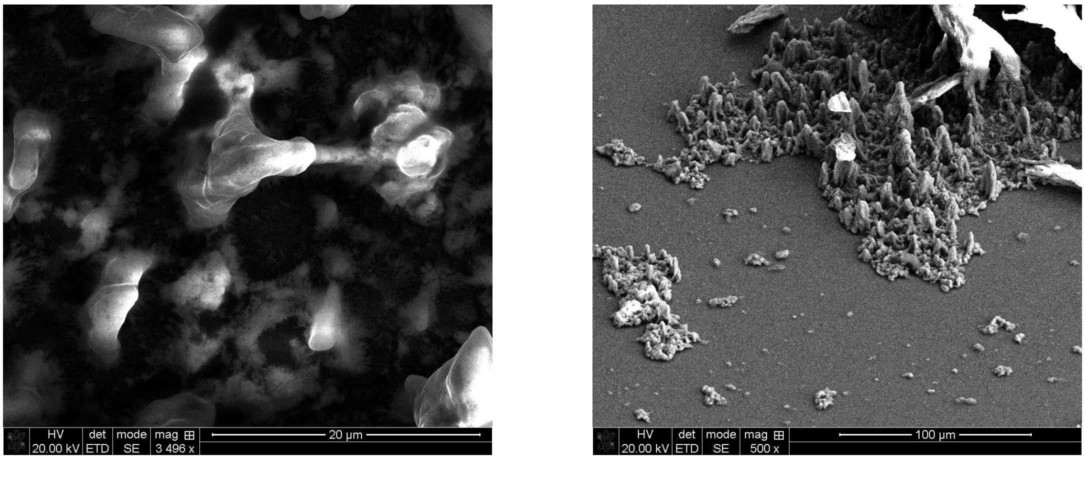

Figure 11.2: tower like structures

To examine the oxidation behaviour of multilayer systems, samples at different stages of oxidation were investigated with EDX to find out how oxidation occurs in multilayers and clusters. In order to study the oxidation process of particle clusters, 2µl of the particle solution was dropcasted onto a piece of silicon wafer and dried in vacuum. The samples were then stored under environmental conditions at room temperature.

In SEM mode at the FIB images were taken and a large particle cluster was chosen. The part of the cluster where a TEM lamella should be cut, was coated with platinum deposited by electron deposition first, to prevent the sample from influences of the ion beam. Afterwards the part was coated with platinum deposited by ion deposition because the platinum deposition by ion beam is faster and more effective than with the electron beam, and a sufficiently thick layer is needed to protect the sample during the milling process and afterwards against oxidation. Then a TEM lamella was milled from the sample by ion milling, removed with a microprobe needle and glued on a sample holder for STEM investigation by platinum deposition. Afterwards the lamella was coated with Pt on both sides to prevent the sample from oxidation during the change of the stage from SEM to STEM mode, where the sample had to be removed from high vacuum. Then the lamella was thinned by ion etching to remove the platinum and material that was deposited on the sides due to sputtering and backscatter effects during the milling.

Some pictures taken at different steps during preparation of a lamella are displayed in image 11.3.

In image part a) an overview over the sample and the particle distribution as clusters is given. Part b) shows a closer view of the cluster chosen for milling, and image c) a top view of the milled lamella, which is still connected to the sample. A view of the freestanding lamella can be found in image part d). The light layer is the deposited platinum, the dark substance are particles and the underlying silicon wafer.

Part e) depicts the part of the sample carrier with attached lamella at a relatively low magnification and f) gives a closeup of the previous picture. The lamella coated with platinum and attached to the sample carrier is visible.

Image g) shows a closeup of the lamella where the platinum layer has been milled from the sides. The particle layer is visible as grained layer on the dark grey silicon wafer. On top of the particle layer the electron deposited platinum can be identified as medium grey layer, while the ion deposited platinum is visible as thick light grey top coat. Details of this image are shown in the subfigures h) and i). The inhomogeneous particle layer can be identified easily.

Afterwards EDX linescans and one element map were taken from the samples.

Two old samples and one relatively fresh sample were investigated.

In the following two subsections the results of the EDX investigations of the older samples and the newer sample are described.

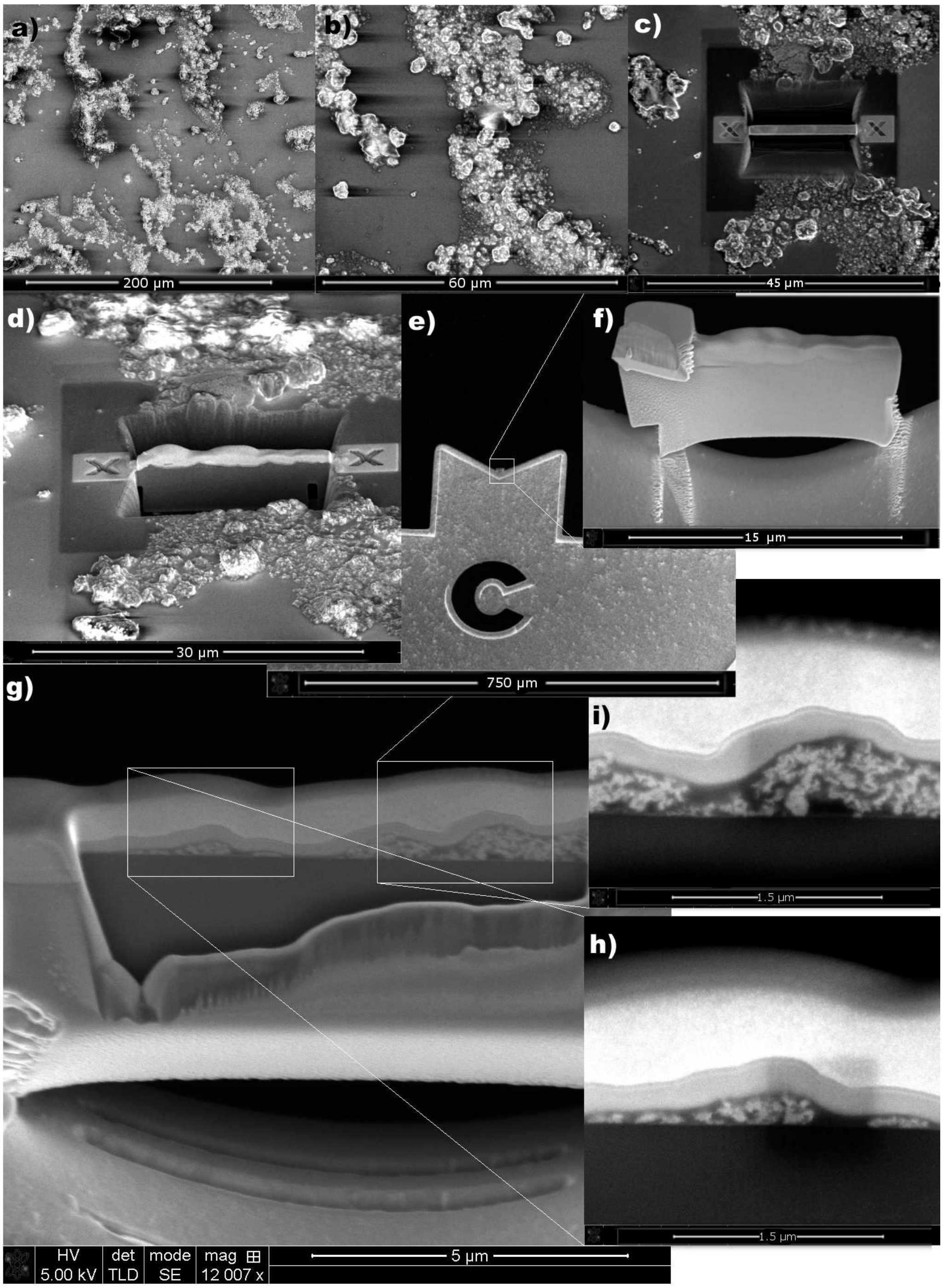

Figure 11.3: Overview over preparation of a TEM lamella

11.1 Older Particles

The particles of the older samples were stored under environmental conditions [1] for over 100 days. At this stage most of the change in the magnetic properties has occurred and a stable state was reached as described in chapter 6 and 7.

The clusters of the first sample are formed by cobalt discs with a mean diameter $\langle \mathrm{D} \rangle =$ 11.86 nm ± 1.32 nm [2].

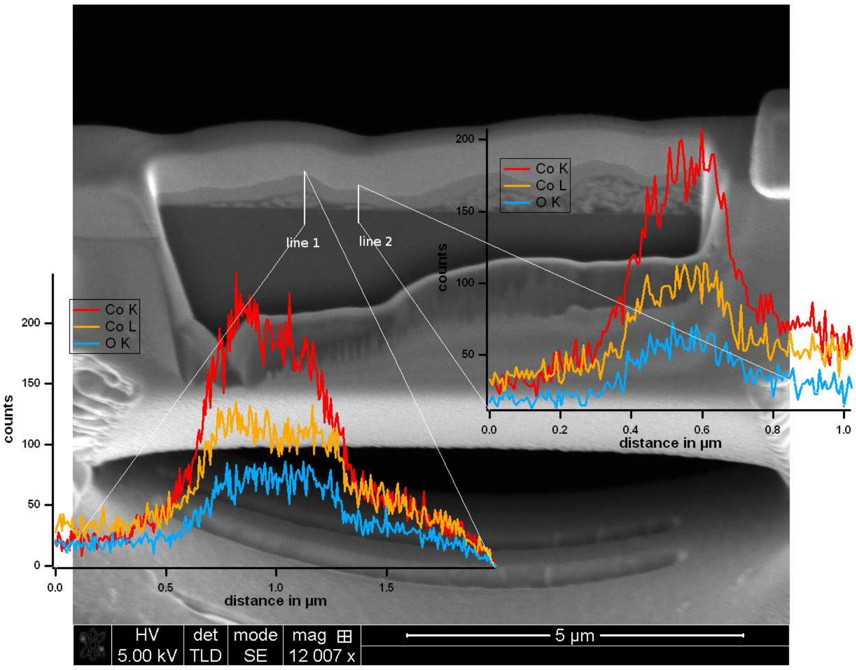

Figure 11.4: Linescans over particleclusters

The linescans are depicted in image 11.4. The counts for the O K shell (blue curve) and the Co K (red curve) and L shell (yellow curve) are plotted over distance. The thickness of the particle clusters can be estimated from the linescans by a strong increase of the counts for the oxygen and the cobalt signals. The cluster investigated by line 1 is about 0.68 µm thick and the cluster examined by linescan line 2 has a thickness of about 0.35 µm at the location of the linescan. Both linescans show a concurrent increase of the oxygen and cobalt signal [3]. This is a clear evidence that this particle cluster is oxidized uniformly.

From the second old sample, a larger cluster was chosen. Linescans and an element map were taken.
An SEM image of the lamella of the cluster and the element maps are displayed in figure

---

[1] in air, at room temperature, at normal pressure

[2] For a detailed description see chapter 5.4 particles prepared with oleylamine.

[3] An increase in the oxygen counts occurs simultaneously to an increase in the cobalt counts.

11.5 and figure 11.6. Image 11.5 shows the SEM image and the overall distribution of cobalt and oxygen. The distribution of the other elements are displayed in image 11.6. The element distribution resulting from sputtering and redeposition of sample material can be deduced from these images as well as further pollution for instance from redeposited material from the sample holder. The particles in the clusters are cobalt discs (and a few spheres) with a mean diameter ⟨D⟩= 11.86 nm ± 2.6 nm [4].

In picture 11.5 a SEM image of the sample and the element maps for cobalt and oxygen are shown. In the electron image the particle cluster is visible in the middle of the lamella. It can be clearly distinguished from the darker surrounding material consisting mainly of platinum from the covering layer applied prior to the etching process and silicon from the wafer used as a substrate for the sample preparation.
The cobalt and the oxygen signals are emitted from the same area. Not much difference in relative intensity is noticeable between those elements, which leads again to the conclusion that this cluster is oxidized completely.

In picture 11.6 the obtained maps for other elements are displayed. It should be mentioned that the part of the cluster exposed to air during the aging process points to the bottom of the image, while the silicon wafer is facing the top of the image. Silicon can be found mainly in the bottom part of the lamella while the platinum signal is stronger on the top and the sides of the particle cluster. Copper and aluminum are distributed over the whole sample but are more prominent in the layer surrounding the particles. These elements did not occur in the sample and were deposited during the preparation of the lamella as contamination from the stage and the semicircular sample holder. Carbon can be found mainly in and on top of the cluster. The carbon inside the cluster is a result of the surfactants that were used to stabilize the particles. The other amount of carbon is a result of the carbon deposition during electron and ion imaging and processing. Gallium ions are used for etching and depositing. They are mainly incorporated in deposited layers and layers build by backsputtered material.

Three linescans werer taken over the height of the cluster. They are displayed in images 11.7, 11.8 and 11.9. The beginning and end of the particle cluster is clearly visible by an increase and drop in the count rates of Co and O. All linescans show correlation with the element distribution obtained from the element map. A decrease in the cobalt signal occurs simultaneously to a decrease in the oxygen signal. In picture 11.7 a thinner part in the sample is clearly visible and can be found in the linescan by a decrease of counts of the Co (and O) signal. The larger count values at the bottom of the cluster can be explained by a slightly tapered shape of the lamella.

It can be summarized that in older particle cluster all particles are oxidized. In the long term no different oxidation states could be observed between the particles on the top and at the bottom of the cluster.

---

[4] For a detailed description see chapter 6.3 particles prepared with oleylamine.

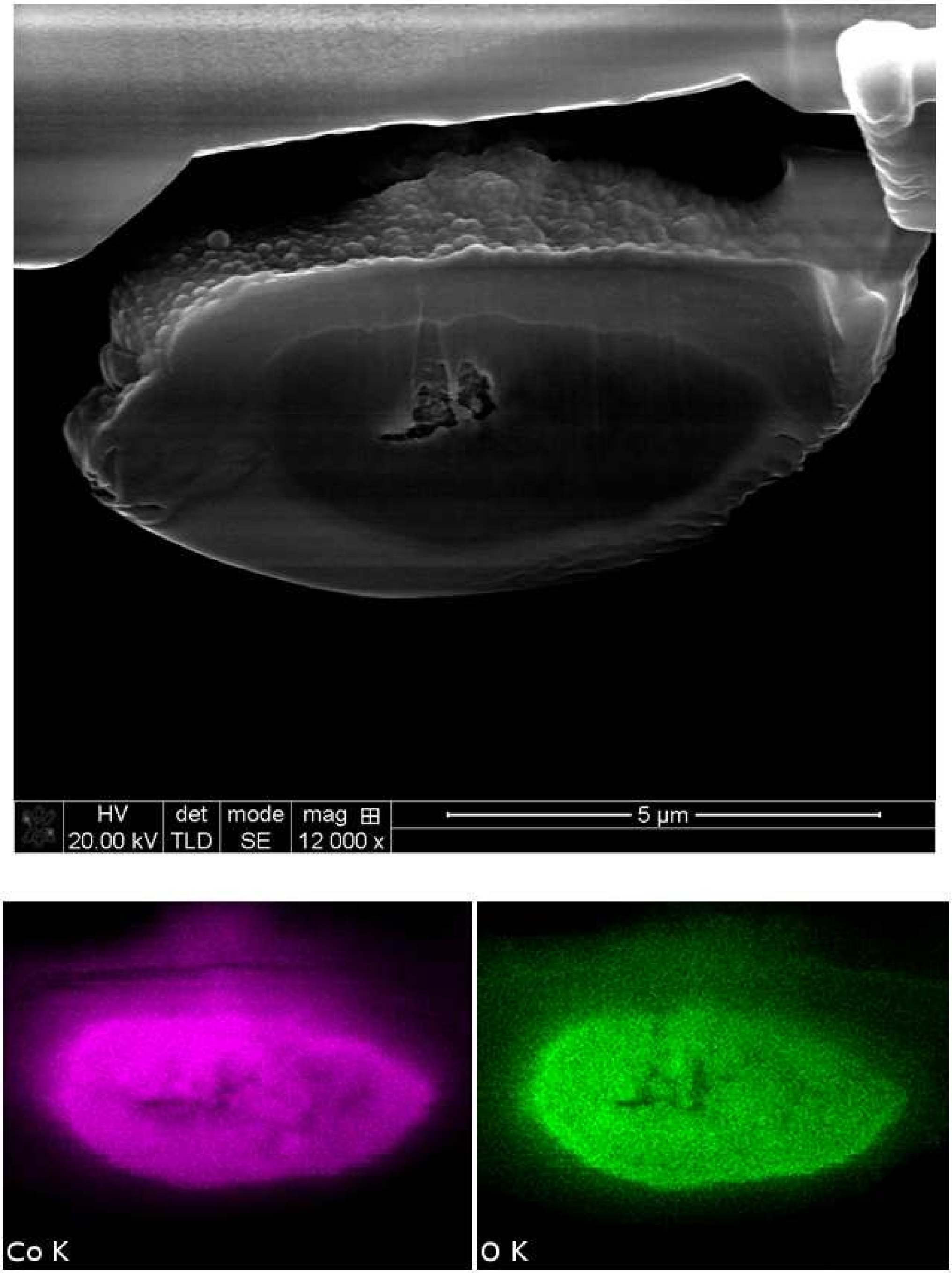

Figure 11.5: Element map: Co and O

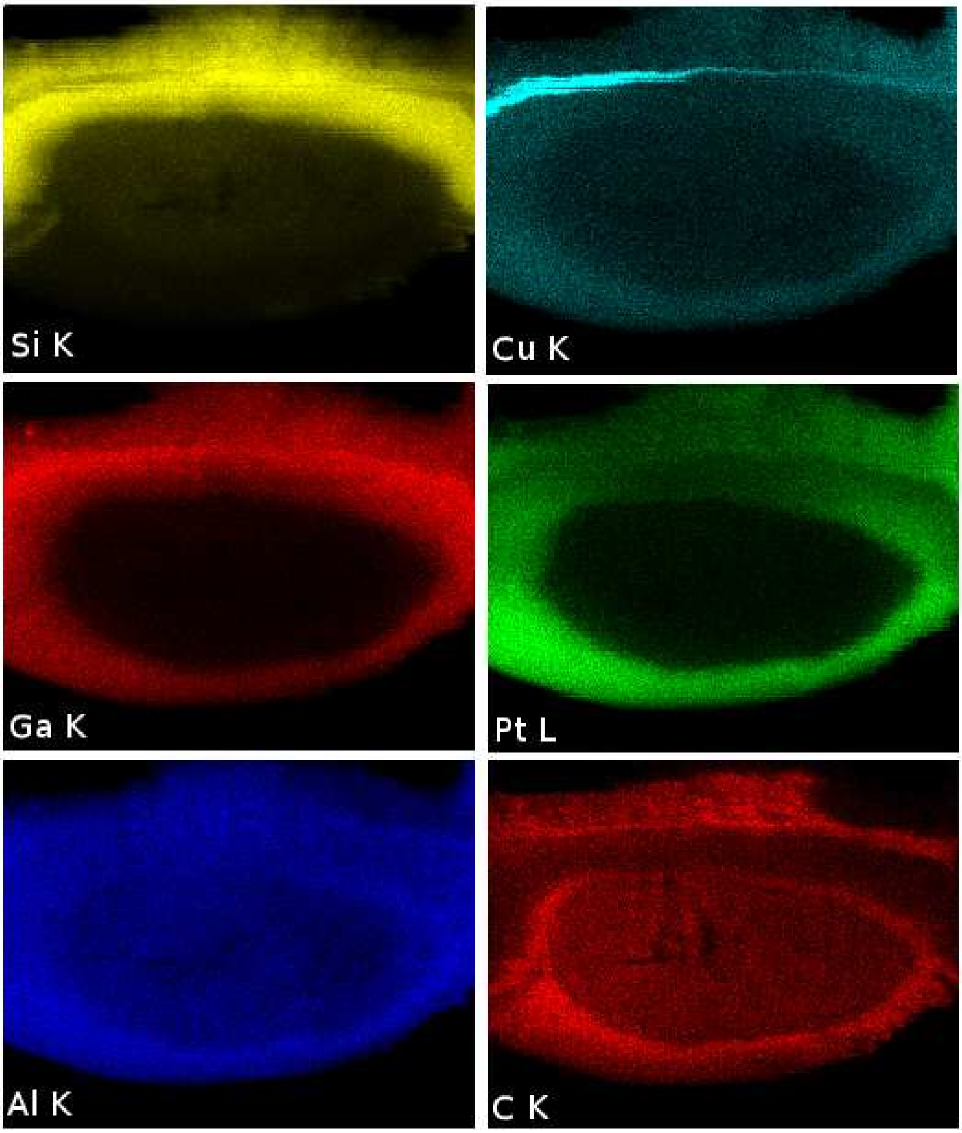

Figure 11.6: Element map: Other elements

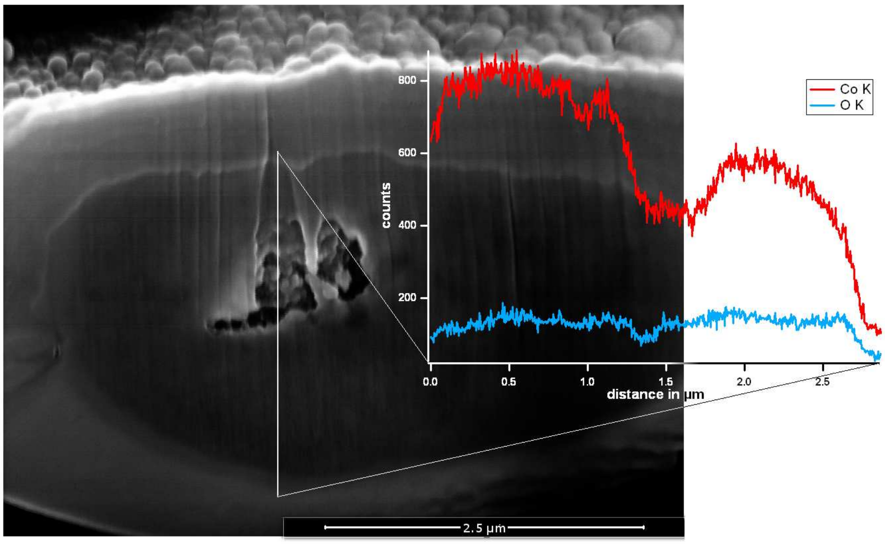

Figure 11.7: Linescans over particle clusters.

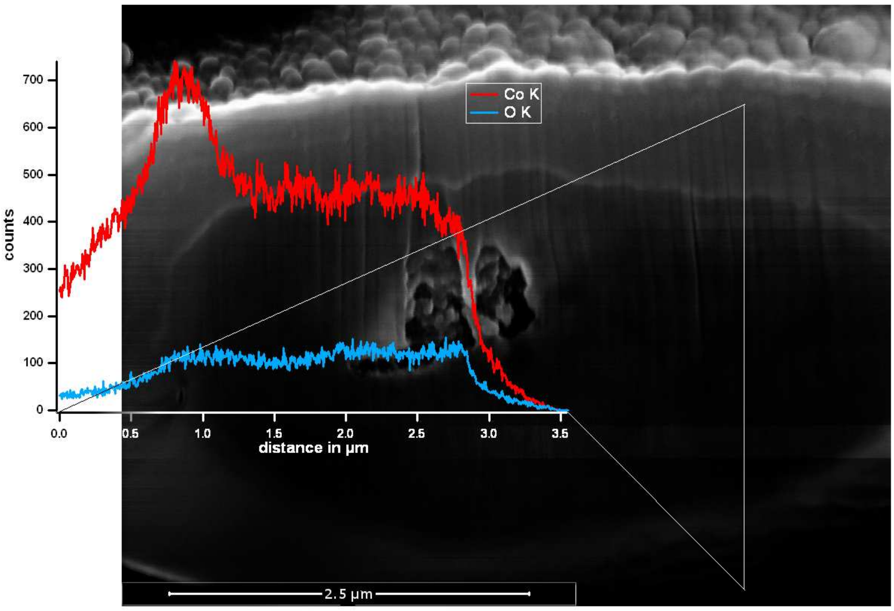

Figure 11.8: Linescan over particle clusters.

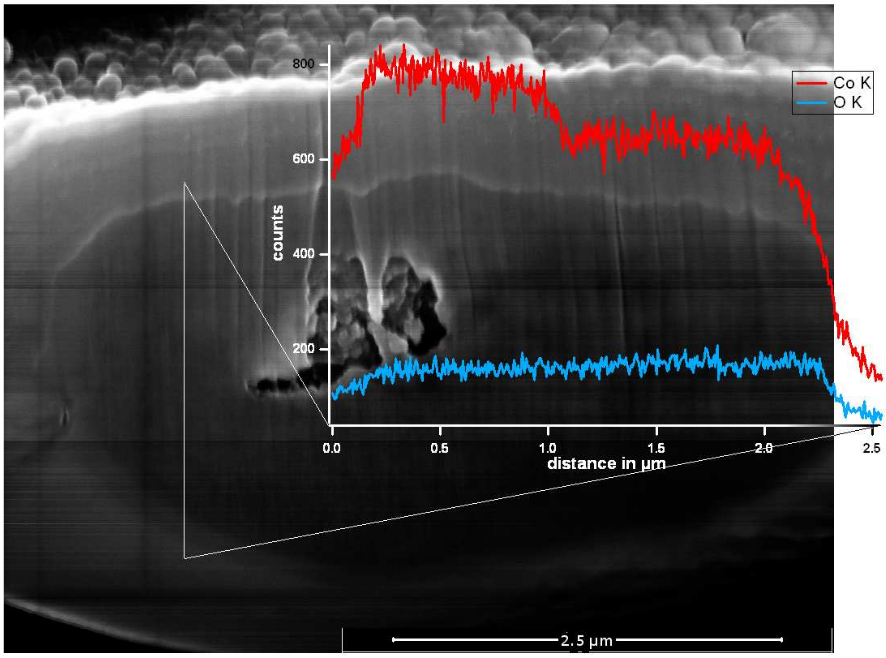

Figure 11.9: Linescan over particle clusters.

11.2 Newer Particles

A sample of fresh particles [5] was treated accordingly to the samples described in the previous section. A TEM lamella was prepared and the distribution of cobalt and oxygen was investigated by linescans. Four linescans were taken, the results are displayed in image 11.10 and image 11.11. Again the part of the cluster facing the air is directed towards the bottom of the image while the silicon wafer is on top of the image. The range of the Co particle cluster can be seen by contrast in the images and the increase and decrease in the cobalt counts of the linescans. It is clearly visible that the oxygen concentration is much higher in the part of the cluster that has faced the air and is very low on the bottom of the cluster, which is incongruent to the cobalt signal. Therefore it can be deduced that these cluster is not oxidized completely, which corresponds well to the oxidation curves obtained through measurements with the AGM.

This shows that this method can be used to observe the oxidation of particles inside of a large cluster and the progression of oxygen through the cluster, because the particles are prevented from further oxidation by deposition of platin on both sides of the lamella during change of sample holders. It shows that large clusters do not oxidize homogeneously, but from top to bottom and that this effect would have to be taken into account for further investigations if particle clusters have formed on the samples.

---

[5] a few days old

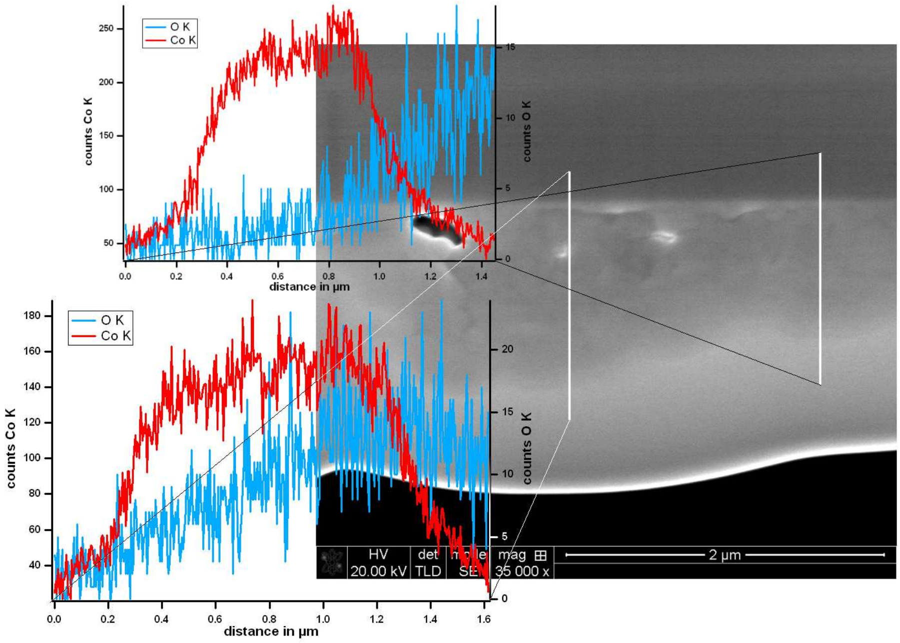

Figure 11.10: Linescans over particle clusters.

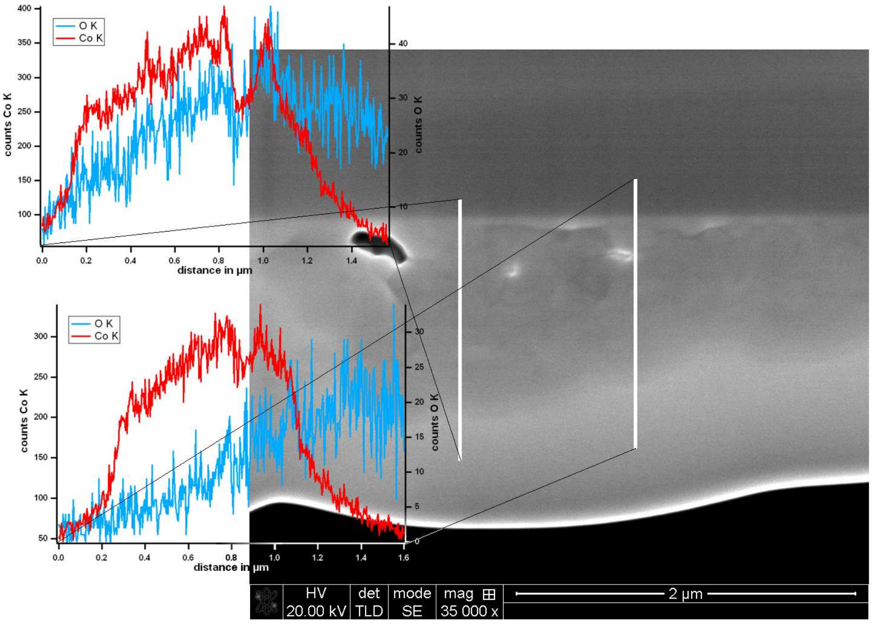

Figure 11.11: Linescans over particle clusters.

11.3 Calculation of the effective oxygen diffusion parameters in nanoparticles clusters

The nanoparticle clusters (examples are depicted in figures 11.1 and 11.2) are simplified as cuboids, see figure 11.12. This simplification leads to an error resulting from the reduced surface in the case of the cuboid compared to the original sample.

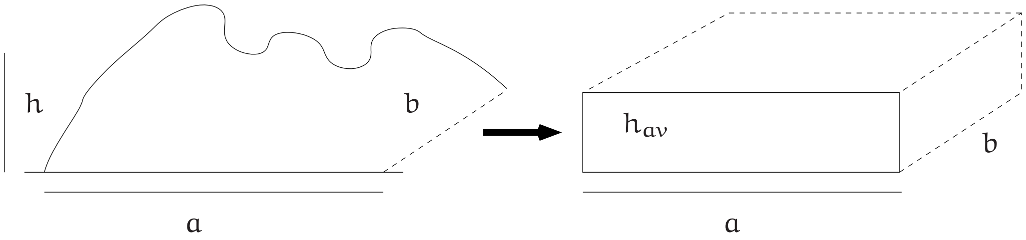

Figure 11.12: Schematic drawing of a cluster and the corresponding cuboid of width a, length b and average height $h_{a}v$.

11.3.1 Oxygen diffusion process in the case of one nanoparticle

The theory of oxidation in terms of the processes that drive the oxidation in the case of one nanoparticle is described in detail in section 2.3. A further look at the effects of the initially oxygen coverage is taken in section 9.4. After about 100 days a 1.3 nm to 2.3 nm thick passivating oxide layer has formed on the particles. The remaining magnetic moment consists of contributions of the cobalt core and the CoO shell.

Here a closer look at the oxygen diffusion is taken.

A short overview over the theory of the diffusion process in a sphere with constant surface concentration is given in the following paragraph. The diffusive mass flux J is related to the diffusivity D and the concentration gradient ∇C by Fick's first law of diffusion

$$\vec{J} = -D\nabla C \tag{11.1}$$

with J: mass flux, D: diffusivity, C: concentration of diffusing component.
Fick's second law of diffusion for constant diffusivity D describes the change of the concentration with time [90].

$$D(\nabla \cdot \nabla C) = \frac{\partial C}{\partial t} \tag{11.2}$$

For spherical geometry and radial diffusion the equation changes to

$$\frac{\partial C}{\partial t} = D\left(\frac{\partial^2 C}{\partial r^2} + \frac{2}{r}\frac{\partial C}{\partial r}\right) \quad . \tag{11.3}$$

Putting $u = Cr$ the equation becomes

$$u = Cr \rightsquigarrow \frac{\partial u}{\partial t} = D\frac{\partial^2 u}{\partial r^2} \quad , \tag{11.4}$$

which describes the linear flow in one dimension [90,91]. Let the surface concentration C_0 be constant, it can be described with an initial distribution function $f(r)$.
The applied boundary conditions are

$$\begin{aligned} u &= 0 \quad r = 0 \quad t > 0 && (11.5)\\ u &= aC_0 \quad r = a \quad t > 0 && (11.6)\\ u &= rf(r) \quad t = 0 \quad 0 < r < a \quad . && (11.7)\end{aligned}$$

The sphere is initially at concentration $C_1 = 0$ and $C = 0$, $t = 0$ and the surface concentration is maintained constant at C_0, $t > 0$ during the whole process. The case of an existing monolayer of oxide at the particle surface resulting from the coverage with surfactants is neglected in the first instance. The solution becomes

$$\frac{C - C_1}{C_0 - C_1} = 1 + \frac{2a}{\pi r} \sum_{n=1}^{\infty} \frac{(-1)^n}{n} \sin \frac{n\pi r}{a} \exp\left(-\frac{Dn^2\pi^2 t}{a^2}\right) \tag{11.8}$$

with C_1: initial uniform concentration of the diffusing substance in the sphere, C_0: surface concentration maintained constant, a: radius of the sphere and C: concentration of the diffusing substance during the progress [91]. [6] The total amount of substance M_t diffused into the sphere at time t is given by

$$\frac{M_t}{M_\infty} = 1 - \frac{6}{\pi^2} \sum_{n^1}^{\infty} \frac{1}{n^2} \exp\left(-n^2\pi^2 t \frac{D}{a^2}\right) \tag{11.9}$$

with M_∞: maximal diffused substance in the case of $t \to \infty$.
In the case of a sphere with radius a and constant surface concentration C_0, this leads to

$$F = 8\pi a D C C_0 \sum_{n=1}^{\infty} \frac{ka^2 + Dn^2\pi^2 \exp\left(-t\left(k + Dn^2\frac{\pi^2}{a^2}\right)\right)}{ka^2 + Dn^2\pi^2} \tag{11.10}$$

with F: rate of uptake.
The total amount of diffusing substance M_t expressed by the rate of uptake F is given by

$$M_t = \int_0^t F dt' \quad . \tag{11.11}$$

For the simplest approach with $n = 1$, equation 11.10 becomes

$$F = 8\pi a D C_0 \frac{ka^2 + D\pi^2 \exp\left(-t\left(k + D\frac{\pi^2}{a^2}\right)\right)}{ka^2 + D\pi^2} \quad . \tag{11.12}$$

---

[6]

$$C = k\int_0^t C_l e^{-kt'} dt' + C_l e^{-kt}$$

C_l is solution of $\frac{\partial C_l}{\partial t} = D\frac{\partial^2 C_l}{\partial r^2}$ linear flow in one dimension.

$$\int_0^t C(x,t) dx = M$$

M: amount of diffused substance.

Solving the integral leads to

$$\begin{aligned}
M_t &= \int_0^t 8\pi a D C_0 \frac{ka^2+D\pi^2 \exp\left(-t'\left(k+D\frac{\pi^2}{a^2}\right)\right)}{ka^2+D\pi^2} dt' && (11.13)\\
&= \frac{8\pi a D C_0}{ka^2+D\pi^2}\left[\int_0^t ka^2 dt' + \int_0^t e^{-t'\left(k+D\frac{\pi^2}{a^2}\right)} dt'\right] && (11.14)\\
&= \frac{8\pi a D C_0}{ka^2+D\pi^2}\left[ka^2 t - \frac{D\pi^2}{k+D\frac{\pi^2}{a^2}} e^{-t\left(k+D\frac{\pi^2}{a^2}\right)} + \frac{D\pi^2}{k+D\frac{\pi^2}{a^2}}\right] && (11.15)\\
&= \frac{8\pi a D C_0}{{}_{k}a^2+D\pi^2}\left[ka^2 t + \frac{D\pi^2}{k+D\frac{\pi^2}{a^2}}\left(1-e^{-t\left(k+D\frac{\pi^2}{a^2}\right)}\right)\right] && (11.16)\\
&= \frac{8\pi a^3 D k C_0}{ka^2+D\pi^2} t + \frac{8\pi^3 a D^2 C_0}{a^2\left(k+D\frac{\pi^2}{a^2}\right)^2}\left(1-e^{-t\left(k+D\frac{\pi^2}{a^2}\right)}\right) && (11.17)
\end{aligned}$$

with D: diffusivity, C_0: surface concentration, k.

The measured data are fitted by the following function

$$M_t = C_1 t + C_2\left(1-e^{-C_3 t}\right) \tag{11.18}$$

with the fitting coefficients

$$C_1 = \frac{8\pi a^3 D k C_0}{ka^2 + D\pi^2} \quad , \tag{11.19}$$

$$C_2 = \frac{8\pi^3 a D^2 C_0}{k^2 a^2 + 2D\pi^2 k + D^2\frac{\pi^4}{a^2}} = \frac{8\pi^3 a D^2 C_0}{a^2\left(k+\frac{\pi^4}{a^2}\right)^2} \tag{11.20}$$

and

$$C_3 = k + D\frac{\pi^2}{a^2} \quad . \tag{11.21}$$

An example is shown in figure 11.16.

The desired parameters $D(T)$, C_0[7] and k can be calculated from the fitting coefficients C_1, C_2, C_3 and sample dependent value a ($\hat{=}$ particle radius) by following equations:

$$D(T) = \frac{a^2}{\pi^2}\frac{C_3^2 C_2}{C_2 C_3 + C_1} \qquad (\left[\frac{m^2}{s}\right]) \quad , \tag{11.22}$$

$$C_0 = \frac{\pi\left(C_2 C_3 + C_1\right)^2}{8a^3 C_2 C_3^2} \qquad (\left[\frac{kmol}{m^3}\right]) \quad (\left[\frac{1}{m^3}\right]) \tag{11.23}$$

and

$$k = \frac{C_1 C_3}{C_2 C_3 + C_1} \qquad (\left[\frac{1}{s}\right]) \quad . \tag{11.24}$$

To estimate the pre-exponential factor D_0 and the diffusion activation energy Q, the obtained values of $D(T)$ are plotted over the inverse of the temperature $\left(\frac{1}{T}\right)$ in an Arhenius-type diagram as depicted in figure 11.17 and fitted with the function

$$f(x) = D_0 e^{-\frac{Qx}{k_B}} \tag{11.25}$$

with $x = \frac{1}{T}$.

---

[7] In this case $C = 0$ is the surface concentration of oxygen of the whole sample and not the surface concentration of oxygen per particle.

11.3.2 Oxidation process in the case of nanoparticle clusters

For the diffusion in particle clusters, the diffusion in particles and in between particles have to be taken into account.

Since no direct data for single particles were obtained, different possible forms of diffusion within each particle such as bulk and grain boundary diffusion (in the case of multigrain particles consisting of several crystallites) [92] are not investigated separately.
Generally, a diffusion process consisting of two separate diffusion processes can be approximated by an effective diffusion.
Two equations are widely used to describe the effective diffusion in multigrain materials with diffusivity D_{eff}.
The Hart equation

$$D_{eff} = gD_{gb} + (1-g)D_{l} \tag{11.26}$$

(with g: volume fraction of grain boundaries, D_{gb}: grain boundary diffusivity, D_{l}: bulk diffusivity) describes the upper limit for the diffusivity for a parallel arrangement of grain boundaries and grains.
The lower limit for the effective diffusivity corresponds to an alternating arrangement of grain boundaries and grains in the direction of diffusion and is described by

$$D_{eff} = \frac{D_{gb}D_{l}}{gD_{l} + (1-g)D_{gb}} \quad . \tag{11.27}$$

For nanocrystalline materials three diffusion processes are described: D_{b}: grain-boundary, D_{v}: bulk in coarse-grained materials, D_{c}: cluster boundary diffusion. At low temperatures the bulk diffusion D_{v} may be neglected, which leads to the D_{n}: effective diffusivity in nanomaterials described by

$$D_{n} = f_{c}D_{c} + f_{b}D_{b} \quad , \tag{11.28}$$

where f_{c} and f_{b} are the fractions of different types of boundaries [92].

Here only the effective diffusion will be examined.

As the measurements of the magnetic moment used for the calculation of the effective diffusion parameters start about half a day after the first exposure to air, the first reaction of chemisorption of oxygen at the top layers particle surfaces, is already finished and the incorporation of oxygen into the particles and the oxidation in this layer is already in progress. A drawing of the oxidation processes and their progress is shown in figure 11.13. The resulting decrease of the saturation magnetic moment makes it impossible to detect a possible occurring induced magnetic moment in phyisorbed oxygen atoms at particle surfaces in the "bulk" of the cluster. Therefore only an effective decrease of the saturation magnetic moment can be measured.
The simplified oxidation progress in the cluster is depicted in figure 11.14. For the calculation, the assumptions of the highly simplified oxidation behaviour of the cluster displayed in figure 11.15 are made. Further has the oxidation of all spheres in the cluster (as described in section 11.3.1) to be taken into account. The diffusion process in between the particles is neglected in this first approach. Only an effective diffusion process is examined. The amount of cobalt on each sample has to be calculated, that one is able able to determine the amount of diffused oxygen. The decrease of the saturation magnetic moment is

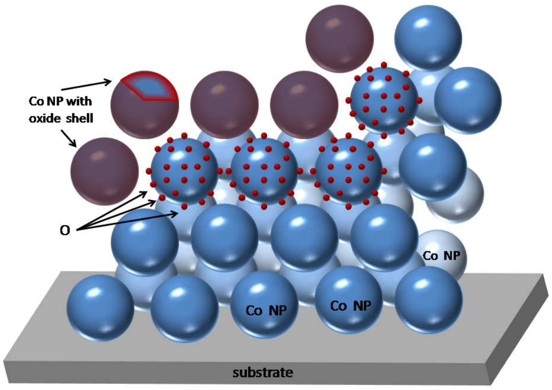

Figure 11.13: Schematic detailed drawing of the oxidation process in a nanoparticle cluster.

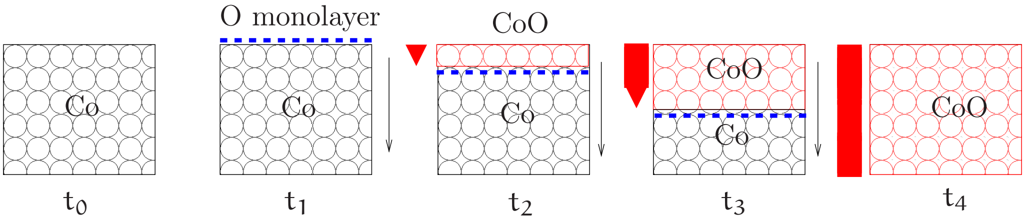

Figure 11.14: Schematic simplified drawing of the oxidation process in a nanoparticle cluster. The blue dotted line denotes the oxygen atoms attached to the particle surface. A front of chemisorbed oxygen atoms moves through the sample if sufficient space in between the particles exists, which can be assumed as a result of the coverage with surfactants. The red particles are oxidized, with a oxygen concentration gradient, depicted by the red arrow/bar, with decrease from the top of the layer towards the oxygen front. The black cobalt particles are unoxidized. The different points in time are denoted by t_0 to t_4.

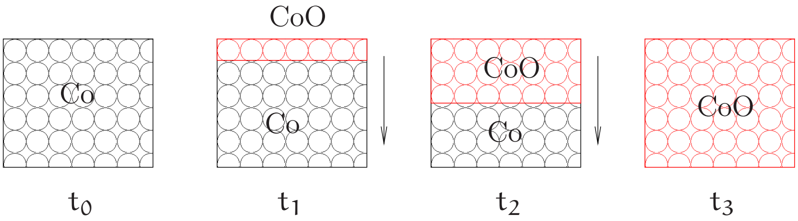

Figure 11.15: Schematic drawing of the further simplified oxidation process in nanoparticle clusters as assumed for the calculations The black particles are unoxidized. The red particles are assumed to be uniformly oxidized with no oxygen concentration gradient from top to bottom. The different points in time are denoted by t_0 to t_3.

proportional to the oxidation and uptake of oxygen of the cobalt particles. The function of $1-\frac{m(t)}{m_0}$ is related to the amount of diffused oxygen M_t in the sample.

$$1-\frac{m(t)}{m_0}\mathrel{\hat{=}}\frac{M_t}{M_\infty} \tag{11.29}$$

It is assumed that the diffused oxygen leads to an instantaneous oxidation of previously unoxidized cobalt atoms, see section 9.4. The oxidation process is assumed to be fast compared to the diffusion process, therefore diffusion in CoO is assumed and not in Co. Hence it is possible to calculate the amount of uptaken oxygen from the curves, if the initially existing amount of cobalt is known.

The amount of Co on the samples can be calculated from the amount of $Co_2(CO)_8$ used for particle preparation. A conversion of 92.67% of the employed amount of cobalt into nanoparticles is described in [29].
In our experiment[8] 55 mg TOPO and 100 mg $Co_2(CO)_8$ were dissolved in 2.5 mL 1,2-dichlorbenzene, which equals a total amount of 0.069 g Co in 2.5 mL 1,2-dichlorbenzene. The cobalt concentration is 27.6 $\frac{mg}{mL}$.
If a transformation rate of 90% is assumed, a cobalt concentration of 24.84 $\frac{mg}{mL}$ exists after washing of the particles.
Each AGM sample, where 2 μL of the particle suspension were dropcasted onto a piece of wafer, contains 49.68 μg of pure cobalt. This is the assumed amount of cobalt for the initially prepared particles stabilized with TOPO. If it is regarded that during the surfactant exchange cobalt is removed from the particles [9] and discarded during washing [10] the loss of cobalt has to be calculated. The calculated volume, the volume reduction factor and the amount of cobalt per sample are displayed in table 11.1. In the case of the maximum appeared volume reduction (d=12.15 nm and V=939.13 nm^3 (TOPO) to d=10.37 nm and V=583.90 nm^3 (tridecanoic acid)) an additional loss of 37.83% of cobalt occurs. The amount of cobalt in μmol is equal to the maximum possible uptake of oxygen for the case of formation of CoO.[11]
For the calculation of D, C_0 and k the radius of the particles contributes. The amount of material has to be changed although, because otherwise in the case of smaller particles the number of particles would grow.

An example of the data and the fitted function is displayed in figure 11.16.

The calculated diffusion parameters and the corresponding amount of cobalt per sample (and maximum possible amount of oxygen per sample in the case of complete oxidation of Co to CoO) for temperatures of ~ $21°C$, $48°C$ $80°C$ $121°C$ and $180°C$ are displayed in tables 11.2 to 11.6. The data obtained from the samples stored at $-18°C$ are not investigated because of the influence of the exposure to room temperature during measurements.

The values for $D(T)$ are plotted over the inverse of the temperature and fitted with the function described in equation 11.25 as depicted in figure 11.17.

The obtained values for the pre-exponential factor D_0 and the activation energy Q are displayed in table 11.7.

---

[8] for the particles that were investigated in the first part of section 5.1

[9] and therefore from each particle equally as described in section 5

[10] and does not form new particles or is reattached

[11] CoO contains an equal amount of Co and O atoms.

surfactant	volume $10^{-27}\mathrm{m}^3$	reduction factor	m_{cobalt} [µg]	cobalt [µmol]
TOPO	939.134	1.00	49.68	1.77
triethylamine	855.923	0.91	45.21	1.61
octylamine	929.889	0.99	49.15	1.76
dioctylamine	798.407	0.85	42.23	1.51
trioctylamine	687.450	0.73	36.27	1.29
tetraoctylamm. bromide	693.116	0.74	36.76	1.31
dodecylamine	1005.570	1.07	~~53.18~~ 49.68	1.77
octadecylamine	679.944	0.72	35.77	1.28
oleylamine	731.685	0.78	38.75	1.38
nonanoic acid	620.091	0.66	32.79	1.17
tridecanoic acid	583.895	0.62	30.80	1.10
oleic acid	655.926	0.70	34.78	1.24
hexacosanoic acid	706.457	0.75	37.26	1.33
4-biphenylacetic acid	759.518	0.81	40.24	1.44
1-pyrenebutyric acid	641.431	0.68	33.78	1.21

Table 11.1: Reduced volume, volume reduction factor and amount of cobalt per 4 µl particle suspension. The enlarged value (striked out in the table) in the case of particles stabilized with dodecylamine, was replaced by the value for the initially prepared particles as no cobalt was added during the surfactant exchange. A dissolution of same particles and attachment of free atoms to other particles offers an explanation for the enlarged radius at a constant amount of cobalt.

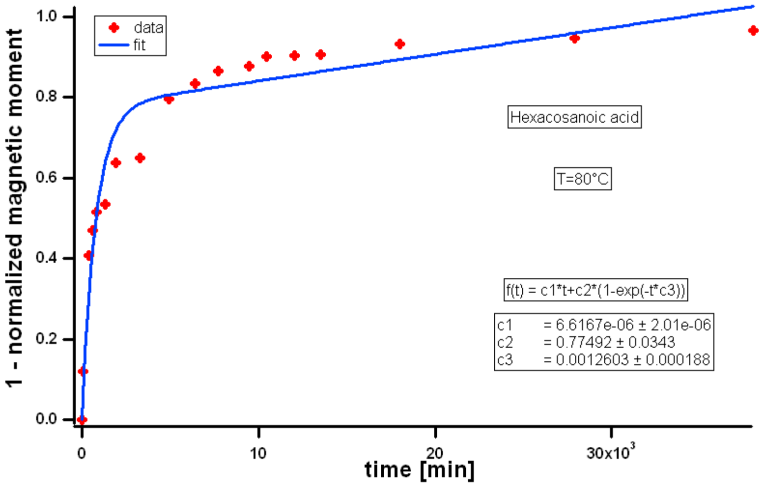

Figure 11.16: Fit of the function described in equation 11.18 to the 1-(normalized saturation magnetic moment) drawn over time, for a sample stored at 80°C.

surfactant	D $\left[\frac{m^2}{s}\right]$	C_0 $\left[\frac{1}{m^3}\right]$	$C_0\vert O$ $\left[\frac{mol}{m^3}\right]$	k $\left[\frac{1}{s}\right]$
TOPO	$2.539 \cdot 10^{-23}$	$2.838 \cdot 10^{23}$	$5.0233 \cdot 10^{17}$	$2.521 \cdot 10^{-7}$
triethylamine	$9.048 \cdot 10^{-24}$	$2.622 \cdot 10^{23}$	$4.221 \cdot 10^{17}$	$1.918 \cdot 10^{-7}$
octylamine	$2.379 \cdot 10^{-23}$	$2.723 \cdot 10^{23}$	$4.792 \cdot 10^{17}$	$1.540 \cdot 10^{-7}$
dioctylamine	$1.633 \cdot 10^{-23}$	$2.233 \cdot 10^{23}$	$3.372 \cdot 10^{17}$	$5.383 \cdot 10^{-7}$
trioctylamine	$9.106 \cdot 10^{-27}$	$3.846 \cdot 10^{25}$	$4.961 \cdot 10^{19}$	$2.611 \cdot 10^{-8}$
tetraoctylammonium bromide	$1.017 \cdot 10^{-23}$	$6.767 \cdot 10^{23}$	$8.865 \cdot 10^{17}$	$6.780 \cdot 10^{-8}$
dodecylamine	$9.043 \cdot 10^{-23}$	$1.368 \cdot 10^{24}$	$2.421 \cdot 10^{18}$	$4.275 \cdot 10^{-8}$
octadecylamine	$2.365 \cdot 10^{-23}$	$2.693 \cdot 10^{23}$	$3.447 \cdot 10^{17}$	$2.062 \cdot 10^{-7}$
oleylamine	$4.623 \cdot 10^{-24}$	$5.210 \cdot 10^{23}$	$7.190 \cdot 10^{17}$	$7.484 \cdot 10^{-8}$
nonanoic acid	$6.428 \cdot 10^{-23}$	$2.709 \cdot 10^{23}$	$3.170 \cdot 10^{17}$	$4.760 \cdot 10^{-7}$
tridecanoic acid	$1.103 \cdot 10^{-23}$	$2.396 \cdot 10^{23}$	$2.636 \cdot 10^{17}$	$3.304 \cdot 10^{-7}$
oleic acid	$8.442 \cdot 10^{-24}$	$2.206 \cdot 10^{23}$	$2.735 \cdot 10^{17}$	$1.367 \cdot 10^{-7}$
hexacosanoic acid	$3.528 \cdot 10^{-27}$	$1.029 \cdot 10^{26}$	$1.369 \cdot 10^{20}$	$1.567 \cdot 10^{-8}$
4-biphenylacetic acid	$3.924 \cdot 10^{-23}$	$1.494 \cdot 10^{23}$	$2.151 \cdot 10^{17}$	$4.900 \cdot 10^{-7}$
1-pyrenebutyric acid	$2.324 \cdot 10^{-23}$	$2.676 \cdot 10^{23}$	$3.238 \cdot 10^{17}$	$3.138 \cdot 10^{-7}$

Table 11.2: Calculated diffusivity for T=21°C.

surfactant	D $\left[\frac{m^2}{s}\right]$	C_0 $\left[\frac{1}{m^3}\right]$	$C_0\vert O$ $\left[\frac{mol}{m^3}\right]$	k $\left[\frac{1}{s}\right]$
TOPO	$3.116 \cdot 10^{-23}$	$4.775 \cdot 10^{23}$	$8.452 \cdot 10^{17}$	$1.312 \cdot 10^{-7}$
triethylamine	$1.290 \cdot 10^{-22}$	$4.904 \cdot 10^{23}$	$7.895 \cdot 10^{17}$	$2.816 \cdot 10^{-7}$
octylamine	$3.013 \cdot 10^{-23}$	$2.181 \cdot 10^{23}$	$3.839 \cdot 10^{17}$	$1.557 \cdot 10^{-7}$
dioctylamine	$1.094 \cdot 10^{-22}$	$2.557 \cdot 10^{23}$	$3.861 \cdot 10^{17}$	$7.329 \cdot 10^{-7}$
trioctylamine	$8.735 \cdot 10^{-23}$	$8.947 \cdot 10^{23}$	$1.154 \cdot 10^{18}$	$6.575 \cdot 10^{-8}$
tetraoctylammonium bromide	$3.392 \cdot 10^{-23}$	$3.292 \cdot 10^{23}$	$4.313 \cdot 10^{17}$	$5.615 \cdot 10^{-7}$
dodecylamine	$1.944 \cdot 10^{-22}$	$3.565 \cdot 10^{23}$	$6.310 \cdot 10^{17}$	$3.285 \cdot 10^{-7}$
octadecylamine	$9.893 \cdot 10^{-23}$	$4.501 \cdot 10^{23}$	$5.761 \cdot 10^{17}$	$5.222 \cdot 10^{-7}$
oleylamine	$6.289 \cdot 10^{-23}$	$2.828 \cdot 10^{23}$	$3.903 \cdot 10^{17}$	$1.206 \cdot 10^{-7}$
nonanoic acid	$1.393 \cdot 10^{-22}$	$6.585 \cdot 10^{23}$	$7.704 \cdot 10^{17}$	$1.473 \cdot 10^{-7}$
tridecanoic acid	$1.825 \cdot 10^{-22}$	$7.809 \cdot 10^{23}$	$8.590 \cdot 10^{17}$	$1.584 \cdot 10^{-7}$
oleic acid	$3.845 \cdot 10^{-23}$	$7.922 \cdot 10^{23}$	$9.823 \cdot 10^{17}$	$6.611 \cdot 10^{-8}$
hexacosanoic acid	$2.012 \cdot 10^{-23}$	$6.012 \cdot 10^{23}$	$7.996 \cdot 10^{17}$	$2.025 \cdot 10^{-7}$
4-biphenylacetic acid	$2.322 \cdot 10^{-22}$	$5.302 \cdot 10^{23}$	$7.635 \cdot 10^{17}$	$1.496 \cdot 10^{-7}$
1-pyrenebutyric acid	$1.661 \cdot 10^{-22}$	$8.487 \cdot 10^{23}$	$1.027 \cdot 10^{18}$	$1.294 \cdot 10^{-7}$

Table 11.3: Calculated diffusivity for T=48°C.

surfactant	D $\left[\frac{m^2}{s}\right]$	C_0 $\left[\frac{1}{m^3}\right]$	$C_0\vert O$ $\left[\frac{mol}{m^3}\right]$	k $\left[\frac{1}{s}\right]$
TOPO	$8.025 \cdot 10^{-23}$	$1.140 \cdot 10^{24}$	$2.018 \cdot 10^{18}$	$2.599 \cdot 10^{-7}$
triethylamine	$7.143 \cdot 10^{-23}$	$1.457 \cdot 10^{24}$	$2.346 \cdot 10^{18}$	$1.508 \cdot 10^{-7}$
octylamine	$1.016 \cdot 10^{-22}$	$9.806 \cdot 10^{23}$	$1.756 \cdot 10^{18}$	$3.657 \cdot 10^{-7}$
dioctylamine	$1.074 \cdot 10^{-22}$	$1.403 \cdot 10^{24}$	$2.119 \cdot 10^{18}$	$2.241 \cdot 10^{-7}$
trioctylamine	$4.342 \cdot 10^{-23}$	$1.727 \cdot 10^{24}$	$2.228 \cdot 10^{18}$	$1.641 \cdot 10^{-7}$
tetraoctylammonium bromide	$5.013 \cdot 10^{-23}$	$1.876 \cdot 10^{24}$	$2.458 \cdot 10^{18}$	$1.375 \cdot 10^{-7}$
dodecylamine	$8.167 \cdot 10^{-23}$	$1.136 \cdot 10^{24}$	$2.011 \cdot 10^{18}$	$2.183 \cdot 10^{-7}$
octadecylamine	$1.153 \cdot 10^{-22}$	$1.691 \cdot 10^{24}$	$2.14 \cdot 10^{18}$	$1.983 \cdot 10^{-7}$
oleylamine	$8.475 \cdot 10^{-23}$	$1.436 \cdot 10^{24}$	$1.982 \cdot 10^{18}$	$2.391 \cdot 10^{-7}$
nonanoic acid	$8.788 \cdot 10^{-23}$	$2.170 \cdot 10^{24}$	$2.539 \cdot 10^{18}$	$1.763 \cdot 10^{-7}$
tridecanoic acid	$6.611 \cdot 10^{-23}$	$2.302 \cdot 10^{24}$	$2.532 \cdot 10^{18}$	$1.239 \cdot 10^{-7}$
oleic acid	$6.181 \cdot 10^{-23}$	$2.004 \cdot 10^{24}$	$2.485 \cdot 10^{18}$	$1.195 \cdot 10^{-7}$
hexacosanoic acid	$6.453 \cdot 10^{-23}$	$1.829 \cdot 10^{24}$	$2.433 \cdot 10^{18}$	$1.414 \cdot 10^{-7}$
4-biphenylacetic acid	$3.575 \cdot 10^{-23}$	$1.683 \cdot 10^{24}$	$2.424 \cdot 10^{18}$	$1.399 \cdot 10^{-7}$
1-pyrenebutyric acid	$4.946 \cdot 10^{-23}$	$2.063 \cdot 10^{24}$	$2.496 \cdot 10^{18}$	$1.287 \cdot 10^{-7}$

Table 11.4: Calculated diffusivity for T=80°C.

surfactant	D $\left[\frac{m^2}{s}\right]$	C_0 $\left[\frac{1}{m^3}\right]$	$C_0\vert O$ $\left[\frac{mol}{m^3}\right]$	k $\left[\frac{1}{s}\right]$
TOPO	$4.913 \cdot 10^{-22}$	$1.671 \cdot 10^{24}$	$2.958 \cdot 10^{18}$	$8.671 \cdot 10^{-8}$
triethylamine	$5.200 \cdot 10^{-22}$	$1.837 \cdot 10^{24}$	$2.958 \cdot 10^{18}$	$1.440 \cdot 10^{-7}$
octylamine	$5.120 \cdot 10^{-22}$	$1.646 \cdot 10^{24}$	$2.897 \cdot 10^{18}$	$2.193 \cdot 10^{-7}$
dioctylamine	$4.819 \cdot 10^{-22}$	$1.965 \cdot 10^{24}$	$2.967 \cdot 10^{18}$	$9.053 \cdot 10^{-8}$
trioctylamine	$3.907 \cdot 10^{-22}$	$2.238 \cdot 10^{24}$	$2.887 \cdot 10^{18}$	$2.190 \cdot 10^{-7}$
tetraoctylammonium bromide	$4.232 \cdot 10^{-22}$	$2.332 \cdot 10^{24}$	$3.055 \cdot 10^{18}$	$5.616 \cdot 10^{-8}$
dodecylamine	$5.596 \cdot 10^{-22}$	$1.562 \cdot 10^{24}$	$2.765 \cdot 10^{18}$	$1.476 \cdot 10^{-7}$
octadecylamine	$4.455 \cdot 10^{-22}$	$2.312 \cdot 10^{24}$	$2.959 \cdot 10^{18}$	$1.540 \cdot 10^{-7}$
oleylamine	$3.756 \cdot 10^{-22}$	$2.118 \cdot 10^{24}$	$2.922 \cdot 10^{18}$	$1.138 \cdot 10^{-7}$
nonanoic acid	$4.196 \cdot 10^{-22}$	$2.606 \cdot 10^{24}$	$3.049 \cdot 10^{18}$	$6.222 \cdot 10^{-8}$
tridecanoic acid	$4.044 \cdot 10^{-22}$	$2.774 \cdot 10^{24}$	$3.051 \cdot 10^{18}$	$5.275 \cdot 10^{-8}$
oleic acid	$3.589 \cdot 10^{-22}$	$2.375 \cdot 10^{24}$	$2.945 \cdot 10^{18}$	$1.865 \cdot 10^{-7}$
hexacosanoic acid	$4.401 \cdot 10^{-22}$	$2.223 \cdot 10^{24}$	$2.957 \cdot 10^{18}$	$1.607 \cdot 10^{-7}$
4-biphenylacetic acid	$2.406 \cdot 10^{-22}$	$2.073 \cdot 10^{24}$	$2.985 \cdot 10^{18}$	$1.554 \cdot 10^{-7}$
1-pyrenebutyric acid	$3.202 \cdot 10^{-22}$	$2.441 \cdot 10^{24}$	$2.954 \cdot 10^{18}$	$1.771 \cdot 10^{-7}$

Table 11.5: Calculated diffusivity for T=121°C.

surfactant	D $\left[\frac{m^2}{s}\right]$	C_0 $\left[\frac{1}{m^3}\right]$	$C_0\|O$ $\left[\frac{mol}{m^3}\right]$	k $\left[\frac{1}{s}\right]$
TOPO	$8.545 \cdot 10^{-21}$	$1.521 \cdot 10^{+24}$	$2.692 \cdot 10^{18}$	$2.388 \cdot 10^{-5}$
triethylamine	$1.360 \cdot 10^{-20}$	$1.826 \cdot 10^{+24}$	$2.940 \cdot 10^{18}$	$2.507 \cdot 10^{-5}$
octylamine	$1.063 \cdot 10^{-20}$	$1.523 \cdot 10^{+24}$	$2.680 \cdot 10^{18}$	$4.835 \cdot 10^{-5}$
dioctylamine	$9.641 \cdot 10^{-21}$	$1.964 \cdot 10^{+24}$	$2.967 \cdot 10^{18}$	$1.644 \cdot 10^{-5}$
trioctylamine	$5.609 \cdot 10^{-21}$	$2.238 \cdot 10^{+24}$	$2.887 \cdot 10^{18}$	$2.554 \cdot 10^{-5}$
tetraoctylammonium bromide	$3.108 \cdot 10^{-20}$	$2.265 \cdot 10^{+24}$	$2.967 \cdot 10^{18}$	$5.205 \cdot 10^{-5}$
dodecylamine	$2.533 \cdot 10^{-20}$	$1.447 \cdot 10^{+24}$	$2.561 \cdot 10^{18}$	$7.199 \cdot 10^{-5}$
octadecylamine	$7.627 \cdot 10^{-21}$	$2.190 \cdot 10^{+24}$	$2.803 \cdot 10^{18}$	$2.551 \cdot 10^{-5}$
oleylamine	$1.110 \cdot 10^{-20}$	$2.104 \cdot 10^{+24}$	$2.904 \cdot 10^{18}$	$1.111 \cdot 10^{-5}$
nonanoic acid	$8.350 \cdot 10^{-21}$	$2.602 \cdot 10^{+24}$	$3.044 \cdot 10^{18}$	$4.327 \cdot 10^{-5}$
tridecanoic acid	$9.351 \cdot 10^{-21}$	$2.773 \cdot 10^{+24}$	$3.050 \cdot 10^{18}$	$1.287 \cdot 10^{-5}$
oleic acid	$5.155 \cdot 10^{-21}$	$2.317 \cdot 10^{+24}$	$2.873 \cdot 10^{18}$	$2.823 \cdot 10^{-5}$
hexacosanoic acid	$1.026 \cdot 10^{-20}$	$2.077 \cdot 10^{+24}$	$2.762 \cdot 10^{18}$	$3.126 \cdot 10^{-5}$
4-biphenylacetic acid	$3.034 \cdot 10^{-21}$	$2.283 \cdot 10^{+24}$	$3.288 \cdot 10^{18}$	$2.652 \cdot 10^{-6}$
1-pyrenebutyric acid	$8.629 \cdot 10^{-21}$	$2.142 \cdot 10^{+24}$	$2.592 \cdot 10^{18}$	$1.426 \cdot 10^{-4}$

Table 11.6: Calculated diffusivity for T=180°C.

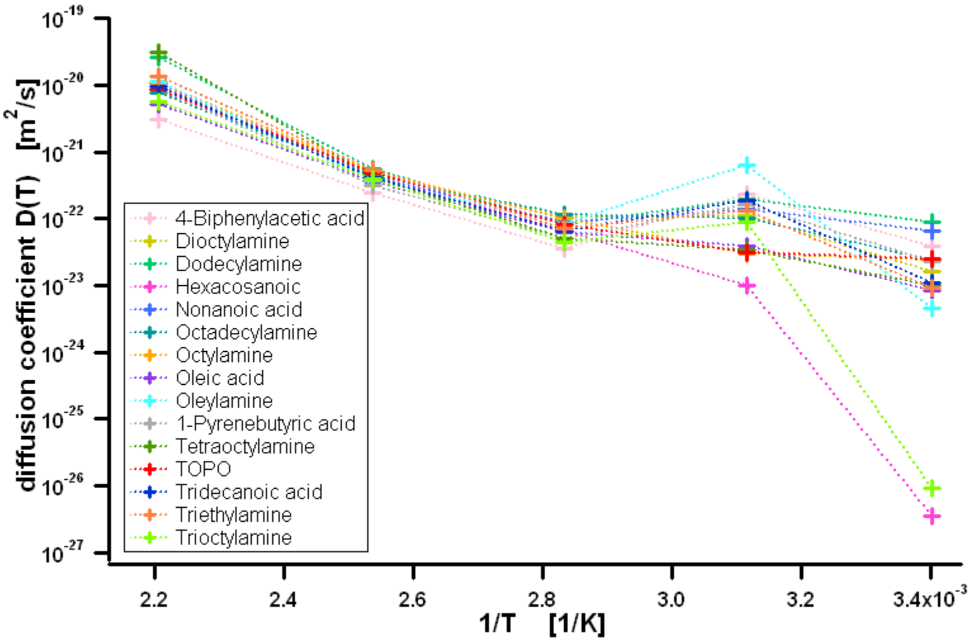

Figure 11.17: Values of D(T) for all surfactants plotted over T^{-1} and fitted with the function described in equation 11.25.

surfactant	$D_0(T)$ $\left[\frac{m^2}{s}\right]$	Q $\left[\frac{kJ}{mol}\right]$
TOPO	$1.8142 \cdot 10^{-17}$	29.9086
triethylamine	$3.1481 \cdot 10^{-17}$	30.2894
octylamine	$2.3545 \cdot 10^{-17}$	30.0940
dioctylamine	$2.0630 \cdot 10^{-17}$	29.9535
trioctylamine	$1.1081 \cdot 10^{-17}$	29.6026
tetraoctylammonium bromide	$8.2866 \cdot 10^{-17}$	30.8971
dodecylamine	$6.3399 \cdot 10^{-17}$	30.6302
octadecylamine	$1.5414 \cdot 10^{-17}$	29.7098
oleylamine	$2.3011 \cdot 10^{-17}$	29.8620
nonanoic acid	$1.7504 \cdot 10^{-17}$	29.8720
tridecanoic acid	$2.0499 \cdot 10^{-17}$	30.0640
oleic acid	$1.0212 \cdot 10^{-17}$	29.6109
hexacosanoic acid	$2.3708 \cdot 10^{-17}$	30.2727
4-biphenylacetic acid	$4.7323 \cdot 10^{-18}$	28.6506
1-pyrenebutyric acid	$1.9496 \cdot 10^{-17}$	30.1962
average	$2.5715 \cdot 10^{-17}$	29.97

Table 11.7: Fitted values of pre exponential factor $D_0(T)$ and activation energy Q.

11.3.3 Conclusion

The obtained values are with an average diffusion prefactor of $D_0 = 2.5715 \cdot 10^{-17} \frac{m^2}{s}$ much smaller than the value for the diffusion of O in $Co_{0.96}O$ for a temperature range of 973K-1473K, $D_{0(CoO)} = 6.6 \cdot 10^{-11} \frac{m^2}{s}$ [93]. This can be explained by the effective diffusivity that was calculated, as the sample consists of several layers of nanoparticles, which lead to a delay in the oxygen diffusion from top to bottom of each cluster in the sample.[12] The surfactants at the particle surface are expected to delay the oxygen diffusion, as well, as is described in section 9.4. The calculated activation energy $Q = 29.97 \frac{kJ}{mol}$ is lower than the activation energy of the diffusion of oxygen in $Fe_{0.8}Co_{0.2}$ with $Q_{FeCo} = 65.9 \frac{kJ}{mol}$, $\alpha - Fe$ with $Q_{\alpha - Fe} = 79.5 \frac{kJ}{mol}$ in a temperature range of 473K-1073K or O in $Co_{0.96}O$ for a temperature range of 973K-1473K with $Q = 102.1 \frac{kJ}{mol}$ [51]. An effective diffusivity of oxygen in Pd nanocluster of $D_n = 8.5 \cdot 10^{-18} \frac{m^2}{s}$ at a temperature of 393K is described in [92]. For metal atoms in metal nanoclusters a diffusivity in the order of $10^{-22} \frac{m^2}{s}$ to $10^{-17} \frac{m^2}{s}$ is described at 293K in [92]. An activation energy for oxygen diffusion in CoO of $Q = 100.27 \frac{kJ}{mol}$ can be found in [94]. An exponential prefactor of $D_0 = 5 \cdot 10^{-3} \frac{m^2}{s}$ and an activation energy of $Q = 11.427 \frac{kJ}{mol}$ are described in [95].

---

[12] The start of the oxidation of the particles closer to the bottom of the clusters is delayed compared to the particles at the cluster surface as the oxygen has to diffuse through the layers above.

12 Summary

Cobalt nanoparticles fabricated with different surfactants vary in their size, shape and crystallinity. Hence they exhibit a different behaviour during oxidation.
To investigate the influence of the surfactants on the oxidation process of the nanoparticles, all above mentioned parameters have to be kept constant. At the present time it is impossible to fabricate nanoparticles with different surfactants and equal parameters. Therefore a surfactant exchange had to be carried out.
Two batches of nanoparticles were fabricated with TOPO as stabilizing surfactant during formation and one batch with oleylamine as stabilizing surfactant. Subsequently a surfactant exchange was carried out. The size of the particles was determinated by charting TEM images.
In the first experiment fourteen surfactants with either an amine or a carboxyl headgroup and different chainlengths and number of chains or benzene rings were exchanged to the particle surface. The success of the exchange was proven by IR-spectroscopy. The surfactant exchange led to a decrease of the particle size which was found to be greater in the case of a carboxyl headgroup due to the formation of cobalt oleate during the exchange.
The long time oxidation behaviour of the samples at room temperature under ambient conditions was monitored indirectly by repeated measurements of the hysteresis curve and determination of the saturation magnetic moment with an AGM. Assumed that the decrease of the saturation magnetic moment is proportional to a decrease of the amount of Co and equal to an increase of the amount of the expected to be neglectable (magnetic) contributing CoO, the amount of CoO can be estimated.
For samples of this batch the oxidation at different temperatures −18°C, 48°C, 80°C, 121°C, 180°C and 300°C was investigated. The samples stored at −18°C, room temperature (~ 21°C) and 48°C developed a passivating oxide layer after 60-100 days and the oxidation process slowed down, partly to a negligible extent. Samples stored at higher temperatures oxidized completely after different time spans.
The second experiment consisted of particles fabricated with TOPO and 4 surfactants for exchange, two with an amine headgroup and two with an carboxyl headgroup. The third batch was fabricated with oleylamine and the surfactant was exchanged to two with carboxyl headgroup and one with an amine headgroup. The room temperature oxidation behaviour is in good agreement with the results from the first experiment.

As the particles were investigated between half an hour and one day after first exposure to air, an oxidation progress had already taken place at the time of the first measurement. The following measurements were always normalized to the first dataset for each sample. As only the qualitative behavior was observed and compared and no direct values were calculated, this was rated sufficient.

For all batches no direct influence of the surfactant on the oxidation could be found.
The particles stored at 180°C underwent a change in the crystallinity. Before the exposure to heat the samples consisted of mono- and polycrystalline particles, afterwards the particles were completely polycrystallinic and the volume had expanded. The measured volume

expansion met the calculated volume for the one expected to occur by complete oxidation. For incomplete oxidation, TEM images showed a greater amount of oxide as calculated from the magnetization measurements. This leads to the conclusion that the antiferromagnetic CoO behaves not completely nonmagnetic but contributes partly to the overall magnetic properties.

A finite elements simulation lead to the assumption that an influence of the surfactants on the oxidation of the particles is only detectable during the first thirty minutes after initial exposure to air. To allow this measurement the setup of the experiment had to be modified. The measurements showed an oxidation dependence on the surfactant during the first minutes of exposure to air. Even a separate influence of headgroup and tailgroup could be detected. But the long time oxidation was found to be dependent on the size, shape and crystallinity of the particles. Additionally it was found that, other than initially expected, the crystal structure is influenced by the exchanged surfactant in terms of single crystal or multigrain particles. Further HRTEM analysis determined the particles to consist of fcc-cobalt and fcc-CoO.

The oxidation dependence on the particle shape was simulated with a finite elements model, but the model was found to be insufficient to describe the obtained data. First contributions were made for a possible improvement of the model, but did not lead to a satisfactory explanation of the oxidation behaviour. The curves can be described best if the antiferromagnetic cobalt oxide is not assumed to be completely non-magnetic, but if it contributes partly to the magnetic properties, especially on the planar surfaces. This offers a good onset for further studies.

At last the oxidation progress in multilayer clusters was investigated. It was found that cluster oxidize gradually from the exposed side to the substrate and that in the long term they oxidize completely.

As most samples used for oxidation studies contain an amount of material that supports cluster formation, the effect of gradual oxidation will have to be taken into account for further investigations.

For the multilayer samples of particles, investigated in section 5.1, section 6 and section 7 with regard to the effect of the surfactant, the effective oxygen diffusivity for the entire sample was calculated with a simplified model. The advance of the oxygen, which is slow compared to bulk values, seems to be additionally retarded by the surfactants on the particle surfaces.

Bibliography

[1] H. Kachkachi, A. Ezzir, M. Nogues, and E. Tronc. Surface effects in nanoparticles: application to maghemite $\gamma - \mathsf{Fe_2O_3}$. *The European Physical Journal B*, 14:681–689, 2000.

[2] H. H. Qi and M. P. Wang. Size and shape dependent melting temperature of metallic nanoparticles. *Materials Chemistry and Physics*, 88:280–284, 2004.

[3] S. P. Gubin, Yu A. Koksharov, G. B. Khomutov, and G. Yu. Yurkov. Magnetic nanoparticles: preparation, structure and properties. *Russian Chemical Reviews*, 74(6):539–574, 2005.

[4] Peter H. M. Hoet, Irene Brüske-Hohlfeld, and Oleg V. Salata. Nanoparticles - known and unknown health risks. *Journal of Nanobiotechnology*, 2(12), 2004.

[5] K. Lance Kelly, Eduardo Coronado, Lin Lin Zhao, and George C. Schatz. The Optical Properties of Metal Nanoparticles: The Influence of Size, Shape, and Dielectric Environment. *Journal of Physical Chemistry B*, 107:667–668, 2003.

[6] Patricia Berger, Nicholas B. Adelman, Katie J. Beckman, Dean J. Campbell, Arthur B. Ellis, and George C. Lisensky. Preparation and Properties of an Aqueous Ferrofluid. *Journal of Chemical Education*, 76(7):943–948, 1999.

[7] Sachiko Kodama, Ysushi Miyajima, and Tetsuhide Hidaka. Morpho Towers - Two Stand. http://www.youtube.com/watch?v=me5Zzm2TXh4&feature=related, 28. February. 2011.

[8] K. Raj, B. Moskowitz, and R. Casciari. Advances in ferrofluid technology. *Journal of Magnetism and Magnetic Materials*, 149:174–180, 1995.

[9] Peter Entel. Simulating complex functional magnetic materials on supercomputers. Talk, Physikalisches Kolloquium Universität Bielefeld, 2009.

[10] Oleg V. Salata. Applications of nanoparticles in biology and medicine. *Journal of Nanobiotechnology*, 2(3), 2004.

[11] Sang Won Lee, Seongtae Bae, Yasushi Takemura, In-Bo Shim, Tae Min Kim, Jeongryul Kim, Hong Jae Lee, Shayne Zurn, and Chul Sung Kim. Self-heating characteristics of cobalt ferrite nanoparticles for hyperthermia application. *Journal of Magnetism and Magnetic Materials*, 310:2868–2870, 2007.

[12] R. Sharma and C. J. Chen. Newer nanoparticles in hyperthermia treatment and thermometry. *Journal of nanoparticle research*, 11(3):671–689, 2009.

[13] A. Weddemann, A. Auge, C. Albon, F. Wittbracht, and A. Hütten. Magnetoresistive Detection of Magnetic Beads and Nanoparticles - Spatial resolution and number sensitive detection. *Fourth International Conference on Quantum, Nano and Microtechnologies, ICONM 2010*, pages 33–37, 2010.

[14] B. D. Cullity and C. D. Graham. *Introduction to magnetic materials.* Wiley, IEEE Press, second edition, 2009.

[15] Andreas Hütten. Festkörper- und Oberflächenphysik. Vorlesungsskript, SoSe 2007.

[16] Charles Kittel. *Einführung in die Festkörperphysik.* Oldenbourg Verlag, München Wien, 14. edition, 2005.

[17] Harals Ibach and Hans Lüth. *Festkörperphysik, Einführung in die Grundlagen.* Springer-Verlag, Berlin, Heidelberg, 7. edition, 2009.

[18] Inga Ennen. *Magnetische Nanopartikel als Bausteine für granulare Systeme: Mikrostruktur, Magnetismus und Transporteigenschaften.* Doktorarbeit, Universität Bielefeld, Fakultät für Physik, 2008.

[19] D. Jiles. *Introduction to magnetism and magnetic materials.* Chapman and Hall, London, first edition, 1991.

[20] B. Cullity. *Introduction to magnetic materials.* Addison Wesley Publishing Company, Massachusetts, 1972.

[21] E. Wohlfahrt. *Ferromagnetic materials.* North Holland Publishing Company, Amsterdam, 1980.

[22] G. F. Goya, T. S. Berquo, F. C. Fonseca, and M. P. Morales. Static and dynamic magnetic properties of spherical magnetite nanoparticles. *Journal of Applied Physics*, 94(3520-3528), 2003.

[23] H. Yang, C. M. Sheng, Y. K. Su, T. Z. Yang, H. J. Gao, and Y. G. Wang. Self-assembly and magnetic properties of cobalt nanoparticles. *Applied Physics Letters*, 82(26):4729–4732, 2003.

[24] A. Hütten, D. Sudfeld, I. Ennen, W. Hachmann, K. Wojczykowski, P. Jutzi, W. Saikaly, and G. Thomas. New magnetic nanoparticles for biotechnology. *Journal of Biotechnology*, 112:47–63, 2004.

[25] Daniela Sudfeld. *Hochauflösende Mikrostrukturanalyse von magnetischen* $(\mathsf{Fe}_{1-x}\mathsf{Co}_x)_{1-y}\mathsf{Pt}_y-$*Nanopartikeln.* Doktorarbeit, Universität Bielefeld, Fakultät für Physik, 2005.

[26] Karsten Wegner, Sotiris E. Pratsinis, Michael Köhler, Winnacker, and Küchler. *Chemische Technik: Prozesse und Produkte, Band 2: Neue Technologien.* WILEY-VCH Verlag GmbH & Co, Weinheim, 2004.

[27] Ferdi Schüth, An-Hui Lu, and Elena Lorena Slabas. Magnetische Nanopartikel: Synthese, Stabilisierung, Funktionalisierung und Anwendung. *Angewandte Chemie*, 11:1242–1266, 2007.

[28] Inga Ennen. Charakterisierung von Cobalt-Nanopartikeln und Untersuchungen zur Herstellung granularer Strukturen. Diplomarbeit, Universität Bielefeld, Fakultät für Physik, 2003.

[29] Klaus Wojczykowski. *Untersuchungen zur Synthese und Stabilisierung metallischer Nanopartikel*. Doktorarbeit, Universität Bielefeld, Fakultät für Chemie, 2006.

[30] Andrea. R. Tao, Susan Habas, and Peidong Yang. Shape Control of colloidal Metal Nanocrystals. *Applied Physics Letters*, 73(19):2841–2843, 1998.

[31] Chao Wang, Hideo Daimon, Taigo Onodera, Tetsunori Koda, and Shouheng Sun. A General Approach to the Size- and Shape-Controlled Synthesis of Platinum Nanoparticles and Their Catalytic Reduction of Oxygen. *Angew. Chem.*, 120:3644–3647, 2008.

[32] Victor K. LaMer and Robert H. Dinegar. Theory, Production and Mechanism of Formation of Monodispersed Hydrosols. *Journal of the American Chemical Society*, 72(11):4847–4854, 1950.

[33] Dieter Horn and Jens Rieger. Organische Nanopartikel in wässriger Phase - Theorie, Experiment und Anwendung. *Angew. Chem.*, 113:4460 – 4492, 2001.

[34] Bin Liu, Hua Chun Zeng, G. B. Khomutov, and G. Yu. Yurkov. Symmetric and Asymmetric Ostwald Ripening in the Fabrication of Homogeneous Core-Shell Semiconductors. *Small*, 1(5):566–571, 2005.

[35] Viktor F. Puntes, Kannan M. Krishnan, and A. Paul Alivisatos. Colloidal Nanocrystal Shape and Size Control: The Case of Cobalt. *Science*, 291:2115–2118, 2001.

[36] Irina Dück. Untersuchungen magnetischer Eigenschaften und spinabhängiger Transportphänomene von Kobalt-Nanopartikeln, February 2009.

[37] Daniel Meißner. *Zitronensäureether als Liganden für die zuverlässige Funktionalisierung von magnetischen Nanopartikeln.* Doktorarbeit, Universität Bielefeld, Fakultät für Chemie, 2010.

[38] Vikas Nandwana, Kevin E. Elkins, Narayn Poudal, Girija s. Chaubey, Kazuaki Yano, and J. Ping Liu. Size and Shape Control of Monodisperse FePt Nanoparticles. *Journal of Physical Chemistry C*, 111:4185–4189, 2007.

[39] Carsten Waltenberg. *Synthese und Charakterisierung von cobalthaltigen, binären, magnetischen Nanopartikeln.* Doktorarbeit, Universität Bielefeld, Fakultät für Chemie, 2007.

[40] Nadine Mill. private discussion.

[41] Michael Peter. private discussion.

[42] Daniel Meissner. Auf dem Weg zu Co-core-Au-shell-Nanopartikeln, Blockpraktikum in der AC III. Assistent: Carsten Waltenberg, 2004.

[43] N. Cabrera and N. F. Mott. Theory of the oxidation of metals. *Reports on Progress in Physics - Rep. Prog. Phys*, 12:163–184, 1949.

[44] P. A. Chernavskii, N. V. Peskov, A. V. Mugtasimov, and V. V. Lunin. Oxidation of Metal Nanoparticles: Experiment and Model. *Russian Journal of Physical Chemistry B*, 1(4):394–411, 2007.

[45] A. Auge, A. Weddemann, F. Wittbracht, B. Vogel, and A. Hütten. A level set based approach for modelling oxidation processes of ligand stabilized metallic nanoparticles. *Applied Physics Letters*, 96:093111, 2010.

[46] JR A. T. Fromhold. Growth rate of low-space-charge oxides on spherical metal particles. *Journal of Physics and Chemistry of Solids*, 49(10):1159–1166, 1988.

[47] Vladimir. P. Zhdanov and Bengt Kasemo. Cabrera-Mott kinetics of oxidation of nm-sized metal particles. *Chemical Physics Letters*, 452:285–288, 2008.

[48] P. A. Chernavskii, G. V. Pankina, A. P. Chernavskii, P. Afanasiev N. V. Penkov, N. S. Perov, and V. A. Tennov. In Situ Magnetic Study of the Low-Temperature Oxidation of Carbon-Supported Cobal Nanoparticles. *Journal of Physical Chemistry C*, 111:5576–5581, 2007.

[49] S. J. Roosendaal, A. M. Vredenberg, and F. H. P. M. Habraken. Oxidation of Iron: The Relation between Oxidation Kinetics and Oxide Electronic Structure. *Physical Review Letters*, 84(15):3366–3369, 2000.

[50] Horst Kuchling. *Taschenbuch der Physik.* Fachbuchverlag Leipzig im Carl Hanser Verlag, München, 19. edition, 2007.

[51] K.-H. Hellwegeand J. L. Olsen. *Landolt-Börnstein, Zahlenwerte und Funktionen aus Physik, Chemie, Astronomie, Geophysik und Technik, Sechste Auflage - Eigenschaften der Materie in ihren Aggregatzuständen, 5. Teil, Bandteil b, Transportphänomene II, Kinetik, Homogene Gasgleichgewichte.* Springer-Verlag, Berlin, Heidelberg, New York, 1968.

[52] Brent Fultz and James M. Howe. *TransmissionElectron Microscopy and Diffractometry of Materials.* Springer-Verlag, Berlin Heidelberg, 3rd edition, 2001.

[53] Paul A. Tipler. *Physik.* Spektrum Akademischer Verlag, Heidelberg, Berlin, Oxford, 1998.

[54] Inga Ennen. private discussion.

[55] Ludwig Reimer and Gerhard Pfefferkorn. *Raster-Elektronenmikroskopie.* Springer Verlag, Berlin Heidelberg New York, 1973.

[56] Ludwig Reimer. *Elektronenmikroskopische Untersuchungs- und Präparationsmethoden.* Springer Verlag, Berlin Heidelberg New York, zweite edition, 1967.

[57] Annalena Wolff. Novel approach to synthesize magnetic nanoparticles, May 2010.

[58] Nan Yao. *Focused Ion Beam Systems.* Cambridge University Press, Cambridge, New York, Melbourne, Madrid, Cape Town, Singapore, Sao Paulo, 2007.

[59] Princeton Measurement Corporation. *MicroMag* ^{TM}*2900, Alternating Gradient Magnetometer (AGM) Instruction Manual.*

[60] Hugo Volkmann. *Handbuch der Infrarot-Spektroskopie.* Verlag Chemie, Weinheim, Bergstrasse, second edition, 1972.

[61] Helmut Günzler and H. Michael. Heise. *IR-Spektroskopie*. VCH, Weinheim, dritte, neubearbeitete edition, 1996.

[62] Helmut Günzler and H. Böck. *IR-Spektroskopie*. Verlag Chemie, Physik Verlag, Weinheim, 1975.

[63] J. H. van der Maas. *Basic Infrared Spectroscopy*. Heyden & Son Ltd., London, New York, Rheine, second edition, 1972.

[64] Huiping Shao, Yuqiang Huang, HyoSook Lee, Yong Jae Suh, and ChongOh Kim. Effect of surfactants on the size and shape of cobalt nanoparticles synthesized by thermal decomposition. *Journal of Applied Physics*, 99:08N702–1 – 08N702–3, 2006.

[65] Katrin Eckstädt. Untersuchung zur Streuung des Partikelwachstums stabilisierter Cobalt-Nanopartikel, 2007.

[66] NIST Chemistry WebBOOK. NIST Standard Reference Data Program, Collection (C) 2009 copyright by the U.S. Secretary of Commerce, on behalf of the United States of America. All rights reserved. http://webbook.nist.gov/chemistry, Sadtler Research Labs Under US-EPA Contract, 02. February. 2011.

[67] K. Ekelund, E. Sparr, J. Engblom, H. Wennerström, and S. Engström. An AFM Study of Lipid Monolayers. 1. Pressure-Induced Physe Behaviour of Single and Mixed Fatty Acids. *Langmuir*, 15:6946–6949, 1999.

[68] Hans-Dieter Dörfler. *Grenzflächen und kolloid-disperse Systeme: Physik und Chemie*. Springer Verlag, Berlin Heidelberg New York, first edition, 2002.

[69] Doris M. Spori, Nagaiyanallur V. Venkatarman, Samuele G. P. Tosatti, Firat Durmaz, Nicholas D. Spencer, and Stefan Zürcher. Influence of Alkyl Chain Length on Phosphate Self-Assembled Monolayers. *Langmuir*, 23:8053–8060, 2007.

[70] Shouheng Sun and G. Murray. Synthesis of monodisperse cobalt nanocrystals and their assembly into magnetic superlattices. *Journal of Applied Physics*, 85(5):4325–4330, 1999.

[71] D. J. Sellmyer, C. P. Luo, Y. Qiang, and J. P. Liu. *Magnetism of Nanophase composite films, Handbook of Thin Film Materials, Volume 5: Nanomaterials and Magnetic Thin Films*. Academic Press, by h. s. nalwa edition, 2002.

[72] D. J. Sellmyer and R. Skomski. Magnetism of nanophase composites. *Scripta materialia*, 47:531–535, 2002.

[73] H. N. Bertram and H. J. Richter. Arhenius-Neel thermal decay in polycrystalline thin film media. *Journal of applied physics*, 85(8):4991–4993, 1999.

[74] R. H. Victora. Predicted Time Dependence of the Switching Field for Magnetic Materials. *Physical Review Letters*, 63(4):457–460, 1989.

[75] Sushin Chizukami and Stanley H. Charap. *Physics of Magnetism*. Krieger Publishing Company, Malabar, 1978.

[76] Parahashu Kharel, Roger D. Kirby, Ralph Skomski, and David J. Sellmyer. Structural, magnetic and magneto-transport properties of Pt-alloyed MnBi thin films. *Journal of applied physics*, 107:09E303, 2010.

[77] X. Liu, M. M. Steiner, R. Sooryakumar, G. A. Prinz, R. F. C. Farrow, and G. Harp. Exchange stiffness, magnetization, and spin waves in cubic and hexagonal phases of cobalt. *Phys. Rev. B*, 53(18):12166–12172, 1996.

[78] D. Sudfeld, K. Wojczykowski, W. Hachmann, S. Heitmann, K. Rott, T. Hempel, S. Kämmerer, P. Jutzi, A. Hütten, and G. Reiss. Magnetic cobalt nanocrystals organized in patches and chains. *IEEE Trans. Magn.*, 38(5):2601, 2002.

[79] Hong Huang and J. Hermanson. Bonding and magnetism of chemisorbed oxygen on Fe(001). *Physical Review B*, 32(10):6312–6318, 1985.

[80] John R. Smith, G. Gay, and Frank J. Arlinghaus. Self-consistent local-orbital methodfor calculating surface electronic structure: Application to Cu (100). *Physical Review B*, 21(6):2201–2221, 1980.

[81] S. R. Chubb and W. E. Pickett. First-Principles Determination of Giant Adsorption-Induced Surface Relaxation in p(1x1)O/Fe(001). *Physical Review Letters*, 58(12):1248–1251, 1987.

[82] Mathias Getzlaff. *Surface Magnetism, Correlation of Structural, Electronic and Chemical Properties with Magnetic Behavior.* Springer Verlag, Berlin Heidelberg, first edition, 2010.

[83] Mathias Getzlaff. *Untersuchungen der magnetischen Eigenschaften dünner Eisen- und Kobaltschichten sowie der Austauschaufspaltung adsorbatinduzierter Zustände auf Eisenkristallen, -legierungen und ferromagnetischen Filmen.* PhD thesis, Universität Bielefeld, Fakultät für Physik, 1993.

[84] Juan Rodriguez-Carvajal and Laboratoire Leon Brillouin (CEA-CNRS). WinPLOTR-2006, a Powder Diffraction graphic tool for Windows, Linux and MacOS, Version 0.50 April - 2009; Toolbar FullProf Suite Program (1.10). http://www.ill.fr/dif/Soft/fp/ , Institut Laue-Langevin, BP 156, 38042 Grenoble Cedex 9, France, 2009.

[85] U.S. National Institute of Standards, Technology, Fachinformationszentrum Karlsruhe, and Germany. Inorganic Crystal Structure Database - ICSD, Version 1.1 (July 2008). http://www.fiz-karlsruhe.de/icsd.html , FIZ Karlsruhe, Hermann-von-Helmholtz-Platz 1, 76344 Eggenstein-Leopoldshafen, Germany, 2010.

[86] 2011 Crystal Maker Software Ltd. Crystal Maker for Windows and Crystal and Molecular structures - Visualization & Diffraction. http://www.crystalmaker.com/crystalmaker/ , CrystalMaker Software Limited, Centre for Innovation & Enterprise, Begbroke Science Park, Sandy Lane, Yarnton, Oxfordshire, OX5 1PF, UK, 19. March. 2011.

[87] Ulf Wiedwald, Kai Fauth, Markus Hessler, Hans-Gerd Boyen, Frank Weigl, Michael Hilgendorff, Michael Giersig, Gisela Schütz, Paul Ziemann, and Michael Farle. From Colloidal Co/CoO Core/Shell Nanoparticles to Arrays of Metallic Nanomagnets: Surface Modification and Magnetic Properties. *ChemPhysChem*, 291(6):2522–2526, 2005.

[88] Ulf Wiedwald. *Interface Magnetism in Co/CoO core-shell nanoparticles and their transformation to pure metallic nanoparticles.* Doktorarbeit, Universität Duisburg-Essen, Fachbereich Physik, 2004.

[89] Stanley Osher and Ronald Fedkiw. *Level Set Methods and Dynamic Implicit Surfaces.* Springer, New York, Berlin,Heidelberg, 2003.

[90] Martin Eden Glicksman. *Diffusion in Solids -Field Theory, Solid-State Principles, and Applications.* Wiley, New York, 2000.

[91] J. Crank. *The mathematics of diffusion.* Clarendon Press, Oxford, second edition, 1975.

[92] D. L. Beke. *Journal of Metastable and Nanocrystalline Materials - Nanodiffusion - Diffusion in Nanostructured Materials.* Trans Tech Publications, Switzerland, 2004.

[93] C. E. Allen, D. L. Beke, F. Bénic, C. M. Bruff, A. V. Chadwick, G. Erdélyi, F. Faupel, C. H. Hsieh, H. Jain, G. Kroll, H. Matzke, G. E. Murch, V. V. Rondinella, and E. G. Seebauer. *Landolt-Börnstein - Group III Condensed Matter Numerical Data and Functional Relationships in Science and Technology: Diffusion in Non-Metallic Solids (Part 1) without Volume Diffusion in Oxides.* Springer-Verlag, 1999.

[94] Earl. A. Gulbransen and Kenneth. F. Andrew. The Kinetics of the Oxidation of Cobalt. *Journal of the electrochemical society*, 98(6):241–251, 1951.

[95] W. K. Chen and R. A. Jackson. Oxygen self-diffusion in undoped and doped cobaltous oxide. *Journal of Physics and Chemistry of Solids*, 30:1309–1314, 1969.

Appendix

Presentations and Publications

.0.4 Conference Contributions

- Britta Vogel, Carsten Waltenberg, Inga Ennen, Harald Rösner, Peter Jutzi und Andreas Hütten, *Synthese von Au-core/Co-shell Nanopartikeln*, 72. Jahrestagung der DPG und DPG Frühjahrstagung des Arbeitskreises Festkörperphysik mit anderen Fachverbänden und den Arbeitskreisen der DPG, 25.-29. Februar 2008, Berlin, Deutschland, Poster MA 22.5.

- Britta Vogel, Axel Dreyer, Nadine Mill, Anna Regtmeier, Inga Ennen, Daniel Ebke, Simone Herth, and Andreas Hütten, *Ligand-dependence of longterm stability of cobalt nanoparticles*, DPG Frühjahrstagung der Sektion Kondensierte Materie (SKM), Dresden, 22. - 27. März 2009, Vortrag MA 36.1

- Britta Vogel, Axel Dreyer, Nadine Mill, Anna Regtmeier, Inga Ennen, Daniel Ebke, Simone Herth, and Andreas Hütten, *Oxygen diffusion in and reaction rate of cobalt nanoparticles stabilized with different ligands*, DPG Frühjahrstagung der Sektion Kondensierte Materie (SKM) Dresden, 22. - 27. März 2009, Poster MM 35.35

- Britta Vogel, A. Dreyer, N. Mill, I. Ennen, A. Hütten *Ligandenstabilisierte Co-Nanopartikel*, 13. Deutsche Physikerinnentagung, Frankfurt, 5.-8. November 2009

- Britta Vogel, Axel Dreyer, Nadine Mill, Katrin Eckstädt, Annalena Wolff, Dieter Akemeier, Alexander Weddemann, Alexander Auge, Simone Herth, and Andreas Hütten, *Oxidation of multilayers of ligand stabilized magnetic cobalt nanoparticles*, DPG Frühjahrstagung der Sektion Kondensierte Materie (SKM) Regensburg, 21. - 26. März 2010, Poster MA 10.68

- Britta Vogel, Katrin Eckstädt, Nadine Mill, Alexander Auge, Jan-Philipp Grote, Andreas Hütten, *Shape dependant oxidation of cobalt nanoparticles*, DPG Frühjahrstagung der Sektion AMOP (SAMOP) und der Sektion Kondensierte Materie (SKM) 75. Jahrestagung der DPG, Dresden, 13. - 18. März 2011, Poster MA 19.13

.0.5 Publications

- A. Auge, A. Weddemann, F. Wittbracht, B. Vogel and A. Hütten, *A level set based approach for modelling oxidation processes of ligand stabilized metallic nanoparticles*, Applied Physics Letters, 96:093111, 2010

- *Oxidation of surfactant stabilized, magnetic Cobalt nanoparticles* - work in progress

Nun, wie fängt man eine Danksagung an?
Ich möchte hierbei chronologisch vorgehen, da alles ohne die vorangegangenen Ereignisse vermutlich anders gekommen wäre.

DANKSAGUNG

Ich möchte meinen Eltern danken, dass sie in jungen Jahren den Grundstein für mein Interesse an Naturwissenschaften und Mathematik legten. Geduldig beantworteten sie kindliche "Warum?" - Fragen und ermutigten mich stets, den Dingen auf den Grund zu gehen und bei der Lösung von Problemen neue Denkansätze auszuprobieren.
Dank gebührt auch meiner Grundschullehrerin Frau Dubbert, welche uns im Sachkundeunterricht auch eigene Ideen ausprobieren liess, sowie meinem Physik-LK-Lehrer Herrn Heuermann, der den Physikunterricht nicht zur trockenen Theorie werden liess, sondern es schaffte, uns mit interessanten, verblüffenden und lehrreichen Experimenten stets aufs Neue zu motivieren und seine eigene Faszination für die Physik an uns weiterzugeben.
Ebenso möchte ich meinen Mitstudenten danken für kurzweiliges Übungszettel rechnen und interessante Versuche fernab des Lehrplanes. [Irgendwann werden wir noch das erste Theremin-Orchester gründen... .]
Besonders erwähnen möchte ich an dieser Stelle Stefan Fröhlich und Andreas Helmstedt, mit denen ich für einige Prüfungen lernte; letzterem auch für physikalische Diskussionen per ICQ; und Annalena Wolff als Mitbewohnerin in der Physikerinnen-WG, wo Diskussionen über Physik beim Frühstück und weit nach dem Abendbrot keine Seltenheit waren.
Dank auch an Prof. Dr. Friederike Schmid für die Betreuung meiner Diplomarbeit in der theoretischen Physik.
Besonders danken möchte ich Prof. Dr. Andreas Hütten, der mir nach meiner Diplomarbeit in der theoretischen Physik eine Doktorarbeit in der Experimentalphysik ermöglichte.
Auch die gesamte Arbeitsgruppe D2 sollte hier Erwähnung finden für ein tolles Arbeitsklima, fruchtbare Diskussionen, hilfreiche Unterstützung bei Schwierigkeiten und vielem mehr; besonders hervorheben möchte ich: Karsten Rott für seine unermüdliche Geduld bei der Erklärung neuer und alter Geräte und Lösungen von Problemen; Nadine Mill für die Herstellung von "Abermillionen von" Nanopartikeln und Unterstützung am TEM; Axel Dreyer, Michael Peter und Katrin Eckstädt für die Herstellung weiterer Nanopartikel. Dieter Akemeier und Annalena Wolff für die Mitarbeit an der FIB; Anna Regtmeier für Unterstützung am TEM und AGM; Jan-Philipp Grote für die Unterstützung am AGM und dort vor allem bei den Tieftemperaturmessungen: Danke für die Übernahme der "Tagschichten" bei den "Rund-um-die-Uhr-Messungen". In diesem Zusammenhang sollten auch Savio Fabretti, Oliver Schebaum und Inga-Mareen Imort genannt werden für die Versorgung mit flüssigen Helium. Dank auch an Alexander Auge für Simulationen der Partikeloxidation. Inga Ennen für HRTEM-Aufnahmen und Korrekturlesen von Teilen der Theorie. Weiter erwähnt werden sollen Daniel Meissner, Carsten Waltenberg, Manuel Glas... und natürlich Aggi Windmann als Sekretärin für Hilfe in Verwaltungsangelegenheiten und Versorgung mit Büromaterial und Hilfsbereitschaft.

Meine wechselnde Bürobesetzung: Volker Drewello, Felix Keseberg, Andreas Bublitz, Hendrik Wulfmeier, Annalena Wolff (Riesendanke fürs Korrekturlesen und die Englischkorrektur) und vor allem meine Bürobesetzung während des Zusammenschreiben: Mahboobeh Safarabadi für die wiederholte Erkenntnis, dass deutsche Umgangssprache sehr kompliziert sein kann, Ansätze zum Nachdenken über Formulierungen und dass manchmal eine präzisere Ausdrucksweise sinnvoller ist. Manuel Glas und vor allem Carolin Rademacher für die Belebung des Büros und Nadine Mill im Austausch für Manuel während der letzten Wochen.

Der Gleichstellungskommission danke ich für die Gewährung eines Anschlussstipendiums für drei Monate.

Weiter Dank gilt Alexander Damke für Onlinemotivation, geniale Fotos und Versorgung mit Musikvorschlägen, Claudia Fritz für unter anderem Carepaketen in den passendsten Momenten und meinem Bruder Martin für morgendliches Schwimmen und anschliessendes Frühstücken nach Nachtschichten.

Und letztendlich möchte ich Aleksandar Hizman danken, für die WG 2.0, seine Unterstützung, Diskussionen fernab der Physik, Bemühung um Ausgleich, seelische Unterstützung, Motivation bei Nachtschichten ... .

Vieles Wichtige, Interessante, Bewegende, Prägende wird hier unerwähnt bleiben. Wie so vieles letztendlich unvollständig bleibt.

Daher nun noch ein Dank an alle, die sich in dieser Aufzählung vermissen und denen die sich hier nicht vermissen, denen aber trotz alledem ein Platz an dieser Stelle gebührt hätte ... .